Modélisation de la propagation des ondes guidées dans les milieux hétérogènes et multiphysiques

Fakhraddin Seyfaddini Rashkolya

Modélisation et Simulation Multi Echelle

MSME UMR 8208

UNIVERSITÉ PARIS-EST SUP

École doctorale SIE : Sciences, Ingénierie et Environnement

Laboratoire MSME : Modélisation et Simulation Multi-Échelle

Thesis

submitted for the grade of Doctor of Philosophy

Speciality : Structures and Materials

Subject :

Modeling of guided wave propagation in heterogeneous and multiphysics media

by

Fakhraddin Seyfaddini Rashkolya

Defended on September 30, 2021

in front of the following board of examiners :

Mme. Marion Darbas	Université Sorbonne Paris Nord	*Présidente du jury*
Mme. Cécile Baron	CNRS, Aix-Marseille Université	*Rapportrice*
M. Marc Deschamps	CNRS, Université de Bordeaux 1	*Rapporteur*
M. Fabien Treyssède	Université Gustave Eiffel	*Examinateur*
M. Hung Nguyen-Xuan	Ho Chi Minh City University of Technology	*Examinateur*
M. Vu-Hieu Nguyen	Université Paris-Est Créteil	*Directeur de thèse*
M. Salah Naili	Université Paris-Est Créteil	*Co-Directeur de thèse*

Contents

Acknowledgments

Throughout this three years of PhD thesis I have received a great deal of support and assistance.

First, I would like to express my sincere gratitude to my supervisor Dr. Vu-Hieu Nguyen for giving me the opportunity to complete this PhD thesis. His knowledge, motivation and patience have given me more power and spirit to excel in my research. I really appreciated his continuous support and encouragement. Moreover, I thank him for his availability and listening. His advice guided me during these three years.

I would say thank you to my co-supervisor Dr. Salah Naili for providing guidance and feedback throughout this project. I'm grateful for my time working with him and for his insightful comments and suggestions which I truly appreciated. His advice and knowledge were a great help during this PhD thesis.

Besides my two supervisors, I would like to thank the members of the jury who have done me the honor of evaluating my work. To Dr. Marion Darbas as president of jury, Dr. Cécile Baron and Dr. Marc Deschamps as referee; and Dr. Fabien Treyssède as examiner.

My thanks also go out to the support I received from the collaborative work with Dr. Hung Nguyen-Xuan. Her guidance and constant feedback was really influential in developing my knowledge of numerical methods.

I would always remember my fellow office too for the fun-time we spent together that gave me the courage to complete tasks. Thanks to: Ali, Bao, Ivan, Thi, Madge. I cannot express enough thanks to all members of the MSME laboratory for creating a positive environment to work in and for always being nice to me. To Sophie, Yoann, Anne-sophie, Katharina, Manon, Léo, Florian, Nicolas, Giuseppe, Thibault, Guillaume, Gilles, Alexandre, Matthieu, Vittorio. I would also like to thank the technician team Hung-Son and Yasmine for their valuable help, as well as Isabelle for her kindness.

I am indebted to all my friends who were always so helpful in numerous ways. Thanks to my best friends Mozhgan, Mohsen R&D, Ali I&P, Anaïs, Virginie, Mahdïs.

Last but not least, I would like to thank my family, who is so important to me. I would like to thank my parents whose love are with me in whatever I pursue. Many thanks to my siblings Fatemeh, Mahdiyeh, Azam, Maryam, Mina, Khatere, Mohammad for their love and their support.

Abstract

Guided wave (GW) technology which is based on knowledge of the wave dispersion characteristics is widely used because it is a robust technique and an economical way for fast non-destructive evaluation (NDE) and structural health monitoring (SHM). Knowing the dispersion characteristics of guided waves, one may perform an inversion to obtain a non-destructive evaluation of a structure such as the earth surface in geophysics, corrosion of oil and gas pipelines, damage detection of planes, as well as ultrasound imaging of biological structures such as arteries or bone tissue. Basically, the inversion procedure is performed by minimizing the error between the dispersion curves obtained from experiments and modeling. Therefore, the development of low-cost and accurate computational methods for evaluating the wave dispersion is very important to enhance GW-based non-destructive techniques and has become a subject of extensive scientific investigations. The semi-analytical finite element method (SAFE) is one of the most popular techniques thanks to its capability in studying functionally graded or complex cross-section waveguides. The SAFE which evolved from the concept of Finite Elements but requires the discretization of the boundary of the computational domain only. To compute dispersion curves and mode shapes of guided-waves, only the cross-section of the waveguide needs to be discretized, while analytical analysis is applied in the direction of propagation. However, when studying heterogeneous and/or multiphysical (e.g. coupled solid-fluid or poroelastic) waveguides with complex geometries using the semi-analytical finite element method, excessive computational effort may be required, especially at high frequencies. In this thesis, we develop highly efficient computational approaches called semi-analytical isogeometric Galerkin (SAIGA-G) and semi-analytical isogeometric collocation (SAIGA-C) to compute the wave dispersion in different types of waveguide having complex geometry and / or material heterogeneities. For the case where the waveguide is immersed in a fluid or coupled to a semi-infinite media, perfectly matched layers (PML) were employed, and for which it has been shown that the method is very efficient for describing leaky guided waves. These approaches are based on the use of Non-Uniform Rational B-splines (NURBS) in the framework of isogeometric analysis as the basis functions for the geometry representation as well as for the approximation of pressure/displacement solution fields. The difference between these two approaches is based on the use of numerical integration. The SAIGA-G uses a numerical integration of type Gauss quadrature to evaluate the integrals. However, the SAIGA-C deals directly with the strong form of the PDE. The IGA collocation method has been developed to combine the accuracy and the smoothness advantages of the IGA method with the computational efficiency of the collocation method. The dispersion curves (phase velocity, wavenumber and energy velocity) are obtained from the resolution of the eigenvalue problem. Throughout the thesis, the obtained results are compared with the analytical solution obtained using the Disperse software and/or with the conventional SAFE method which uses Lagrange polynomials. It is shown that for computing the dispersion of GWs, using an approach based on SAIGA-G leads to a much faster convergence rate than using the conventional SAFE with the same shape function's order. Moreover, the continuity

of pressure/displacement at the interfaces could be significantly improved thanks to the smoothness feature of NURBS, showing advantage of SAIGA over SAFE in the evaluation of the shape modes of GWs in coupled systems. Although the accuracy of the SAIGA-C is lower than the others approaches, its implementation is simple and the required computational time may significantly be reduced.

Résumé

La technologie des ondes guidées (GW, pour Guided Wave), basée sur la connaissance des cactéristiques de dispersion des ondes, est largement utilisée pour l'évaluation non destructive (NDE, pour Non-Destructive Evaluation) et le contrôle de la santé des structures (SHM, pour Structural Health Monitoring). La connaissance des caractéristiques de dispersion des ondes guidées, permet d'obtenir via la résolution d'un problème inverse l'évaluation non destructive des propriétés d'une structure telle que la surface de la terre en géophysique, des tuyaux d'oléoducs et de gazoducs, ainsi que des structures biologiques telles que les artères ou les tissus osseux. Plus précisément, la procédure d'inversion est effectuée en minimisant une fonction coût laquelle fait intervenir les résultats issus d'expériences et de la modélisation. Par conséquent, le développement de méthodes de calculs précises et peu coûteuses pour évaluer la dispersion des ondes est devenu un sujet de recherches scientifiques d'intérêt. La méthode des éléments finis semi-analytique (SAFE, pour Semi-Analytical Finite Element) est l'une des techniques les plus populaires grâce à sa capacité permettant d'étudier des guides d'ondes ayant une section-droite transverse complexe ou un gradient de propriétés. La méthode SAFE s'est enrichie en utilisant uniquement la discrétisation de la frontière du domaine de calcul. Pour calculer les courbes de dispersion et les modes des ondes guidées, seule la section-droite transverse du guide d'ondes doit être discrétisée, tandis que la solution analytique est utilisée dans la direction de propagation. Cependant, lors de l'étude de guides d'ondes hétérogènes et/ou multiphysiques (par exemple dans le cas de couplage solide-fluide ou de la poroélastique) avec des géométries complexes, la méthode SAFE exige un temps de calculs relativement important, en particulier, pour les hautes fréquences. Dans ce contexte, le présent travail développe une nouvelle approche de calcul, très efficace, dite semi-analytique isogéométrique Galerkin (SAIGA-G) et semi-analytique isogéométrique collocation (SAIGA-C) pour calculer la dispersion des ondes dans différents types de guides d'ondes possédant une géométrie complexe et/ou une hétérogénéité. Dans le cas de guides d'ondes immergés dans un fluide ou couplés à un milieu semi-infini, des couches absorbantes parfaitement adaptées (PML, pour perfectly matched layer) ont été employées pour atténuer les ondes au bord du domaine. Ces approches sont basées sur l'utilisation de fonctions B-Splines Rationnelles Non Uniformes (NURBS) dans le cadre de l'analyse isogéométrique non seulement comme fonctions de base pour la représentation géométrique mais aussi pour l'approximation des champs solutions en pression/déplacement. Les approches (SAIGA-G et SAIGA-C) se différencient par le type d'intégrations numériques. La méthode SAIGA-G utilise une intégration numérique de type quadrature de Gauss pour évaluer les intégrales. Alors que la méthode SAIGA-C traite directement la forme forte de l'équation aux dérivées partielles. La méthode de collocation isogéométrique a été développée pour combiner les avantages de la précision de la méthode de l'isogéométrie avec l'efficacité de calcul de la méthode de collocation. Les courbes de dispersion (vitesse de phase, nombre d'onde et vitesse d'énergie) sont obtenues à partir de la résolution d'un problème de valeurs propres. Quand cela est possible, les résultats obtenus dans ce travail sont comparés avec ceux du logiciel Disperse sinon avec ceux de la méthode classique

SAFE qui utilise des polynômes de Lagrange. On montre que pour le calcul de la dispersion des GW, l'utilisation d'une approche basée sur la méthode SAIGA-G conduit à un taux de convergence beaucoup plus rapide que l'utilisation de la méthode SAFE conventionnelle avec le même ordre pour les fonctions d'interpolations. De plus, la continuité de la pression/déplacement aux interfaces pourrait être considérablement améliorée grâce à l'utilisation des fonctions NURBS, montrant l'avantage de la méthode SAIGA par rapport à celle de SAFE dans l'évaluation des modes des GW dans les systèmes couplés. Bien que la précision de la méthode SAIGA-C soit inférieure à celle des autres approches, sa mise en œuvre est simple et le temps de calcul requis peut être considérablement réduit.

Résumé étendu

0.1 Motivation

Les travaux présentés dans cette thèse sont motivés par les contrôles non destructifs (NDE, pour Non-Destructive Evaluation) et la surveillance de la santé des structures (SHM, pour Structural Health Monitoring). Les ondes guidées (GW, pour Guided Wave) sont l'une des méthodes d'inspection les plus populaires pour les NDE modernes et font l'objet d'une vaste investigation scientifique. Les structures à inspecter sont souvent de grande taille et seulement partiellement accessibles. Les ondes guidées ont (1) la capacité d'inspecter non seulement les structures longues tout en conservant le revêtement et l'isolation, mais également toute la section transversale d'une structure ; (2) une sensibilité élevée aux défauts multiples avec une grande précision d'identification ; (3) une faible consommation d'énergie et une grande rentabilité ; (4) une facilité de mise en œuvre et une instrumentation portable.

La connaissance des caractéristiques de dispersion des ondes guidées, permet d'obtenir via la résolution d'un problème inverse l'évaluation non destructive des propriétés d'une structure telle que la surface de la terre en géophysique, des tuyaux d'oléoducs et de gazoducs, ainsi que des structures biologiques telles que les artères ou les tissus osseux. Plus précisément, la procédure d'inversion est effectuée en minimisant une fonction coût laquelle fait intervenir les résultats issus d'expériences et de la modélisation.

Dans de nombreux cas, les courbes de dispersion sont plus complexes que dans le cas d'une plaque isotrope homogène. Les guides d'ondes peuvent avoir une géométrie complexe, une forte hétérogénéité et une accessibilité limitée. De plus, ils sont généralement couplés à un milieu infini. Par conséquent, le développement de méthodes de calculs précises et peu coûteuses pour évaluer la dispersion des ondes est devenu un sujet de recherches scientifiques d'intérêt. Le calcul des propriétés de dispersion joue un rôle prépondérant dans cette thèse.

Ces dernières années, plusieurs méthodes ont été développées pour l'analyse de dispersion des guides d'ondes qui ont été rassemblées dans Tab. 1. Les techniques matricielles bien connues, souvent appelées méthode de matrice de transfert (TMM, pour Transfer Matrix Method) ou méthode de matrice globale (GMM, pour Global Matrix Method), sont basées sur des solutions de forme fermée et peuvent être appliquées à des guides d'ondes réguliers (cylindre et plaque) constitués de quelques couches. Les solutions de forme fermée ont été appliquées avec succès au problème des cylindres noyés remplis de fluide et des cylindres avec un gradient de propriétés, entre autres. La formulation fondamentale est analytique, mais nécessite un calcul numérique pour obtenir les racines des équations de dispersion qui offre souvent une solution rapide et précise. Cependant, pour les structures complexes,

Méthode	Caractéristique	Avantage et désavantage
Analytique	Basée sur la matrice de transfert, la méthode matricielle globale et la méthode asymptotique.	Faible coût de calcul, structure simple (*e.g.* plaque et cylindre).
Différences finies	Les développements de Taylor et la substitution directe dans les équations gouvernantes nécessitent la mise en place d'une grille de points pour l'ensemble de la structure.	Un nombre élevé de degrés de liberté est nécessaire pour obtenir des résultats précis pour les analyses de propagation des ondes.
Elements finis	Basé sur la formulation faible et nécessite la discrétisation de l'ensemble de la structure.	Structure complexe, matériaux hétérogènes, coût de calcul élevé.
SAFE	Discrétisation de la section transversale au sens éléments finis tout en permettant le mouvement harmonique dans le direction axial.	Uniform selon 1 ou 2 directions, faible coût de calcul, structure complexe, matériaux hétérogènes.

Table 1 – Méthodes de résolution des équations aux dérivées partielles de l'onde guidée.

les racines des équations de dispersion peuvent devenir à la fois inefficaces et peu fiables (car cela dépend fortement de l'estimation initiale). De plus, développer un algorithme de traçage universel applicable à toutes les configurations est une tâche assez lourde. Les racines peuvent être manquées dans le processus de recherche à haute fréquence lorsque deux modes s'approchent très près l'un de l'autre.

Contrairement à ces formulations principalement analytiques, l'application de différentes méthodes numériques a été décrite dans la littérature, la plupart d'entre elles étant basées sur la méthode des éléments finis réguliers (FEM) ou la méthode des différences finies (FDM). Généralement, les techniques de calcul conventionnelles telles que les méthodes d'éléments finis et de différences finies, ou la structure entière est divisée en un nombre suffisant d'éléments, nécessitent une grande quantité de temps de calcul et de mémoire. Concernant la FDM, un nombre élevé de degrés de liberté est nécessaire pour obtenir des résultats précis pour les analyses de propagation des ondes.

Le présent travail se concentre sur l'approche des éléments finis semi-analytiques (SAFE) pour le calcul de la relation de dispersion pour une variété de guides d'ondes, en particulier les structures élastiques et poroélastiques à couplage fluide.

0.2 Méthode des éléments finis semi-analytiques (SAFE)

La méthode des éléments finis semi-analytiques (SAFE) suppose une solution de forme harmonique dans une (ou deux) direction et utilise une discrétisation par éléments finis dans la section transversale du guide d'onde considéré. La méthode SAFE est un choix approprié pour traiter les guides d'ondes dont les sections transversales arbitraires et les propriétés des matériaux varient dans la section transversale tout en conservant les avantages connus des approches purement analytiques, telles que la possibilité de traiter des dimensions infinies de guide d'ondes. Ainsi, cette méthode exploite les avantages des approches numériques et analytiques.

Dans la littérature, il existe différents types de guides d'ondes qui ont été traités selon la méthode SAFE. Ces structures ont été considérées dans ce travail et peuvent être décrites comme suit :

Guides d'ondes avec gradient de propriétés Une grande variété de matériaux naturels et artificiels ont des propriétés élastiques variables unidirectionnelles. Croûte du manteau terrestre, certains composites ou tissus osseux font partie de ces milieux fonctionnellement gradués. Le développement de techniques d'évaluation non destructives pour caractériser les comportements mécaniques de ces matériaux est un enjeu clé. Dans le cas de structures multicouches, l'évaluation de l'endommagement/ discontinuité aux interfaces peut être réalisée en examinant les composantes de contraintes à ces interfaces. De plus, un modèle stochastique est requis pour prendre en compte l'hétérogénéité aléatoire des propriétés élastiques (coefficients de rigidité C_{ij} dans la notation Voigt et densité de masse ρ).

Structures en plaques et cylindres La méthode SAFE a été principalement utilisée pour obtenir des courbes de dispersion des ondes de Lamb pour les structures en plaques, y compris les plaques homogènes, les composites et les plaques semi-infinies. Pour décrire une plaque ou un cylindre, il suffit de discrétiser une droite. Pour les plaques, la direction de l'épaisseur doit être discrétisée et la direction de propagation est résolue analytiquement. Pour les cylindres, la direction radiale doit être discrétisée et les directions circonférentielle et longitudinale sont décrites analytiquement. Les ondes guidées multimodes dans une configuration cylindrique peuvent se propager le long de différents chemins, notamment circonférentiels, longitudinaux et à travers l'épaisseur du cylindre. Cependant, en raison de la courbure de la surface des guides d'ondes cylindriques, les modes d'ondes guidées dans ces structures sont généralement différentes et plus complexes que ceux dans les structures en forme de plaque.

Guides d'ondes à section transversale complexe La section transversale des guides d'ondes peut être courbe. Dans ce cas, la méthode SAFE a été popularisée par les travaux de Gavric [1] qui permet de calculer des courbes de dispersion dans un rail libre. Thompson et Jones [2] ont étudié les courbes de dispersion d'un rail dans le but de réduire le bruit. Cependant, en pratique, pour étudier les ondes guidées dans des structures à section complexe, un raffinement important du maillage peut être nécessaire pour obtenir les solutions convergées, notamment aux hautes fréquences. Le raffinement du maillage conduit à des problèmes de valeurs propres complexes et de grande dimension, entraînant une augmentation significative du coût de calcul.

Guides d'ondes ouverts Le type de guides d'ondes susmentionné est connu sous le nom de guides d'ondes fermés. Dans les guides d'ondes fermés, les ondes peuvent se propager le long de l'axe du guide d'ondes sans atténuation. Cependant, dans la pratique, les guides d'ondes sont souvent encastrés ou immergés dans de grands supports (qui sont souvent considérés comme non bornés). Dans ce cas, les guides d'ondes sont dits ouverts en raison du rayonnement énergétique dans le milieu environnant. Trois types de modes d'ondes peuvent apparaître dans les guides d'ondes ouverts : les modes de rayonnement, les modes piégés et les modes à fuite. Les modes de rayonnement sont des ondes stationnaires dans les directions transversales et peuvent être oscillants ou évanescents dans la direction longitudinale. Résonnant principalement dans le milieu environnant, les modes de rayonnement présentent peu d'intérêt pour les NDE. A l'inverse, les modes piégés sont particulièrement intéressants. Ces modes décroissent de façon exponentielle dans les directions transversales et se propagent le long de l'axe du guide d'ondes sans atténuation. Néanmoins, les modes piégés ne se produisent pas toujours. Pour les guides d'onde ouverts, caractérisés par un champ scalaire tel que la pression acoustique ou le déplacement d'onde SH, les modes piégés n'existent que si la vitesse globale dans le cœur est plus faible que dans le milieu environnant. Contrairement aux modes piégés, les modes de fuite existent toujours dans les guides d'ondes ouverts. Leur fuite d'énergie dans le milieu environnant entraîne une atténuation le long de l'axe du guide d'ondes (positive pour les modes positifs et négative pour

les modes négatifs), ce qui peut fortement limiter leur distance de propagation. Un comportement inhabituel des modes de fuite est que, tout en diminuant le long de l'axe du guide d'ondes, leurs amplitudes augmentent dans les directions transversales.

L'extension de la méthode SAFE aux guides d'ondes ouverts n'est pas simple en raison de la nature infini du problème dans la direction transversale. Cette difficulté est renforcée par la croissance transversale des modes de fuite. Pendant longtemps, cette difficulté a été considérée comme un inconvénient majeur des approches SAFE et a conduit l'autre formulation à calculer numériquement les modes de guides d'ondes ouverts. La première classe de méthodes évite la discrétisation du milieu d'inclusion en utilisant des conditions aux limites appropriées telles que la méthode des éléments aux limites (BEM) et les conditions aux limites dashpot. La deuxième classe de méthodes nécessite une discrétisation du milieu environnant, qui doit être tronquée comme des conditions aux limites non réfléchissantes (NRBC), des couches absorbantes (AL) et des couches parfaitement appariées (PML).

Guides d'ondes poroélastiques De nombreux matériaux rencontrés en génie civil, géophysique et biomécanique peuvent être considérés comme des milieux poreux constitués d'un squelette solide dans lequel existe un réseau de pores. Au cours de la dernière décennie, l'inspection par ondes guidées de ces matériaux a attiré l'attention en tant qu'outil prometteur dans les NDE et les SHM. Des jalons de modélisation dans ce domaine ont été proposés par Biot il y a plus de 50 ans, sur la base des travaux de Terzaghi. Les matériaux poroélastiques sont connus pour être multiphysiques par nature à l'échelle macroscopique et impliquent des interactions entre deux ou plusieurs variables de champ (composants fluides et solides en interaction). Ils présentent un comportement beaucoup plus compliqué que celui des matériaux (visco-)élastiques par exemple. Certaines grandeurs physiques importantes, comme la porosité et la perméabilité, sont en dehors du modèle d'élasticité mais elles sont naturellement présentes dans le modèle poroélastique. Récemment, la méthode des éléments finis semi-analytique (SAFE) a été utilisée pour la propagation d'ondes guidées dans le domaine temporel pour des plaques osseuses poroélastiques couplées à un fluide. L'étude des relations de dispersion pour les matériaux poroélastiques en utilisant l'approche SAFE est un sujet peu exploré dans la littérature et a été étudié dans ce travail.

0.3 Objectifs

Au cours du présent travail, les aspects les plus importants dans la simulation des propriétés des ondes guidées sont considérés. Les critères suivants ont été pris en compte : (1) la capacité à décrire le comportement de dispersion des ondes guidées *via* une résolution efficace des équations de dispersion. La solution des équations de dispersion visualisées par des courbes de dispersion est très utile dans les applications NDT; (2) la possibilité de décrire la propagation des ondes guidées dans des milieux poroélastiques complexes et hétérogènes : ceci est d'une grande importance pour les applications traitant de la propagation des ondes ultrasonores dans les plaques composites anisotropes; (3) la flexibilité afin de modéliser des géométries arbitraires : la géométrie des guides d'ondes affecte de manière significative le comportement de propagation des ondes en général; (4) le temps de calcul et les besoins en stockage mémoire : ces éléments sont toujours un enjeu important lorsqu'on travaille avec des méthodes de simulation numérique. Lorsque plusieurs méthodes peuvent être utilisées pour une même tâche, il est toujours préférable de choisir celle pour laquelle les exigences sont les moins élevées à condition que la précision puisse être similaire.

Pour atteindre les objectifs susmentionnés, nous avons adopté la méthodologie suivante : sur la base d'innovations récentes, nous proposons d'employer l'analyse isogéométrique au lieu de la discrétisation conventionnelle par éléments finis dans le cadre de l'analyse SAFE. L'analyse isogéométrique

(IGA) consiste à combiner des outils de CAD (pour Computer Aided Design) tels que les B-splines rationnelles non uniformes (NURBS) pour représenter des géométries complexes et des solveurs d'éléments finis (FE) en une seule entité. Une approche plus prometteuse, qui élimine l'intégration, consiste à travailler directement avec la forme forte de l'équation aux dérivées partielles (PDE, pour Partial Differential Equations). La méthode de collocation IGA a été développée pour combiner les avantages de précision et de régularité de la méthode IGA avec l'efficacité de calcul de la méthode de collocation. Comme il n'y a pas d'intégrales de volume dans la collocation IGA, la méthode est considérablement moins chère d'un point de vue du temps de calcul.

Lorsqu'il s'agit d'un domaine infini, nous introduisons des PML afin d'absorber les ondes de fuite. Du point de vue mathématique, les PML peuvent être considérées comme le résultat d'un transformation vers un système de coordonnées complexe, ou les solutions des équations d'onde décroissent de façon exponentielle (la nouvelle coordonnée étant un nombre complexe). Par conséquent, le milieu infini peut être à ramener à un domaine fini.

0.4 Organisation du manuscrit

Le chapitre 2 décrit un cadre probabiliste pour analyser les propriétés de dispersion de guides d'ondes cylindriques axisymétriques avec des propriétés matérielles aléatoires couplées à des fluides. Dans un premier temps, nous présentons le développement d'une formulation semi-analytique par éléments finis pour résoudre le problème de propagation des ondes dans le système considéré. Ensuite, le modèle stochastique est présenté en introduisant une hétérogénéité aléatoire des propriétés élastiques (coefficients de rigidité et densité de masse) dans la direction radiale. Une étude paramétrique a été réalisée pour mettre en évidence les effets de la géométrie tridimensionnelle et des propriétés aléatoires sur la dispersion de la vitesse de phase et de la vitesse d'énergie.

Le chapitre 3 traite des ondes guidées dans des structures en plaques multicouches. Une approche basée sur l'analyse isogéométrique est développée pour calculer les relations de dispersion et les formes modales pour les plaques multicouches et à couplage fluide. Seule la direction d'épaisseur des structures doit être discrétisée par éléments finis (?), tandis que la direction de propagation est décrite analytiquement. Pour la discrétisation, une classe récemment développée de fonctions de base NURBS d'ordre supérieur est utilisée, ce qui augmente l'efficacité de calcul. La continuité de déplacement et la continuité de traction sont obtenues en utilisant un seul patch pour une plaque multicouche.

Le chapitre 4 présente une méthode de Galerkin isogéométrique semi-analytique (SAIGA-G) pour le calcul de la dispersion des ondes dans des guides d'ondes élastiques anisotropes 3D couplés à des fluides acoustiques. Les résultats obtenus sont comparés à ceux dérivés de l'utilisation de la méthode SAFE conventionnelle qui utilise des polynômes de Lagrange. Il est montré que pour le calcul de la dispersion des guides d'ondes *via* SAIGA-G conduit à une vitesse de convergence beaucoup plus rapide que celle des fonctions d'interpolation SAFE *via* conventionnelles pour le même ordre. De plus, la continuité du déplacement normal à l'interface fluide-solide pourrait être considérablement améliorée grâce à la fonctionnalité de lissage de NURBS, montrant l'avantage de SAIGA-G par rapport à SAFE dans l'évaluation des modes de forme des guides d'ondes dans les systèmes couplés fluide-solide.

Dans le chapitre 5, une formulation d'éléments spectraux d'ordre élevé est proposée pour calculer les coefficients de réflexion et de transmission avec une incidence oblique à l'interface entre le fluide et la couche poreuse. Cette formulation conduit à des résultats numériques plus précis, comme le montre cet article. Des illustrations numériques sur des plaques homogènes et hétérogènes avec différentes porosités et fréquences montrent une grande efficacité de la formulation proposée.

Dans le chapitre 6, des procédures basées sur SAIGA pour l'étude de guides d'ondes poroélastiques couplés à un fluide sont présentées. La première utilise la méthode isogéométrique de Galerkin, qui est basée sur la discrétisation NURBS de la formulation faible dérivée dans le domaine fréquence-nombre d'onde pour dériver le système d'équations des valeurs propres (dispersion). La seconde utilise la méthode isogéométrique de la collocation, qui est basée sur une approximation NURBS de la forme forte du problème considéré pour dériver le système d'équations des valeurs propres (dispersion). La comparaison a inclus une analyse détaillée de la précision des coûts *vs.* entre les méthodes de collocation proposées (SAIGA-C) et Galerkin (SAIGA-G). Il est montré que le SAIGA-G a un bien meilleur taux de convergence par rapport aux autres méthodes tandis que le temps de calcul pourrait être réduit en utilisant la méthode SAIGA-C.

Chapter 1

Introduction

1.1 Background

The work presented in this thesis is motivated by the non-destructive testing (NDT) and the structural health monitoring (SHM). The guided waves are nowadays one of the most popular inspection methods for the modern NDT and are a subject of extensive scientific investigations [3]. The structures that need inspections are often large and only partially accessible. The guided waves have (1) the ability to inspect not only long structures while retaining coating and insulation but also the entire cross sectional area of a structure; (2) a high sensitivity to multiple defects with high precision of identification; (3) a low energy consumption and great cost-effectiveness; (4) an ease to implement and portable instrumentation [4, 5, 6]. A few examples of non-destructive evaluations of structures using guided waves are shown in Figs. 1.1 (a,b,c) including the detection of damages in rails, the properties of geophysics surfaces and earthquake engineering, as well as the properties of biological structures such as bone.

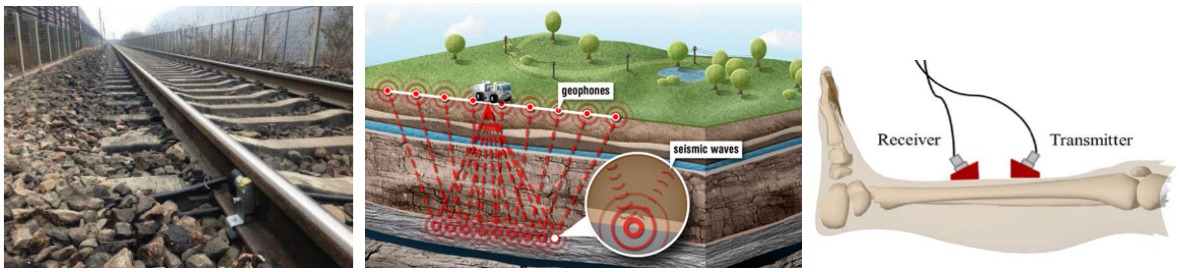

(a) (b) (c)

Figure 1.1 – Examples of application of guided waves in (a) rail industry [7] (b) seismic characterization (picture from earthsky.org) and (c) medical imaging (courtesy of prof L Le, Univ of Alberta).

It is well known that ultrasonic guided waves are a special type of elastic waves, which require a structural boundary (called waveguide) for propagation. Guided waves origin from the interference of bulk waves. Essentially, these bulk waves are obliquely reflected/refracted by each boundary, causing them to propagate back and forth in the waveguide [4]. Inevitably, the interference between them

will take place and the result of this effect is that propagating bulk waves are guided in a certain direction. This can lead to covering the entire surface of the structures (see Fig. 1.2). However, the bounded configuration of the waveguide often results in multi-modal, dispersive and attenuating wave propagation. This is in contrast to bulk wave propagation used in conventional NDT. Consequently, analysis and implementation of waveguide is more challenging.

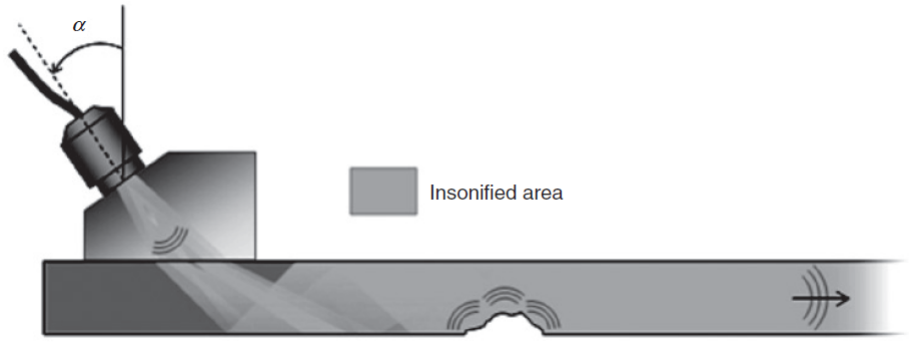

Figure 1.2 – Schematic of inspection of the entire area of a structure using guided waves [4].

Several types of guided waves have been studied for the application of SHM and NDT. One of the most common is the Lamb waves. They propagate through thin plates and shells bounded by parallel stress free surfaces [8]. Two basic types of Lamb wave modes can be distinguished in an homogeneous isotropic plate, namely symmetric $S_1, S_2, ..., S_n$ and anti-symmetric $A_1, A_2, ..., A_n$ ones. For each excitation frequency, a number of propagating modes exists. They correspond to the solution of the mathematical model description of Lamb's problem. Both symmetric and anti-symmetric modes are highly dispersive and can furthermore convert into each other. Despite their complex propagation characteristics, there are certain properties which make them interesting for NDT applications. Lamb waves are utilized for nondestructive evaluations such as identification of cracks in beams and slabs, damage detection in composite laminates and thickness prediction of oil and gas pipelines [6].

Another major group of guided waves includes surface waves such as Rayleigh, Love and Stoneley waves. Rayleigh waves are non-dispersive for homogeneous material properties. They can be easily excited and recorded along a free surface [9]. Being sensitive to the surface topography, Rayleigh waves are employed mostly to detect surface defects [10], pavement structures characterization [11] and near surface geophysics [12]. Stoneley waves occur at an interface between two media. They are closely related to Rayleigh waves. The existence of Stoneley waves depends on the density and shear modulus ratios of the neighbouring two media. Love waves are horizontally polarized shear waves which also exist on the surface. In contrast to the other two types (Rayleigh and Stoneley) of surface waves, they are highly dispersive. Love waves are the fastest propagating surface waves. Due to the in-plane polarization, the Love waves are suitable for travel at a surface contacting a liquid environment [13]. Apart from these, circumferential, axial and radial wave propagation in cylindrical structures and pipes are also studied extensively in the literature.

1.2 Dispersion relations

In general, analysis of wave propagation starts with obtaining the governing elastodynamic equations and associated boundary conditions. These equations are often transformed to frequency-wavenumber

domain to obtain the dispersion characteristics. The number of propagating modes that can be excited in the structure, increases with frequency, tending towards infinity. Figure 1.3 shows typical dispersion curves for a simple aluminium plate, where the phase velocities and wavenumbers are plotted as a function of frequency.

Dispersion relations define the behavior of wave propagation, namely, the propagating modes and wave velocity as a function of frequency. Apart from obtaining the dispersion characteristics, the governing equations are also solved in time domain to analyze the wave amplitudes, reflections from edges and boundaries, and interaction with damages. The computation of the dispersion properties and the corresponding mode shapes plays a predominant role in this thesis.

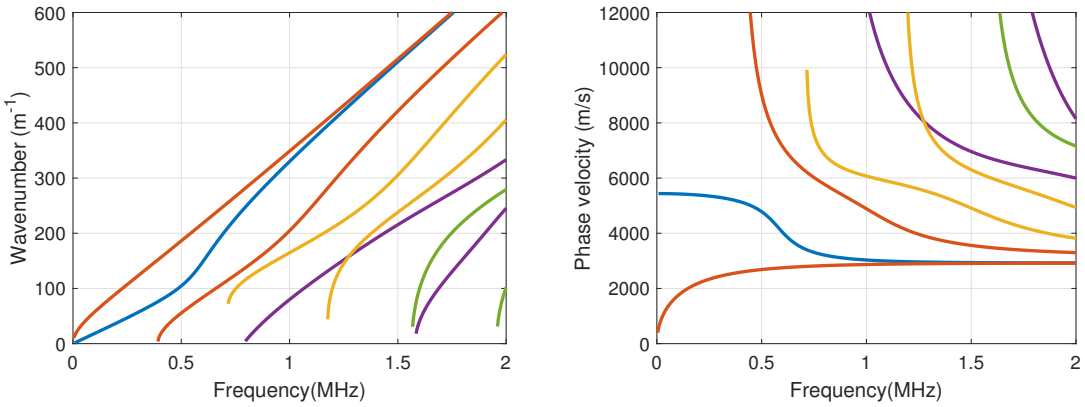

(a) (b)

Figure 1.3 – Dispersion curves of (a) wavenumber and (b) phase velocities of propagating modes in a homogeneous isotropic plate.

In many cases, the dispersion curves are more complicated than in the case of a homogeneous isotropic plate. The waveguides can have a complex geometry, a strong heterogeneity and a limited accessibility. Furthermore, they are usually coupled with an infinite media. Consequently, the development of low-cost and accurate computational methods for evaluating the wave dispersion is very important and has become the subject of extensive scientific investigations. The crucial point in the process of numerical modelling of guided waves is typically the balance between the computation time and complication level of the resolution method. Several methodologies for computing the dispersion curves of guided waves have been discussed in the following section.

1.3 Simulation of guided waves dispersion

In recent years, several methods have been developed for dispersion analysis of waveguides which have been roughly gathered in Tab. 1.1. The well-known matrix techniques, which are often referred to as Transfer Matrix Method (TMM) or Global Matrix Method (GMM), are based on closed-form solutions and can be applied to regular waveguides (cylinder and plate) consisting of few homogeneous layers [14, 15, 16]. The closed-form solutions were successfully applied to the problem of embedded, fluid-filled cylinders [17] and functionally graded cylinders [18], among others. The global matrix method originates from the description of the motion of the structure as a superposition of bulk waves propagating in each layer (the number of layers and material properties can be arbitrary). The fundamental formulation is analytical, but requires a numerical computation to obtain the roots of

Method	Feature	Advantage and limitation
Analytic	Based on transfer matrix, global matrix method and asymptotic method.	Low computational cost, simple structure (*e.g.* plate and cylinder).
Finite differences	Taylor expansions and direct substitution into the governing equations needs a grid of points to be set up for whole structure.	High number of degrees of freedom is needed to obtain accurate results for wave propagation analyses.
Finite elements	Based on the weak formulation and needs the discretization of whole structure.	Complex structure, heterogeneous materials, high computation cost.
SAFE	Discretization of the cross section in a finite element sense while allowing the harmonic motion in the axial direction.	Uniform in one or two directions, low computational cost, complex structure, heterogeneous materials.

Table 1.1 – Methods for solving partial differential equations of guided waves.

dispersion equations which often offers a fast and accurate solution. However, for complex structures, the roots of dispersion equations may become both inefficient and unreliable (as it strongly depends on the initial guess). Moreover, developing a universal tracing algorithm applicable to all configurations is a rather cumbersome task. Roots may be missed in the searching process at high frequency when two modes approach very close to each other or matrix size becomes larger [19].

In contrast to these mainly analytical formulations, the application of different numerical methods have been described in the literature, most of them being based on the regular finite element method (FEM) [20, 21] or the finite difference method (FDM) [22, 23]. Generally, the conventional calculation techniques such as finite element and finite difference methods, where whole structure is divided into a sufficient number of elements, requires large amount of calculation time and memory. Concerning FDM, a high number of degrees of freedom is needed to obtain accurate results for wave propagation analyses. Usually the point grid associated to these methods has rectangular parallelepiped or cubic cells and therefore the physical geometry of curved boundaries is approximated by a staircase function. Either a fine grid or a derivative of the original finite difference schemes is needed to obtain accurate results while modeling ultrasonic guided wave propagation in waveguides with arbitrary geometries.

For more detailed information about simulation of guided waves, the reader is referred to the works by Willberg et al. [24, 25], Mitra et al. [5]. The present work, focus on Semi-Analytical Finite Element (SAFE) approach for computation of dispersion relation for a variety of waveguides specially fluid-coupled elastic and poroelastic structures.

1.4 Semi analytical finite element method

The semi-analytical finite element (SAFE) method assumes a harmonic form of solution in one (or two) direction and employs a finite element discretization in the cross-section of the considered waveguide. The SAFE method is a suitable candidate for dealing with the waveguides whose arbitrary cross-sections and material properties varying in the cross-section while retaining advantages known from purely analytical approaches, such as the possibility to treat infinite dimensions of waveguide. Thus, this method exploits the benefits of numerical and analytical approaches.

In the literature, there are different types of waveguides that have been processed using the SAFE method. These structures have been considered in this work and can be described as follow:

Functionally graded and random waveguides A large variety of natural and artificial materials have unidirectional varying elastic properties. Mantle crust of the terrestrial, certain composites or bone tissues are some of these functionally graded media. The development of non-destructive evaluation techniques to characterize mechanical behaviors of these materials is a key issue. In the case of multilayered structures, the evaluation of the damage/discontinuity at the interfaces can be realised by examining the stress components at these interfaces. Furthermore, stochastic model is required to take into account the random heterogeneity of elastic properties (stiffness coefficients C_{ij} in the Voigt notation and mass density ρ).

Plate-like and cylinder structures The SAFE method has been primarily used to obtain Lamb wave dispersion curves for plate-like structures including homogeneous plates, composites laminates [26] and semi-infinite plates [27, 28, 29]. To describe a plate or a cylinder, a straight line has to be discretized only. For the plates, the thickness direction has to be discretized and propagation direction is solved analytically. For the cylinders, the radial direction has to be discretized and circumferential and longitudinal directions are described analytically. The multi-mode guided waves in a cylindrical configuration such as pipe can propagate along different paths including circumferential, longitudinal and through the thickness of the cylinder. However, due to the curvature of the surface of cylindrical waveguides, guided wave modes in cylindrical structures are generally more complex than those in plate-like structures. Guided wave modes in cylinders are called and denoted longitudinal $L(0,n)$, torsional $T(0,n)$ and flexural $F(m,n)$, where m stands for the harmonic number of circumference variation and n is the order of wave modes [4].

Complex cross-section waveguides The cross-section of the waveguides can be curved. In this case, the SAFE method has been popularised by the Gavric's works [1] which allows to compute dispersion curves in a free rail. Thompson and Jones [2] studied dispersion curves of a rail for the purpose of noise reduction. However, in practice, for studying the guided waves in structures with a arbitrary cross-section, a significant mesh refinement may be required to obtain the converged solutions, especially at high frequencies. The mesh refinement leads to complex-valued eigenvalue problems of high dimension, causing a significant increase in computational cost.

Opened waveguides The aforementioned type of waveguides are known as the closed waveguides. In closed waveguides, waves can propagate along the waveguide axis without attenuation. However, in practice, waveguides are often embedded or immersed in large media (which is often considered as unbounded). In this case, waveguides are called open because of the energy radiation into the surrounding medium. Three kinds of wave modes can occur in opened waveguides: radiation modes, trapped modes and leaky ones. Radiation modes are standing waves in the transverse directions and can be either oscillating or evanescent in the longitudinal direction. Resonating mainly in the surrounding medium, radiation modes are of little interest for the NDE [30]. Conversely, trapped modes are of particular interest. These modes exponentially decay in the transverse directions and propagate along the waveguide axis without attenuation. Nevertheless, trapped modes do not always occur. For opened waveguides, characterized by a scalar field such as the acoustic pressure or the SH wave displacement, trapped modes exist only if the bulk velocity in the core is lower than in the surrounding medium. As opposed to trapped modes, leaky modes always exist in opened waveguides. Their energy leakage into the surrounding medium yields attenuation along the waveguide axis (being

positive for positive-going modes and negative for negative-going ones), which can strongly limit their propagation distance. An unusual behavior of leaky modes is that, while decaying along the waveguide axis, their amplitudes increase in the transverse directions.

Extending the SAFE method to open waveguides is not straightforward due to the unbounded nature of the problem in the transverse direction. This difficulty is enhanced by the transverse growth of leaky modes. For a long time, this difficulty has been considered as a major drawback of the SAFE approaches and has conducted the other formulations to numerically compute the modes of opened waveguides. The first class of methods avoids the discretization of the embedding medium by using appropriate boundary conditions such as the boundary element method (BEM) [31, 32, 33] and dashpot boundary conditions [34, 35]. The second class of methods requires a discretization of the surrounding medium, which must be truncated such as non-reflecting boundary conditions (NRBC) [36], absorbing layers (AL) [37, 38] and perfectly matched layers (PML) [39, 40, 41, 42, 43].

Poroelastic waveguides Many materials encountered in civil, geophysical and biomechanical engineering can be considered as porous media is made up of a solid skeleton in which exists a pore network. Over the last decade, guided waves inspection of such materials have gained attention as a promising tool in NDE and SHM. Modeling milestones in this field have been proposed by Biot more than 50 years ago [44, 45, 46], based on the Terzaghi work [47]. Poroelastic materials are known to be multiphysical by nature at the macroscopic scale and involve interactions between two or more field variables (interacting fluid and solid components). They evince much more complicated behavior than the one of (visco-)elastic materials for instance. Certains important physical quantities, like the porosity and permeability, are outside of the elasticity model but they are naturally present in the poroelastic model. Recently, the semi-analytical finite element method (SAFE) has been used for the guided wave propagation in the time domain for poroelastic bone plates coupled with a fluid [48]. The investigation of dispersion relations for the poroelastic materials using the SAFE approach is a topic not much explored in the literature and has been investigated in this work.

1.5 Aims and objectives

In the course of the present work, the most important aspects in the simulation of guided waves properties are considered. The following criteria were taken into account: (1) the capability to describe the guided wave dispersion behavior *via* a resolution efficient of the dispersion equations. The solution of the dispersion equations visualized by dispersion curves is very useful in the NDT applications. (2) the possibility to describe guided wave propagation in complex and heterogeneous poroelastic media: this is of great importance for applications dealing with ultrasonic wave propagation in anisotropic composite plates. (3) the flexibility in order to model arbitrary geometries: the geometry of the waveguides significantly affect the wave propagation behavior in general. (4) the calculation time and memory storage requirements: these elements are always an important issue when working with numerical simulation methods. When several methods can be used for the same task, it is always preferable to choose the one for which the least requirements provided that the accuracy can be similar.

To achieve the aforementioned objectives, we adopted the following methodology: based on recent innovations, we propose to employ the higher order basis functions instead of Lagrange basis function in the context of SAFE analysis. The isogeometric analysis (IGA) consists to combine Computer Aided Design (CAD) tools such as Non-uniform Rational B-splines (NURBS) to represent complex geometries and finite-elements (FE) solvers into a single entity. A more promising approach, which

eliminates integration, is to work directly with the strong form of the partial differential equation (PDE). The IGA collocation method has been developed to combine the accuracy and the smoothness advantages of the IGA method with the computational efficiency of the collocation method. Since there are no volume integrals in the IGA collocation, the method is considerably cheaper from a computational point of view.

When dealing with an unbounded domain, we introduce PMLs in order to absorb the leaky waves. From the mathematical point of view, the PMLs can be considered like a result from a mapping to a complex coordinate system, where the solutions of wave equations decay exponentially (as the new coordinate is complex number). Therefore, the infinite medium can be to bring back to a finite domain.

1.6 Organization of the manuscript

First, basic concepts that are useful to throughout the thesis, are presented in the chapter 1. A literature review of the different SAFE methods to compute the dispersion properties of waveguides is given.

Chapter 2 describes a probabilistic framework to analyze dispersion's properties of axisymmetric cylinder waveguides with random material properties coupled with fluids. First, we present the development of a semi-analytical finite element formulation to solve the wave propagation problem in the considered system. Next, stochastic model is presented by introducing random heterogeneity of elastic properties (stiffness coefficients and mass density) in the radial direction. Parametric study has been performed to highlight the effects of three-dimensional geometry and random properties on the dispersion of the phase velocity and energy velocity.

Chapter 3 addresses the analyse of guided waves in multilayered plate-like structures. An approach based on isogeometric analysis is developed to compute dispersion relations and mode shapes for multilayered and fluid coupled plates. Only the through-thickness direction of structures has to be discretized by finite elements, while the direction of propagation is described analytically. For the discretization, a recently developed class of higher-order NURBS basis functions is employed which increases computational efficiency. The displacement continuity and traction continuity are obtained using one single patch for a multilayered plate.

Chapter 4 presents a Semi-analytical isogeometric Galerkin method (SAIGA-G) procedures for computing the wave dispersion in 3D anisotropic elastic waveguides coupled with acoustic fluids. The obtained results are compared with the ones derived from using the conventional SAFE method which uses Lagrange polynomials. It is shown that for computing the dispersion of waveguides *via* SAIGA-G leads to much faster convergence rate than the one of the conventional SAFE *via* interpolation functions for the same order. Moreover, the continuity of normal displacement at the fluid-solid interface could be significantly improved thanks to the smoothness feature of NURBS, showing advantage of SAIGA-G over SAFE in the evaluation of the shape modes of waveguides in coupled fluid-solid systems.

In Chapter 5, a high-order spectral finite element formulation is proposed for computing the reflection and transmission coefficients with oblique incidence to the interface between fluid and poroelastic layer. This formulation lead to more accuracy numerical results as shown in this chapter. Numerical illustrations on homogeneous and heterogeneous plates with different porosities and frequencies show the high effectiveness of the proposed formulation.

In Chapter 6, SAIGA-based procedures for studying poroelastic waveguides coupled with a fluid are presented. The first one employs the isogeometric Galerkin method, which is based on the NURBS discretization of the weak formulation derived in the frequency-wavenumber domain to derive the equation system of eigenvalues (dispersion). The second one uses the collocation isogeometric method, which is based on an NURBS approximation of the strong form of the considered problem to derive the the equation system of eigenvalues (dispersion). The comparison has included a detailed cost *vs.* accuracy analysis between proposed collocation (SAIGA-C) and Galerkin (SAIGA-G) methods. It is shown that the SAIGA-G has much better convergence rate in comparing to the other methods while the computational time could be reduced when using the SAIGA-C method.

Chapter 7 presents a conclusion of the obtained results and discuss them in the framework of further developments and potential applications.

Note that the content of chapter two to chapter six comes mainly from the scientific papers which are published, submitted for publication or to be submitted for publication. Each chapter is relatively self-contained, and some repetition of material is therefore unavoidable.

Chapter 2

Wave dispersion in random elastic cylinders

2.1 Introduction

A large variety of the natural and artificial materials have unidirectional heterogeneous and random elastic properties. Mantel crust, oceans, composites or bone materials are some of these randomly inhomogeneous media. Due to the hidden nature and/or use in-services, inspection of these structures using non-destructive techniques have grown rapidly over the last decades. Guided waves are perhaps the most common principle upon which modern non-destructive methods for are developed [4]. Due to the presence of boundaries, variation of material properties and the existing of surrounding medium (most commonly fluid), the guided waves show a strong dispersive behavior, i.e. the phase velocity and attenuation vary with frequency-content of wave package. Therefore, the knowledge of the dispersion properties of guided waves is of fundamental importance in many practical applications and can be used to identify the material properties or evaluate their change over time.

In this context, there is a considerable number of publications dealing with the dispersion of guided waves using the deterministic models. The deterministic models assume that the modeling parameters are perfectly known. However, most of the time, only partial information is available on these parameters and the actual values which are obtained via experimental measurements. So, it is useful to consider these parameters as uncertain in order to describe correctly the propagation of waves. Among other approaches, probability theory provides an effective and robust framework to take into account such uncertainties. The uncertainty introduced on the parameters allows, in particular, to assess its impact on the interest parameters.

The aim of this chapter[1] is to investigate the dispersion curves of guided waves through the cylindrical cortical bone coupled with fluid. The semi-analytical finite element (SAFE) method will be used to compute the dispersion curves of random elastic cylinders. The elasticity tensor of bone tissue is randomly varied in the thickness direction. A sensitivity analysis of material properties will be performed. In the deterministic model from which the stochastic model is constructed, the cortical bone cylinder is assumed to be homogeneous and transversely isotropic elastic. Whereas in the stochastic model, the structure is anisotropic and heterogeneous with material properties that vary along the thickness axis. In principle, it will be possible to estimate the physical parameters of bone from the acoustic response. This can be done by solving an inverse problem which will require

[1] The work presented in this chapter will be submitted for a publication

appropriate resolution strategy. This study presents therefore the first step in the modeling of the direct problem which is indispensable to the identification of material properties.

2.2 Problem formulation

In the following, the SAFE formulation is derived for an axisymmetric waveguides. Owing to the axisymmetric assumption the cross-section is represented with monodimensional elements. The idea is to discretize the radial direction of the waveguide using finite element method, and wave dispersion relation is assumed in the longitudinal direction.

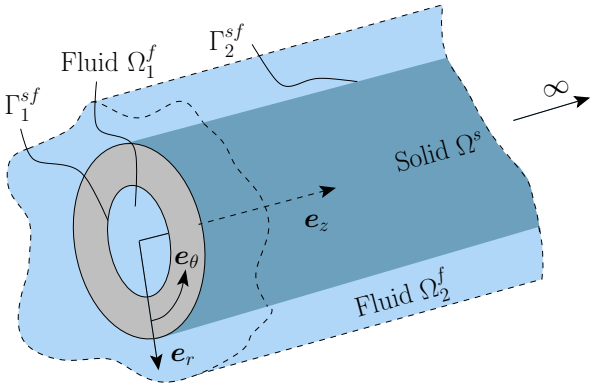

Figure 2.1 – Schematics of fluid-filled and immersed cylinder

2.2.1 Governing equation

Geometry description The geometry of an hollow cylindrical waveguides is shown in Fig. 2.1. The structure is described in the cylindrical coordinate system with an orthogonal basis $(\mathbf{e}_r, \mathbf{e}_\theta, \mathbf{e}_z)$ and the position vector $\boldsymbol{x} = (r, \theta, z)$. The cross section of the solid is constant along $\mathbf{e}_z$. The domains occupied by the solid body and the fluids are denoted by $\Omega^s = \{x(r,\theta,z)|z \in (-\infty,+\infty), r \in [r_i, r_e]\}$, $\Omega_1^f = \{x(r,\theta,z)|z \in (-\infty,+\infty), r \in [0, r_i]\}$, $\Omega_2^f = \{x(r,\theta,z)|z \in (-\infty,+\infty), r \in [r_e,+\infty)\}$, where r_i , r_e are the internal and external radius, respectively. The interfaces between Ω^s and the fluid domains Ω_α^f are denoted by Γ_α^{sf} $(\alpha = \{1, 2\})$, respectively. As the thickness of the cylinder is constant, the outward directed, normal vectors of Ω^s at Γ_1^{sf} and Γ_2^{sf} are given by $\mathbf{n}_1 = \{-1, 0, 0\}^T$ and $\mathbf{n}_2 = \{1, 0, 0\}^T$, respectively.

Dynamic equations in the solid layer In the solid domain Ω^s, the infinitesimal displacement vector at a point $\mathbf{x}(r, \theta, z)$ and at time t is denoted by $\boldsymbol{u}(\mathbf{x}, t) = \{u_r, u_\theta, u_z\}^T$. For the purpose of convenience, here we use the Voigt notation which represent the stress and strain under vectorial form as:

$$\boldsymbol{s}(\mathbf{x},t) = \{\sigma_{rr}, \sigma_{\theta\theta}, \sigma_{zz}, \sigma_{\theta z}, \sigma_{rz}, \sigma_{r\theta}\}^T, \quad \boldsymbol{e}(\mathbf{x},t) = \{\varepsilon_{rr}, \varepsilon_{\theta\theta}, \varepsilon_{zz}, 2\varepsilon_{\theta z}, 2\varepsilon_{rz}, 2\varepsilon_{r\theta}\}^T, \tag{2.1}$$

where σ_{ij} and ε_{ij} are the components of the stress and infinitesimal strain tensors, respectively. As $\varepsilon_{ij} = \frac{1}{2}(\partial_i u_j + \partial_j u_i)$, the strain vector $\boldsymbol{e}$ can be expressed by: $\boldsymbol{e} = \mathbf{L}\boldsymbol{u}$, where the operator $\mathbf{L}$ is

defined by:

$$\mathbf{L} = \mathbf{L}_r\partial_r + \mathbf{L}_\theta\frac{1}{r}\partial_\theta + \mathbf{L}_z\partial_z + \mathbf{L}_0\frac{1}{r}, \tag{2.2}$$

$$\mathbf{L}_r = \begin{bmatrix}1&0&0\\0&0&0\\0&0&0\\0&0&0\\0&0&1\\0&1&0\end{bmatrix}, \quad \mathbf{L}_\theta = \begin{bmatrix}0&0&0\\0&1&0\\0&0&0\\0&0&1\\0&0&0\\1&0&0\end{bmatrix}, \quad \mathbf{L}_z = \begin{bmatrix}0&0&0\\0&0&0\\0&0&1\\0&1&0\\1&0&0\\0&0&0\end{bmatrix}, \quad \mathbf{L}_0 = \begin{bmatrix}0&0&0\\1&0&0\\0&0&0\\0&0&0\\0&0&0\\0&-1&0\end{bmatrix} \tag{2.3}$$

The balance equations of linear momentum at a point $\boldsymbol{x} \in \Omega^s$ and the linear elastic constitutive law read :

$$\rho\ddot{\boldsymbol{u}} - \mathbf{L}^T\boldsymbol{s} = 0\,, \tag{2.4}$$
$$\boldsymbol{s} = \mathbf{C}\boldsymbol{e}\,, \tag{2.5}$$

where the ρ is the mass density and $\mathbf{C}_{6\times6}$ is the matrix containing the components of the anisotropic elasticity tensor. In this problem, the structure is assumed to be homogeneous along the longitudinal direction $\mathbf{e}_z$ and $\mathbf{e}_\theta$ but it could be heterogeneous in the $\mathbf{e}_r$ direction, *i.e.* $\rho = \rho(r)$ and $\mathbf{C} = \mathbf{C}(r)$.

Wave equations in the fluids In the fluid domains Ω^f_α ($\alpha = 1, 2$), the linearized wave equations can be expressed as

$$\rho^f_\alpha\ddot{p}_\alpha - K^f_\alpha\nabla^2 p_\alpha = 0\,, \tag{2.6}$$

where p_α are the acoustic pressure fields in Ω^f_α, K^f_α and ρ^f_α are the bulk modulus at rest and the mass density at rest of the Ω^f_α, respectively; $\nabla^2(\star)$ is the Laplace operator. The wave celerity in Ω^f_α can be defined as $c^f_\alpha = \sqrt{K^f_\alpha/\rho^f_\alpha}$.

Boundary conditions The boundary conditions of this system consist of the continuity condition of the normal displacement and traction at the solid-fluid interfaces $\Gamma^{sf}_\alpha (\alpha = \{1, 2\})$ and the radiation condition at infinity, i.e.

$$\left.\begin{aligned}\boldsymbol{u}\cdot\mathbf{n}_\alpha &= \boldsymbol{u}^f\cdot\mathbf{n}_\alpha\\ \boldsymbol{t} &= -p_\alpha\mathbf{n}_\alpha\end{aligned}\right\} \quad \forall\boldsymbol{x}\in\Gamma^{sf}_\alpha\,, \tag{2.7}$$

$$p_\alpha \to 0 \qquad \text{when } |\boldsymbol{x}| \to \infty\,, \tag{2.8}$$

where $\mathbf{n}_\alpha$ is the outward unit vector at the interfaces (Fig. 2.1). It is worth to note that $\boldsymbol{t} = \mathbf{L}_r^T\boldsymbol{s} = \{\sigma_{rr}, \sigma_{r\theta}, \sigma_{rz}\}^T$.

2.2.2 Weak formulation

We look for the solution of harmonic waves propagating along the axial direction ($\mathbf{e}_z$) which may be expressed under following form:

$$p_\alpha(r,\theta,z,t) = \tilde{p}_\alpha(r)e^{in\theta}e^{i(k_z z-\omega t)}\ , \tag{2.9}$$

$$\boldsymbol{u}(r,\theta,z,t) = \tilde{\boldsymbol{u}}(r)e^{in\theta}e^{i(k_z z-\omega t)}\ , \tag{2.10}$$

where $i^2=-1$; $\omega\in\mathbb{R}$ is the angular frequency; k_z is the wavenumber in the $\mathbf{e}_z$-direction; and $n\in\mathbb{N}$ denotes circumferential wave number; the $\tilde{p}_\alpha(r)=\tilde{p}_\alpha$ is the amplitudes of the pressure fields in the $\bar{\Omega}^f_\alpha$ and the vector $\tilde{\boldsymbol{u}}(r)=(\tilde{u}_r,\tilde{u}_\theta,\tilde{u}_z)^T$ is the amplitudes of the displacement vector in the $\bar{\Omega}^s$

Weak formulation in the fluid domain Upon integrating Eq. (2.6) against a test function $\delta\tilde{p}_\alpha$ and applying the Gauss theorem taking into account the interface conditions Eq. (2.7) , the weak formulation of the boundary value problem in the fluid domains Ω^f_α may be derived as [49]:

$$\begin{aligned}&-\omega^2\int_{\bar{\Omega}^f_\alpha}\delta\tilde{p}^*_\alpha\rho_\alpha\tilde{p}_\alpha r dr+k_z^2\int_{\bar{\Omega}^f_\alpha}\delta\tilde{p}^*_\alpha K_\alpha\tilde{p}_\alpha r dr-\int_{\bar{\Omega}^f_\alpha}\partial_r\delta\tilde{p}^*_\alpha K_\alpha\partial_r\tilde{p}_\alpha r dr\\&+n^2\int_{\bar{\Omega}^f_\alpha}\delta\tilde{p}^*_\alpha K_\alpha\tilde{p}_\alpha r dr+\Big[\omega^2\delta p^*_\alpha\rho_\alpha K_\alpha(\boldsymbol{u}^s)\Big]_{r_i}^{r_e}=0\ ,\quad\forall\delta\tilde{p}_\alpha\in\mathcal{C}^{ad},\end{aligned} \tag{2.11}$$

Weak formulation in the solid domain In the same manner the weak formulation of the boundary valued problem in the solid domain Ω^s may be derived:

$$-\omega^2\int_{\bar{\Omega}^s}\delta\tilde{\boldsymbol{u}}\cdot\rho\tilde{\boldsymbol{u}}r dr+\int_{\bar{\Omega}^s}\tilde{\mathbf{L}}^T\delta\tilde{\boldsymbol{u}}\cdot(\mathbf{C}\tilde{\mathbf{L}}\tilde{\boldsymbol{u}})dr-\Big[\delta\tilde{\boldsymbol{u}}\cdot\tilde{p}\mathbf{n}_\alpha\Big]_{r_i}^{r_e}=0\ ,\quad\forall\delta\tilde{\boldsymbol{u}}\in\mathcal{C}^{ad}\ , \tag{2.12}$$

2.2.3 Perfectly matched layer

2.2.4 Perfectly Matched Layer (PML)

In order to introduce the behavior of the infinite exterior fluid domain, we used the perfectly matched layers (PML) in the cross-section plane, following the procedures proposed in [41, 50]. From a mathematical point of view, the PML can be considered as a result of a mapping into complex coordinates, where the solutions of wave equations decay exponentially [51]. Therefore, the infinite medium can be truncated into a finite domain as shown in Fig. 2.1. The new stretched coordinates in the waveguide are defined as

$$\tilde{r}(r)=\int_0^r\gamma(r)dr, \tag{2.13}$$

where $\gamma(r)$ is called PML function, which satisfies:

$$\gamma(r)=1\text{ for }|r|\le d\text{ and }\mathrm{Im}\{\gamma(r)\}>0\text{ for }|r|>d, \tag{2.14}$$

On the exterior boundary of the PML, the boundary condition can be arbitrarily chosen (Dirichlet or Neumann type). The absorption efficiency of leaky waves in the PML strongly depends on the choice

of the PML function γ, the position of the interfaces d and the thickness h^{pml} in the $\mathbf{e}_r$. There are a number of variants to choose for the γ functions. For this study, a continuous parabolic function for both the real and imaginary parts of the PML function, which has been demonstrated to be efficient in the frequency domain [50, 41], was used:

$$\gamma(r) = \begin{cases} 1 & \text{if } |r| \leq d, \\ 1 + \hat{\gamma}\left(\frac{|r|-d}{h^{pml}}\right)^2 & \text{if } |r| > d, \end{cases}, \tag{2.15}$$

where $\hat{\gamma} = a_j + \mathrm{i}b_j$ quantify the PML absorption and will be given explicitly in each case study. As leaky waves grow exponentially in the transverse directions, placing the PML close to the waveguide can reduce the effect of the exponential growth of the leaky modes. In order to estimate the length of the PML, a simplified 2D plane wave propagation model can be used to approximately predict the length of the PML:

$$h^{pml} \geq \frac{6.9}{k_{\text{leak}} b}, \tag{2.16}$$

where k_{leak} represents the wavenumber of the longitudinal wave in the fluid. When the PML function is given, b can be determined as $\mathrm{Im}\,(\hat{\gamma})$. The length of the PML can be obtained by calculating the smallest wavenumber in the frequency range of interest [41].

2.2.5 Finite element discretization

In this study, the conventional finite element method is employed, in which the same approximations are applied for both functions $\tilde{\boldsymbol{u}}^h$ and $\delta\tilde{\boldsymbol{u}}^h$ (as well as for $\tilde{p}^h_\alpha$ and $\delta\tilde{p}^h_\alpha$) on each patch:

$$\tilde{\boldsymbol{u}}^h = \mathbf{N}^u\mathbf{U}, \quad \delta\tilde{\boldsymbol{u}}^h = \mathbf{N}^u\delta\mathbf{U}, \tag{2.17a}$$

$$\tilde{p}^h_\alpha = \mathbf{N}^p_\alpha\mathbf{P}_\alpha, \quad \delta\tilde{p}^h_\alpha = \mathbf{N}^p_\alpha\delta\mathbf{P}_\alpha, \tag{2.17b}$$

where $\mathbf{N}^u$, $\mathbf{N}^p$ are the interpolation matrix containing the Lagrange basis functions; $\mathbf{U}$ and $\delta\mathbf{U}$ are the vectors of nodal displacements; $(\mathbf{P}_\alpha)$ and $(\delta\mathbf{P}_\alpha)$ are the displacement vectors of nodal pressures. In this chapter we consider the Lagrange basis functions for approximation of the solution fields in Eqs. (2.17a)-(2.17b). We use the same order of basis function for the solid and both fluid domains, therefore we refer to the $\mathbf{N}$ as the basis function. By substituting the approximations Eqs. (2.17a)-(2.17b) into the weak formulations Eqs. (2.11)-(2.12), then assembling the elementary matrices, one obtains

$$(-\omega^2\mathbf{M} + \mathbf{K}_0 + \mathrm{i}k_z\mathbf{K}_1 + k_z^2\mathbf{K}_2)\mathbf{V} = \mathbf{0}\ , \tag{2.18}$$

where $\mathbf{V} = (\mathbf{P}_1, \mathbf{U}, \mathbf{P}_2)^T$ containing the global eigenvectors of pressure ($\mathbf{P}_1$, $\mathbf{P}_2$) and of displacement ($\mathbf{U}$); the global matrices $\mathbf{M}$, $\mathbf{K}_0$, $\mathbf{K}_1$, $\mathbf{K}_2$ are defined by:

$$\mathbf{M} = \begin{bmatrix} \mathbf{M}^{f_1} & \mathbf{M}^{f_1 s} & \mathbf{0} \\ \mathbf{0} & \mathbf{M}^{s} & \mathbf{0} \\ \mathbf{0} & \mathbf{M}^{f_2 s} & \mathbf{M}^{f_2} \end{bmatrix}, \ \mathbf{K}_0 = \begin{bmatrix} \mathbf{K}_0^{f_1} & \mathbf{0} & \mathbf{0} \\ \mathbf{K}^{s f_1} & \mathbf{K}_0^{s} & \mathbf{K}^{s f_2} \\ \mathbf{0} & \mathbf{0} & \mathbf{K}_0^{f_2} \end{bmatrix}, \tag{2.19a}$$

$$\mathbf{K}_1 = \begin{bmatrix} \mathbf{0} & \mathbf{0} & \mathbf{0} \\ \mathbf{0} & \mathbf{K}_1^{s} & \mathbf{0} \\ \mathbf{0} & \mathbf{0} & \mathbf{0} \end{bmatrix}, \ \mathbf{K}_2 = \begin{bmatrix} \mathbf{K}_2^{f_1} & \mathbf{0} & \mathbf{0} \\ \mathbf{0} & \mathbf{K}_2^{s} & \mathbf{0} \\ \mathbf{0} & \mathbf{0} & \mathbf{K}_2^{f_2} \end{bmatrix}, \tag{2.19b}$$

in which the sub-matrices are determined from the assembling of corresponding elementary matrices in solid and fluid domains: the sub-matrices with superscript ^{s} and ^{f} representing the behavior of the solid and fluid domains, respectively, are defined as:

$$\mathbf{M}^s = \int_{r_i}^{r_e} \rho \mathbf{N}^T \mathbf{N} r dr \tag{2.20}$$

$$\begin{aligned}\mathbf{K}_0^s = &\int_{r_i}^{r_e} \left(r\mathbf{B}^T \mathbf{A}^{rr} \mathbf{B} + \frac{1}{r} \mathbf{N}^T \mathbf{A}^{00} \mathbf{N} \right) dr + \int_{r_i}^{r_e} 2 \left\{ \mathbf{B}^T \mathbf{A}^{r0} \mathbf{N} \right\}_s dr \\ &+ \mathrm{i}n \int_{r_i}^{r_e} 2 \left(\left\{ \mathbf{B}^T \mathbf{A}^{r\theta} \mathbf{u}_n \right\}_a - \frac{1}{r} \left\{ \mathbf{N}^T \mathbf{A}^{\theta 0} \mathbf{N} \right\}_a \right) dr + n^2 \int_{r_i}^{r_e} \frac{1}{r} \mathbf{N}^T \mathbf{A}^{\theta\theta} \mathbf{N} dr\end{aligned} \tag{2.21}$$

$$\mathbf{K}_1^s = \int_{r_i}^{r_e} 2 \left(r \left\{ \mathbf{B}^T \mathbf{A}^{rz} \mathbf{N} \right\}_a - \left\{ \mathbf{N}^T \mathbf{A}^{0z} \mathbf{N} \right\}_a \right) dr - \mathrm{i}n \int_{r_i}^{r_e} 2 \left\{ \mathbf{N}^T \mathbf{A}^{\theta z} \mathbf{N} \right\}_s dr \tag{2.22}$$

$$\mathbf{K}_2^s = \int_{r_i}^{r_e} r \mathbf{N}^T \mathbf{A}^{zz} \mathbf{N} dr \tag{2.23}$$

Note that $\{\mathbf{A}\}_s$ and $\{\mathbf{A}\}_a$ respectively denote the symmetric and antisymmetric parts of a square matrix $\mathbf{A}$. Similarly the sub-matrices related to the fluid domains are defined as:

$$\mathbf{M}^f = \int_{r_i}^{r_e} \gamma \rho_\alpha \mathbf{N}^T \mathbf{N} r dr \tag{2.24}$$

$$\mathbf{K}_0^f = -\int_{r_i}^{r_e} \frac{1}{\gamma} K_\alpha \mathbf{B}^T \mathbf{B} r dr + n^2 \int_{r_i}^{r_e} \gamma K_\alpha \mathbf{N}^T \mathbf{N} r dr \tag{2.25}$$

$$\mathbf{K}_2^f = \int_{r_i}^{r_e} \gamma \rho_\alpha K_\alpha \mathbf{N}^T \mathbf{N} r dr \tag{2.26}$$

2.2.6 Dispersion analysis

The system of characteristic equations (2.18) is an eigenvalue problem which is used to determine the relationship between the pulsation ω and the wavenumber k_3. By noting that all global matrices ($\mathbf{M}$, $\mathbf{K}_0$, $\mathbf{K}_1$, $\mathbf{K}_2$) do not depend on k_3, Eq. (2.18) is a quadratic eigenvalue problem with respect to k_3 and could be solved by reformulating it under following linearized eigenvalue problem:

$$\left(\begin{bmatrix} \mathbf{0} & -\omega^2 \mathbf{M} + \mathbf{K}_0 \\ -\omega^2 \mathbf{M} + \mathbf{K}_0 & \mathrm{i}\mathbf{K}_1 \end{bmatrix} - k_3 \begin{bmatrix} -\omega^2 \mathbf{M} + \mathbf{K}_0 & \mathbf{0} \\ \mathbf{0} & -\mathbf{K}_2 \end{bmatrix} \right) \begin{pmatrix} \mathbf{V} \\ k_3 \mathbf{V} \end{pmatrix} = \mathbf{0} \,. \tag{2.27}$$

For each value of the angular frequency ω, solving Eq. (2.27) allows us to determine the eigenvalues k_3 and their associated eigenvectors (also called by wave structures) [4], $\mathbf{V}(\omega, k_3)$ of guided modes. The frequency-dependent phase velocity (C_{ph}) and the attenuation (att) of a guided mode are given by:

$$C_{\mathrm{ph}} = \frac{\omega}{\mathrm{Re}\,(k_3)} \ [\mathrm{m.s}^{-1}], \quad \mathrm{att} = \mathrm{Im}\,(k_3) \ [\mathrm{Np.m}^{-1}] \,, \tag{2.28}$$

where Re () and Im () denote the real and imaginary parts of a complex function.

2.3 Three-dimensional stochastic model

2.3.1 Probabilistic model of the elasticity tensor

In this section, we describe briefly the probabilistic model used to generate the random medias. As recalled in previous sections, a cortical bone may be modeled by a cylinder having random properties

in the radial direction. The uncertainties are introduced via the heterogeneity which is randomly varied in the bone layer along the $\mathbf{e}_r$ direction. A probabilistic model which has been developed by Soize in [52] is deemed to be more suitable for such problem (Nguyen et al. [53]). Note that this model is mainly constructed to generate random elastic tensors by using two ingredients: the maximum entropy principle (Jaynes, [54, 55]) and the random matrix theory (Mehta, [56]) in three dimensions (21 components). In this chapter, we only sketch out the main features of the model in the context of cortical bone study, a more detailed description may be found in [52].

Henceforth, the writing in upper and lowercase will be used to denote random and mean quantities, respectively. As result, we denote by $\mathbf{C}(r)$ the random elastic matrix at a material point $\boldsymbol{x}(r;\theta;z)$ and by $\mathbf{c}(r)$ its mean value, respectively. The following relationship is satisfied $\mathbb{E}\{\mathbf{C}(r)\} = \mathbf{c}(r)$, where $\mathbb{E}\{\star\}$ designates the mathematical expectation. Moreover, the random and mean elastic tensors both belong in set of all the (6×6) real symmetric positive-definite matrices $\mathbf{M}_6^+(\mathbb{R})$ (R).

The random matrix $\mathbf{C}(r)$ is parameterized by its mean value $\mathbf{c}(r)$, the dispersion level and three spacial correlation length λ_r, λ_θ and λ_z in the $\mathbf{e}_r$, $\mathbf{e}_\theta$ and $\mathbf{e}_z$-directions, respectively. However, material properties in the bone cylinder being assumed to be homogeneous is the $\mathbf{e}_z$-direction and invariant in the circumferential directions, $\mathbf{C}(r)$ has been generated in three dimensions (21 components) with a high value of the spatial correlation lengths in the $\mathbf{e}_\theta$ and $\mathbf{e}_z$-directions. The matrix $\mathbf{c}(r) \in \mathbf{M}_6^+(\mathbb{R})$ can be decomposed into a product of a unique upper triangular real matrix $\mathbf{L}(r)$ with strictly positive diagonal entries and its transpose:

$$\mathbf{c}(r) = \mathbf{L}^T(r)\mathbf{L}(r) \; , \tag{2.29}$$

Using this model, the random matrix $\mathbf{C}(r)$ is parameterized by its mean value $\mathbf{c}(r)$, the dispersion level δ and the correlation length λ_r in the $\mathbf{e}_r$-direction, which is denoted by $\mathbf{C}(r;\mathbf{c},\delta,\lambda_r)$ and can be decomposed in following form:

$$\mathbf{C}(r;\mathbf{c},\delta,\lambda_r) = \mathbf{L}^T(r)\mathbf{G}(r;\mathbf{c},\delta,\lambda_r)\mathbf{L}(r) \; , \tag{2.30}$$

where $\mathbf{G}(r;\mathbf{c},\delta,\lambda_r)$, is a stochastic field called the stochastic germ matrix, which is a homogeneous and normalized non-Gaussian positive-definite matrix-valued second-order random field with values in $\mathbf{M}_6^+(\mathbb{R})$.

The dispersion parameter δ, which is a scalar, controls the dispersion of the random matrix $\mathbf{G}(r;\mathbf{c},\delta,\lambda_r)$ and must satisfy the following inequality $0 < \delta < \sqrt{(p+1)/(p+5)}$, which allows the mean-square convergence condition for the germ matrix to be hold [57]. It is proved that the dispersion parameter δ is related to a parameter δ_C which evaluates the dispersion of the random matrix $\mathbf{C}(r)$ by the relation given by:

$$\delta_C(r) = \frac{\delta}{\sqrt{p+1}} \left\{ 1 + \frac{\{\mathrm{Tra}(\mathbf{c}(r))\}^2}{\mathrm{Tra}([\mathbf{c}(r)]^2)} \right\}^{1/2} \; , \tag{2.31}$$

where Tra is the trace operator. Note that the dispersion of the random matrix $\mathbf{c}(r)$ is a scalar field and depends on r, p and δ.

2.4 Numerical results

Although the wide variety of natural materials can be inspired by proposed model, for the numerical example in this section we consider cortical long bones which has been considered as functionally graded cylindrical waveguides by many researches (see Baron [18]). Bone tissue has been shown to be heterogeneous, anisotropic and porous materials. Osteoporosis in long bone may reduce bone's layer thickness and bone's rigidity by increasing porosity, especially in the endosteal region, and by degrading the mineral content of bone matrix. In most studies, the bone has been considered as a 2D plate with deterministic properties [58, 59]. Recently, probabilistic studies haven been conducted by our group to examine the effects of random heterogeneity in bone plates to different ultrasound responses such as first arriving velocity or reflection coefficient. The dispersion of guided waves, which has been shown to be able to provide richer information on the characteristics of bone plates (Pereira et al. [60]; Tran et al. [61]), has still not been investigated from a probabilistic point of view for 3D geometry. For each computation, around 30 elements are used resulting in 183, 60 and 60 degrees of freedom in solid , inner fluid and outer fluid respectively. We verified that decreasing the maximum size of the elements does not modify the results obtained in the present study.

As described in subsection 2.3, the dispersion δ and one correlation length λ_r are needed to control the statistical fluctuations of the elasticity field in the $\mathbf{e}_r$-direction. A fixed spatial correlation length λ_r=100 will be used, which may be seen as a center-to-center distance between osteons in cortical bone (see [62, 63]). Three different values of dispersion δ=0.1,0.2 and 0.3 will be investigated, these three values lead to δ_C=0.1251; 0.2431 and 0.3647 three different values of the dispersion at material points. Figs. 2.2 shows an illustration of a realization of the spatial variation of the components of the random field $C_{11}(r)$ and $C_{12}(r)$ with respect to r when δ=0.1.

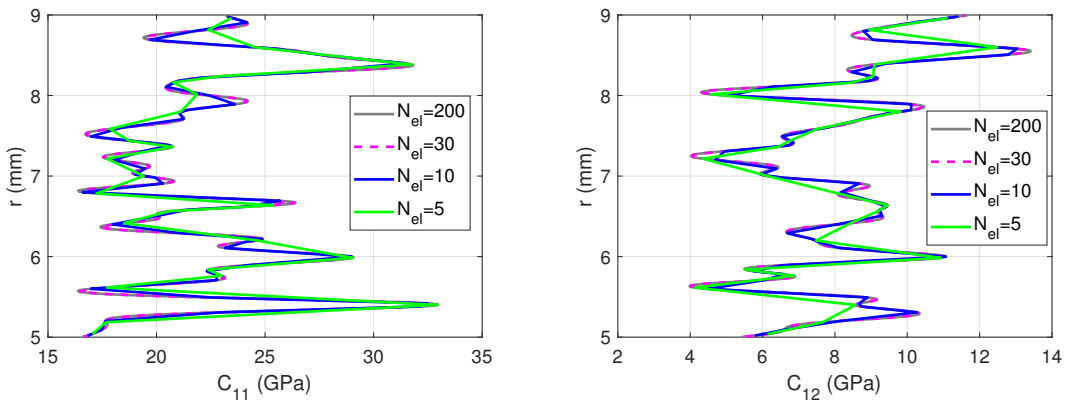

(a) (b)

Figure 2.2 – r-profiles of C_{11} and C_{12} components for different discretization using $\delta = 0.3$

2.4.1 Deterministic homogeneous model

Before investigating the ultrasonic behavior of random cylinders, we first validate our numerical approach by a typical example of cortical bone cylinder with transversely isotropic (TI) elastic properties which are taken from the mechanical test results obtained by Dong and Guo [64]. The validation is made by comparing our results to the analytical dispersion curves obtained with Disperse software. Three cases are considered: hollow, fluid-filled and immersed cylinders.

Table 2.1 – Mechanical parameters for the mean model of cortical bone materials

ρ (kg.m^{-3})	c_{11} (GPa)	c_{33} (GPa)	c_{13} (GPa)	c_{55} (GPa)	c_{66} (GPa)
1722	15.1	23.05	8.71	4.7	3.3

2.4.1.1 Free hollow cylinder

In this first example the cylinder is assumed to be made of transverse isotropic materials (cortical bone). The cylinder has a thickness equal to $h = 4$ mm and its material properties are given in Table 2.1. Dispersion curves of the phase velocity and of the wave number are plotted in Figs. 2.3 within the frequency range f=0-1 MHz (or 4 MHz.mm). We compare the numerical solutions computed by using SAFE to the analytical results obtained by using Disperse software. Each point on the dispersion

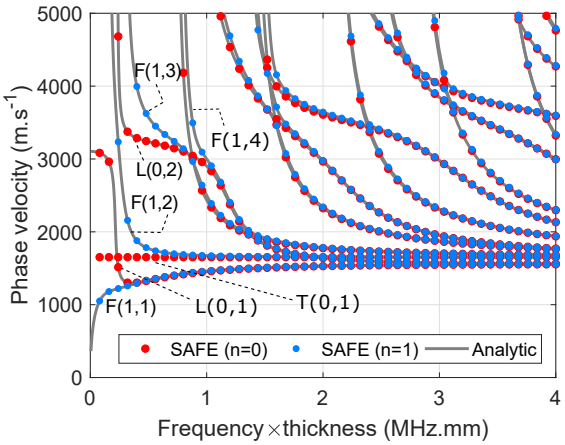

(a)

Figure 2.3 – Case of hollow cylinder: phase velocity dispersion curves of a homogeneous model: comparison between SAFE solution (red and blue marker), and analytical solution (grey line).

curves of phase velocity (or of energy velocity) corresponds to a particular vibration mode. The dispersion curves are in very good agreement with those of the analytic solution. The longitudinal $L(0,m)$ modes and the torsional $T(0,m)$ modes are marked with red markers. In the vicinity of each longitudinal mode, there are the flexural mode $F(1,m)$ which are shown with red markers. The $T(0,1)$ mode has a slight dispersion over the entire frequency range. The $L(0,1)$ mode phase velocity first decreases sharply with increasing frequency. After reaching a minimum value, it then slowly increased with frequency and approached to the Rayleigh wave velocity together with the $T(0,1)$ and $L(0,2)$ mode. As for the higher-order axisymmetric modes, there will also exist the weak coupling effects between them (see Figs. 2.3), which presents a hyperbolic shape of the repulsive behavior. Figs. 2.4(a,b,c) depict the solutions of normalized displacements (u_r^s, u_θ^s and u_z^s) associated to the longitudinal mode $L(0,1)$, flexural modes $F(1,1)$ and $F(1,2)$. It can be seen from these figures that the displacement fields obtained by SAFE and analytical solution agree well. In addition, it can be seen that the circumferential displacement u_θ^s of the $L(0,1)$ mode is 0, which is consistent with the expectation that the circumferential displacement component of longitudinal modes is 0.

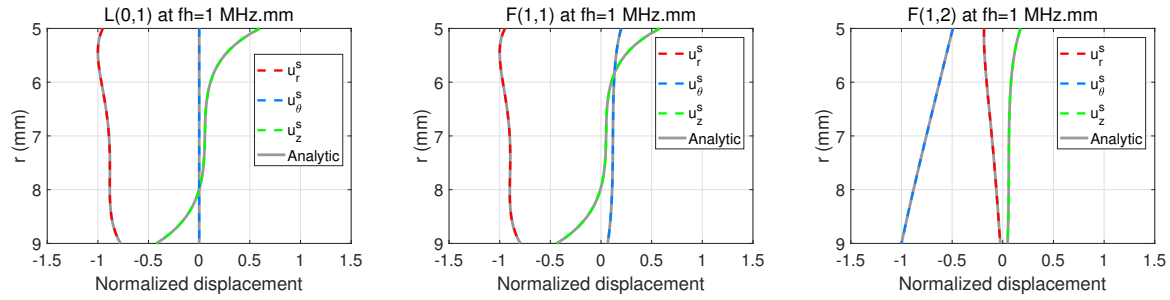

(a) (b) (c)

Figure 2.4 – Case of hollow cylinder: displacement along the thickness of the hollow cylinder: comparison between SAFE solution (color dashes line) and analytical solution (grey line).

2.4.1.2 Fluid-coupled cylinder

This section consider fluid coupled cylinders which have been studied in the literature using both analytical approach [65] and SAFE approach [66]. We first consider a bone cylinder filled by marrow. The bone cylinder has the same geometry and material properties as the one studied in the previous section. The acoustic properties of bone marrow are given by the density $\rho_1^f = 930$ kg.m^{-3} and the sound speed $c_1^f = 1480$ m.s^{-1}. The outer surface of the cylinder is assumed to to be free.

We validate the proposed SAFE formulations for calculating C_{ph}'s dispersion curves. Thanks to the axisymmetric geometry of the cylinder, the considered fluid-filled cylinder can also be solved by using semi-analytical method [65] which was implemented in the Disperse software [67]. Note that when analyzing a coupled fluid-solid system, solving the dispersion equation may sometimes have numerical issues due to singularities when establishing transfer matrices. For this example, Disperse software starts to have difficulties to compute analytical solutions at frequencies higher than 4 MHz.mm, and consequently some modes are missed. On the contrary, using finite element method, allows to avoid this kind of difficulty.

In Fig. 2.5(a), we compare the numerical solutions of C_{ph} obtained by SAFE methods to the analytical ones over the frequency range from 0 to 1 MHz. The discretization is performed by using cubic Lagrange basis functions. The total number of degrees of freedom is equals to N_{dof}=125. A similar filtering procedure as the presented in the previous section was applied to extract the modes of interest. It is shown that the dispersion curves computed by SAFE method agree well with the analytical dispersion ones.

As a final example in this section, we consider a fluid-filled bone cylinder immersed in an infinite fluid domain, which has been considered in numerous works [68] to investigate a numerical solution of leaky wave propagation in fluid immersed structures. The material properties of the bone cylinder and inner fluid are the same as the ones presented in the previous section. The acoustic properties of outer fluid are given by the bone marrow using density $\rho_1^f = 930$ kg.m^{-3} and the sound speed $c_1^f = 1480$ m.s^{-1}. The infinite domain is described by introducing a Perfectly Matched Layer (PML). The PML functions in the simulation are chosen as $\gamma_r = 3 + 12\text{i}$ as given in [41]. The minimum thicknesses of the PMLs can be based on, which allows us to choose $h_r^{\text{pml}} = 2.5$ mm for PML domain in $\mathbf{e}_r$ direction.

We first perform a validation of the proposed SAFE formulation for calculating the dispersion

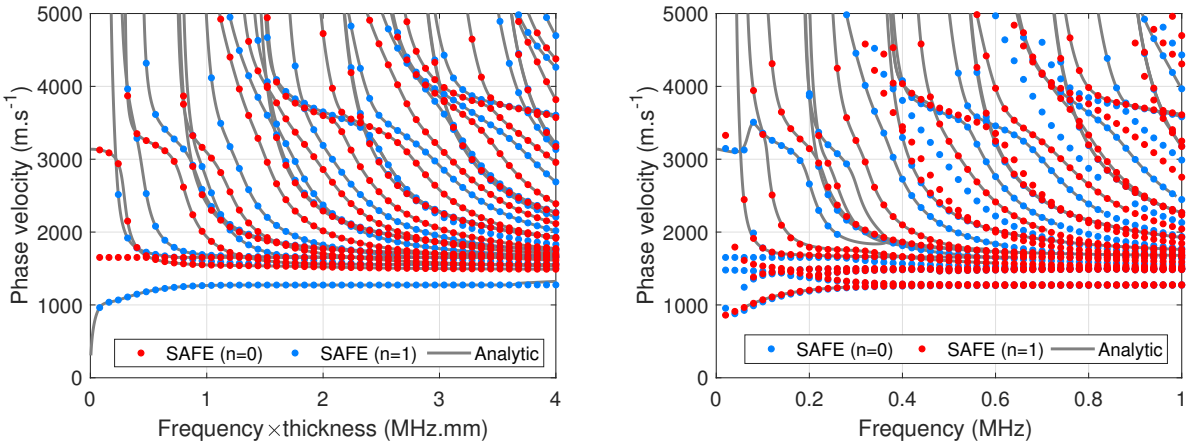

(a) (b)

Figure 2.5 – Dispersion curves of a (a) fluid-filled and (b) fluid-filled and immersed, cylinder: comparison between SAFE solution (red and blue marker), and analytical solution (grey line)

curves of the phase of the considered fluid-filled and immersed cylinder within the frequency range f=0-4 MHz.mm. Fig. 2.5, depicts the phase velocities over the frequency range from 0 to 4 MHz.mm obtained by SAFE and the analytical solution obtained by Disperse software. The discretization is performed by using quadratic Lagrange basis functions. It is shown that the dispersion curves obtained from the proposed approach agree well with the analytical dispersion curves. In this case for analytical solution which is based on the root searching algorithm several modes including first fundamental modes have been missed. Whereas the solution based on SAFE method does not miss any eigenvalues and therefore one can be certain that the solution is complete and no modes have been missed.

2.5 Stochastic heterogeneous model

For the stochastic model, one dispersion value δ and one correlation length λ are used to control the statistical fluctuations of the elasticity tensor in the $\mathbf{e}_2$-direction. A fixed correlation length λ= 100 μm is used, which may be seen as a center-to-center distance between osteons in cortical bone (see Cowin [69], Wang et al. [62] and Nguyen et al. [63]). The dispersion level will be varied from δ=0.1 to δ= 0.3 to investigate the effect of elasticity's random fluctuation on the quantities of interest which are the phase and energy velocities. For each realization, the procedure presented in Section 2 was applied to distinguish the different modes.

For the purpose of practical applications, the fundamental longitudinal mode has been found to be the most suitable at low frequencies due to high phase velocities and small attenuation rates.

2.5.1 Case of hollow cylinder

2.5.1.1 Stochastic convergence analysis

In order to realise the statistics on the interest quantities, a stochastic convergence analysis must first be carried out. Convergence with respect to number of realizations n_r is performed by studying the convergence of the estimated second-order moment. Stochastic convergence analysis leads to determine the minimal number of realizations to do by using the Monte Carlo solver. For instance,

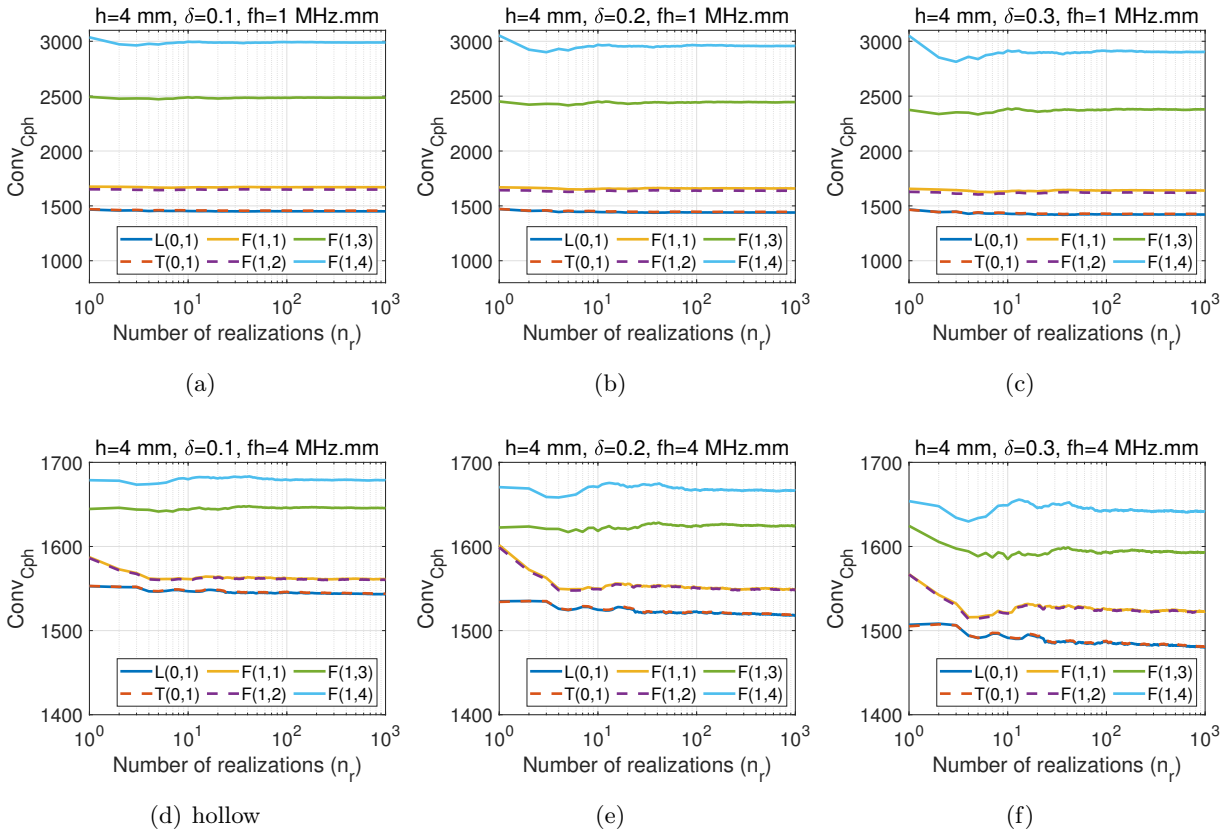

Figure 2.6 – Case of 4-mm thickness hollow cylinder: Stochastic convergence analysis at $fh = 1$ MHz.mm (a,b,c) and at $f = 4$ MHz.mm (d,e,f)

let us consider two cases of 4 mm- and 2 mm-thickness hollow cylinder with the dispersion parameters $\delta = 0.1$, $\delta = 0.2$ and $\delta = 0.3$. In the case of the 4 mm-thickness cylinder, Fig. 2.6 show the graphs of function $n_r \to \mathrm{Conv}_{\mathrm{Cph}}(n_r)$ of the modes $L(0,1)$, $T(0,1)$, $F(1,1)$, $F(1,2)$, $F(1,3)$ and $F(1,4)$ at the two frequencies of $fh = 1$ MHz.mm and $fh = 4$ MHz.mm. It can be observed that the graph of $n_r \to \mathrm{Conv}_{\mathrm{Cph}}(n_r)$ convergences with n_r. The convergences of the modes $L(0,1)$ and $L(0,1)$ and of the modes $F(1,1)$ and $F(1,2)$ are similar having close phase velocities.

At the low frequency, convergence is reached when $n_r \geq 100$ for the modes $L(0,1)$, $T(0,1)$, $F(1,1)$ and $F(1,2)$ and $n_r \geq 200$ for the modes $F(1,3)$ and $F(1,4)$ (see Figs. 2.6 (a,b,c)). We can also observe that the required number of realization increases as the dispersion parameters $\delta =$ increases. Basing on these convergence studies, one may expect that the phase velocity of the first modes $L(0,1)$ $T(0,1)$, $F(1,1)$ and $F(1,2)$ modes are less dispersive than the higher modes $F(1,3)$ and $F(1,4)$ from

statistical point of view. At the high frequency the number of required realization for all modes increases and might be $n_r \geq 500$ for the modes $F(1,3)$ and $F(1,4)$ (see Figs. 2.6 (d,e,f)).

In the case of 2 mm-thickness hollow cylinder, the convergences of the previous modes are shown in the Fig. 2.7. We can observe that the convergences has been changed compare to the 4 mm-thickness hollow cylinder. The error of all the modes increases and may require a higher number of realisation.

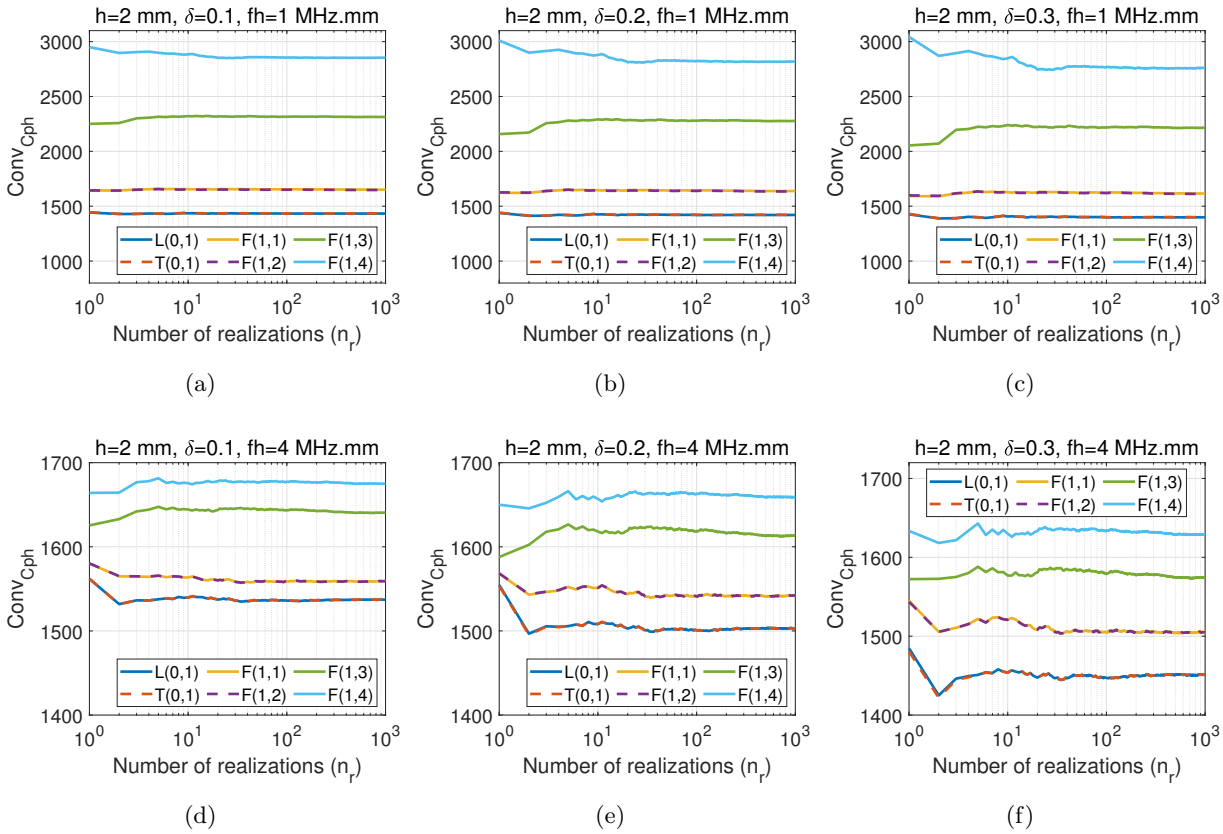

Figure 2.7 – Case of 2-mm thickness hollow cylinder: Stochastic convergence analysis at $fh = 1$ MHz.mm (a,b,c) and at $fh = 4$ MHz.mm (d,e,f)

2.5.1.2 Dispersion curves

In this section, we examine the phase velocity of guided waves in the random hollow cylinder with two thicknesses ($h = 2$ mm, $h = 4$ mm). For each thickness case, we consider by 3 random dispersion levels: $\delta = 0.1$, $\delta = 0.2$ and $\delta = 0.3$. Fig. 2.8 depict the phase velocity and energy velocity computed by all Monte-Carlo realizations for all combination of h and δ. Note that only propagating modes, which have zero or very small attenuation are displayed.

For a 4mm-thickness cylinder, the results depicted in Figs. 2.8(a) show that the fluctuation of the phase velocity is strongly affected by the heterogeneity along the radial direction $\mathbf{e}_r$. For all propagating modes, higher dispersion level δ causes higher fluctuations in estimated phase velocity. Meanwhile, the pattern of dispersion curves is globally unchanged. For a small value of dispersion

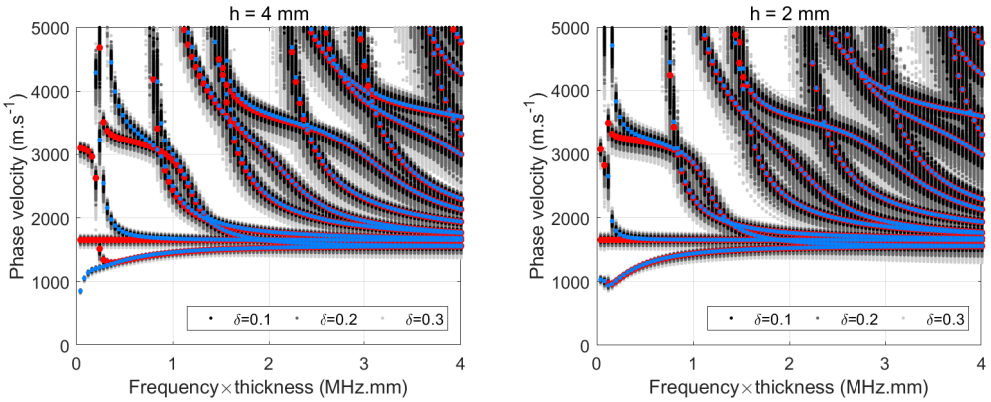

Figure 2.8 – Phase velocity of a 2 and 4 mm-thickness hollow cylinder with 3 dispersion levels: $\delta = 0.1$ (black region), $\delta = 0.2$ (dark gray region) and $\delta = 0.3$ (light gray region).

level ($\delta = 0.1$), random fluctuations of the phase velocity are small then the modes may still be distinguished. When δ becomes greater ($\delta = 0.2$ and $\delta = 0.3$), random fluctuations of the phase velocity become more and more important and it is harder to distinguish different branches, especially at high frequency region. As it can be expected, guided-wave phase velocity is more sensitive to the heterogeneity in the cylinder at higher frequency. Moreover, the modes of higher order may be observed to be more sensitive to the parameter δ. Similar remarks regarding to the fluctuation of phase velocity may be made by considering the 2mm-thickness cylinders. By comparing these 2 cases, we can see that for a same mode at a same frequency, fluctuations of thinner cylinder are more important than the one of thicker cylinder (see the Fig. 2.8(b)).

This effect can be checked from probability density functions (PDF) presented in Fig. 2.9. At a low frequency $f = 1$ MHz.mm, the support of $L(0,1)$ and $F(1,1)$ mode's PDFs are much lower than the other modes. When the frequency increases, the support of all modes gets closer. It can be observed that the PDF of $F(1,4)$ mode is lower than the other modes at all frequencies range. Similar remarks regarding to the fluctuation of phase velocity may be made by considering the 2mm-thickness cylinder (see the Fig. 2.10). By comparing these 2 cases, we can see that for a same mode at a same frequency, fluctuations of thinner cylinder are more important than the one of thicker cylinder.

2.5.2 Case of fluid coupled cylinder

2.5.2.1 Stochastic convergence analysis

Let us consider the case of a random cylinder, which has been studied in the previous section, but now is coupled with two inner and outer fluids. The acoustic properties of inner fluid are given by the bone marrow using density $\rho_1^f = 930$ kg.m^{-3} and the sound speed $c_1^f = 1480$ m.s^{-1}, while the characteristics of outer fluid are given by the soft tissue using $\rho_2^f = 1043$ kg.m^{-3} and $c_2^f = 1561$ m.s^{-1}.

The convergence with respect to number of realizations n_r is performed by studying the convergence of the estimated second-order moment. Stochastic convergence analysis leads to determine the minimal number of realizations to do by using the Monte Carlo solver. In the same manner as presented in the previous case, here we consider two cases of 4 mm- and 2 mm-thickness coupled-fluid

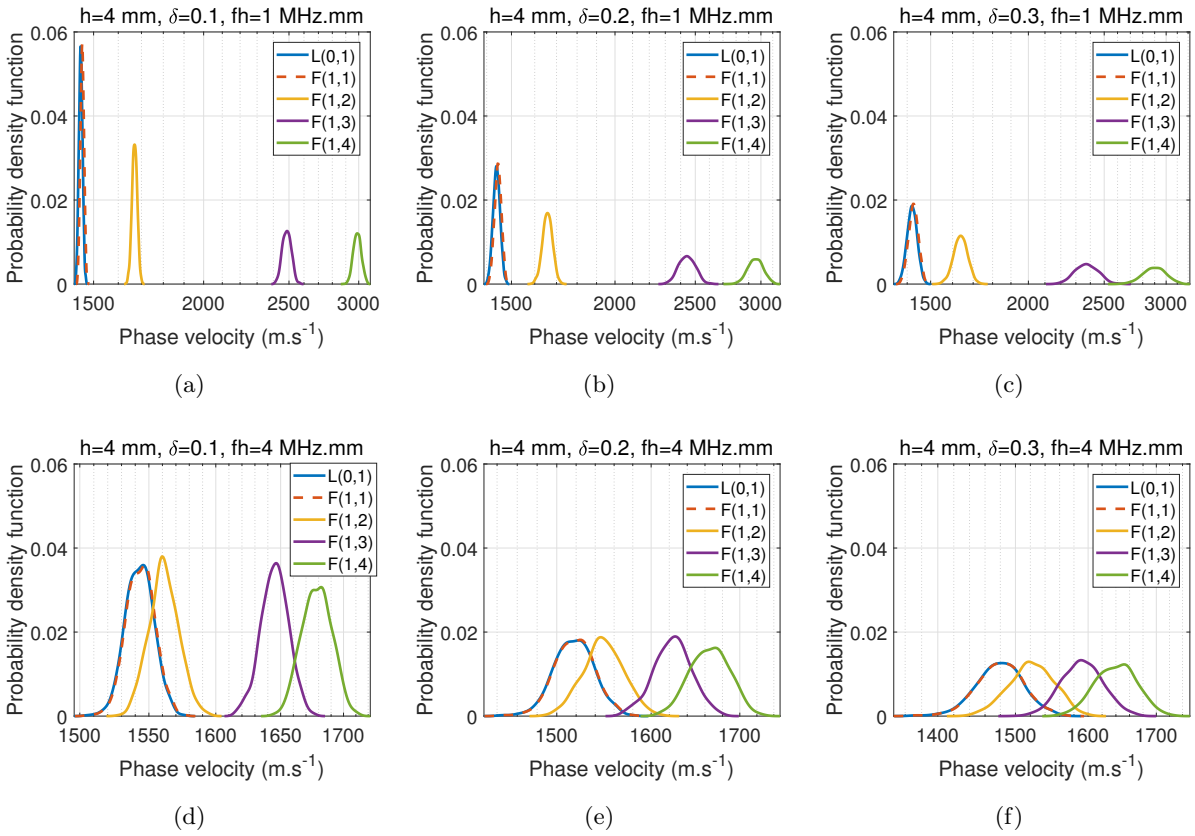

Figure 2.9 – Case of 4-mm thickness hollow cylinder: probability density function at $fh = 1$ MHz.mm (a,b,c),at $fh = 2$ MHz.mm (d,e,f) and at $fh = 4$ MHz.mm (g,h,i)

cylinder with the dispersion parameters $\delta = 0.1$, $\delta = 0.2$ and $\delta = 0.3$. In the case of the 4 mm-thickness cylinder, Fig. 2.11 show the graphs of function $n_r \to \text{Conv}_{\text{Cph}}(n_r)$ of the modes $L(0,1)$, $T(0,1)$, $F(1,1)$, $F(1,2)$, $F(1,3)$ and $F(1,4)$ at the two frequencies of $f = 0.25$ kHz and $f = 1$ MHz. It can be observed that the graph of $n_r \to \text{Conv}_{\text{Cph}}(n_r)$ convergences with n_r. The convergences of the modes $L(0,1)$ and $L(0,1)$ and of the modes $F(1,1)$ and $F(1,2)$ are similar having close phase velocities.

At the low frequency, convergence is reached when $n_r \geq 100$ for the modes $L(0,1)$, $T(0,1)$, $F(1,1)$ and $F(1,2)$ and $n_r \geq 200$ for the modes $F(1,3)$ and $F(1,4)$ (see Figs. 2.11 (a,b,c)). We can also observe that the required number of realization increases as the dispersion parameters $\delta =$ increases. Basing on these convergence studies, one may expect that the phase velocity of the first modes $L(0,1)$ $T(0,1)$, $F(1,1)$ and $F(1,2)$ modes are less dispersive than the higher modes $F(1,3)$ and $F(1,4)$ from statistical point of view. At the high frequency the number of required realization for all modes increases and might be $n_r \geq 500$ for the modes $F(1,3)$ and $F(1,4)$ (see Figs. 2.11 (d,e,f)).

In the case of 2 mm-thickness fluid coupled cylinder, the convergences of the previous modes are shown in the Fig. 2.12. We can observe that the convergences has been changed compare to the 4 mm-thickness hollow cylinder. The error of all the modes increases and may require a higher number of realisation.

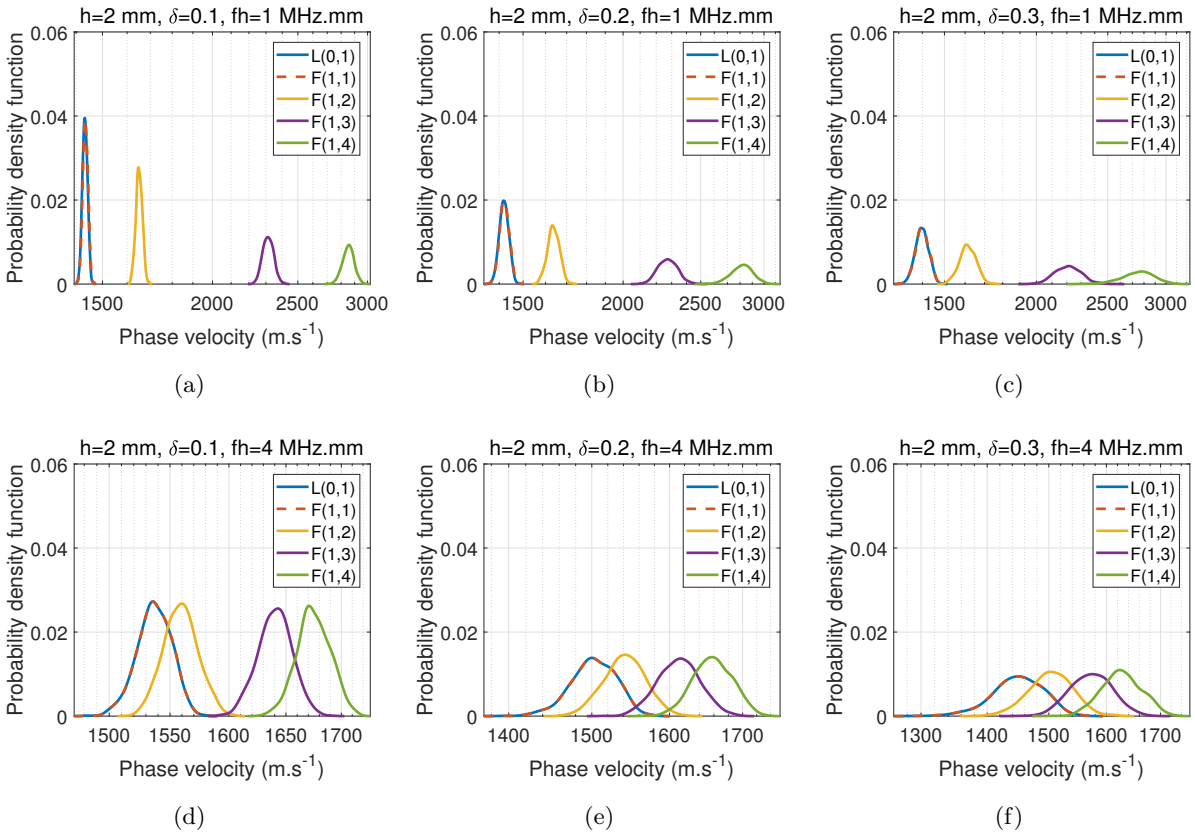

Figure 2.10 – Case of 2-mm thickness hollow cylinder: probability density function at $f = 1$ MHz.mm (a,b,c),at $f = 2$ MHz.mm (d,e,f) and at $f = 4$ MHz.mm (g,h,i)

2.5.2.2 Dispersion curves of fluid coupled cylinder

For a 4mm-thickness fluid-coupled cylinder, the results depicted in Figs. 2.13(a) show that the fluctuation of the phase velocity is strongly affected by the heterogeneity along the radial direction $\mathbf{e}_r$ as well as the presence of the fluid. For all propagating modes, higher dispersion level δ causes higher fluctuations in estimated phase velocity. The pattern of dispersion curves is changed and the number of modes increases for at a given frequency. As in the case of hollow cylinder, for a small value of dispersion level ($\delta = 0.1$), random fluctuations of the phase velocity are small then the modes may still be distinguished. When δ becomes greater ($\delta = 0.2$ and $\delta = 0.3$), random fluctuations of the phase velocity become more and more important and it is harder to distinguish different branches, especially at high frequency region. Moreover, the modes of higher order may be observed to be more sensitive to the parameter δ. However, the fundamental modes $L(0,1)$ and $F(1,1)$ are located at a lower level of phase velocity. They can be found below the wave velocity of fluid. Due to the degradation process the thickness of the cortical bone can be reduced. In order to detect cortical bone alteration we investigate the dispersion curves of a cortical cylinder with 2mm-thickness. The phase velocity dispersion curves are plotted in Figs. 2.13(b). The dispersion curves are more altered compare to the same process of the hollow cylinder.

In Figs. 2.14 and 2.15, the probability density functions of the phase velocity are presented for three frequencies given by f = 250 kHz , f = 500 kHz and f = 1 MHz respectively when δ = 0.1-0.3. For each frequency, the probability density function is plotted for the modes $L(0,1)$, $F(1,1)$,

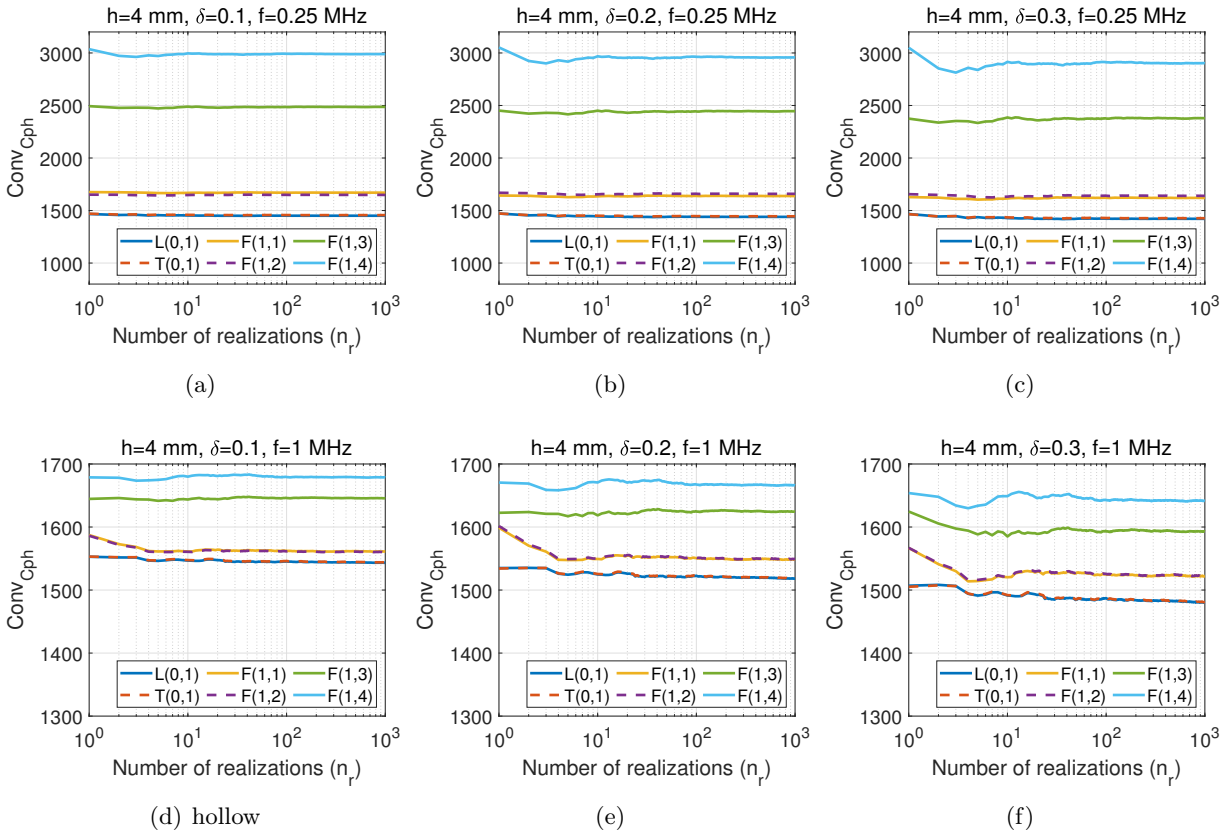

(a) (b) (c)

(d) hollow (e) (f)

Figure 2.11 – Case of 2-mm thickness fluid coupled cylinder: Stochastic convergence analysis at $fh = 1$ MHz.mm (a,b,c) and at $f = 4$ MHz.mm (d,e,f)

$F(1,2)$ $F(1,3)$ and $F(1,4)$. The findings show that the dispersion and the asymmetry degree of the probability density functions increase with f for all incidence angles.

From Fig. 4.14, in which non-axisymmetric modes dispersions curves are presented, analogous behavior can be observed. In this case, as the second index m increases, flexural mode F(1;m) become more dispersive. Thus, F(1; 1) mode is the less dispersive flexural mode, at least from a statistical sens. For all axisymmeric modes, as well as non-axisymmetric modes, statistical dispersion increases with the frequencies thickness products (see. Fig. 4.13(b) and 4.14)

2.5.3 Conclusion

In this chapter, we presented a three-dimensional numerical model of wave propagation in random cylindrical waveguide mimicking the physical properties of cortical bone. The bone is assumed to be anisotropic and to have random heterogeneity in the radial direction. The application motivation was to give birth to a framework which should be able to take into account both uncertainties on heterogeneity and three-dimensional geometry of bone. We investigate especially the guides waves present in cylinder.

We first validated the proposed three-dimensional formulation against the results calculated using Disperse software. The dispersion curve extracted by our approach agreed well with those calculated via Disperse software in which the global matrix method is implemented.

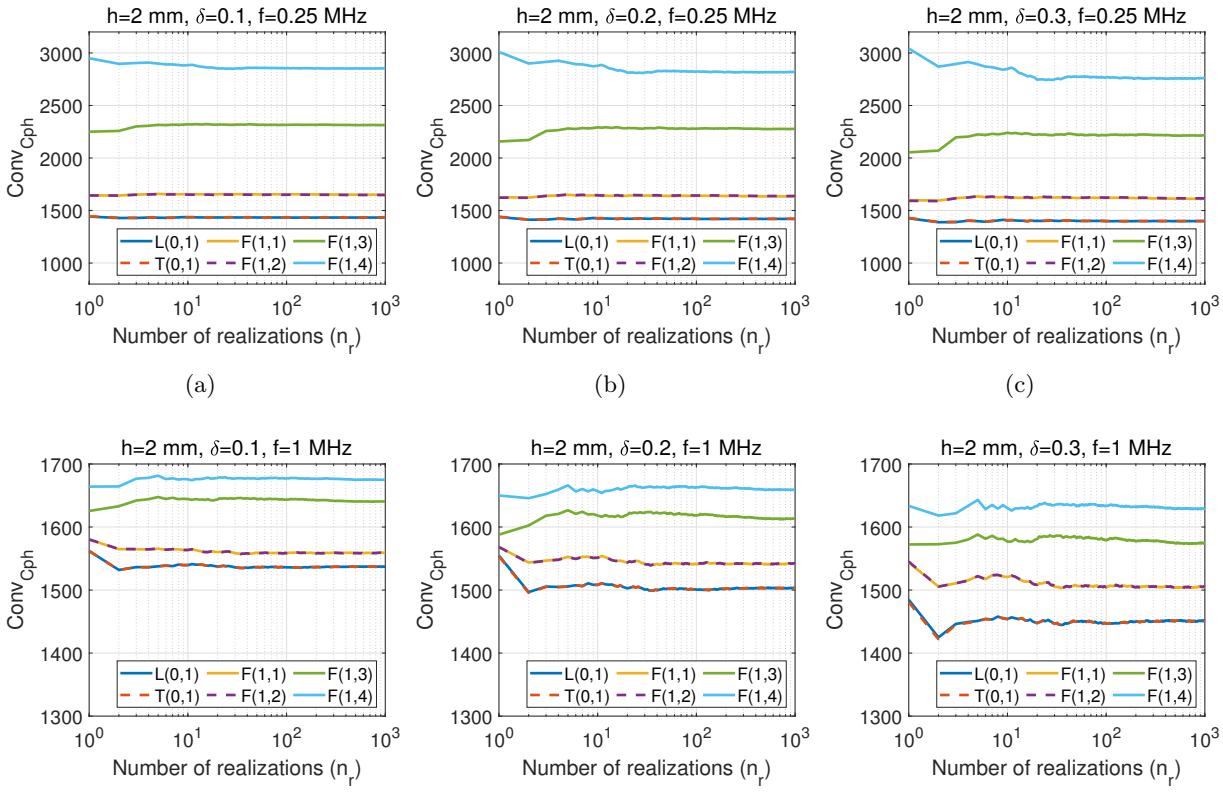

(a) (b) (c)

(d) hollow (e) (f)

Figure 2.12 – Case of 2-mm thickness fluid coupled cylinder: Stochastic convergence analysis at $fh = 1$ MHz.mm (a,b,c) and at $f = 4$ MHz.mm (d,e,f)

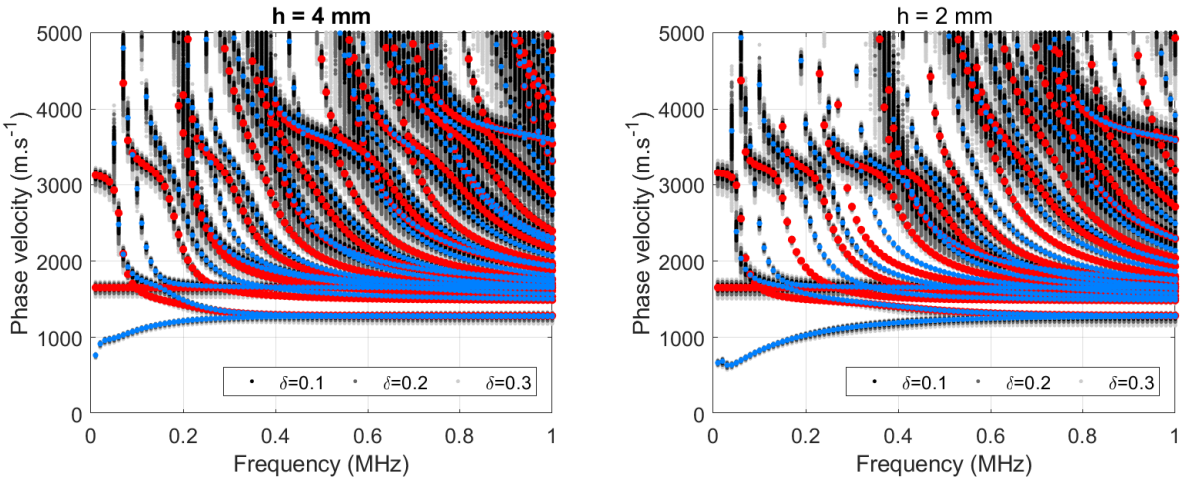

(a) (b)

Figure 2.13 – Phase velocity of a 2 and 4 mm-thickness hollow cylinder with 3 dispersion levels: $\delta = 0.1$ (black region), $\delta = 0.2$ (dark gray region) and $\delta = 0.3$ (light gray region).

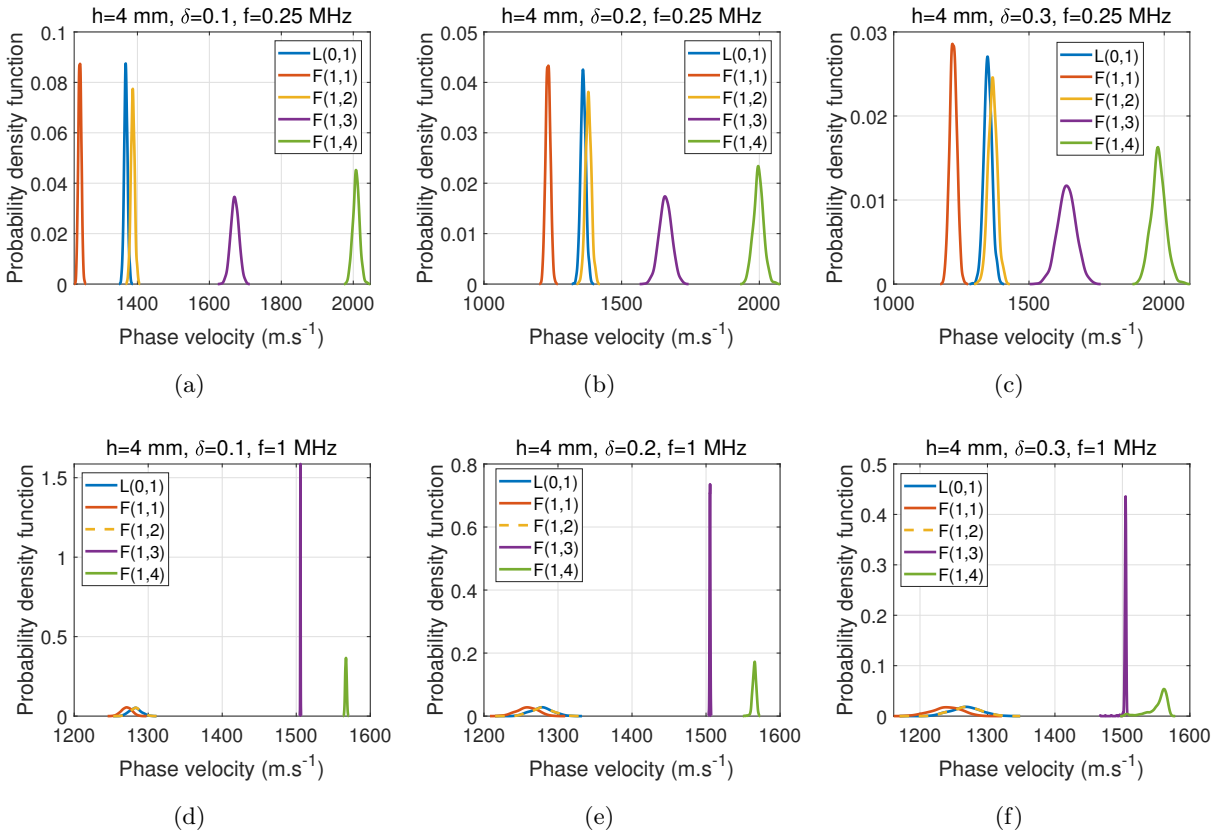

Figure 2.14 – Case of 4-mm thickness fluid coupled cylinder: probability density function at $f = 0.25$ MHz (a,b,c),at $f = 0.5$ MHz (d,e,f) and at $f = 1$ MHz (g,h,i)

Next, we investigated the effect of three-dimensional geometry on the propagation of guides waves. Thus, the effect of curvature is discussed. The trend of cylindrical dispersion curves when increasing the radius of bone cylinder is shown. The convergence of the cylindrical 3D model results to a 2D model results is analyzed. It has been shown that in certain geometric conditions, one can use a two-dimensional plate model instead of a three-dimensional cylindrical model. The sensitivity of Lamb wave characteristic to an intra-cortical bone degradation is explored. Results show a slight modification on cylindrical dispersion curves with respect to cortical bone loss.

Modes shapes in the cross section are extracted. The lowest axisymmetric modes seem to be more suitable for QUS bone evaluation. The relevance of using the three firsts Breathing modes for Quantitative Ultrasound testing is pointed out. The longitudinal mode L(0; 2) seems to be more sensitive in statistical sens. Furthermore, the lowest torsional mode T(0; 1), which has no dependence with frequency, is now dispersive form probabilistic point of view. This three-dimensional stochastic study shows that, we can used it to help on fitting missing branches on experimentally dispersion curves.

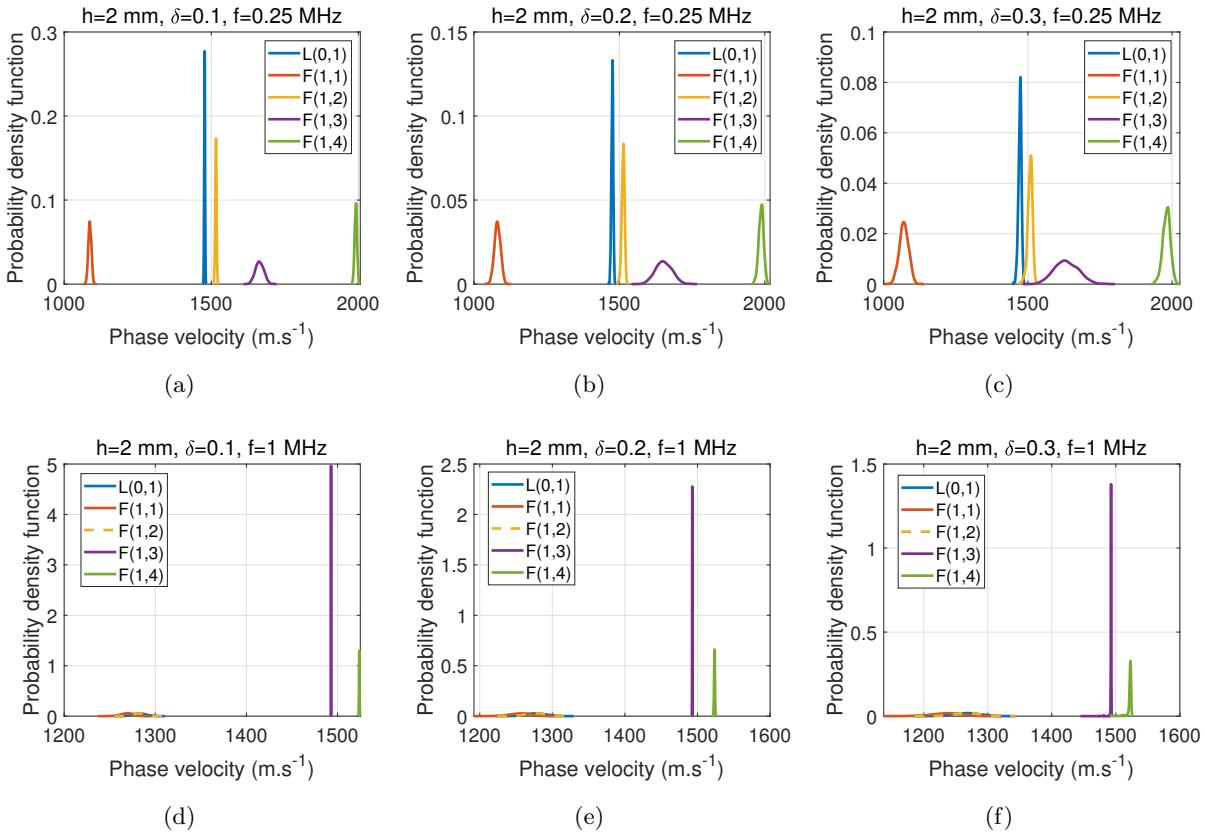

Figure 2.15 – Case of 2-mm thickness fluid coupled cylinder: probability density function at $f = 0.25$ MHz (a,b,c),at $f = 0.5$ MHz (d,e,f) and at $f = 1$ MHz (g,h,i)

Chapter 3

Wave dispersion in functionally-graded plates immersed in fluids

3.1 Introduction

This chapter[1] presents a semi-analytical isogeometric analysis (SAIGA) to calculate the dispersion relation of functionally-graded or multilayered plates coupling with fluids. High-order elements based on Non-Uniform B-Splines (NURBS) basis functions are used. Several numerical examples are then studied for different problems in order to assess the efficiency of proposed method: (i) homogeneous plates; (ii) functionally-graded plates; (iii) composite plates (with strong contrast of rigidity between layers); (iv) fluid-immersed plates. The results obtained are compared with the ones derived from analytical approaches and by the conventional SAFE method using Lagrange polynomials.

The idea is to replacing the conventional element-based discretisation and the associated polynomial shape function by Computer Aided Design (CAD) mappings and associated spline-based functions results in the concept of Isogeometric Analysis (IGA). These powerful CAD-based tools, most commonly NURBS, are used to represent not only the complex geometries but also to construct approximations for finite element analysis. NURBS-based Isogeometric analysis has given promising results on diverse applications allowing the use of globally C^{p-k}-continuous basis functions, with $1 \leq k \leq p+1$, being p the polynomial degree, as highlighted, e.g., in shell and plate problems [71, 72, 73, 74], fluid dynamics [75], structural dynamics [76, 77], etc. NURBS basis functions benefit of three refinement strategies including knot-insertion and order-elevation which are analogue to the FEM counterparts of h- and p-refinements, and a new k-refinement strategy that increases the inter-element continuity beyond the standard C^0-continuity of conventional finite elements and presents superior accuracy and efficiency compared with the classical p-refinement; see e.g. [78, 79]. In the context of the wave propagation problem, the use of NURBS basis functions yields more accurate solutions compared to the conventional finite element analysis (FEA) for a fixed number of degrees of freedom [76, 80, 81]. In [81], the numerical dispersion analysis has been performed for NURBS-based IGA for the Helmholtz equation in the 1D setting on an infinite domain. Dedè et al. [82] reported the reduced errors of dispersion analysis using higher continuous B-spline basis functions in two-dimensional elastic wave propagation simulation. Recently, Liu et al [83] applied IGA to numerical investigation of dispersive behaviors for helical thread waveguides. In this work, investigation

[1] The work presented in this chapter is published in the Acta Mechanica Journal [70].

on the strong frequency dependency of dispersion properties, has not been addressed. The IGA was employed to the dispersion analysis of homogeneous solid waveguides [84] however a more investigation is required for non-homogeneous plates coupled with fluids. The continuity of stress in the case of closed waveguides as well as the continuity of the stress and pressure in the case of immersed waveguides are not yet investigated in the literature.

This work aims to investigate a semi-analytical isogeometric formulation (SAIGA) for analyzing the dispersion of guided-wave propagation in heterogeneous plate-like or prism-like structures coupled with fluid. NUBRS basis functions are used to establish solution space for analyzing anisotropic elastic guided-wave structures and its surrounding fluids in the frequency-wavenumber domain. It is shown that using high degree NURBS basis functions could significantly improve the accuracy of the numerical solutions of the wave dispersion with significant reduction of computational cost. The convergence analysis has been applied for homogeneous and non-homogeneous plates and the optimal NURBS order was suggested for these cases. The present chapter addresses also the problem of stress-continuity of conventional SAFE approach and proposed a new approach by taking the advantage of IGA approach for predicting the stresses.

The chapter is organized as follows. Section 3.2 describes the governing equations for heterogeneous waveguide coupled with fluid. In Section 3.3 after introducing the concept of isogeometirc analysis and NURBS basis functions, the SAFE formulation using NURBS discretization will be discussed. Section 3.4 subsequently carries out the numerical dispersion analysis through several numerical examples. The convergence analysis will be obtained for these cases. The stress and displacement fields will be discussed for each cases. The chapter ends with a conclusion.

3.2 Problem formulation

3.2.1 Governing equation

Geometry description Consider an anisotropic elastic solid layer (Ω^s) of infinite extent which has a constant thickness h along $\mathbf{e}_1$-axis. The surfaces of the solid layer may be free or loaded by two surrounding fluid half-spaces media (Ω_1^f and Ω_2^f) as shown in Fig. 3.1. The domains occupied by the solid layer and the fluids are denoted by $\Omega^s = \{(x_1, x_2) \in [-\infty, \infty] \times [0, h]\}$, $\Omega_1^f = \{(x_1, x_2) \in (-\infty, \infty) \times (-\infty, 0]\}$, $\Omega_2^f = \{(x_1, x_2) \in (-\infty, \infty) \times [h, +\infty)\}$, respectively. The interfaces between Ω^s and the fluid domains Ω_α^f are denoted by Γ_α^{sf} ($\alpha = \{1, 2\}$), respectively. As the thickness is constant, the outward directed, normal vectors of Ω^s at Γ_1^{sf} and Γ_2^{sf} are given by $\boldsymbol{n}_1 = \{0, -1\}^T$ and $\boldsymbol{n}_2 = \{0, 1\}^T$, respectively.

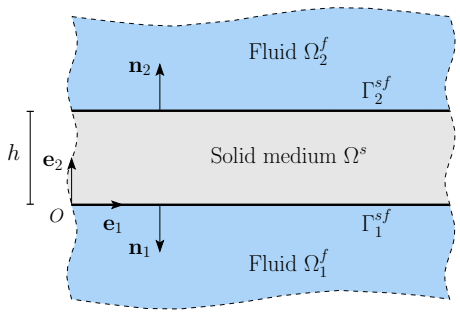

Figure 3.1 – Geometry description of waveguide surrounding by two fluid half-spaces

For modeling the ultrasound wave propagation in this coupled system, we used the infinitesimal motion assumption. Therefore, linear elastic equation was used for the solid layer (i.e the model doesn't take into account large deformation effects) and the fluid domains are described by linear acoustic media which are compressible, inviscid fluids.

Dynamic equations in the solid layer In the solid domain Ω^s, the displacement vector is denoted by $\boldsymbol{u} = \{u_1, u_2\}^T$. For the purpose of convenience, the Voigt notation is used to represent the stress and strain under vectorial forms as:

$$\boldsymbol{s}(\mathbf{x}, t) = \{\sigma_{11}, \sigma_{22}, \sigma_{12}\}^T, \quad \boldsymbol{e}(\mathbf{x}, t) = \{\varepsilon_{11}, \varepsilon_{22}, 2\varepsilon_{12}\}^T, \tag{3.1}$$

where σ_{ij} and ε_{ij} are the components of the stress and infinitesimal strain tensors, respectively. Noting that $\varepsilon_{ij} = \frac{1}{2}(\partial_i u_j + \partial_j u_i)$, the strain vector $\boldsymbol{e}$ can be expressed by: $\boldsymbol{e} = \mathbf{L}\boldsymbol{u}$, where the operator $\mathbf{L}$ is defined by:

$$\mathbf{L} = \mathbf{L}_1\partial_1 + \mathbf{L}_2\partial_2, \quad \text{with} \quad \mathbf{L}_1 = \begin{bmatrix} 1 & 0 \\ 0 & 0 \\ 0 & 1 \end{bmatrix}, \quad \mathbf{L}_2 = \begin{bmatrix} 0 & 0 \\ 0 & 1 \\ 1 & 0 \end{bmatrix}, \tag{3.2}$$

where the symbol $\partial_1(\star)$ and $\partial_2(\star)$ stand for the partial derivative of $(\star)$ with respect to x_1 and x_2, respectively. The balance equations of linear momentum at a point $\boldsymbol{x} \in \Omega^s$ and the linear elastic constitutive law read:

$$\rho\ddot{\boldsymbol{u}} - \mathbf{L}^T\boldsymbol{s} = \mathbf{0}, \tag{3.3}$$

$$\boldsymbol{s} = \mathbf{C}\boldsymbol{e}, \tag{3.4}$$

where the ρ is the mass density and $\mathbf{C}_{3\times3}$ is the matrix containing the components of the anisotropic elasticity tensor. Here, the structure is assumed to be homogeneous along the longitudinal direction $\mathbf{e}_1$ but it could be heterogeneous in the vertical direction $\mathbf{e}_2$, *i.e.* $\rho = \rho(x_2)$ and $\mathbf{C} = \mathbf{C}(x_2)$.

Wave equations in the fluids In the fluid domains Ω^f_α $(\alpha = 1, 2)$, the linearized wave equations reads:

$$\rho_\alpha\ddot{p}_\alpha - K_\alpha\nabla^2 p_\alpha = 0 \tag{3.5}$$

where p_α denotes the acoustic pressure in Ω^f_α, K_α and ρ_α are the bulk modulus at rest and the mass density of the fluid, respectively; $\nabla^2(\star)$ is the Laplace operator. The wave celerity in Ω^f_α can be defined as $c_\alpha = \sqrt{K_\alpha/\rho_\alpha}$.

Boundary conditions The boundary conditions of this system consists of the (i) continuity condition of the normal velocity along the solid-fluid interfaces; (ii) continuity of pressure at the solid-fluid interfaces; and (ii) the radiation condition at infinity, *i.e.*

$$\left.\begin{aligned} \partial_2 p_\alpha &= -\rho_\alpha\ddot{u}_2 \\ \boldsymbol{t} &= \{0, -p_\alpha\}^T \end{aligned}\right\} \quad \forall\boldsymbol{x} \in \Gamma^{sf}_\alpha, \tag{3.6}$$

$$p_\alpha \to 0 \qquad \text{when } \boldsymbol{x} \to \pm\infty, \tag{3.7}$$

where $\alpha = 1, 2$ and $\boldsymbol{t} = \mathbf{L}_2^T\boldsymbol{s} = \{\sigma_{12}, \sigma_{22}\}^T$.

3.2.2 Equations in the frequency-wavenumber $(\omega - k_1)$ domain

We look for the solutions of harmonic waves propagating along the axial direction ($\mathbf{e}_1$) which may be expressed under following forms:

$$\boldsymbol{u}(x_1, x_2, t) = \tilde{\boldsymbol{u}}(x_2) e^{\mathrm{i}(k_1 x_1 - \omega t)} , \tag{3.8}$$

$$p_\alpha(x_1, x_2, t) = \tilde{p}_\alpha(x_2) e^{\mathrm{i}(k_1 x_1 - \omega t)} , \tag{3.9}$$

where $\mathrm{i}^2 = -1$; $\omega \in \mathbb{R}$ is the angular frequency; k_1 is the wavenumber in the $\mathbf{e}_1$-direction; $\tilde{\boldsymbol{u}}(x_2) = (\tilde{u}_1, \tilde{u}_2)^T$ and $\tilde{p}_\alpha(x_2) = \tilde{p}_\alpha$ are the amplitudes of the displacement vector in the Ω^s and of the pressures in Ω^f_α, respectively.

In the frequency-wavenumber $(\omega - k_1)$ domain, the derivatives with respect to t and to x_1 can respectively replaced by: $(\dot{\star}) \to -\mathrm{i}\omega(\star)$ and $\partial_1(\star) \to \mathrm{i}k_1(\star)$, then the amplitudes of the strain and stress vectors ($\tilde{\boldsymbol{e}}$ and $\tilde{\boldsymbol{s}}$) may be expressed by:

$$\tilde{\boldsymbol{e}} = (\mathrm{i}k_1 \mathbf{L}_1 + \mathbf{L}_2 \partial_2)\tilde{\boldsymbol{u}}, \tag{3.10}$$

$$\tilde{\boldsymbol{s}} = \mathbf{C}\tilde{\boldsymbol{e}}, \tag{3.11}$$

and the balance equation (3.3) can be reformulated as a 1D system of equations with respect to x_2:

$$-\rho\omega^2 \tilde{\boldsymbol{u}} - (\mathrm{i}k_1 \mathbf{L}_1 + \mathbf{L}_2 \partial_2)\, \tilde{\boldsymbol{s}} = 0, \quad \forall x_2 \in [0, h]. \tag{3.12}$$

Similarly, by substituting (Eq. 3.9) into (Eq. 3.5), the wave equations in the fluid domains are simplified into:

$$(-\rho_1\omega^2 + k_1^2 K_1)\tilde{p}_1 - K_1 \partial_2^2 \tilde{p}_1 = 0, \quad \forall x_2 \in (-\infty, 0], \tag{3.13a}$$

$$(-\rho_2\omega^2 + k_1^2 K_2)\tilde{p}_2 - K_2 \partial_2^2 \tilde{p}_2 = 0, \quad \forall x_2 \in [h, \infty). \tag{3.13b}$$

The boundary conditions (Eqs. 3.6-3.7) reads:

$$\left.\begin{aligned} \partial_2 \tilde{p}_\alpha &= -\rho_\alpha \omega^2 \tilde{u}_2 \\ \tilde{\boldsymbol{t}} &= \{0, -\tilde{p}_\alpha\}^T \end{aligned}\right\} \quad \text{at } x_2 = 0 \text{ or } x_2 = h, \tag{3.14a}$$

$$\tilde{p}_\alpha \to 0 \qquad \text{when } x_2 \to \pm\infty. \tag{3.14b}$$

3.2.3 Perfectly Matched Layer (PML)

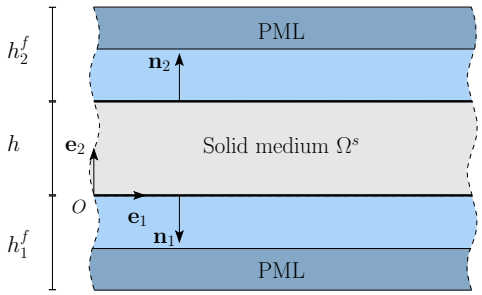

Figure 3.2 – Schematic of a plate immersed in fluids with PMLs

As mentioned in the previous chapter, the PML can be considered as a result of a mapping into complex coordinate, where the solutions of wave equations decay exponentially (as the new coordinate is complex)[51]. Therefore, the infinite medium can be truncated into a finite domain as shown in Fig. 3.2. The new stretched coordinates $\tilde{x}_1(x_1)$ and $\tilde{x}_2(x_2)$ in the waveguide are defined as

$$\tilde{x}_1(x_1) = x_1, \quad \tilde{x}_2(x_2) = \int_0^{x_2} \gamma_2(x_2) dx_2, \tag{3.15}$$

where $\gamma_2(x_2)$ are non-zero, continuous, complex-valued coordinate stretching functions, also called PML functions, which satisfy:

$$\gamma_2(x_2) = 1 \text{ for } |x_2| \leq d_{x_2} \text{ and } \mathrm{Im}\{\gamma_2(x_2)\} > 0 \text{ for } |x_2| > d_{x_2} \tag{3.16}$$

where (d_{x_2}) is the position of the interfaces. We denote by h^{pml} the PML thicknesses in the e_2 directions Fig. 3.2. On the exterior boundary of the PML, the boundary condition can be arbitrarily chosen (Dirichlet or Neumann type). The absorption efficiency of leaky waves in the PML strongly depends on the choice of the PML function (γ_2), the position of the interface (d_{x_2}) and the thickness (h^{pml}). There are a number of variants to choose for the γ_2 function. For this study, a continuous parabolic function for both the real and imaginary parts of the PML function is therefore used which has demonstrated good performance in problems in the frequency domain [50, 85]:

$$\gamma_2(x_2) = \begin{cases} 1 & \text{if } |x_2| \leq d_{x_2}. \\ 1 + \hat{\gamma}_2 \left(\frac{|x_2| - d_{x_2}}{h^{pml}} \right)^2 & \text{if } |x_2| > d_{x_2}. \end{cases} \tag{3.17}$$

3.2.4 Weak formulation

In order to proceed the finite element analysis, we define 3 one-dimensional domains representing the solid and the fluid regions: $\bar{\Omega}^s = \{x_2; x_2 \in [0, h]\}$, $\bar{\Omega}_1^f = \{x_2; x_2 \in [-h_1^f, 0]\}$ and $\bar{\Omega}_2^f = \{x_2; x_2 \in [h, h + h_2^f]\}$.

Upon integrating Eq. (3.3) against a test function $\delta\tilde{u}_2$ and applying the Gauss theorem the taking into account the interface conditions (3.6), the weak formulation of the boundary value problem in the solid layer Ω^s may be derived as [49]:

$$\begin{aligned} &- \omega^2 \int_{\bar{\Omega}^s} \delta\tilde{\boldsymbol{u}} \cdot \rho\tilde{\boldsymbol{u}} dx_2 + k_1^2 \int_{\bar{\Omega}^s} \delta\tilde{\boldsymbol{u}} \cdot \mathbf{A}_{11}\tilde{\boldsymbol{u}} dx_2 + \mathrm{i}k_1 \int_{\bar{\Omega}^s} \Big(- \delta\tilde{\boldsymbol{u}} \cdot \mathbf{A}_{12}\partial_2\tilde{\boldsymbol{u}} + (\partial_2\delta\tilde{\boldsymbol{u}}) \cdot \mathbf{A}_{21}\tilde{\boldsymbol{u}} \Big) dx_2 \\ &+ \int_{\bar{\Omega}^s} \Big(\partial_2\delta\tilde{\boldsymbol{u}}) \cdot \mathbf{A}_{22}\partial_2\tilde{\boldsymbol{u}} \Big) dx_2 + \delta\tilde{u}_2(h)\tilde{p}_2(h) + \delta\tilde{u}_2(0)\tilde{p}_1(0) = 0 \,, \quad \forall \delta\tilde{u}_2 \in \mathcal{C}^{ad} \end{aligned} \tag{3.18}$$

where the matrices $\mathbf{A}_{\alpha\beta}$ defined by: $\mathbf{A}_{\alpha\beta} = \mathbf{L}_\alpha^T \mathbf{C} \mathbf{L}_\beta$, $\{\alpha, \beta\} = \{1, 2\}$, By noting that the elasticity tensor $\mathbf{C}$ is symmetric, on may deduce that $\mathbf{A}_{12} = (\mathbf{A}_{21})^T$, and $\mathbf{A}_{11}$, $\mathbf{A}_{22}$ are symmetric.

For the lower fluid domain $\bar{\Omega}_1^f$, by introducing the test function $\delta\tilde{p}_1$, the weak formulation of the wave equation may be derived from (Eq. 3.13a):

$$\begin{aligned} &- \omega^2 \int_{\bar{\Omega}_1^f} \delta\tilde{p}_1^* \rho_1 \tilde{p}_1 dx_2 + k_1^2 \int_{\bar{\Omega}_1^f} \delta\tilde{p}_1^* K_1 \tilde{p}_1 dx_2 + \int_{\bar{\Omega}_1^f} \partial_2\delta\tilde{p}_1^* K_1 \partial_2\tilde{p}_1 dx_2 \\ &\qquad - \rho_1 K_1 \omega^2 \delta\tilde{p}_1^*(0)\tilde{u}_2(0) = 0 \,, \quad \forall \delta\tilde{p}_1 \in \mathcal{C}^{ad} \end{aligned} \tag{3.19}$$

Similarly, the weak formulation of the wave equation in the fluid domain $\bar{\Omega}_2^f$ reads:

$$-\omega^2 \int_{\bar{\Omega}_2^f} \delta\tilde{p}_2^* \rho_2 \tilde{p}_2 dx_2 + k_1^2 \int_{\bar{\Omega}_2^f} \delta\tilde{p}_2^* K_2 \tilde{p}_2 dx_2 + \int_{\bar{\Omega}_2^f} \partial_2 \delta\tilde{p}_2^* K_2 \partial_2 \tilde{p}_2 dx_2 + \rho_2 K_2 \omega^2 \delta\tilde{p}_2^*(h)\tilde{u}_2(h) = 0 \ , \quad \forall \delta\tilde{p}_2 \in \mathcal{C}^{ad} \tag{3.20}$$

3.3 Approximation using Isogeometric Analysis and implementation

In this section first, we briefly recall the concept of IGA with the main focus on the B-spline and NURBS basis functions, their properties, their use for the geometrical representation as well as incorporating the interface with the C^0-continuity. For a more detailed review of these topics, we refer the interested reader to [86, 87]. Then we use the NURBS basis functions in order to descritize the Eqs. 3.18-3.20.

3.3.1 B-spline and NURBS basis functions

A B-spline basis functions of order $p \in \mathbb{N}$ is determined in a parameter domain $\hat{\Omega} \subset \mathbb{R}$ using a sequence of non-decreasing set of coordinates called *knot vector* defined as $\Xi = \{\xi_1, \xi_2, \xi_3, ..., \xi_{i+p+1}\}$, where $\xi_i \in \mathbb{R}$ is the i^{th} knot, i is the knot index, $i = 1, 2, ..., n + p + 1$, and $n \in \mathbb{N}$ is the number of basis functions used to construct the B-spline curve. Most commonly, open knot vectors are used for which the first and last knots are repeated $k = p + 1$ times. If the internal knots are equally spaced in the parameter space the knot vector is called uniform. The knot vector partition the parametric space into intervals usually referred to as knot spans (ξ_1, ξ_{i+1}). A patch is defined as the intervals $[\xi_i, \xi_{i+p+1}] \subset \mathbb{R}$ which contains all knot spans. In general the multiplicity of the knots determine the continuity of basis functions across the elements boundaries. If a knot value ξ_i is repeated $1 \leq k_i \leq p + 1$ times, the basis functions has $p - k_i$ continuous derivatives across ξ_i.

Given a knot vector, the B-spline basis functions are defined recursively starting for $p = 0$ as

$$N_{i,0}(\xi) = \begin{cases} 1 & \text{if } \xi_i < \xi < \xi_{i+1}, \\ 0 & \text{otherwise,} \end{cases} \tag{3.21a}$$

and for $p = 1, 2, 3, ...$, they are defined by the well-known Cox-de Boor recursion formula as

$$N_{i,p}(\xi) = \frac{\xi - \xi_i}{\xi_{i+p} - \xi_i} N_{i,p-1}(\xi) + \frac{\xi_{i+p+1} - \xi}{\xi_{i+p+1} - \xi_{i+1}} N_{i+1,p-1}(\xi). \tag{3.21b}$$

Note that the quotient $0/0$ is assumed to be zero. However, apart from the versatility of these bases over Lagrangian and Bernstein functions, one of the major limitation associated with the use of B-splines is its inability to accurately represent the circle, sphere and cylinder shaped geometries. On the other hand, NURBS, which are the rationale of these functions, overcome this limitation inherently. Thus, non-uniform rational B-spline (NURBS) basis functions are built from the B-spline functions by multiplying weighting functions w_i for each basis

$$R_{i,p}(\xi) = \frac{N_{i,p}(\xi) w_i}{\sum_{j=1}^{n} N_{j,p}(\xi) w_j}, \tag{3.22}$$

where w_i denotes the weight value associated with control point vector P_i, and weighted function $\sum_{j=1}^{n} N_{j,p}(\xi) w_j$ is the weighted linear combination of B-spline basis functions.

The NURBS basis functions have some advantage such as higher continuity across the element boundaries, partition of unity, variation diminishing, linear independence and compact support. Examples of univariate B-spline basis functions of different continuities are reported in Fig. 3.3 (a) for the polynomial degrees $p = 3$. The Lagrange polynomials of the same order are plotted in Fig. 3.3 (b)

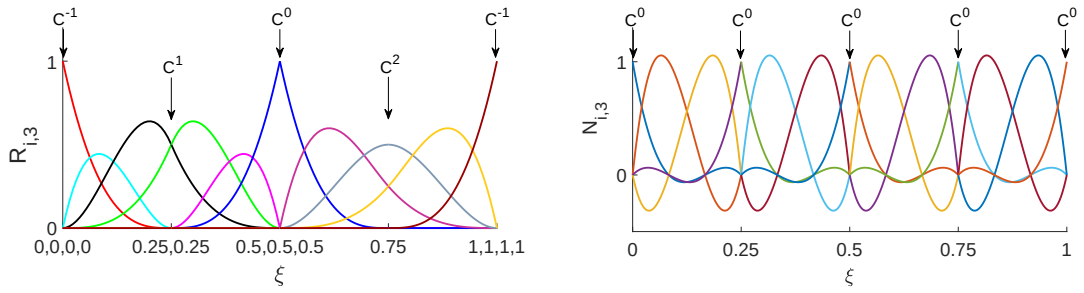

(a) (b)

Figure 3.3 – (a) NURBS basis functions of order $p = 3$ with knot vector $\Xi = \{0, 0, 0, 0, 0.25, 0.25, 0.5, 0.5, 0.5, 0.75, 1, 1, 1, 1\}$ with different desired continuities (b) Lagrange basis function of the same order of a non-avoided C^0 continuities across the elements boundaries

3.3.2 Solution approximation

Let us consider the functions $\hat{v}^h$ which is defined in the parametric domain $\hat{\Omega}$ as the approximate solution $v(x)$. According to the isogeometric concept we use the same basis functions as for geometric representation in order to approximate the solution fields, *i.e*:

$$v(x) \approx \hat{v}^h = \sum_{i=1}^{n} R_{i,p}(\xi) V_i \ , \tag{3.23}$$

where the coefficients $V_i \in \mathbb{C}$ are the corresponding control variables (values at the control points). The properties of the function $\hat{v}^h$ follow those of the NURBS basis functions. Using the inversion of geometrical mapping $x_2(\xi)$ the function $\hat{v}^h$ over the physical domain Ω can be define such that $v^h = \hat{v}^h \circ x^{-1}$. As mentioned in Section 3.3.1, the NURBS basis functions are defined in a parametric space, which is descritized by introducing a set of non-decreasing sequence of real numbers, i.e. $\Xi = \{\xi_1, \xi_2, \xi_3, ..., \xi_{n+p+1}\}$.

In this study, the Galerkin finite element method is employed, in which the same approximations are applied for both functions $\tilde{\boldsymbol{u}}^h$ and $\delta\tilde{\boldsymbol{u}}^h$ (as well as for $\tilde{p}^h_\alpha$ and $\delta\tilde{p}^h_\alpha$) on each patch:

$$\tilde{\boldsymbol{u}}^h = \mathbf{R}^s\mathbf{U}, \quad \delta\tilde{\boldsymbol{u}}^h = \mathbf{R}^s\delta\mathbf{U}, \tag{3.24a}$$

$$\tilde{p}^h_\alpha = \mathbf{R}^f_\alpha\mathbf{P}_\alpha, \quad \delta\tilde{p}^h_\alpha = \mathbf{R}^f_\alpha\delta\mathbf{P}_\alpha, \tag{3.24b}$$

where $\mathbf{R}^s_{2\times 2n}$, $\mathbf{R}^f_{1\times n}$ are the interpolation matrix containing the NURBS basis functions (Eq. 3.22); $\mathbf{U}_{2n\times 1}$ and $\delta\mathbf{U}_{2n\times 1}$ are the vectors of control displacements; $(\mathbf{P}_\alpha)_{n\times 1}$ and $(\delta\mathbf{P}_\alpha)_{n\times 1}$ are the displacement vectors of control pressures.

By substituting the approximations (Eqs. 3.24a-3.24b) into the weak formulations (Eqs. 3.18-3.20), then assembling the elementary matrices, one obtains

$$(-\omega^2\mathbf{M} + \mathbf{K}_0 + \mathrm{i}k_1\mathbf{K}_1 + k_1^2\mathbf{K}_2)\mathbf{V} = \mathbf{0}\,, \tag{3.25}$$

where $\mathbf{V} = (\mathbf{P}_1, \mathbf{U}, \mathbf{P}_2)^T$ containing the global eigenvectors of pressure ($\mathbf{P}_1$, $\mathbf{P}_2$)) and of displacement ($\mathbf{U}$); the global matrices $\mathbf{M}$, $\mathbf{K}_0$, $\mathbf{K}_1$, $\mathbf{K}_2$ are determined from the assembling of corresponding elementary matrices in solid and fluid domains:

$$\mathbf{M} = \begin{bmatrix} \mathbf{M}^{f_1} & \mathbf{M}^{f_1 s} & \mathbf{0} \\ \mathbf{0} & \mathbf{M}^{s} & \mathbf{0} \\ \mathbf{0} & \mathbf{M}^{f_2 s} & \mathbf{M}^{f_2} \end{bmatrix}, \mathbf{K}_0 = \begin{bmatrix} \mathbf{K}_0^{f_1} & \mathbf{0} & \mathbf{0} \\ \mathbf{K}^{s f_1} & \mathbf{K}_0^{s} & \mathbf{K}^{s f_2} \\ \mathbf{0} & \mathbf{0} & \mathbf{K}_0^{f_2} \end{bmatrix}, \tag{3.26a}$$

$$\mathbf{K}_1 = \begin{bmatrix} \mathbf{0} & \mathbf{0} & \mathbf{0} \\ \mathbf{0} & \mathbf{K}_1^{s} & 0 \\ \mathbf{0} & \mathbf{0} & \mathbf{0} \end{bmatrix}, \mathbf{K}_2 = \begin{bmatrix} \mathbf{K}_2^{f_1} & \mathbf{0} & \mathbf{0} \\ \mathbf{0} & \mathbf{K}_2^{s} & \mathbf{0} \\ \mathbf{0} & \mathbf{0} & \mathbf{K}_2^{f_2} \end{bmatrix} \tag{3.26b}$$

in which the sub-matrices are determined by:

$$\mathbf{M}^s = \bigcup_e \int_{\bar{\Omega}^{s(e)}} \mathbf{R}^{(e)T} \rho \mathbf{R}^{(e)} dx_2 \tag{3.27a}$$

$$\mathbf{K}_0^s = \bigcup_e \int_{\bar{\Omega}^{s(e)}} \Big(\partial_2 \mathbf{R}^{(e)T} \mathbf{A}_{22} \partial_2 \mathbf{R}^{(e)} \Big) dx_2 \tag{3.27b}$$

$$\mathbf{K}_1^s = \bigcup_e \int_{\bar{\Omega}^{s(e)}} \Big(-\mathbf{R}^{(e)T} \mathbf{A}_{12} \partial_2 \mathbf{R}^{(e)} + \partial_2 \mathbf{R}^{(e)T} \mathbf{A}_{21} \mathbf{R}^{(e)} \Big) dx_2 \tag{3.27c}$$

$$\mathbf{K}_2^s = \bigcup_e \int_{\bar{\Omega}^{s(e)}} \mathbf{R}^{(e)T} \mathbf{A}_{11} \mathbf{R}^{(e)} dx_2 \tag{3.27d}$$

$$\mathbf{M}^{f_\alpha} = \bigcup_e \int_{\bar{\Omega}^{f(e)}} \mathbf{R}^{(e)T} \rho_\alpha^f \mathbf{R}^{(e)} dx_2 \tag{3.27e}$$

$$\mathbf{K}_0^{f_\alpha} = \bigcup_e \int_{\bar{\Omega}^{f(e)}} \Big(\partial_2 \mathbf{R}^{(e)T} K_\alpha \partial_2 \mathbf{R}^{(e)} \Big) dx_2 \tag{3.27f}$$

$$\mathbf{K}_2^{f_\alpha} = \bigcup_e \int_{\bar{\Omega}^{f(e)}} \mathbf{R}^{(e)T} K_\alpha \mathbf{R}^{(e)} dx_2 \tag{3.27g}$$

The matrices $\mathbf{M}^{f_1 s}$, $\mathbf{M}^{f_2 s}$, $\mathbf{K}^{s f_1}$, $\mathbf{K}^{s f_2}$ represent the coupled terms between the solid and the fluids. Each of these matrices has only one non-zero element, which may be formally represented by:

$$\left(\mathbf{M}^{f_1 s}\right)_{mn} = \rho_1 K_1, \quad \left(\mathbf{M}^{f_2 s}\right)_{mn} = -\rho_2 K_2, \quad \left(\mathbf{K}^{s f_1}\right)_{mn} = 1, \quad \left(\mathbf{K}^{s f_2}\right)_{mn} = 1, \tag{3.28}$$

where m and n are the indexes of the degrees of freedom of the fluid and the solid at in interfaces, which are concerned by the continuity conditions. The matrices $\mathbf{M}$, $\mathbf{K}_0$, $\mathbf{K}_1$, $\mathbf{K}_2$ are computed by using Gauss Legendre quadrature formula with $r = p+1$ quadrature points per element in parametric space, which has been shown to be efficient [82].

By noting that $\mathbf{A}_{\alpha\beta} = \mathbf{A}_{\beta\alpha}^T$, it can be shown all matrices in (Eqs 3.27a-3.27g) are symmetric except $\mathbf{K^s}_1$ which is is anti-symmetric. In this chapter, as no viscous effects in the solid as well as in the fluids are taken into account, these matrices are real and constant with respect to ω and k_1. When considering the viscoelastic solid and/or viscous acoustic fluid, the elasticity tensor $\mathbf{C}$ and/or the bulk modulus K_α are complex and frequency-dependent. In such cases, same formulations (Eqs. 3.27a-3.27g) can be used. However, the matrices $\mathbf{K}_0$, $\mathbf{K}_1$, $\mathbf{K}_2$ will depend on ω, but are still independent to k_1.

3.3.3 Dispersion analysis

The system of characteristic equations (3.25) is a eigenvalue problem serving to determine the relationship between the pulsation ω and the wavenumber k_1. By noting that all global matrices ($\mathbf{M}$, $\mathbf{K}_0$, $\mathbf{K}_1$, $\mathbf{K}_2$) do not depend on k_1, Eq. (3.25) is a quadratic eigenvalue problem with respect to k_1, and could be solved by reformulating it under following linearized eigenvalue problem:

$$\left(\begin{bmatrix} \mathbf{0} & -\omega^2\mathbf{M}+\mathbf{K}_0 \\ -\omega^2\mathbf{M}+\mathbf{K}_0 & \mathrm{i}\mathbf{K}_1 \end{bmatrix} - k_1 \begin{bmatrix} -\omega^2\mathbf{M}+\mathbf{K}_0 & \mathbf{0} \\ \mathbf{0} & -\mathbf{K}_2 \end{bmatrix} \right) \begin{pmatrix} \mathbf{V} \\ k_1\mathbf{V} \end{pmatrix} = \mathbf{0} \, . \tag{3.29}$$

For each value of the angular frequency ω, solving Eq. (3.29) allows us to determine the eigenvalues k_1 and their associated eigenvectors (also called by wave structures), $\mathbf{V}(\omega, k_1)$ of guided modes. The frequency-dependent phase velocity (C_{ph}) and the attenuation (att) of a guided mode are given by:

$$C_{\mathrm{ph}} = \frac{\omega}{\mathrm{Re}\,(()\,k_1)}\ [\mathrm{m.s}^{-1}], \quad \mathrm{att} = \mathrm{Im}\,(()\,k_1)\ [\mathrm{Np.m}^{-1}] \, , \tag{3.30}$$

where $\mathrm{Re}\,(())$ and $\mathrm{Im}\,(())$ denote the real and imaginary parts of a complex function. Conventionally, the group velocity c_{g} is determined by taking the differentiation of ω with respect to k_1 ($C_{\mathrm{g}} = \partial\omega(k_1)/\partial k_1$). However, as mentioned in [88], this definition of group velocity is only valid in undamped waveguides. For damped waveguides, the wavenumber k_1 becomes complex and it is more appropriate to evaluate the energy velocity (C_{energy}) along the propagation direction. The energy velocity along the direction $\mathbf{e}_1$ is defined by the ratio between the time-average of Poynting vector and the time-average of the energy density, i.e.

$$C_{\mathrm{energy}} = \frac{\int_{\bar{\Omega}} \langle \boldsymbol{p} \rangle \cdot \mathbf{e}_1 \mathrm{d}x_2}{\int_{\bar{\Omega}} \left(\langle E_p \rangle + \langle E_k \rangle \right) \mathrm{d}x_2} \tag{3.31}$$

where $< . >= \frac{1}{T}\int_0^T (.)dt$ is the time-averaging operator and $T = 2\pi/\omega$ is the period of the considered harmonic wave and the terms related to the time-averaged Poynting vector ($\langle \boldsymbol{p} \rangle$), to the time-averaged strain and kinetic energy densities ($\langle E_p \rangle$, and $\langle E_k \rangle$, respectively) in (Eq. 3.31) may be computed by (see e.g [89]). In the fluid domains, these quantities may be computed by noting that $\boldsymbol{\sigma}^f = -p\mathbf{I}$ and $\dot{\boldsymbol{u}}^f = \frac{1}{\mathrm{i}\omega}\nabla p$, where $\mathbf{I}$ is the identity matrix.

3.4 Numerical results

This section presents some numerical examples in order to validate the accuracy of the proposed SAIGA formulations for the analysis of dispersion of guided waves in elastic structures. First, plate-like waveguides in vacuum (including the cases of a homogeneous plate, a functionally-graded plate, and a layered plate) will be considered. Second, the wave dispersion of the waveguides coupled with an infinite fluid as leaky medium will be studied. The validation will be done by comparing the solutions obtained by using the proposed SAIGA approach, by the conventional SAFE method and by analytical analysis (which are only exist for the homogeneous or layered plates). In this study, all analytical solutions were obtained by using the software DISPERSE [67].

3.4.1 Dispersion of guided-waves in plates with free boundaries

3.4.1.1 Homogeneous isotropic plate

Let us first consider a homogeneous and 4mm-thickness aluminum plate. The isotropic elastic properties of the plate are characterized by the density (ρ=2700 kg/m^3), the longitudinal and shear wave

velocities ($c_L = 6320$ m/s and $c_T = 3130$ m/s, respectively). The analytical solution of Lamb wave's dispersion of this homogeneous elastic plate does exist and was used as a reference for the validation purpose.

The IGA modeling is based on only one patch. The NURBS basis functions with degree p over an uniform knot vector were used. For comparison purpose, we introduce the total number of degree of freedom $N_{\text{dof}} = n_{\text{P}} \times n_{\text{dof}}$, where n_{P} is the number of control points (or nodes) and $n_{\text{dof}} = 2$ is the number of DOF per controls points. The number of elements (spans) using the SAIGA procedure is then given by $N_{\text{el}} = n_{\text{P}} - p$. For standard SAFE method, using a p-degree Lagrange interpolation function and a degree of freedom ($N_{\text{dof}}^{\text{SAFE}}$) leads to a number of elements given by $N_{\text{el}}^{\text{SAFE}} = (N_{\text{dof}}/n_{\text{dof}} - 1)/p$.

Figs. 3.4(a,b) present a comparison between the results of the phase velocity (C_{ph}), obtained by the SAIGA, conventional SAFE and analytical methods (DISPERSE). To obtain the results presented in Fig. 3.4(a), we first used a SAIGA mesh with 7 quadratic elements and a SAFE mesh with 4 quadratic elements. As a consequence, both SAIGA and SAFE models have $N_{\text{dof}} = 18$ and $p = 2$. One may observe that the SAIGA solutions have a better accuracy than the SAFE ones, especially at the frequencies higher than 1.5 MHz. The branches corresponding to A_4 and S_4 modes computed by SAFE are not well captured by using these numerical parameters. The solutions obtained by using traditional SAFE with more refined meshes ($\{N_{\text{el}} = 7,\ N_{\text{dof}} = 30\}$ and $\{N_{\text{el}} = 13,\ N_{\text{dof}} = 58\}$) are also presented in this figure, confirming that increasing the number of elements allows us to better capture high-order modes.

The results obtained by using a higher-order basis functions ($p = 4$) are presented in Fig. 3.4(b). With a same number of DOF ($N_{\text{dof}} = 18$), the number of elements of SAIGA and SAFE meshes in this case are respectively $N_{\text{el}}^{\text{SAIGA}} = 5$ and $N_{\text{el}}^{\text{SAFE}} = 2$. By using high-order elements, the precision of SAFE's results is much more improved but still lower than the precision of the SAIGA results.

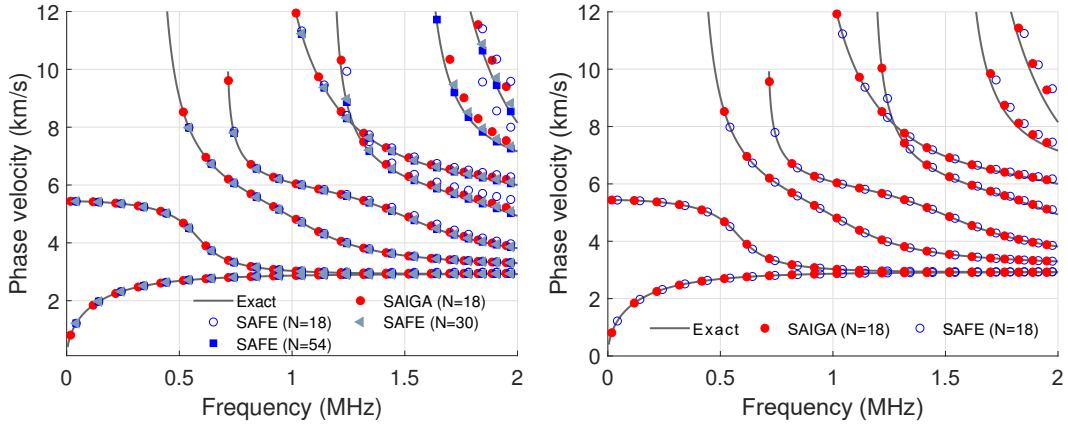

(a) $p = 2$ (b) $p = 4$

Figure 3.4 – Dispersion curves of homogeneous isotropic aluminum plate: comparison between the analytical, SAFE and SAIGA solutions

3.4.1.2 Functionally graded plate

Functionally-graded material is a composite material, which is commonly fabricated by mixing two distinct material phases, for which properties change continuously along certain dimensions of the

structure. This example considers a 4-mm-thick functionally graded plate of which the densities and the elastic properties varies continuously from the lower surface to the upper surface. To do so, we suppose that the material at the lower surface has following physical parameter set: $\rho_1 = 1100kg/m^3$, $c_{L1} = 2610m/s$ and $c_{T1} = 1100m/s$, which corresponds to the properties of epoxy. At the upper surface, properties of aluminum were imposed: $\rho_2 = 2700kg/m^3$, $c_{L2} = 6320m/s$ and $c_{T2} = 3130m/s$. The elasticity matrices $\mathbf{C}(x_2)$ and the mass density $\rho(x_2)$ are chosen to be a quadratic function along the thickness's direction: $\mathbf{C}(x_2) = (\mathbf{C}_2 - \mathbf{C}_1)(\frac{x_2}{h})^2 + \mathbf{C}_1$ and $\rho(x_2) = (\rho_2 - \rho_1)(\frac{x_2}{h})^2 + \rho_1$. As the analytical solution is not easy to obtain in this situation, a SAFE calculation using very fine mesh (with $N_{\text{dof}} = 162$) was performed determine the "reference" solution.

Figure 3.5 presents the SAIGA and SAFE solutions of the phase velocity comparing with the reference solutions. As introducing softer materials implies shorter wavelengths in the plate, finer meshes need to be used in comparing with the previous case where a homogeneous aluminum plate has been considered. For this study, the number of DOF for all SAIGA and SAFE calculations are fixed by $N_{\text{dof}} = 34$. For $p = 2$, the SAFE model consists of 7 quadratic Lagrangian elements and the SAIGA models consists of 17 elements (spans) using quadratic NURBS basis functions. Similarly to the previous study on homogeneous plate, it may be observed again in Figure 3.5(a) that the SAIGA solutions at high frequency have a much better precision than the SAFE ones, especially when $f > 1$ MHz. Figure 3.5(b) presents the numerical solutions obtained when using $p = 4$ and fixing $N_{\text{dof}} = 34$, which correspond to $N_{\text{el}}^{\text{SAFE}} = 4$ and $N_{\text{el}}^{\text{SAFE}} = 4$. Both SAFE and SAIGA solutions of C_{ph} match better to the reference solution than the case $p = 2$. Nevertheless, in the frequency range between 1.5 MHz and 2 MHz, the SAIGA solutions are very close to the reference values while the SAFE solutions are still incorrect.

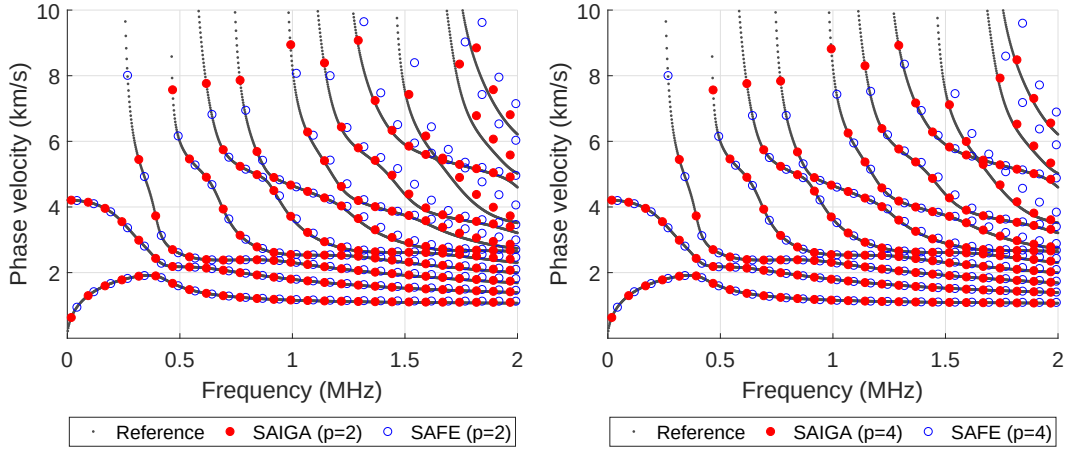

(a) $p = 2$ (b) $p = 4$

Figure 3.5 – Dispersion curves of a functionally-graded plate: comparison between the analytical, SAFE and SAIGA solutions; both FE models have the same number of DOF ($N_{dof} = 34$).

3.4.1.3 Convergence study

In this section, the convergence analysis is performed for two cases previously studied on homogeneous and functionally graded plates. In order to carry out a convergence analysis of the proposed method

at a given frequency, we introduce a function err which estimates summation of the relative errors of the numerical solution for the first m modes as

$$\text{err} = \sum_{i=1}^{m} \frac{\left| C_{\text{ph}}^{i,num} - C_{\text{ph}}^{i,ref} \right|}{C_{\text{ph}}^{i,ref}} , \tag{3.32}$$

where $C_{\text{ph}}^{i,num}(f)$ is the phase velocity of i-th mode at a frequency f calculated by using SAFE or SAIGA, $C_{\text{ph}}^{i,ref}$ is the corresponding reference solution obtained analytically by using Disperse software (homogeneous case) or numerically by using a very fine mesh (functionally graded case). Fig. 3.6 presents the variation of the error estimated for first 5 modes ($m = 5$) with respect to the number of DOF at $f = 2$ MHz, using different orders p of NURBS and Lagrange basis functions. For isotropic homogeneous plate, Fig. 3.6a shows that the SAIGA errors using p-order NURBS decrease much faster in comparing with to SAFE's ones using p-order Lagrange basis functions. For example, to obtain solutions with the same error (10^{-3}), while using cubic Lagrange basis function requires solving a system of 38 DOFs, using cubic NURBS basis function only requires a system with only 24 DOFs. It can be seen that the convergence rate improves up to an order $p = 5$. Further increasing the order p does not lead to a significant improvement of the convergence. It should be noted that, when only one element of the same order is used, both SAIGA and SAFE types of shape functions yield almost exactly the same results. Note that similar statement may be found in some studies in literature [24, 84].

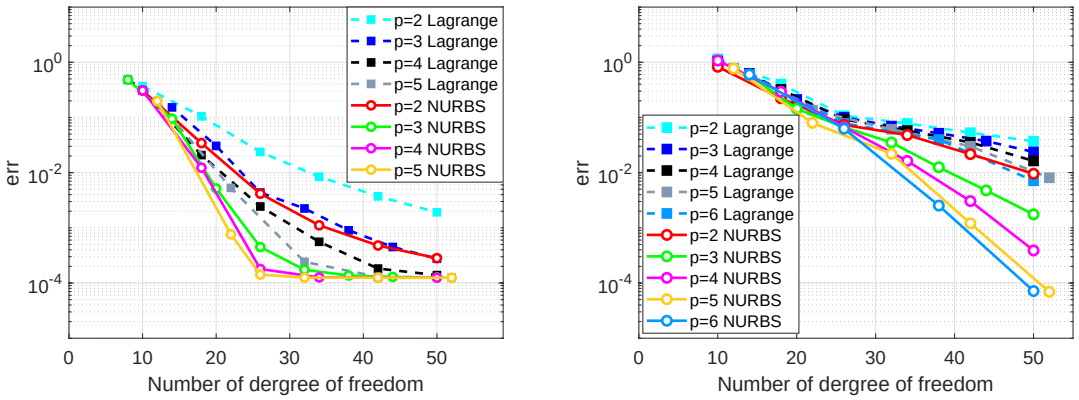

(a) (b)

Figure 3.6 – Relative error at the frequency of $f = 2$ MHz for (a) homogeneous plate and (b) functionally graded plate.

Fig. 3.6b presents a convergence analysis of the plate with functionally graded materials. Due to the plate heterogeneity, both models require much more nodes to obtain converged solutions. By using Lagrange basis functions, the slopes of the error functions are much lower than the ones obtained for the homogeneous plate (Fig. 3.6a). It may be observed that the increasing the order of Lagrange basis function didn't significantly improve the convergence rate. Interestingly, using NURBS based basis function allows to obtain much higher convergence rates. Moreover, the results show that p-convergence rate is significant when using NURBS for the considered functionally graded plate. Furthermore, the convergence rate improves up to an order $p = 6$ rather than $p = 5$ as seen for homogeneous case.

3.4.1.4 Multilayered plate

In this section, we aim to study the efficiency of the proposed SAIGA method for computing the wave dispersion in a multilayer plate. The plate is assumed to be made of three layers of isotropic materials (aluminum-epoxy-aluminum) as shown in Figure 3.7. The thickness of the layers are given by $h_1 = h_3 = 0.05$ mm and $h_2 = 3$ mm, respectively. The properties of aluminum and epoxy were given in the previous examples.

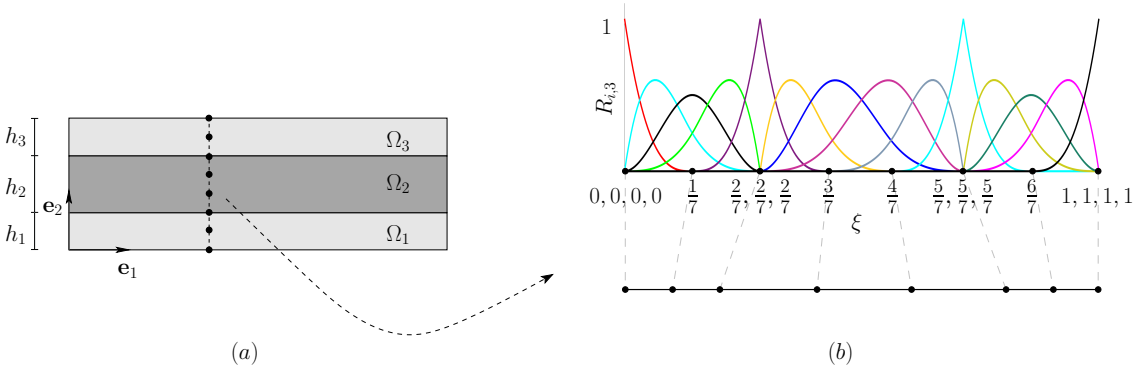

Figure 3.7 – (a) Geometry description of multilayered waveguides, (b) NURBS discretization of thickness ($p = 3$)

Different to the functionally-graded plate studied previously, the heterogeneity in this case is not continuous but a piecewise constant function. By using conventional SAFE method, each layer may be discretized into certain number of elements. By using SAIGA method, there are two possible strategies. The first one is to consider each layer by a patch. Discretization using NURBS may be done separately in each patch and then elementary matrices determined in each patch will be assembled to obtain the global system, similarly to the conventional SAFE procedure. The second strategy, which is used in this study, is to consider all of 3 layers as one single patch. To describe the discontinuity between the layers, the knot vector may be enriched by inserting some knot values at specific locations corresponding the points at the interfaces, where C^0-continuity is imposed. Fig. 3.7b displays an example of discretizing the considered three-layer plate using non-uniform cubic NURBS. The physical domain was divided into 7 spans (including 2 for the lower layer, 3 for the median layer and 2 for the upper layer) and mapped into the parametric space. Multiple knot values were introduced at two locations 2/7 and 5/7, which correspond to 2 points at the interfaces. As $p = 3$, introducing a multiplicity $k = 3$ reduces the continuity of NURBS to C^{p-k}, *i.e* C^0-continuity, at those locations. A detailed description of how to fit these knots may be found in [90].

Dispersion curves of the phase velocity and of the energy velocity are plotted in Fig. 3.8. We compare the numerical solutions computed by using SAFE and SAIGA to the analytical results obtained by using Disperse. The SAFE and SAIGA computations used the same number of DOF and the order of basis functions ($p = 4$). Again, the SAIGA solution was shown to be better than the SAFE's one. The advantageous of using NURBS was found to be significant for the evaluation of the energy velocity as presented in Fig. 3.8b. As it may be observed in a zoom window at a low frequency ($f \approx 0.7$ MHz), the SAIGA solution matches much better to the analytical one than the SAFE solution.

The shape modes of the stress are useful for the evaluation of the damage/discontinuity at the interfaces of laminate structures by knowing the fact that the stress components are continuous at a

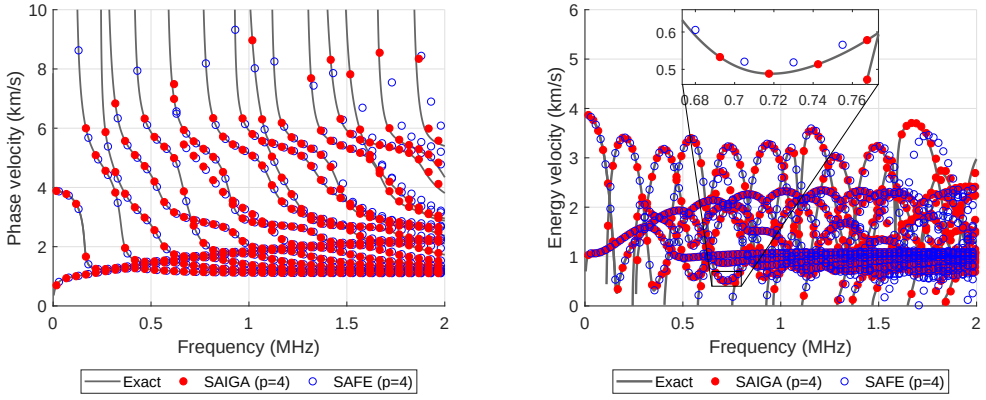

(a) (b)

Figure 3.8 – Phase velocity (a) and energy velocity (b) of a multilayered plate: analytical solution and numerical solutions obtained by SAIGA and SAFE methods ($p = 4$, $N_{dof} = 66$).

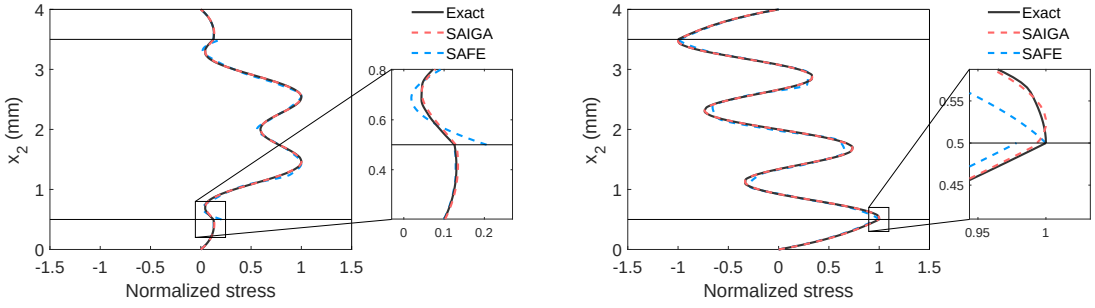

(a) (b)

Figure 3.9 – Stress modes shapes of multi-layer plate: (a) σ_{22}; (b) σ_{12} using single patch SAIGA (red dashed line), SAFE (blue dashed line) and exact solution (grey line)

.

perfectly bonded interface. Nevertheless, it is well known that by using the displacement-based FEM, the stresses are numerically not continuous from element-to-element. Fig. 3.9 depicts an example of the shape modes of stresses (σ_{12} and σ_{22}) with respect to vertical coordinate x_2. By using SAFE, profiles of σ_{22} and of σ_{12} are discontinuous at both interfaces. In contrast, the SAIGA solution using one patch is continuous through the interfaces and matches much better to the analytical one.

3.4.2 Plate immersed in fluids

Let us consider typical example of an isotropic aluminum plate coupled with two halfspaces of water loaded on both sides as shown in Fig. 3.2. The characteristics of water are given by $\rho_1^f = \rho_2^f = 1000$ kg.m^{-3} and $c_1 = c_2 = 1500$ m.s^{-1}. The simulation of leaky Lamb wave by using SAFE method has been investigated in several works [91, 41]. In this section, we examine the efficiency of the SAIGA approach to study this problem. For describing the infinite halfspace, the PML layers were introduced in two fluid domains Ω_1^f and Ω_2^f. The PML parameters including h^{pml} (PML thickness)

and $\gamma_2(x_2)$ (PML function) (see Eq. 3.17) were chosen as it has been done in [41]. For this study, in which the range of frequencies of interest is from 0 to 2 MHz, we used $\hat{\gamma}_2 = 3+12\mathrm{i}$ and $h^{\mathrm{pml}} = 2.5$ mm. In addition, free boundary conditions ($p = 0$) were imposed at the exterior boundaries of two fluid domains.

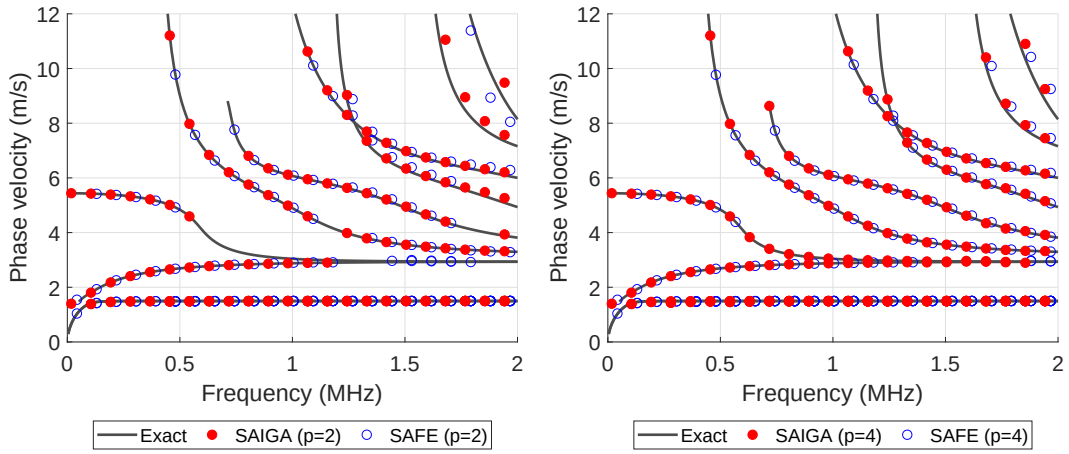

(a) (b)

Figure 3.10 – Phase velocity of a plate immersed in infinite fluid using SAIGA (red marker), conventional SAFE (blue marker) and exact analytical solution (grey line): (a) $p = 2$ and N_{dof}=52; (b) $p = 4$ and N_{dof}=52

Fig. 3.10 aims to compare the dispersion curves of leaky guided waves obtained using SAIGA method, the conventional SAFE method and the analytical solution obtained using Disperse software. In Fig. 3.10(a), we depict the results using quadratic ($p = 2$) NURBS and Lagrange basis functions. Both SAIGA and SAFE procedures lead to a system of $N_{\mathrm{dof}} = 52$ in which the numbers of DOF in the solid and fluid domains are $N^s_{\mathrm{dof}} = 18$ and $N^{f_1}_{\mathrm{dof}} = N^{f_2}_{\mathrm{dof}} = 17$, respectively. Two cases of shape function's order ($p = 2$ and $p = 4$) were examined in Fig. 3.10(a) and Fig. 3.10(b), respectively. In both cases, the SAIGA solutions were shown to be in better agreement to the analytical solution. When using $p = 2$, the numerical calculations using SAIGA or SAFE at high frequencies were failed for some modes (*e.g* on the A0 and S0 branches) as it has been reported in [91]. Fig. 3.10(b) shows that using $p = 4$ allows to improve this numerical issue for both methods. In particular, almost modes were found except several ones which could not determined by SAFE.

The attenuation of the leaky guide waves calculated by using $p = 4$ and $N_{\mathrm{dof}} = 52$ are presented in Fig 3.11(a). The quality of attenuation solution is not as good as the solution of the phase velocity, especially at frequencies higher than 1.5 MHz. When using a finer mesh ($N_{\mathrm{dof}} = 76$), SAIGA solution of attenuation is in very good agreement with the analytical solution (Fig 3.11(b)). In this case, SAFE solution was much improved in comparing with the case $N_{\mathrm{dof}} = 52$, but still worst than the SAIGA's one. In particular, the modes with attenuation's value more than 600 dB/m, which are couldn't found by using SAFE, can be well predicted using SAIGA.

Figures 3.12(a,b) depict the mode shape of the vertical displacement u_2 at $f = 1.55$ MHz and $C_{\mathrm{ph}} = 6.16$ km/s. The displacement in fluid domains were derived from the gradient of pressure field. As it could be expected, the both SAIGA and SAFE solutions of u_2 are progressively attenuated in the PML domains, showing that introducing PMLs is a simple and efficient manner for absorbing leaky waves in the fluids. It has also been checked that the obtained numerical solutions are not influenced by the distance between the PML and the solid-fluid interface (data not shown). By comparing with

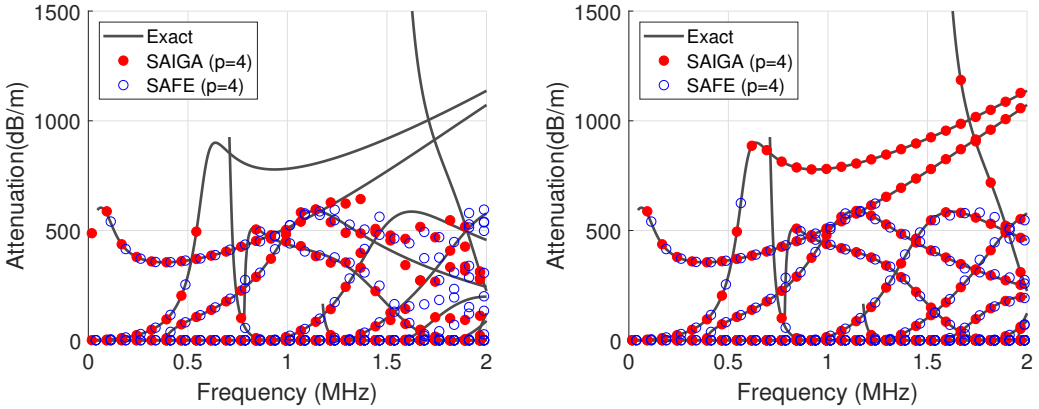

(a) $p = 4$, N_{dof}=52 (b) $p = 4$, N_{dof}=76

Figure 3.11 – Attenuation of an aluminum plate immersed water: comparison between SAIGA solution (red marker), conventional SAFE solution (blue marker), and analytical solution (grey line)

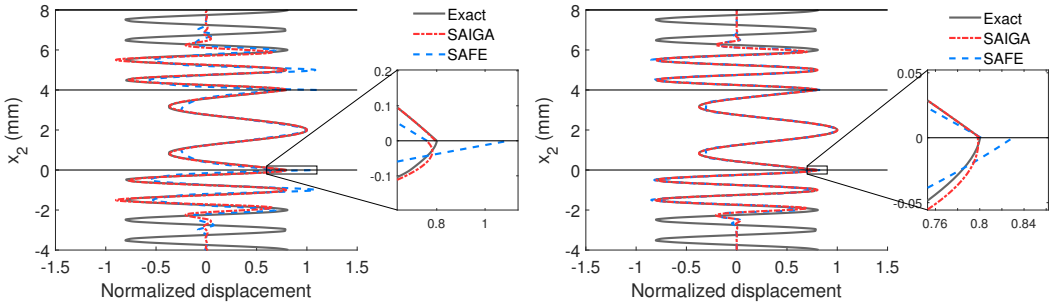

(a) $p = 4$, $N_{\text{dof}} = 52$ (b) $p = 4$, $N_{\text{dof}} = 76$

Figure 3.12 – Mode shape of vertical displacement components of an aluminum plate immersed the immersed in water at $f = 1.55$ MHz, $C_{ph} = 6.16$ km/s: comparison between SAIGA solution (dashed red line), SAFE solution (dashed blue line) and analytical solution (grey line)

the analytical solution, the results obtained by using the proposed SAIGA formulation are shown to be more accurate than SAFE's ones. Moreover, the continuity of u_2 at the fluid-solid interfaces can be much better calculated by using SAIGA method, as it may be observed in the zoomed windows in Fig. 3.12(a,b). Figure 3.13 presents the images of the horizontal and vertical displacement shape modes of an anti-symmetric mode (A2) and a symmetric mode (S1) at the frequency $f = 1.55$ MHz.

Figures 3.14(a,b) present the mode shapes of the normal stress σ_{22} and of the shear stress σ_{12}. Note that the stress components in the fluid domains are given by $\sigma^f_{22} = -p$ and $\sigma^f_{12} = 0$. The SAIGA and SAFE results of stresses in the solid layer were derived from the displacement vectors obtained by using $p = 4$ and $N_{\text{dof}} = 52$ presented in Fig 3.12(b). A close look at the solid-fluid interfaces (Γ^{sf}_1 and Γ^{sf}_2) show that for both numerical approaches, the stress-pressure continuity conditions are not verified at the interfaces. However, the errors of standard SAFE solution are much more significant

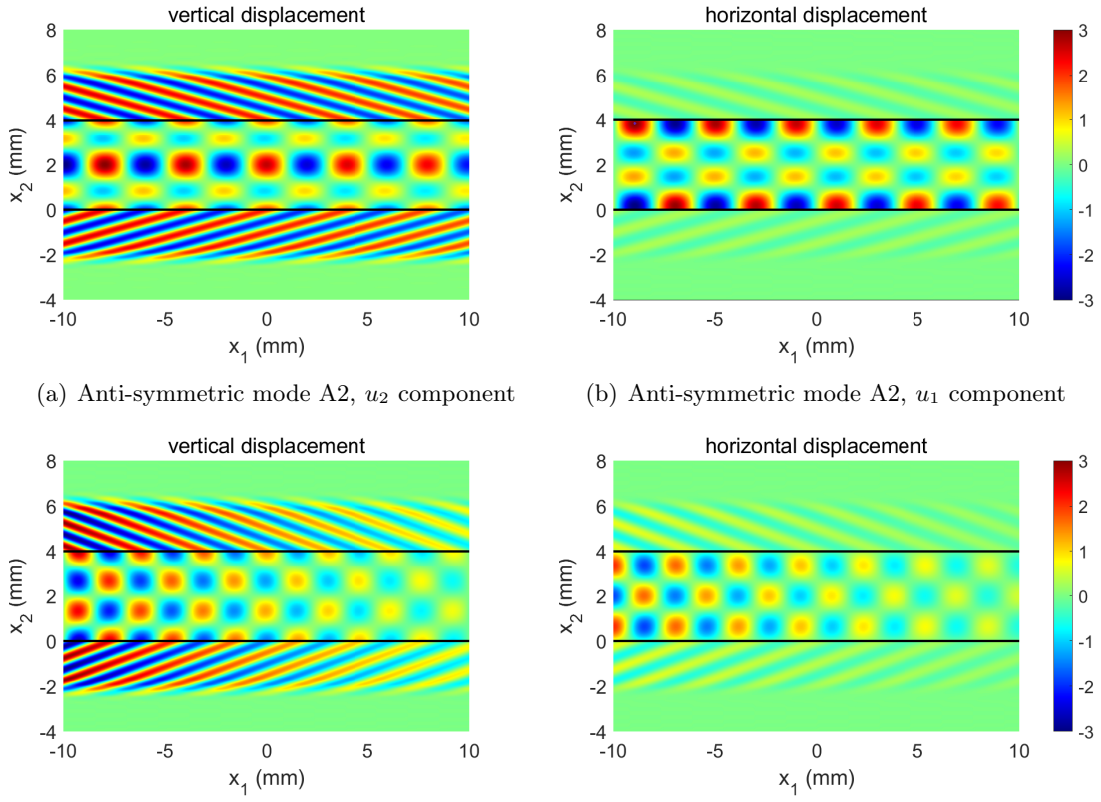

(a) Anti-symmetric mode A2, u_2 component

(b) Anti-symmetric mode A2, u_1 component

(c) Symmetric mode S1, u_2 component

(d) Symmetric mode S1, u_1 component

Figure 3.13 – Leaky wave propagation in a system of a plate immersed fluid: anti-symmetric mode (A2) $C_{ph} = 6.16$ km/s and symmetric mode (S1) $C_{ph} = 4.76$ at $f = 1.55$ MHz

than the SAIGA ones. When a h-refinement is applied ($N_{\text{dof}} = 76$), using the SAIGA approach leads to nearly perfect stress-pressure continuity (Figs. 3.14(c,d)).

3.5 Conclusion

Due to the strong frequency dependency of dispersion properties, determination of guided waves using SAFE at high frequency range often requires high computational cost. In this work, we investigated the efficiency of applying isogeometric analysis in comparing with the SAFE method for studying the wave dispersion in plates. The convergence analysis for isotropic homogeneous plate showed that increasing the order of NURBS basis function yields a much faster convergence rate in comparison with a similar procedure using Lagrange polynomials. The advantage of using higher order NURBS basis functions is even more significant for computing the dispersion curves of functionally graded plates. In addition, we proposed a strategy to use only one patch to model multilayered plates which allows to obtain a very good continuity of the stresses at the interfaces of layers. For studying the waveguides immersed in a fluid, the using SAIGA approach also leads to a better prediction of dispersion curves. The ability of the PML to absorb the leaky modes using NURBS was also validated. The shape modes of pressure and stress fields estimated by using SAIGA were shown to be more accurate compared to the standard SAFE method and a refinement of the NURBS allowed to obtain perfect continuities of

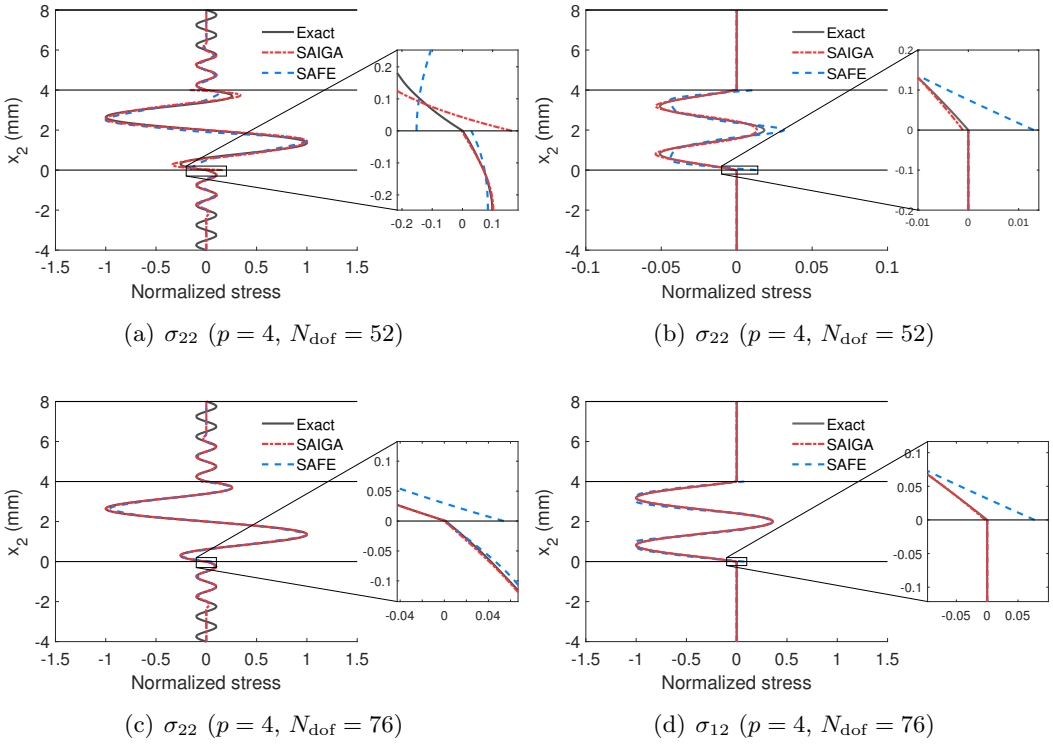

(a) σ_{22} ($p = 4$, $N_{\text{dof}} = 52$)

(b) σ_{22} ($p = 4$, $N_{\text{dof}} = 52$)

(c) σ_{22} ($p = 4$, $N_{\text{dof}} = 76$)

(d) σ_{12} ($p = 4$, $N_{\text{dof}} = 76$)

Figure 3.14 – Mode shapes of the stress of an aluminum plate immersed the immersed in water at $f = 1.55$ MHz, $C_{ph} = 6.16$ km/s: comparison between SAIGA solution (dashed red line), SAFE solution (dashed blue line) and analytical solution (grey line). In the fluid domain, $\sigma_{22}^f = -p$ and $\sigma_{12}^f = 0$.

stress and displacement at fluid-solid interface. Extension of proposed SAIGA formulation would be interesting for the guided wave propagation in arbitrary cross-sectional structures. Employment of NURBS-based finite elements in such situations is the topic of the next chapter.

Chapter 4

Wave dispersion analysis of three-dimensional vibroacoustic waveguides

4.1 Introduction

In this chapter[1], a semi-analytical isogeometric formulation (SAIGA) was proposed for analyzing the wave dispersion in arbitrary cross-section structures immersed in fluids. To do so, the NURBS basis functions were used within the SAFE formulation established for an anisotropic elastic domain coupled with acoustic fluids in the frequency-wavenumber domain. It is expected that using high-degree NURBS basis functions could significantly improve the accuracy of the numerical solutions of the wave dispersion with a significant reduction of computational cost. The convergence analysis was carefully performed for several cases including an empty/fluid-filled cylinder and an arbitrary cross-section waveguide, which represent a typical cortical long bone geometry, in order to find optimal NURBS order for these cases. We were particularly interested in studying the continuities of stress and displacement at solid-fluid interfaces, which are important for the evaluation of the mode excitability, computed by the proposed NURBS-based analysis. To the best of the author's knowledge, the NURBS-based modeling guided waves in 3D coupling solid-fluid structures has not been investigated in the literature. It is worth to notice that the term "semi-analytical isogeometric analysis" has also been used in the literature but in different contexts. For example, in the so-called IGA-SBFEM method [84], the IGA was used for computing the coefficient matrices of SBFEM (Scaled Boundary Finite Element Method). In [93], the W-IGA (Wave Isogeometric Analysis) method was used for the simulation wave propagation in periodic media, in which the IGA can be used for dealing with cell problems derived from Floquet-Bloch theory. In [94], a "semi-analytical isogeometric analysis" approach named as SIGA, was used for studying two-dimensional Rayleigh waves in layered composite piezoelectric structures. However, the term SIGA also widely stands for the so-called Stochastic Isogeometric Analysis and hence, we would like to not use this term to avoid confusion.

The chapter is organized as follows. Section 4.2 describes the governing equations for three-dimensional waveguides coupled with fluid. After introducing the concept of isogeometric analysis and NURBS basis functions, Section 4.4 formulates the SAIGA method. Section 4.5 subsequently carries out the numerical dispersion analysis through several numerical examples including the free

[1]The work presented in this chapter is published in the journal of Computer Methods in Applied Mechanics and Engineering [92].

waveguide, the waveguides coupled with interior and/or exterior fluids. The convergence analysis of the phase velocities will be studied for these cases. The mode shapes and their continuities will be carefully investigated for each case. The last section ends with some conclusions and perspectives.

4.2 Problem formulation

4.2.1 Governing equation

Geometry description The geometry of an immersed waveguides with arbitrary cross-section is shown in Fig. 4.1. The structure is described in the Cartersian coordinate system with an orthogonal basis $(\mathbf{e}_1, \mathbf{e}_2, \mathbf{e}_3)$ and the position vector $\boldsymbol{x} = (x_1, x_2, x_3)$. The cross section of the solid is constant along $\mathbf{e}_3$. The surfaces of the solid body my be free or loaded by two inner and outer fluids (Ω_1^f and Ω_2^f as shown in Fig. 4.1). The domains occupied by the solid body and the fluids are denoted by $\Omega^s = \{(x_1, x_2, x_3) | x_3 \in [-\infty, +\infty], (x_1, x_2) \in \bar{\Omega}^s\}$, $\Omega_1^f = \{(x_1, x_2, x_3) | x_3 \in [-\infty, +\infty], (x_1, x_2) \in \bar{\Omega}_1^f\}$ and $\Omega_2^f = \{(x_1, x_2, x_3) | x_3 \in [-\infty, +\infty], (x_1, x_2) \in \bar{\Omega}_2^f\}$, where $\bar{\Omega}^s$, $\bar{\Omega}_1^f$ and $\bar{\Omega}_2^f$ are the cross-section of the solid and two fluid domains. The interfaces between Ω^s and Ω_α^f ($\alpha = \{1, 2\}$) are denoted by Γ_α^{sf} ($\alpha = \{1, 2\}$). As the cross sections are unchanged along $\mathbf{e}_3$, the outward directed, normal vectors of Ω^s at Γ_α^{sf} are always perpendicular to $\mathbf{e}_3$ and may be represented by $\boldsymbol{n}^s = \{n_1, n_2, 0\}^T$. In what follows, the symbol $\partial_i(\star)$ $(i = 1, 2, 3)$ stands for the partial derivative of $(\star)$ with respect to x_i.

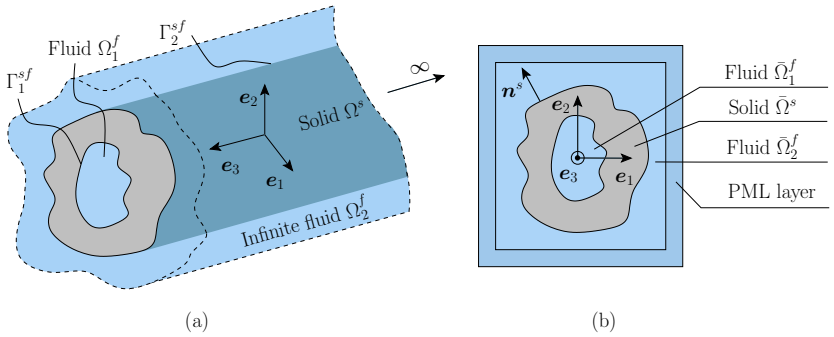

Figure 4.1 – Schematic of (a) fluid-filled solid waveguide with arbitrary cross-section immersed in an infinite fluid (b) cross-section with the PML layer

Dynamic equations in the solid layer In the solid domain Ω^s, the infinitesimal displacement vector at a point $\boldsymbol{x}$ and at time t is denoted by $\boldsymbol{u}^s(\boldsymbol{x}, t) = \{u_1, u_2, u_3\}^T$. For the purpose of convenience, here we use the Voigt notation which represents the stress and strain under the vectorial form as follows $\boldsymbol{s}(\mathbf{x}, t) = \{\sigma_{11}, \sigma_{22}, \sigma_{33}, \sigma_{23}, \sigma_{13}, \sigma_{12}\}^T$ and $\boldsymbol{e}(\mathbf{x}, t) = \{\varepsilon_{11}, \varepsilon_{22}, \varepsilon_{33}, 2\varepsilon_{23}, 2\varepsilon_{13}, 2\varepsilon_{12}\}^T$, respectively. As $\varepsilon_{ij} = \frac{1}{2}(\partial_i u_j + \partial_j u_i)$, the strain vector $\boldsymbol{e}$ can be expressed by: $\boldsymbol{e} = \mathbf{L}\boldsymbol{u}^s$, where $\mathbf{L} = \mathbf{L}_1\partial_1 + \mathbf{L}_2\partial_2 + \mathbf{L}_3\partial_3$. The matrices $\mathbf{L}_1$, $\mathbf{L}_2$ and $\mathbf{L}_3$ are 3×2 matrices of which the nonzero entries are: $\mathbf{L}_1(1,1) = \mathbf{L}_1(5,3) = \mathbf{L}_1(6,2) = 1$, $\mathbf{L}_2(2,2) = \mathbf{L}_2(4,3) = \mathbf{L}_2(6,1) = 1$ and $\mathbf{L}_3(3,3) = \mathbf{L}_3(4,2) = \mathbf{L}_3(5,1) = 1$, respectively.

The balance equations of linear momentum at a point $\boldsymbol{x} \in \Omega^s$ and the linear elastic constitutive

law read

$$\rho\ddot{\boldsymbol{u}}^s - \mathbf{L}^T\boldsymbol{s} = 0\ , \tag{4.1}$$
$$\boldsymbol{s} = \mathbf{C}\boldsymbol{e}\ , \tag{4.2}$$

where ρ is the mass density, $\mathbf{C}_{6\times6}$ is the matrix containing the components of the anisotropic elasticity tensor. In this problem, the structure is assumed to be homogeneous along the longitudinal direction $\mathbf{e}_3$ but it could be heterogeneous in the section $\bar{\Omega}^s$, *i.e.* $\rho = \rho(x_1, x_2)$ and $\mathbf{C} = \mathbf{C}(x_1, x_2)$.

Wave equations in the fluids In the fluid domains Ω^f_α ($\alpha = 1, 2$), the linearized wave equations can be expressed as

$$\rho^f_\alpha\ddot{p}_\alpha - K^f_\alpha\nabla^2 p_\alpha = 0\ , \tag{4.3}$$

where p_α are the acoustic pressure fields in Ω^f_α, K^f_α and ρ^f_α are the bulk modulus at rest and the mass density at rest of the Ω^f_α, respectively; $\nabla^2(\star)$ is the Laplace operator. The wave celerity in Ω^f_α can be defined as $c^f_\alpha = \sqrt{K^f_\alpha/\rho^f_\alpha}$.

Boundary and interface conditions The boundary conditions of this system (Eqs. 4.1 & 4.3) consist of the continuity conditions of the traction and of the normal displacement at the solid-fluid interfaces $\bar{\Gamma}^{sf}_\alpha (\alpha = \{1, 2\})$, and the radiation condition at infinity, i.e.

$$\left.\begin{aligned} \boldsymbol{t} &= -p_\alpha\boldsymbol{n}^s \\ \boldsymbol{u}^s\cdot\boldsymbol{n}^s &= \boldsymbol{u}^f_\alpha\cdot\mathbf{n}^s \end{aligned}\right\} \quad \forall\boldsymbol{x}\in\bar{\Gamma}^{sf}_\alpha\ , \tag{4.4}$$
$$p_\alpha \to 0 \qquad \text{when } |\boldsymbol{x}|\to\infty\ , \tag{4.5}$$

where $\boldsymbol{n}^s$ is the outward unit vector at the interfaces (Fig. 4.1), which is is opposed to the one of the fluid domain: $\boldsymbol{n}^s{=}{-}\boldsymbol{n}^f$. It is worth noting that $\boldsymbol{t} = \boldsymbol{\sigma}\cdot\boldsymbol{n}^s = (n_1\mathbf{L}_1^T + n_2\mathbf{L}_2^T)\boldsymbol{s}$ and the fluid displacement may be calculated from the pressure field by using the Euler's equation:

$$\rho^f_\alpha\ddot{\boldsymbol{u}}^f_\alpha + \nabla p_\alpha = 0. \tag{4.6}$$

4.3 Equations in the frequency-wavenumber domain

We look for the solution of harmonic waves propagating along the axial direction ($\mathbf{e}_3$) which may be expressed by the following form

$$\boldsymbol{u}^s(x_1, x_2, x_3, t) = \tilde{\boldsymbol{u}}^s(x_1, x_2)e^{\mathrm{i}(k_3x_3-\omega t)}\ , \tag{4.7a}$$
$$p_\alpha(x_1, x_2, x_3, t) = \tilde{p}_\alpha(x_1, x_2)e^{\mathrm{i}(k_3x_3-\omega t)}\ , \tag{4.7b}$$

where $\mathrm{i}^2 = -1$; $\omega\in\mathbb{R}$ is the angular frequency; k_3 is the wavenumber in the $\mathbf{e}_3$-direction; the vector $\tilde{\boldsymbol{u}}^s(x_1, x_2) = (\tilde{u}_1, \tilde{u}_2, \tilde{u}_3)^T$ and $\tilde{p}_\alpha(x_1, x_2) = \tilde{p}_\alpha$ which represents are the amplitudes of the displacement vector in the $\bar{\Omega}^s$ and of the pressures in $\bar{\Omega}^f_\alpha$, respectively. By applying harmonic forms (Eqs. 4.7a,4.7b), the problem presented in Sec. 4.2.1 can be transformed to a 2D system of equations with respect only to x_1 and x_2. Noting that in the frequency-wavenumber ($\omega - k_3$) domain, the time derivative

and the spatial derivative with respect to x_1 can be replaced by: $(\dot{\star}) \rightarrow -\mathrm{i}\omega(\star)$ and $\partial_1(\star) \rightarrow \mathrm{i}k_3(\star)$, respectively, then the amplitudes of the strain and stress vectors ($\tilde{\boldsymbol{e}}$ and $\tilde{\boldsymbol{s}}$) are expressed by:

$$\tilde{\boldsymbol{e}} = (\mathbf{L}_1\partial_1 + \mathbf{L}_2\partial_2 + \mathrm{i}k_3\mathbf{L}_3)\tilde{\boldsymbol{u}}^s, \tag{4.8}$$

$$\tilde{\boldsymbol{s}} = \mathbf{C}\tilde{\boldsymbol{e}}, \tag{4.9}$$

and the balance equation Eq. (4.1) can be reformulated as a 2D system of equations with respect to (x_2, x_3) :

$$-\rho\omega^2\tilde{\boldsymbol{u}}^s - \left(\mathbf{L}_1^T\partial_1 + \mathbf{L}_2^T\partial_2 + \mathrm{i}k_3\mathbf{L}_3^T\right)\mathbf{C}(\mathbf{L}_1\partial_1 + \mathbf{L}_2\partial_2 + \mathrm{i}k_3\mathbf{L}_3)\tilde{\boldsymbol{u}}^s = 0\ , \quad \forall\bar{\boldsymbol{x}} \in \bar{\Omega}^s. \tag{4.10}$$

Similarly, by substituting Eq. (4.7b) into Eq. (4.3), the wave equations in the fluid domains are simplified into a two-dimensional problem:

$$(-\rho_\alpha^f\omega^2 + k_3^2K_\alpha^f)\tilde{p}_\alpha - K_\alpha^f(\partial_1^2 + \partial_2^2)\tilde{p}_\alpha = 0, \quad \forall\bar{\boldsymbol{x}} \in \bar{\Omega}_\alpha^f. \tag{4.11}$$

The boundary conditions in Eqs. (4.4)-(4.5) reads:

$$\left.\begin{aligned}\tilde{\boldsymbol{u}}^s \cdot \mathbf{n}^s &= \frac{1}{\rho_\alpha^f\omega^2}(n_1\partial_1 + n_2\partial_2)\tilde{p}_\alpha \\ \tilde{\boldsymbol{t}} &= -\tilde{p}_\alpha\mathbf{n}^s\end{aligned}\right\} \quad \forall\tilde{\boldsymbol{x}} \in \bar{\Gamma}_\alpha^{sf}(\alpha = \{1,2\}), \tag{4.12}$$

$$\tilde{p}_\alpha \rightarrow 0 \qquad \text{when } |\tilde{\boldsymbol{x}}| \rightarrow \infty, \tag{4.13}$$

where $\tilde{\boldsymbol{t}} = (n_1\mathbf{L}_1^T + n_2\mathbf{L}_2^T)\tilde{\boldsymbol{s}}$.

4.3.1 Perfectly Matched Layer (PML)

In order to introduce the behavior of the infinite exterior fluid domain, we used the perfectly matched layers (PML) in the cross-section plane, following the procedures proposed in [41, 50]. From a mathematical point of view, the PML can be considered as a result of a mapping into complex coordinates, where the solutions of wave equations decay exponentially [51]. Therefore, the infinite medium can be truncated into a finite domain as shown in Fig. 4.1. The new stretched coordinates $\tilde{x}_1(x_1)$, $\tilde{x}_2(x_2)$ in the waveguide are defined as

$$\tilde{x}_1(x_1) = \int_0^{x_1}\gamma_1(x_1)dx_1, \qquad \tilde{x}_2(x_2) = \int_0^{x_2}\gamma_2(x_2)dx_2, \tag{4.14}$$

where $\gamma_1(x_1)$ and $\gamma_2(x_2)$ are called PML functions, which satisfy:

$$\gamma_j(x_j) = 1 \text{ for } |x_j| \leq d_j \text{ and } \mathrm{Im}\{\gamma_j(x_j)\} > 0 \text{ for } |x_j| > d_j, \quad \text{for } j = \{1,2\}, \tag{4.15}$$

On the exterior boundary of the PML, the boundary condition can be arbitrarily chosen (Dirichlet or Neumann type). The absorption efficiency of leaky waves in the PML strongly depends on the choice of the PML function (γ_1, γ_2), the position of the interfaces (d_1, d_2) and the thickness $(h_1^{\mathrm{pml}}, h_2^{\mathrm{pml}})$ in the $\mathbf{e}_1$ and $\mathbf{e}_2$ directions, respectively. There are a number of variants to choose for the γ_1 and γ_2 functions. For this study, a continuous parabolic function for both the real and imaginary parts of the PML function, which has been demonstrated to be efficient in the frequency domain [50, 41], was used:

$$\gamma_j(x_j) = \begin{cases} 1 & \text{if } |x_j| \leq d_j, \\ 1 + \hat{\gamma}_j\left(\frac{|x_i| - d_j}{h_j^{pml}}\right)^2 & \text{if } |x_j| > d_j, \end{cases} \quad \text{for } j = \{1,2\}, \tag{4.16}$$

where $\hat{\gamma}_j = a_j + \mathrm{i}b_j$ quantify the PML absorption and will be given explicitly in each case study. As leaky waves grow exponentially in the transverse directions, placing the PML close to the waveguide can reduce the effect of the exponential growth of the leaky modes. In order to estimate the length of the PML, a simplified 2D plane wave propagation model can be used to approximately predict the length of the PML:

$$h_j^{pml} \geq \frac{6.9}{k_{\text{leak}} b_j}, \quad \text{for } j = \{1, 2\}, \tag{4.17}$$

where k_{leak} represents the wavenumber of the longitudinal wave in the fluid. When the PML function is given, b_j can be determined as $\mathrm{Im}\left(()\,\hat{\gamma}_j\right)$. The length of the PML can be obtained by calculating the smallest wavenumber in the frequency range of interest [41].

It is worth noting that in the context of the SAFE analysis, several techniques have been proposed for representing the radial boundary condition in semi-infinite domains. For example, in [31], the coupled boundary element and finite element method (referred as 2.5D FEM-BEM) has been used. However, this method leads to a nonlinear eigenvalue problem that requires an expensive solution strategy. In [34], an iterative procedure was proposed to solve the nonlinear eigenvalue problem derived from exact radiation condition. For the case of an immersed plate, the nonlinear eigenvalue problem with exact radiation condition was transformed into a cubic polynomial eigenvalue problem using a change of variables [91]. However, its extension to 3D cases is not trivial. Although using a PML within SAFE formulation requires a supplement layer with a thickness about two wavelengths, it has some attractive advantages because (i) it allows us to avoid the nonlinear term in the exact radiation condition and thus the final eigenvalue problem established for the coupled fluid-solid system still has the quadratic polynomial form, which may efficiently be solved (as it will be shown in Sec. 3); (ii) the implementation of PMLs in the SAFE formulation is straightforward and requires very little modifications.

4.3.2 Weak formulation in the frequency-wavenumber domain

Upon integrating Eqs. (4.10)-(4.11) against test function $\delta\tilde{\boldsymbol{u}}^s$ and $\delta\tilde{p}_\alpha$, respectively, then applying the Gauss theorem and taking into account the interface conditions (4.12), the weak formulation of the boundary value problem in the solid layer $\bar{\Omega}^s$ and in the fluid domain $\bar{\Omega}^f_\alpha(\alpha = \{1, 2\})$ may be derived as in [49]:

$$\begin{aligned}
&-\omega^2 \int_{\bar{\Omega}^s} \delta\tilde{\boldsymbol{u}}^s \cdot \rho\tilde{\boldsymbol{u}}^s d\bar{\Omega}^s + \int_{\bar{\Omega}} \left(\mathbf{L}_1\partial_1 + \mathbf{L}_2\partial_2 - \mathrm{i}k_3\mathbf{L}_3\right)\delta\tilde{\boldsymbol{u}}^s \cdot \left(\mathbf{C}(\mathbf{L}_1 + \mathbf{L}_2\partial_2 + \mathrm{i}k_3\mathbf{L}_3)\tilde{\boldsymbol{u}}^s\right) d\bar{\Omega}^s \\
&\quad + \int_{\bar{\Gamma}^{sf}_\alpha} \delta\tilde{\boldsymbol{u}}^s \cdot \left(\tilde{p}_\alpha \boldsymbol{n}^s\right) d\bar{\Gamma}^{sf}_\alpha = 0\,, \quad \forall \delta\tilde{\boldsymbol{u}}^s \in \mathcal{C}^{ad}. \qquad (4.18a) \\
&-\omega^2 \int_{\bar{\Omega}^f_\alpha} \delta\tilde{p}^*_\alpha \rho^f_\alpha \tilde{p}_\alpha d\bar{\Omega}^f_\alpha - \omega^2 \int_{\bar{\Gamma}^{sf}_\alpha} \delta\tilde{p}^*_\alpha \rho^f_\alpha K^f_\alpha \tilde{\boldsymbol{u}}^s \cdot \boldsymbol{n}^s d\bar{\Gamma}^{sf}_\alpha + k_3^2 \int_{\bar{\Omega}^f_\alpha} \delta\tilde{p}_\alpha K^f_\alpha \tilde{p}_\alpha d\bar{\Omega}^f_\alpha \\
&\quad + \int_{\bar{\Omega}^f_\alpha} \left((\partial_1\delta\tilde{p}_\alpha)^* K^f_\alpha \partial_1\tilde{p}_\alpha + (\partial_2\delta\tilde{p}_\alpha)^* K^f_\alpha \partial_2\tilde{p}_\alpha\right) d\bar{\Omega}^f_\alpha = 0\,, \quad \forall \delta\tilde{p}_\alpha \in \mathcal{C}^{ad}. \qquad (4.18b)
\end{aligned}$$

4.4 NURBS-based isogeometric approximation

The formulation presented in Eqs. (4.18a) -(4.18b) is valid irrespective of the numerical discretization employed in the cross-section. In the framework of conventional SAFE, the Lagrange polynomials

are used to discretized these equations. The main drawback of this approach, which is also called a SAFE method, is the fact that discretization should be fine enough to achieve the required accuracy. The consequence of fine discretization is a significant increase in computational cost. Furthermore, the Lagrange functions give a non-smoothness profile across the PML interfaces, which leads to imperfect absorption of the leaky modes. We propose to use a different technique for computational efficiency. The idea is based on the NURBS-based isogeometric analysis allowing the use of globally C^k-continuous basis functions, with $k \leq p-1$, p being the polynomial degree. In this section, we briefly recall the concept of isogeometric analysis with the main focus on the B-spline and NURBS basis functions, their properties, their use for the geometrical representation as well as incorporating the interface with the C^0-continuity. For a more detailed review of these topics, we refer the interested reader to [86, 87].

4.4.1 Geometrical representation

NURBS are piecewise rational functions of degree p that are connected in so-called knots. Let $\Xi = \{\xi_1, \xi_2, \xi_3, ..., \xi_{n+p+1}\}$ and $H = \{\eta_1, \eta_2, \eta_3, ..., \eta_{m+p+1}\}$ be the knot vectors in the bi-dimensional parametric domain $\hat{\Omega}$, each consisting of nondecreasing real numbers ξ_i and η_i, respectively. The bivariate NURBS basis functions are defined by:

$$R_{ij}^{p,q}(\xi,\eta) = \frac{N_{i,p}(\xi)N_{j,q}(\eta)w_{ij}}{\sum_{k=1}^{n}\sum_{\ell=1}^{m} N_{k,p}(\xi)N_{\ell,q}(\eta)w_{k\ell}}, \tag{4.19}$$

where $N_{i,p}$ denotes the ith B-spline basis function of p-degree, $w_{k\ell} \in \mathbb{R}$ is the weight values and n,m are the numbers of basis functions used to construct the B-spline curve in each dimension. By using the well-known Cox-de Boor formula, the B-spline basis functions are defined recursively as:

$$N_{i,0}(\xi) = \begin{cases} 1 & \text{if } \xi_i < \xi < \xi_{i+1}, \\ 0 & \text{otherwise,} \end{cases} \tag{4.20a}$$

$$N_{i,p}(\xi) = \frac{\xi - \xi_i}{\xi_{i+p} - \xi_i} N_{i,p-1}(\xi) + \frac{\xi_{i+p+1} - \xi}{\xi_{i+p+1} - \xi_{i+1}} N_{i+1,p-1}(\xi). \tag{4.20b}$$

Note that the quotient $0/0$ is assumed to be zero. By introducing a set of control points $\mathbf{P}_{ij} \in \mathbb{R}^2$, the NURBS surfaces are constructed by:

$$\boldsymbol{S}(\xi,\eta) = \sum_{i=1}^{n}\sum_{j=1}^{m} R_{ij}^{p,q}(\xi,\eta)\mathbf{P}_{ij} \ . \tag{4.21}$$

4.4.2 Solution approximation

Let v^h denotes the approximation of a function $v(x_1, x_2)$ defined in the physical domain Ω. According to the isogeometric concept [87], the function v^h may be given by a composition between a function $\hat{v}^h$, defined in the parametric domain $\hat{\Omega}$, with the inverse of geometrical mapping: $v^h = \hat{v}^h \circ \boldsymbol{x}^{-1}$. The function $\hat{v}^h$ is built over the parametric domain by:

$$\hat{v}^h(\xi,\eta) = \sum_{i=1}^{n}\sum_{j=1}^{m} R_{ij}^{p,q}(\xi,\eta)V_{ij} \ , \tag{4.22}$$

where the coefficients $V_{ij} \in \mathbb{C}$ are the corresponding control variables (values at the control points $\mathbf{P}_{ij}$). The properties of the function $\hat{v}^h$ follow those of the NURBS basis functions.

In this study, by using Galerkin's method, the same approximations are applied for both functions $\tilde{\boldsymbol{u}}^h$ and $\delta\tilde{\boldsymbol{u}}^h$ (as well as for $\tilde{p}^h_\alpha$ and $\delta\tilde{p}^h_\alpha$) on each patch:

$$\tilde{\boldsymbol{u}}^h = \mathbf{R}^u\mathbf{U}, \quad \delta\tilde{\boldsymbol{u}}^h = \mathbf{R}^u\delta\mathbf{U}, \tag{4.23a}$$

$$\tilde{p}^h_\alpha = \mathbf{R}^p_\alpha\mathbf{P}_\alpha, \quad \delta\tilde{p}^h_\alpha = \mathbf{R}^p_\alpha\delta\mathbf{P}_\alpha, \tag{4.23b}$$

where $\mathbf{R}^u$, $\mathbf{R}^p$ are the interpolation matrix containing the NURBS basis functions (Eq. 4.19); $\mathbf{U}$ and $\delta\mathbf{U}$ are the vectors of control displacements; $\mathbf{P}_\alpha$ and $\delta\mathbf{P}_\alpha$ are the vectors of control pressures. By substituting the approximations (Eqs. 4.23a-4.23b) into the weak formulations (Eqs. 4.18a-4.18b), then assembling the elementary matrices, one obtains

$$(-\omega^2\mathbf{M} + \mathbf{K}_0 + \mathrm{i}k_3\mathbf{K}_1 + k_3^2\mathbf{K}_2)\mathbf{V} = \mathbf{0}\,, \tag{4.24}$$

where $\mathbf{V} = (\mathbf{P}_1, \mathbf{U}, \mathbf{P}_2)^T$ containing the global eigenvectors of pressure ($\mathbf{P}_1$, $\mathbf{P}_2$) and of displacement ($\mathbf{U}$); the global matrices $\mathbf{M}$, $\mathbf{K}_0$, $\mathbf{K}_1$, $\mathbf{K}_2$ are defined by:

$$\mathbf{M} = \begin{bmatrix} \mathbf{M}^{f_1} & \mathbf{M}^{f_1 s} & \mathbf{0} \\ \mathbf{0} & \mathbf{M}^{s} & \mathbf{0} \\ \mathbf{0} & \mathbf{M}^{f_2 s} & \mathbf{M}^{f_2} \end{bmatrix}, \; \mathbf{K}_0 = \begin{bmatrix} \mathbf{K}_0^{f_1} & \mathbf{0} & \mathbf{0} \\ \mathbf{K}^{s f_1} & \mathbf{K}_0^{s} & \mathbf{K}^{s f_2} \\ \mathbf{0} & \mathbf{0} & \mathbf{K}_0^{f_2} \end{bmatrix}, \tag{4.25a}$$

$$\mathbf{K}_1 = \begin{bmatrix} \mathbf{0} & \mathbf{0} & \mathbf{0} \\ \mathbf{0} & \mathbf{K}_1^{s} & \mathbf{0} \\ \mathbf{0} & \mathbf{0} & \mathbf{0} \end{bmatrix}, \; \mathbf{K}_2 = \begin{bmatrix} \mathbf{K}_2^{f_1} & \mathbf{0} & \mathbf{0} \\ \mathbf{0} & \mathbf{K}_2^{s} & \mathbf{0} \\ \mathbf{0} & \mathbf{0} & \mathbf{K}_2^{f_2} \end{bmatrix}, \tag{4.25b}$$

in which the sub-matrices are determined from the assembling of corresponding elementary matrices in solid and fluid domains: the sub-matrices (with superscript ^{s}) representing the behavior of the solid domain are defined by:

$$\mathbf{M}^s = \bigcup_e \int_{\bar{\Omega}^{s(e)}} (\mathbf{R}^u)^T \rho \mathbf{R}^u d\bar{\Omega}^s, \tag{4.26a}$$

$$\mathbf{K}_0^s = \bigcup_e \int_{\bar{\Omega}^{s(e)}} \Big(\partial_i(\mathbf{R}^u)^T \mathbf{A}_{ij} \partial_j \mathbf{R}^u\Big) d\bar{\Omega}^s, \quad \text{for } i,j = \{1,2\}, \tag{4.26b}$$

$$\mathbf{K}_1^s = \bigcup_e \int_{\bar{\Omega}^{s(e)}} \Big(- (\mathbf{R}^u)^T \mathbf{A}_{3i} \partial_i \mathbf{R} + \partial_i(\mathbf{R}^u)^T \mathbf{A}_{i3} \mathbf{R}^u\Big) d\bar{\Omega}^s, \quad \text{for } i = \{1,2\}, \tag{4.26c}$$

$$\mathbf{K}_2^s = \bigcup_e \int_{\bar{\Omega}^{s(e)}} (\mathbf{R}^u)^T \mathbf{A}_{33} \mathbf{R}^u d\bar{\Omega}^s, \tag{4.26d}$$

the sub-matrices (with superscript ^{f}) representing the behavior of the fluid domains are defined by

$$\mathbf{M}^{f_\alpha} = \bigcup_e \int_{\bar{\Omega}^f_\alpha} (\mathbf{R}^p)^T \rho^f_\alpha \gamma_1 \gamma_2 \mathbf{R}^p d\bar{\Omega}^f_\alpha, \tag{4.27a}$$

$$\mathbf{K}_0^{f_\alpha} = \bigcup_e \int_{\bar{\Omega}^f_\alpha} \partial_2(\mathbf{R}^p)^T K^f_\alpha \gamma_1 \gamma_2 \partial_2 \mathbf{R}^p d\bar{\Omega}^f_\alpha, \tag{4.27b}$$

$$\mathbf{K}_2^{f_\alpha} = \bigcup_e \int_{\bar{\Omega}^f_\alpha} (\mathbf{R}^p)^T K^f_\alpha \gamma_1 \gamma_2 \mathbf{R}^p d\bar{\Omega}^f_\alpha, \tag{4.27c}$$

and sub-matrices $\mathbf{M}^{f_\alpha s}$ and $\mathbf{K}^{s f_\alpha}$ representing the coupling operator at fluid-solid interfaces:

$$\mathbf{M}^{f_\alpha s} = \int_{\bar{\Gamma}^{sf}_\alpha} (\mathbf{R}^p)^T \rho^f_\alpha K^f_\alpha \mathbf{R}^u d\bar{\Gamma}^{sf}_\alpha\,, \tag{4.28a}$$

$$\mathbf{K}^{s f_\alpha} = \int_{\bar{\Gamma}^{sf}_\alpha} (\mathbf{R}^u)^T \mathbf{R}^p d\bar{\Gamma}^{sf}_\alpha\,. \tag{4.28b}$$

The matrices $\mathbf{M}$, $\mathbf{K}_0$, $\mathbf{K}_1$, $\mathbf{K}_2$ are computed by using two-dimensional Gauss–Legendre quadrature formula with $r = p+1$ quadrature nodes per element along each parametric direction which has been shown to be efficient [82]. Due to the fact that $\mathbf{A}_{\alpha\beta} = \mathbf{A}_{\beta\alpha}^T$, it can be shown that that $\mathbf{M}$, $\mathbf{K}_0$, $\mathbf{K}_2$ are symmetric while the matrix $\mathbf{K}_1$ is anti-symmetric. In this chapter, where the material is assumed to be elastic, these matrices are real and constant with respect to ω and k_3. In the case where viscoelastic materials are considered, the elasticity tensor $\mathbf{C}$ can be by replaced by a complex tensor $\mathbf{C}(\omega)$, which depends to the frequency. Then same formulations (Eqs. 4.26a-4.28b) can be used for taking into account viscosity effects. In that case, the matrices $\mathbf{K}_0$, $\mathbf{K}_1$, $\mathbf{K}_2$ will depend on ω, but still independent to k_3.

It is worth to note that the quadratic eigenvalue Eq. (4.24) can be converted into a generalized linear eigenvalue problem for the media possessing orthorhombic symmetry (more detail can be found in [66].

4.4.3 Dispersion analysis

The system of characteristic equations (4.24) is an eigenvalue problem which is used to determine the relationship between the pulsation ω and the wavenumber k_3. By noting that all global matrices ($\mathbf{M}$, $\mathbf{K}_0$, $\mathbf{K}_1$, $\mathbf{K}_2$) do not depend on k_3, Eq. (4.24) is a quadratic eigenvalue problem with respect to k_3 and could be solved by reformulating it under following linearized eigenvalue problem:

$$\left(\begin{bmatrix} \mathbf{0} & -\omega^2\mathbf{M}+\mathbf{K}_0 \\ -\omega^2\mathbf{M}+\mathbf{K}_0 & \mathrm{i}\mathbf{K}_1 \end{bmatrix} - k_3 \begin{bmatrix} -\omega^2\mathbf{M}+\mathbf{K}_0 & \mathbf{0} \\ \mathbf{0} & -\mathbf{K}_2 \end{bmatrix} \right) \begin{pmatrix} \mathbf{V} \\ k_3\mathbf{V} \end{pmatrix} = \mathbf{0} \,. \tag{4.29}$$

For each value of the angular frequency ω, solving Eq. (4.29) allows us to determine the eigenvalues k_3 and their associated eigenvectors (also called by wave structures), $\mathbf{V}(\omega, k_3)$ of guided modes. The frequency-dependent phase velocity (C_{ph}) and the attenuation (att) of a guided mode are given by:

$$C_{\mathrm{ph}} = \frac{\omega}{\mathrm{Re}\,(()\,k_3)}\ [\mathrm{m.s}^{-1}], \quad \mathrm{att} = \mathrm{Im}\,(()\,k_3)\ [\mathrm{Np.m}^{-1}]\,, \tag{4.30}$$

where $\mathrm{Re}\,(())$ and $\mathrm{Im}\,(())$ denote the real and imaginary parts of a complex function.

Three kinds of modes can be found for the immersed waveguides: the trapped mode, the leaky mode and and the radiation mode. As the name indicates, trapped modes propagate in the waveguide with energy concentrating in the waveguide. Leaky modes propagate along the waveguide with some energy leaking into the surrounding fluid. Radiation modes resonate mainly in the fluid domain, and they are of less interest in practical applications [95]. For the studies presented in this work, the following filtering condition is applied in post-processing to identify and remove the radiation modes: $\frac{|E_k^f|}{|E_k|} > \eta$, where E_k^f and E_k are the kinetic energy of the fluid domain and the total kinetic energy of all domains, respectively; η is a user-defined parameter, identifying the criterion of the model and depends on PML parameters (in this work, a value η=0.98 was used for all examples).

4.5 Numerical results

This section presents some numerical examples in order to validate the accuracy of the proposed SAIGA formulations for the analysis of the dispersion of guided waves in 3D elastic structures. First, a hollow cylinder in vacuum will be considered (Fig. 4.2(a)). Second, the wave dispersion of the waveguides coupled with fluids (inner and outer) will be studied (Fig. 4.2(b) and Fig. 4.2(c)). The

PML is applied to absorb the leaky wave in the infinite exterior fluid. Third, the wave dispersion within a 3D waveguide with a complex section representing an anisotropic cortical bone will be analyzed (Fig. 4.2(d)). The validations were done by comparing the solutions obtained using the proposed SAIGA approach, by the conventional SAFE method and by analytical analysis (which are only exist for the homogeneous or layered plates and cylinders). In this study, all analytical solutions were obtained by using the software DISPERSE [67] and the conventional SAFE solutions by implementing the weak formulations (Sec. 4.3.2) into the software COMSOL Multiphysics (COMSOL AB, Stockholm, Sweden), in which the isoparametric elements were used for the discretization. In all examples, the order of basis functions in the direction $\mathbf{e}_1$ and $\mathbf{e}_2$ are assumed to be the same and denoted by p.

The convergence analysis was performed for two cases: free hollow cylinder and fluid-filled cylinder. In order to carry out a convergence analysis of the proposed method at a given frequency, we introduced a function err which is estimated as the summation of the relative errors of the numerical solutions of the first m modes:

$$\mathsf{err} = \sqrt{\sum_{i=1}^{m} \frac{(C_{\mathrm{ph}}^{i,num} - C_{\mathrm{ph}}^{i,ref})^2}{(C_{\mathrm{ph}}^{i,ref})^2}}\,, \tag{4.31}$$

where $C_{\mathrm{ph}}^{i,num}(f)$ is the phase velocity of i-th mode at a frequency f calculated by using SAFE or SAIGA, $C_{\mathrm{ph}}^{i,ref}$ is the corresponding reference solution. For the case of a homogeneous cylinder, the reference solution can be obtained analytically by using Disperse software (homogeneous cylindrical case). When the section has irregular shapes, the analytical solution doesn't exist, then the reference solutions were numerically computed by using the conventional SAFE method with a very fine mesh.

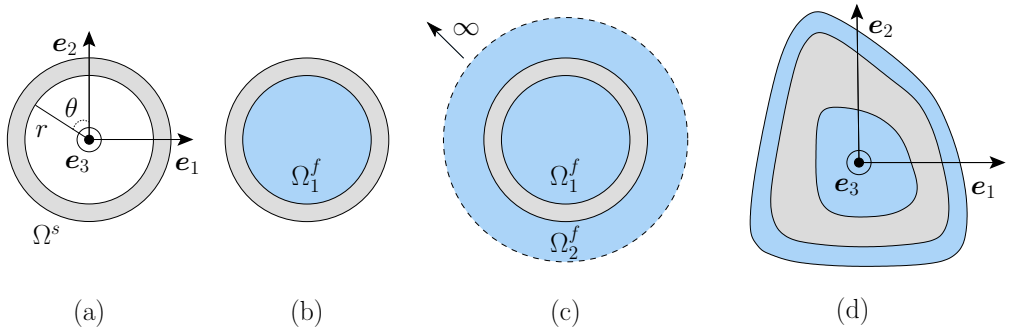

Figure 4.2 – Overview of the studied waveguides: (a) hollow cylinder (without fluid); (b) fluid-filled cylinder; (c) immersed fluid-filled cylinder; and (d) cortical bone with arbitrary cross-section.

4.5.1 Dispersion of guided-waves in a hollow cylinder

Let us first consider a free hollow cylinder, which is a well-known case and has been studied in many works using analytical or the conventional SAFE methods (see *e.g* [4]). Although the solutions of dispersed guided-waves in a free hollow cylinders were well-known, this benchmark example will allow us to validate and show the effectiveness of the proposed SAIGA method in compared with the conventional SAFE method, especially for the evaluation of the phase velocities and mode shapes at the high-frequency range.

In this example, the hollow cylinder is made by 2 mm-thickness steel material with the inner radius of 5 mm Fig. 4.2(a). The isotropic elastic properties of the steel are characterized by the density $\rho = 7840$ kg.m^{-3}, the longitudinal wave velocity $c_P = 5900$ m/s and the shear wave velocity $c_S = 3200$ m/s. Cubic NURBS basis functions are used for SAIGA and cubic Lagrange polynomials are used for SAFE analysis, so that the number of degrees of freedom $N_{\text{dof}} = 1080$ of both numerical approaches. When employing SAIGA, four patches are used to represent the geometry of the annular section. Phase velocities are computed within a frequency range from 0 to 2 MHz.

The results of both numerical approaches are shown in Figs. 4.3 and are compared with the analytical solution using global matrix method. Fig. 4.3(a) depicts all propagating modes (of which k_3 are reals and positives) computed by SAIGA and SAFE methods. Among them, three fundamental modes were interested : axisymmetric longitudinal modes $L(0,n)$, non-axisymmetric flexural modes $F(1,n)$ and torsional modes $T(0,n)$, where integer n represents the group order of a mode. After applying the filtering procedure to the solutions presented in Fig. 4.3(a), the mentioned modes may be be separated as shown in Fig. 4.3(b). One may notice that in the dispersion curves obtained by using SAFE method, some modes are missed, namely in high frequency range. It is because when the mesh is not sufficiently fine, the fundamental modes defined by proposed criteria may not be identified due to numerical errors. On contrary, SAIGA solutions show a very well agreement with the analytical ones over entire frequency range and for all the considered modes. It means that by using SAIGA formulation allows to obtain better estimations not only of the eigenvalues but also of the eigenvectors of the considered system.

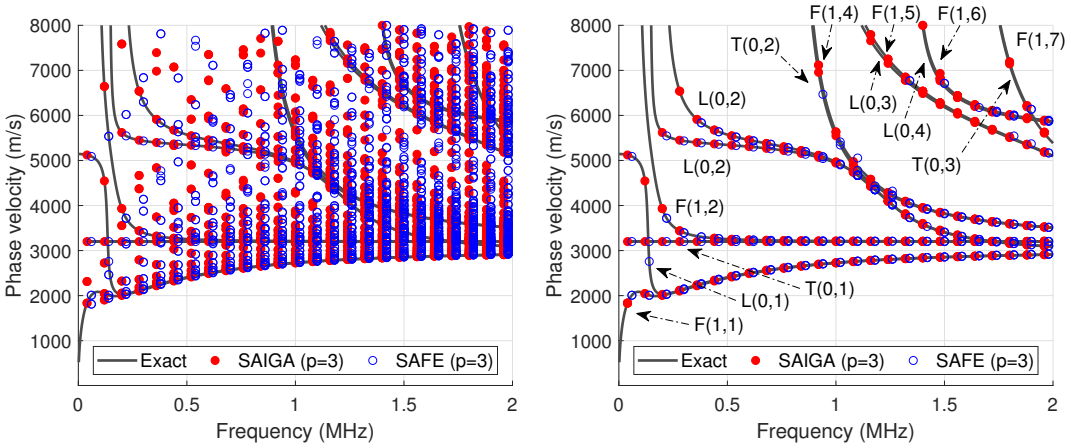

(a) numerical solution without mode filtering (b) numerical solution with mode filtering

Figure 4.3 – Dispersion curves of a steel cylinder: comparison between SAIGA solution (red marker), SAFE (blue marker) and analytical solutions (grey line); both SAIGA and SAFE used $p = 3$, N_{dof}=1080

To quantify the accuracy of the phase velocity computed by SAIGA, we first study the p-convergence of SAIGA method at two different frequencies: $f = 0.2$ MHz and $f = 2$ MHz. To do so, the section is discretized into 4 patches (with C^0 continuity between the patches) and one single span (element) in each patch (*e.g.* the knot vectors for $p = 2$ and $p = 3$ are $\Xi = H = \{0,0,0,1,1,1\}$ and $\Xi = H = \{0,0,0,0,1,1,1,1\}$, respectively). The p-refinement is then applied in which the order of NURBS basis functions is varied: $p = 2,3,4,6$. The numerical errors of the phase velocities (Eq. (4.31)) associated to different modes (see Fig. 4.3(b)) are presented in Table 4.1. At the low frequency $f = 0.2$ MHz, the p-convergence could be quickly achieved. For example, using the cubic

Table 4.1 – Case of a homogeneous hollow cylinder: error analysis of SAIGA solutions based on p-refinement (one single element per patch)

Mode	f (MHz)	$C_{\text{ph}}^{\text{Exact}}$ (m.s^{-1})	$\text{err}^{\text{SAIGA}}$ (p=2, N_{dof}=72)	$\text{err}^{\text{SAIGA}}$ (p=3, N_{dof}=144)	$\text{err}^{\text{SAIGA}}$ (p=4, N_{dof}=240)	$\text{err}^{\text{SAIGA}}$ (p=6, N_{dof}=504)
L(0,1)	0.2	2027.64	0.0082	1.8020×10^{-4}	2.5573×10^{-6}	8.8473×10^{-7}
F(1,1)	0.2	2007.44	0.0156	5.4788×10^{-4}	2.3993×10^{-5}	8.5000×10^{-7}
L(0,1)	2	2910.29	0.0526	0.0241	0.0044	4.7768×10^{-5}
L(0,3)	2	5095.31	0.2002	0.0926	0.0135	1.1250×10^{-4}
L(0,4)	2	5845.90	0.1381	0.0250	0.0068	9.0413×10^{-5}
F(1,1)	2	2912.34	0.0528	0.0241	0.0044	4.7835×10^{-5}
F(1,5)	2	5103.56	0.2021	0.0938	0.0134	1.1138×10^{-4}
F(1,6)	2	5864.83	0.1392	0.0251	0.0069	9.1223×10^{-5}
F(1,7)	2	5403.87	-	-	0.0070	3.7099×10^{-5}
T(0,3)	2	5385.32	-	-	0.0068	3.5097×10^{-5}

function ($p = 3$) is sufficient to obtain a good estimation (with errors of order 10^{-4}) of the phase velocities of L(0,1) and F(1,1) modes. At a high frequency ($f = 2$ MHz), the errors are significant and have orders of 10^{-1} and 10^{-2} when using the quadratic and cubic NURBS basis functions, respectively. Eventually, the higher modes F(1,7) and T(0,3) cannot be identified by filtering the numerical solutions of eigenvectors. Using higher-order NURBS basis functions ($p = 4$ and $p = 6$) clearly allows to obtain much smaller errors for all modes, showing the p-convergence of NURBS-based formulations.

Table 4.2 – Case of a homogeneous hollow cylinder: error analysis of SAIGA and SAFE solutions based on h-refinement with basis function's order p=3

Mode	f (MHz)	$C_{\text{ph}}^{\text{Exact}}$ (m.s^{-1})	$\text{err}^{\text{SAIGA}}$ (N_{dof}=360)	$\text{err}^{\text{SAIGA}}$ (N_{dof}=504)	$\text{err}^{\text{SAIGA}}$ (N_{dof}=1080)	err^{SAFE} (N_{dof}=504)	err^{SAFE} (N_{dof}=1080)
L(0,1)	0.2	2027.64	7.3118×10^{-7}	1.4290×10^{-7}	5.7945×10^{-9}	3.4599×10^{-5}	2.9142×10^{-6}
F(1,1)	0.2	2912.34	8.8493×10^{-6}	1.5434×10^{-6}	4.3057×10^{-8}	1.5836×10^{-4}	1.8420×10^{-5}
L(0,1)	2	2910.29	0.0016	3.5389×10^{-4}	1.5429×10^{-5}	0.0047	9.0892×10^{-4}
L(0,3)	2	5095.31	0.0046	7.6841×10^{-4}	1.5385×10^{-5}	0.0110	0.0025
L(0,4)	2	5845.90	0.0014	2.8549×10^{-4}	5.7720×10^{-6}	0.0043	3.3196×10^{-4}
F(1,1)	2	2912.34	0.0016	3.5434×10^{-4}	1.5451×10^{-5}	0.0047	9.1307×10^{-4}
F(1,5)	2	5103.56	0.0047	7.7035×10^{-4}	1.5441×10^{-5}	0.0100	0.0054
F(1,6)	2	5864.83	0.0014	2.8804×10^{-4}	5.8241×10^{-6}	0.0043	3.4168×10^{-4}
F(1,7)	2	5403.87	0.0078	8.1188×10^{-4}	1.8269×10^{-5}	0.0171	8.0496×10^{-5}
T(0,3)	2	5385.32	0.0078	8.0536×10^{-4}	1.8147×10^{-5}	0.0197	4.2228×10^{-4}

Table 4.2 presents the numerical errors of SAIGA and SAFE solutions obtained when applying the h-refinement. The basis function's order was fixed at $p = 3$ for all cases. Note that when using SAFE with a mesh of $N_{\text{dof}} = 360$, the studied modes could not be identified as the annular geometry cannot

correctly be described by few quadratic elements. As it would be expected, the numerical errors of all modes, computed by SAFE or by SAIGA methods, decrease when N_{dof} increases. At low frequency ($f = 0.2$ MHz), the SAFE results of modes L(0,1) and F(1,1) have good precision when $N_{\text{dof}} = 504$, and the errors significantly decrease when $N_{\text{dof}} = 1080$. The precision of SAIGA solutions is even better: for example, the error of L(0,1) obtained by SAIGA with $N_{\text{dof}} = 360$ is smaller than the one obtained by SAFE with $N_{\text{dof}} = 1080$. At high frequency ($f = 2$ MHz), the h-convergence is achieved much faster when using SAIGA. The errors of SAIGA solution are typically about hundreds of times smaller than the SAFE's ones based on the same N_{dof}. Using SAIGA method with $N_{\text{dof}} = 504$ leads to similar precision than the one computed by using SAFE with $N_{\text{dof}} = 1080$.

In Fig. 4.4, we present the mode shapes of displacements computed for the mode L(0,1) at the frequency of 2 MHz. To be able to compare to the analytical solution which is derived in cylindrical coordinates system, the normalized displacement components U_r (radial), U_θ (circumferential), U_z (longitudinal) along the thickness's direction are determined from the eigenvectors $\mathbf{U}$. The graphs show that the mode shapes obtained by the proposed SAIGA approach are in very good agreement with the exact solutions. It can also be checked that the SAIGA's solutions of circumferential displacement U_θ have vanished over the cylinder's section, which is consistent with our expectation for a longitudinal mode L(0,1). By using the SAFE method with the same numerical parameters ($p = 3$, $N_{\text{dof}} = 1080$), the differences between numerical and exact solutions of mode shapes are visibly much more important. In particular, one may see that the U_θ components estimated by SAFE method are not zeros along the thickness's direction, which does not give a good representation of the axisymmetric feature of the considered mode L(0,1). Though, a good precision of the phase velocity computed by the SAFE method using the same numerical parameters has been achieved (error $= 9.0892\times10^{-4}$, see Tab. 4.2). Note that in this example, in comparison to the SAIGA method, using SAFE method disposes of some disadvantages due not only to the interpolation function but also to the description of the geometry.

To further investigate the efficiency of the proposed SAIGA formulation, we focus on some specific points in the dispersion curves of the phase velocity (C_{ph}). Fig. 4.5(a) depicts the numerical errors of C_{ph} of the mode L(0,1) at $f = 2$ MHz with respect to the total number of DOFs, which are computed by using Lagrange or NURBS basis functions with different orders (p). Conformity to the results presented in Tab. 4.2, it may be checked that the error obtained by employing SAIGA method is much smaller than the one obtained by the conventional SAFE method which has the same p and N_{dof}. Using NURBS-based basis function, even with low order ($p = 2, 3$), is shown to significantly improve the precision of C_{ph}'s numerical results. Moreover, convergence rates of the SAIGA solutions are much faster than SAFE's ones, especially when using high-order basis functions, *i.e* $p = 6$. Fig. 4.5(b) shows the k-refinement (increasing the polynomial order and then inserts knots (or elements)) of NURBS and Lagrange basis function at $N_{\text{dof}} = 1080$ and $N_{\text{dof}} = 1872$. It is shown that by increasing the order of basis function p, which increase the continuity of the NURBS basis function acorss the span, the global slope of the convergence curve of SAIGA's results is higher than SAFE's one.

4.5.2 Dispersion of guided-waves in fluid-filled cylinder

Guided-wave propagation in a steel cylinder filled by water, as shown in Fig. 4.2(b), is considered in this example. The steel cylinder has the same geometry and material properties as the one studied in the previous section. The acoustic properties of water are given by the density $\rho_1^f = 998$ kg.m^{-3} and the sound speed $c_1^f = 1478$ m.s^{-1}. The outer surface of the cylinder is assumed to be free.

Fig. 4.6 depicts illustrations of meshes used for simulations using SAIGA approach. For the

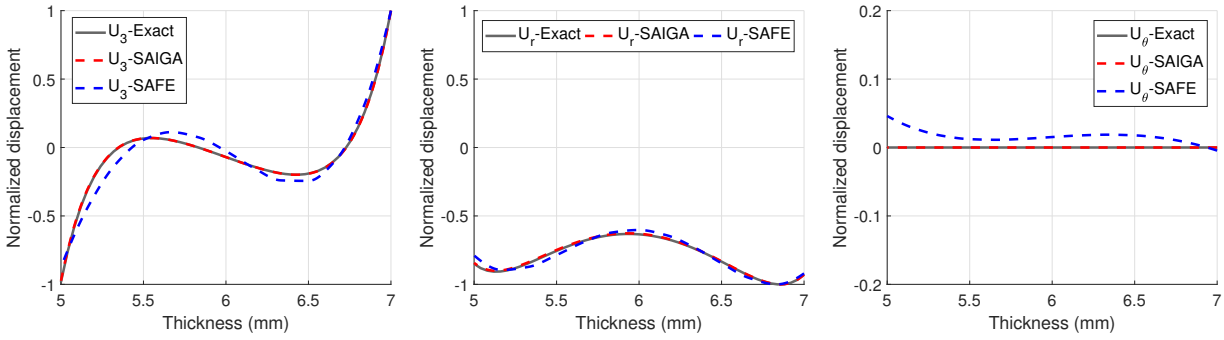

(a) Longitudinal displacement (b) Radial displacement (c) Circumferential displacement

Figure 4.4 – Mode shape of the mode L(0,1) at $f = 2$ MHz of a steel hollow cylinder: comparison between SAIGA solution (red dashed line), SAFE solution (blue dashed line) and analytical solution (grey line); both SAIGA and SAFE solutions are computed with $p = 3$, N_{dof}=1080.

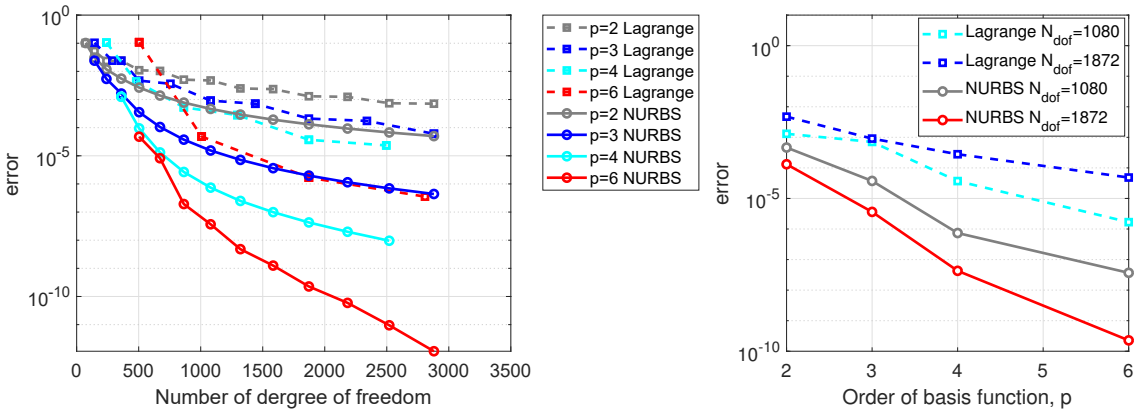

(a) (b)

Figure 4.5 – Case of a homogeneous hollow cylinder: (a) relative error of the phase velocity of the mode L(0,1) at $f = 2$ MHz (b) k-refinement at the N_{dof}=1080 and N_{dof}=1080

geometrical description using IGA, four patches are used for the solid domain and five patches are used for the fluid's one (Figs. 4.6 (a),(b),(c)). It is worth noting that the fluid domain cannot be meshed by using one single patch because it leads to the singularity of the stress due to the collinearity of the control points. For the SAFE modeling, both fluid and solid domains are meshed by using quadrilateral elements.

We first validate the proposed FE formulations for calculating C_{ph}'s dispersion curves. Thanks to the simple cylindrical geometry, the considered fluid-filled hollow cylinder can also be solved by using the semi-analytical method [65] which was implemented in the Disperse software [67]. Note that when analyzing a coupled fluid-solid system, solving the dispersion equation may sometimes have numerical issues due to singularities when establishing transfer matrices. For this example, DISPERSE software starts to have difficulties to compute analytical solutions at frequencies higher than 1 MHz, and consequently, some modes are missed. On the contrary, using the finite element

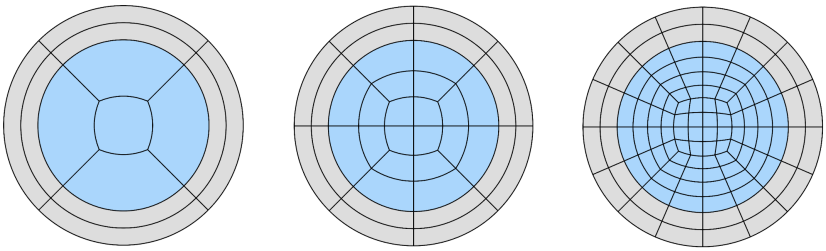

(a) SAIGA (N_{dof}=232) (b) SAIGA (N_{dof}=329) (c) SAIGA (N_{dof}=553)

Figure 4.6 – Mesh discretization of a fluid filled cylinder using NURBS and Lagrange basis functions of order $p = 3$

method, which requires higher computational costs, allows to avoid this kind of difficulty.

In Fig. 4.7, we compare the numerical solutions of C_{ph} obtained by SAIGA or SAFE methods to the analytical ones over the frequency range from 0 to 1 MHz. The discretization is performed by using cubic NURBS or Lagrange basis functions, respectively. The total number of degrees of freedom for both models equals to N_{dof}=1321. A similar filtering procedure as presented in the previous section was applied to extract the modes of interest according to their symmetries. It is shown that the dispersion curves computed by both SAIGA and SAFE methods agree well with the analytical dispersion ones. However, at high frequencies, some of the modes obtained from SAFE solutions couldn't be identified due to imprecise computed shape modes.

To quantify the accuracy SAIGA and SAFE methods in guided wave dispersion analysis, the relative errors of the phase velocity are investigated (Eq. (4.31)) at two frequencies of 0.2 MHz and 2 MHz. Similar to the previous study on the free hollow cylinder, we perform a h-refinement when fixing the basis function to be of order 3. Table 4.3 shows that the SAIGA solutions using $N_{\text{dof}} = 329$

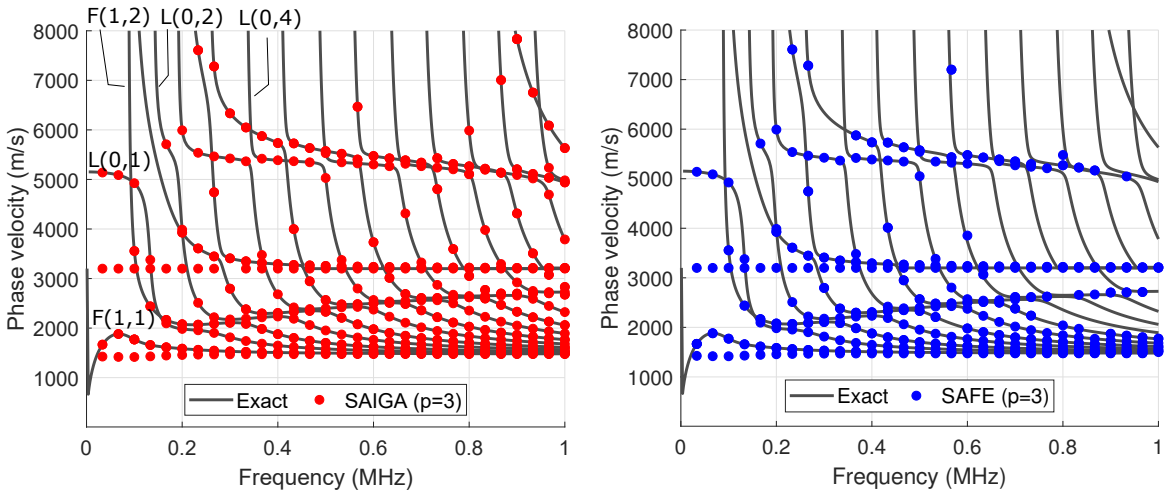

(a) SAIGA $p = 3$, N_{dof}=1321 (b) SAFE $p = 3$, N_{dof}=1321

Figure 4.7 – Dispersion curves of a fluid-filled steel cylinder: comparison between the analytical solution (grey line) and: (a) SAIGA solution (red marker), (b) SAFE solution (blue marker)

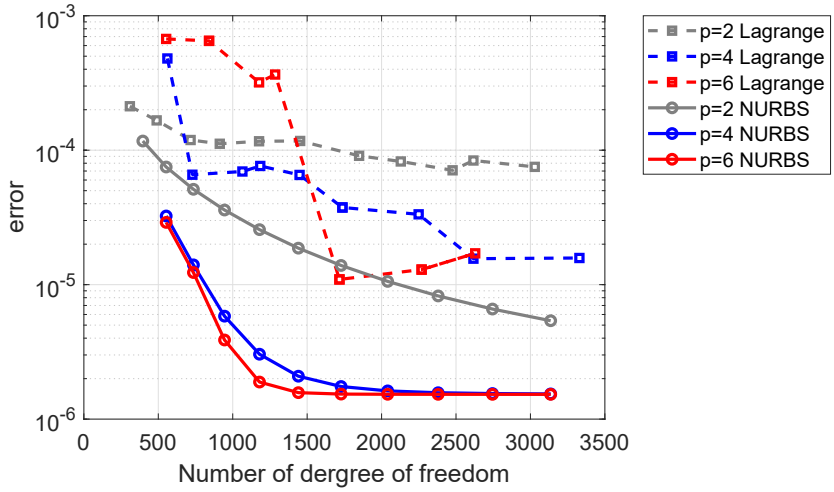

Figure 4.8 – Case of a fluid-filled cylinder: relative error of the phase velocity of the mode L(0,1) at $f = 2$ MHz

or $N_{\text{dof}} = 553$ have negligible errors at both low and high frequencies. On the contrary, by employing the conventional SAFE approach with $N_{\text{dof}} = 616$ or $N_{\text{dof}} = 1321$, which are much bigger than the ones used for SAIGA, the errors have greater values at both low and high frequencies. The results of a convergence analysis of C_{ph} of the mode L(0,1) at $f = 2$ MHz, in which SAFE and SAIGA methods are employed by using different orders of basis functions ($p = 2, 4, 6$), are presented in Fig. 4.8. It is shown that by using the same basis function order p, the global slope of the convergence curve of SAFE's results is much lower than SAIGA's one. Moreover, using higher-order basis functions in SAIGA allows to manifestly reduce the numerical errors. For the SAFE analysis, while the results using $p = 4$ clearly have better convergence than the ones obtained with $p = 2$, the advantage of using $p = 6$ is not clearly found in this example.

Table 4.3 – Case of a fluid-filled cylinder: error analysis based on h-refinement of SAIGA and SAFE ($p = 3$)

Mode	f (MHz)	$C_{\text{ph}}^{\text{Exact}}$ (m.s^{-1})	$\text{err}^{\text{SAIGA}}$ N_{dof}=329	$\text{err}^{\text{SAIGA}}$ N_{dof}=553	err^{SAFE} N_{dof}=616	err^{SAFE} N_{dof}=1321
L(0,1)	0.2	1983.24	6.4898×10^{-6}	6.3073×10^{-6}	5.7993×10^{-5}	2.542×10^{-6}
L(0,1)	2	1584.89	2.7430×10^{-4}	4.484077×10^{-6}	1.6472×10^{-4}	5.2118×10^{-5}
L(0,2)	0.2	3986.96	1.6823×10^{-4}	3.5105×10^{-6}	0.0076	8.8835×10^{-5}
L(0,2)	2	1497.71	1.2490×10^{-4}	1.0421×10^{-4}	0.0042	7.2485×10^{-5}
L(0,4)	2	1567.14	0.00753	5.2335×10^{-4}	-	0.0016
F(1,1)	0.2	1584.89	1.0500×10^{-5}	4.4841×10^{-6}	1.3547×10^{-5}	3.4830×10^{-5}
F(1,1)	2	1478.05	1.9460×10^{-4}	1.9460×10^{-4}	9.1997×10^{-5}	1.2939×10^{-4}
F(1,2)	0.2	2078.20	5.0153×10^{-5}	7.0398×10^{-6}	3.0751×10^{-4}	3.2647×10^{-6}
F(1,2)	2	1488.92	1.0684×10^{-4}	1.0433×10^{-4}	3.1601×10^{-4}	5.7643×10^{-5}

Note that the asymptotic behavior of the errors when the becomes smaller than 10^{-6} is due to inaccurate reference solution, which was calculated using the Disperse software. In fact, although the Disperse's solutions were computed by using an analytical method, the results were exported in a format with limited digits after decimal point.

Fig. 4.9 presents the displacement shapes of the mode (L(0,4)) at high frequency $f = 2$ MHz. As the eigenvectors of the fluid domain derived from (Eq. 4.29) is defined in terms of pressures, the fluid displacements shape modes may be determined using Euler's equation: $\boldsymbol{u}^f = -\frac{1}{\omega^2}\nabla p$. In this figure, the color isolvalue surface represents the radial displacement component U_r of particles in both fluid and solid domains which are expected to be axisymmetric. Moreover, the radial displacements at the solid-fluid interface should theoretically be continuous to verify the interface condition (Eq. 4.4). The SAIGA solution of U_r field, computed with $N_{\text{dof}} = 553$ and has a C_{ph}'s error of 0.052% (see Tab. 4.3), shown to be axisymmetric and continuous in agreeing with mentioned conditions. However, the solution of U_r in the fluid domain computed by SAFE method with $N_{\text{dof}} = 1321$ is unlikely axisymmetric (Fig. 4.9(b)), despite the fact that a correct solution of C_{ph} has been found (Tab. 4.3). Moreover, the fluid's radial displacements, computed by deriving the pressure solutions, do not conform to tho the solid's ones at the solid-fluid interface. The expected axisymmetry and continuity can be found by refining the FE mesh as shown in Fig. 4.9(c), requiring $N_{\text{dof}} = 1696$ which is about three times more than the number of DOFs required by SAIGA method ($N_{\text{dof}} = 553$). Using SAIGA has a greater advantage in this coupled problem thanks to the higher continuity of NURBS basis functions across the elements.

To further investigate the robustness of using SAIGA for mode shape calculation, in Fig. 4.10, we present the results of a higher-order mode (F(2,2)) at $f = 0.5$ MHz, computed by using SAIGA and SAFE approaches with different discretizations as plotted in Figs. 4.6. The isovalue surface represents the radial displacement in the solid or fluid domains. Again, the displacement fields in the fluid domain, which are derived from the pressure eigenvector, can be found to be more smooth when using SAIGA, even with much fewer elements. The mode shape obtained by using SAIGA with $N_{\text{dof}} = 329$ seems to have better quality than the one obtained by using SAFE with $N_{\text{dof}} = 1321$. Figs. 4.11 depicts the variation of the radial displacement components U_r of both fluid and solid phases along the solid-fluid interface. It can be checked that while fluid and solid solutions using SAIGA are perfectly matched from each to other (Fig. 4.11(b)), significant discontinuities are obtained when the SAFE method is used (Fig. 4.11(b)). Note that the errors of the phase velocity evaluated with SAIGA and SAFE methods are 3.297×10^{-5} and 8.867×10^{-5}, respectively.

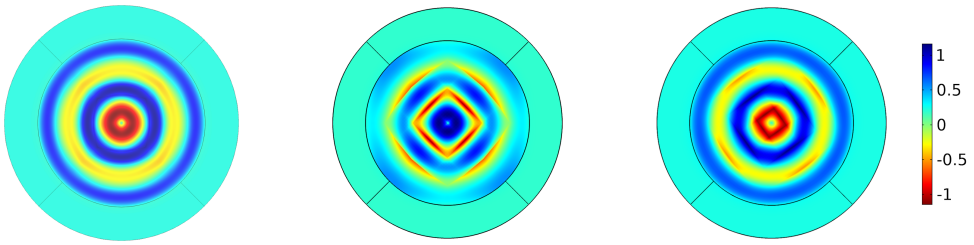

(a) SAIGA, N_{dof}=553 (b) SAFE, N_{dof}=1321 (c) SAFE, N_{dof}=1696

Figure 4.9 – Displacement U_r mode shape for L(0,4) at the frequency f =2 MHz (a) SAIGA with $p = 3$, N_{dof}=553, (b) SAFE with $p = 3$, N_{dof}=1321 and (b) SAFE with $p = 3$, N_{dof}=1696

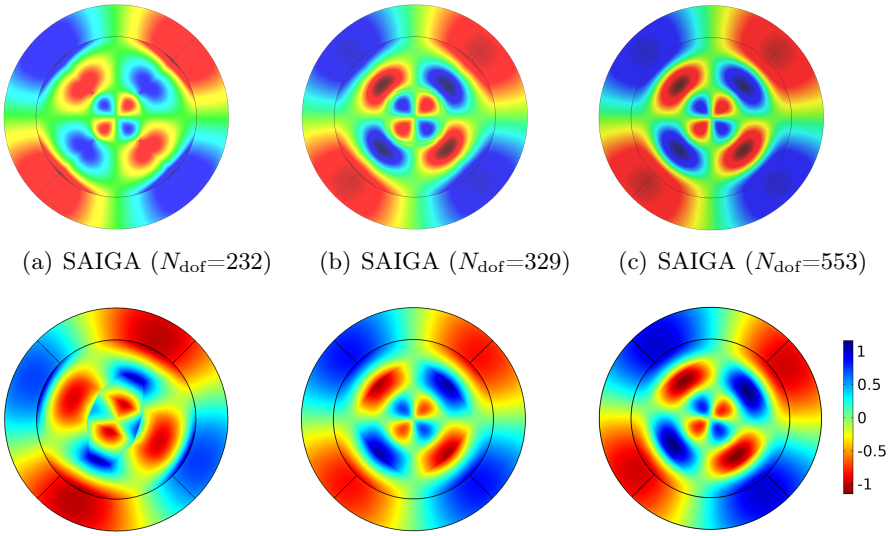

(a) SAIGA (N_{dof}=232) (b) SAIGA (N_{dof}=329) (c) SAIGA (N_{dof}=553)

(d) SAFE (N_{dof}=616) (e) SAFE (N_{dof}=1321) (f) SAFE (N_{dof}=1696)

Figure 4.10 – Displacement mode shape (U_r) of a flexural mode (F(2,2)) at low frequency (f=0.5 MHz) and C_{ph}=2452.5 m/s: (a,b,c) SAIGA with $p = 3$; (d,e,f) SAFE with $p = 3$

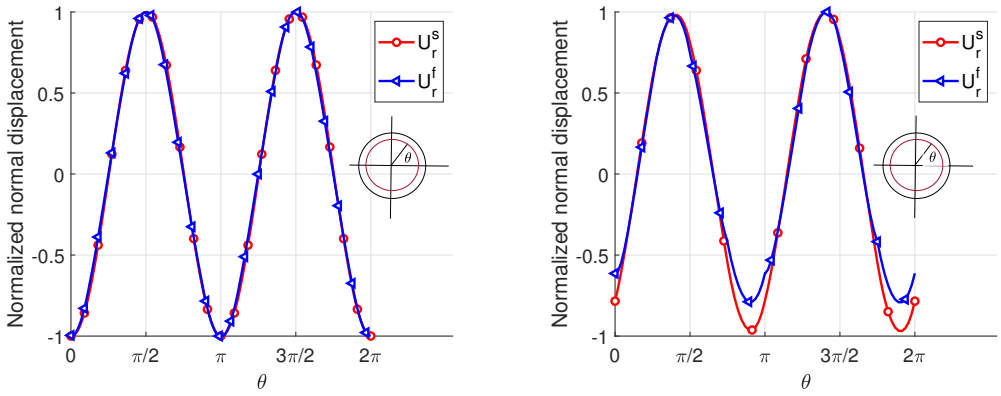

(a) SAIGA ($p = 3$, N_{dof}=553) (b) SAFE ($p = 3$, N_{dof}=616)

Figure 4.11 – Continuity of displacement for the solid-fluid interfaces of flexural mode (F(2,2)) U_r^s (solid domain) and U_r^f (fluid domain) of fluid-filled cylinder (a) SAIGA solution (b) SAFE solution

4.5.3 Dispersion of guided-waves in a hollow cylinder immersed in fluid

Let consider a water-filled steel cylinder immersed in an infinite water domain (Fig. 4.2(c)), which has been considered in [68] to investigate a numerical solution of leaky wave propagation in fluid immersed structures. The material properties of the steel cylinder and of the water are the same as the ones presented in the previous section. The infinite water domain is described by introducing a Perfectly Matched Layer (PML) as described in Section 4.3.1. The PML functions in the simulation are chosen as $\gamma_1 = \gamma_2 = 3 + 12\text{i}$ as given in [41]. The minimum thicknesses of the PMLs can be based on Eq. (4.17), which allows us to choose $h_1^{\text{pml}} = h_2^{\text{pml}} = 3.5$ mm for both PML domains in $\mathbf{e}_1$ and $\mathbf{e}_2$

directions.

We first perform a validation of the proposed FE formulations for calculating the dispersion curves of the phase of the considered fluid-filled and immersed cylinder within the frequency range f=0-1 MHz. In Fig. 4.12, we compare the analytical solutions of the phase velocities over the frequency range from 0 to 1 MHz with the numerical ones obtained by SAIGA and SAFE methods. The discretization is performed by using cubic NURBS basis functions. The total number of degrees of freedom required for the SAIGA and for SAFE equal to N_{dof}=1508 and N_{dof}=1945, respectively. A similar filtering procedure as presented in the previous section has been applied to extract the modes of interest according to their symmetries. It is shown that the dispersion curves obtained from the proposed approach agree well with the analytical dispersion curves.

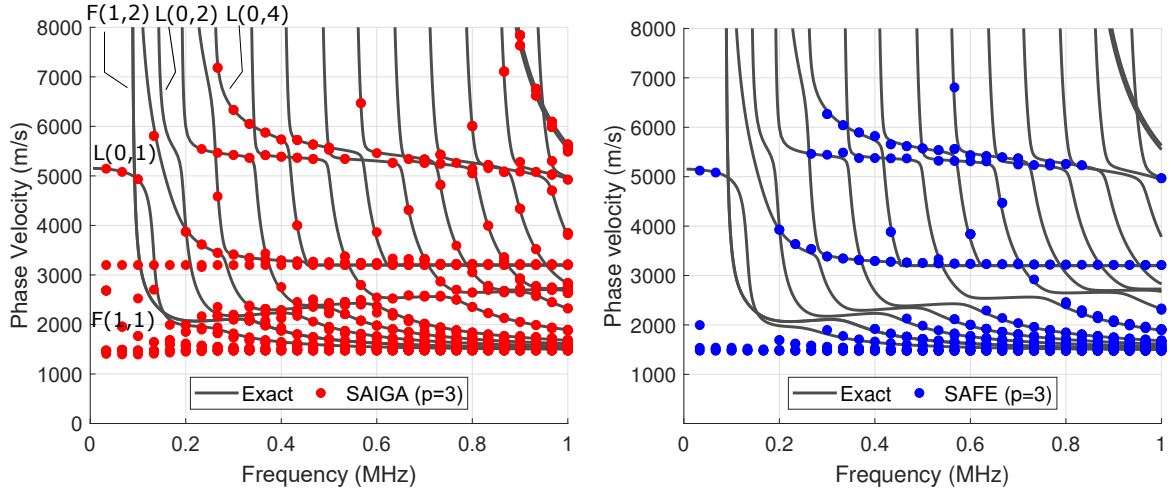

(a) SAIGA ($p = 3$, N_{dof}=1508) (b) SAFE ($p = 3$, N_{dof}=1945)

Figure 4.12 – Dispersion curves of a fluid-filled and immersed steel cylinder: comparison between (a) SAIGA solution (red marker), (b) SAFE solution (blue marker) and analytical solution (grey line).

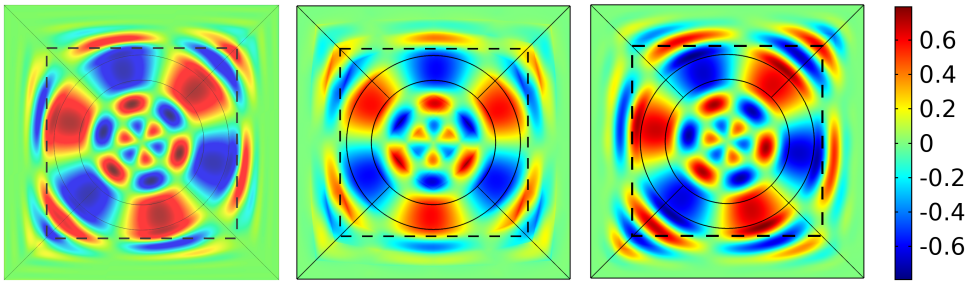

(a) SAIGA (N_{dof}=1508) (b) SAFE (N_{dof}=1945) (c) SAFE (N_{dof}=9001)

Figure 4.13 – Displacement U_r shape for a flexural mode (F(3,3)) at the frequency of f=0.5 MHz and C_{ph}=3791 m/s (a) SAIGA with $p = 3$, N_{dof}=1508 (b) SAFE with $p = 3$, N_{dof}=1945 (b) SAFE with $p = 3$, N_{dof}=9001

Mode shapes in terms of radial displacements are presented in Fig. 4.13. One may observe that

leaky waves are totally damped in a very short distance when they go into the PML. It has been numerically checked with several larger domains (data not shown) that the solutions of interests don't depend on the location of the PMLs, showing the PML could efficiently attenuate leaky waves. As discussed previously, the displacement field in the fluid domains simulated by using the conventional SAFE method may have some discontinuities, as shown *e.g* in Fig. 4.13b ($N_{\text{dof}} = 1945$), due to the smoothness drawback of the Lagrange polynomials. Consequently, the FE mesh should be extensively refined to obtain an accurate calculation of differentiation operators (Fig. 4.13c with $N_{\text{dof}} = 9001$). Using SAIGA approach allows significantly improves the smoothness of fluid's displacement with much fewer elements (Fig. 4.13a with $N_{\text{dof}} = 1508$) thanks to the higher continuity of NURBS basis functions across the elements. Moreover, the conventional SAFE approach suffers from a non-smoothness profile across the PML interfaces, which leads to imperfect absorption of the leaky modes. Using NURBS leads to better continuity of solid and fluid normal displacements at the interface, and consequently, it would be preferable to use higher-order NURBS basis functions for modeling leaky wave in fluid-solid coupled systems.

4.5.4 Anisotropic waveguide with arbitrary cross-section coupling with fluids

As a final example, we demonstrate the merits of using SAIGA in the analysis of guided wave propagation in a more complex geometry structure. Let us consider a waveguide representing a long cortical bone with real cross-section, which has been reported by many authors using the conventional SAFE method in the literature [60, 61]. The domain of interests consists of one transversely isotropic elastic solid sandwiched between two homogeneous fluid domains, which represents the cortical bone, the marrow (inner fluid) and the soft tissue (outer fluid), respectively. The cortical has a mean thickness of 7 mm. The inner fluid (bone marrow) has approximately 15 mm-diameter and the outer fluid (soft tissue) has a thickness of 3 mm (Fig. 4.2(d)) [96]. The mass density of the cortical bone is given by $\rho = 1722$ kg.m^{-3}. The non-zero entries of the elasticity tensor taken by: $C_{11} = C_{22} = 15.1$ GPa, $C_{13} = C_{23} = 8.7$ GPa, $C_{33} = 23.5$ GPa, $C_{44} = C_{55} = 4.7$ GPa and $C_{66} = 3.3$ GPa [59]. The bone marrow and soft tissue were modeled as homogeneous idealized acoustic fluids. The bone marrow is characterized with the density $\rho_1^f = 930$ kg.m^{-3} and sound speed $c_1^f = 1480$ m.s^{-1}, while the characteristics of soft tissue are given by the density $\rho_2^f = 1043$ kg.m^{-3} and sound speed $c_2^f = 1561$ m.s^{-1} [60].

The geometry is built from 13 patches including four patches for the outer fluid domain, four patches for the bone's section and five patches for the inner fluid domain. Thus, we have several interfaces with C^0-continuity between the patches and C^{p-k}-continuity between the elements within the patches, which is a useful feature in the majority of practical applications. The NURBS geometries and positions of control points for these three domain are depicted in Figs. 4.14(a,b,c).

As the analytical solution doesn't exist for this coupled system, the validation of SAIGA method was performed by comparing to SAFE solution. Figs. 4.15 depicts the fine FE mesh of cubic Lagrangian elements ($N_{\text{dof}} = 12929$) used to obtain a "reference" solution. We also present Figs. 4.15a and 4.15b two NURBS-based meshes which are built with cubic ans eight-order NURBS basis functions, respectively. Note that the numbers of DoFs associated to these meshes are nearly equals, which are $N_{\text{dof}} = 2683$ and $N_{\text{dof}} = 2689$, respectively. As NURBS allows represent exact curvature of this geometry, the SAIGA meshes shown in Fig. 4.15b,c require less number of elements and are much more regular than the FE mesh with triangular elements (Fig. 4.15a) which requires fine refinement at high curvature zones. When using $p = 8$, only one element is needed for each patch.

Fig. 4.16 presents the dispersion curves of phase velocity in the frequency range 0-100 kHz, computed by using SAFE and SAIGA methods. The SAIGA solutions were computed with $p = 3$, $p = 6$,

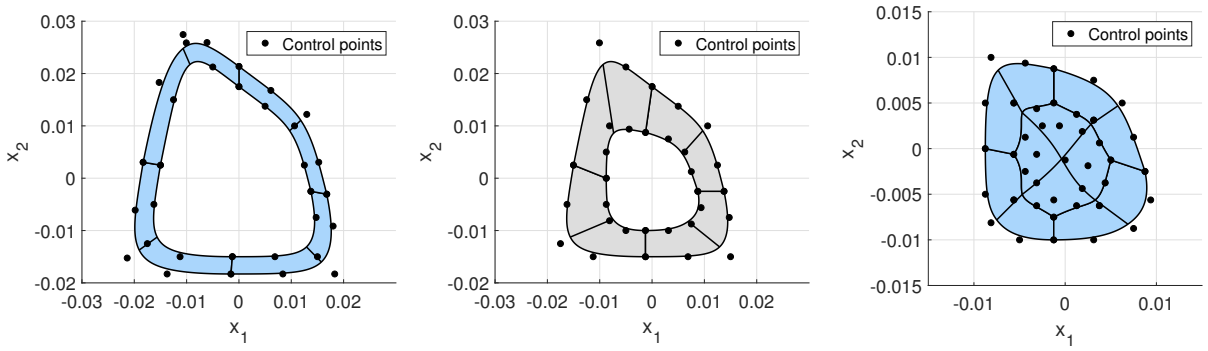

(a) Outer fluid (b) Solid bone (c) Inner fluid

Figure 4.14 – Geometry illustration and position of control points created from NURBS of p=3 for (a) outer soft tissue (b) core of cortical bone and (c) inner bone marrow.

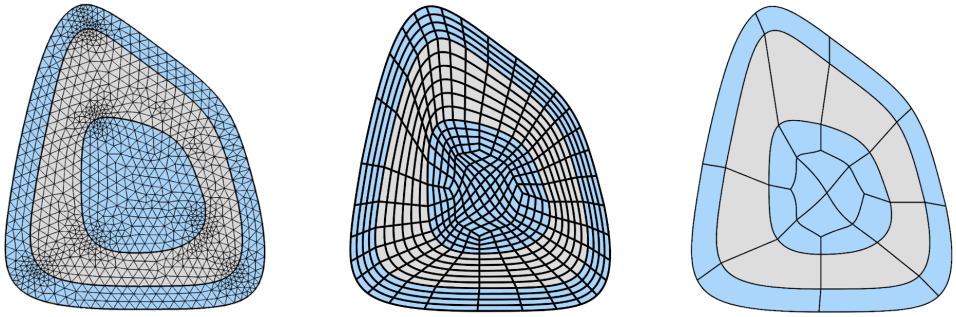

(a) SAFE ($p = 3$, N_{dof}=12929) (b) SAIGA ($p = 3$, N_{dof}=2683) (c) SAIGA ($p = 8$, N_{dof}=2689)

Figure 4.15 – Meshes of a bone's section coupled with marrow and soft tissue

$p = 8$ and $p = 10$. Similar to the examples previously presented, using SAIGA with all orders $p = 3, 6, 8, 10$ allows to capture very well the reference solution at low frequencies. Figs. 4.17(a,b,c) depict the mode shape in terms of the radial displacement computed by using SAIGA method with ($p = 3$ or $p = 8$) or using SAFE method ($p = 3$) with very fine discretization. The presented mode is found at $f = 50$ kHz and C_{ph}=1160 m/s. It may be observed that SAIGA results of the considered mode shape, which are computed by using $p = 3$ and $p = 8$ and have almost the same N_{dof}, have both good agreements with the reference solution.

The calculation of higher-order modes at high frequency requires more refinement. Hence, we focus to examine the solutions of the phase velocity in a zoomed window as shown in Fig. 4.16. It is clearly seen that the difference between SAIGA solution with $p = 3$ and the reference ones are significant. The solutions with $p = 6$ are better, yet they still do not match well with the reference values at some locations. The solutions obtained with $p = 8$ and $p = 10$ are perfectly in agreement with reference ones, showing that the convergence is archived. Note that while the N_{dof} of the cases $p = 3, 6, 8$ are quite similar (about 2600 dofs), using $p = 10$ requires a greater value of N_{dof} ($N_{\text{dof}} = 4249$). Therefore, employing NURBS with $p = 8$, for which only one element per patch is needed, would be the best choice for this example for calculating the phase velocities.

In Fig. 4.18, we investigated the continuity of solid and fluid displacements at the interfaces of

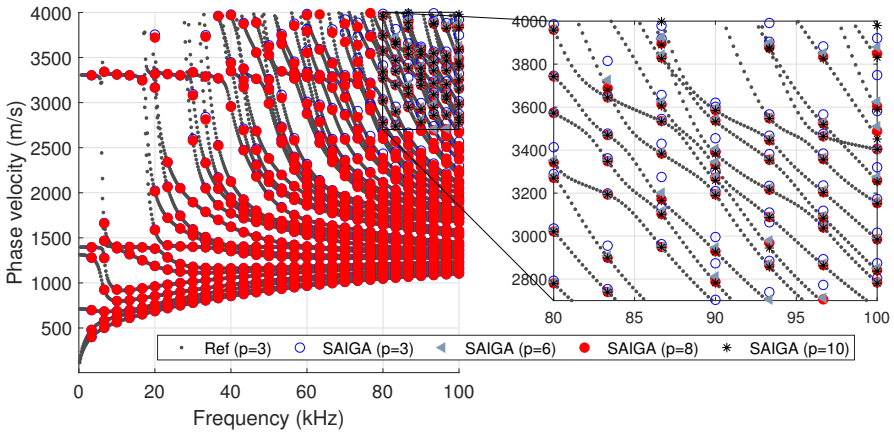

Figure 4.16 – Phase velocity versus frequency in a coupled soft tissue-cortical bone system: comparison between the reference SAFE solution (grey marker, $p = 3$, $N_{dof} = 12929$) and SAIGA solutions (blue marker: $p = 3$, N_{dof}=2689; grey marker: p=6, N_{dof}=2683; grey marker: $p = 6$, N_{dof}=2689; black marker: $p = 10$, N_{dof}=4249)

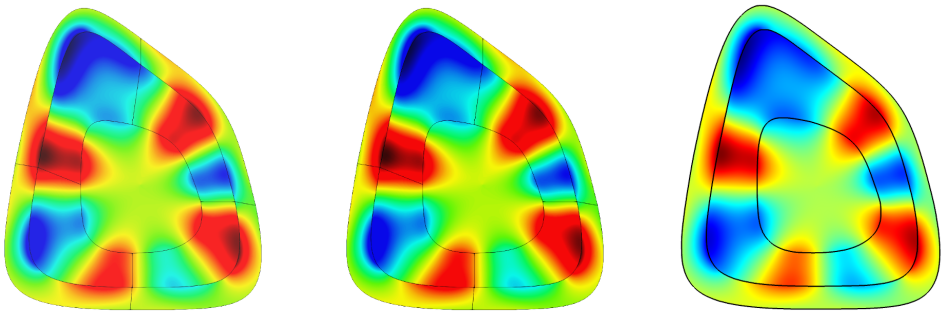

(a) SAIGA ($p = 3$, N_{dof}=2683) (b) SAIGA ($p = 8$, N_{dof}=2689) (c) SAFE ($p = 3$, N_{dof}=12929)

Figure 4.17 – Displacement U_r of flexural mode at the $f = 50$ kHz and C_{ph}=1160 m/s for cortical bone coupled with bone marrow and soft tissue (a) SAIGA with $p = 3$, N_{dof}=2683, (b) SAIGA with $p = 8$, N_{dof}=2689 and (c) SAFE with $p = 3$, N_{dof}=12929.

a mode at $f = 100$ kHz. To do so, the solid and fluid displacement components, which are normal to the fluid-solid interfaces, are compared. It is worth noting that the SAFE's mesh used for the simulation has a similar N_{dof} to the SAIGA's one, in which each patch is modeled by only one eight-order NURBS element. It was shown that while fluid-solid displacement's continuity condition may be precisely satisfied by using SAIGA's results, SAFE's solution suffers significant errors at both interior and exterior interfaces. Furthermore, the errors of the fluid's displacement seemed to be more significant than the solid's ones. This would be due to the numerical errors of the fluid pressure's gradient estimation. This comparison confirms again the advantage of using NURBS for studying the mode shapes in coupled fluid-solid system.

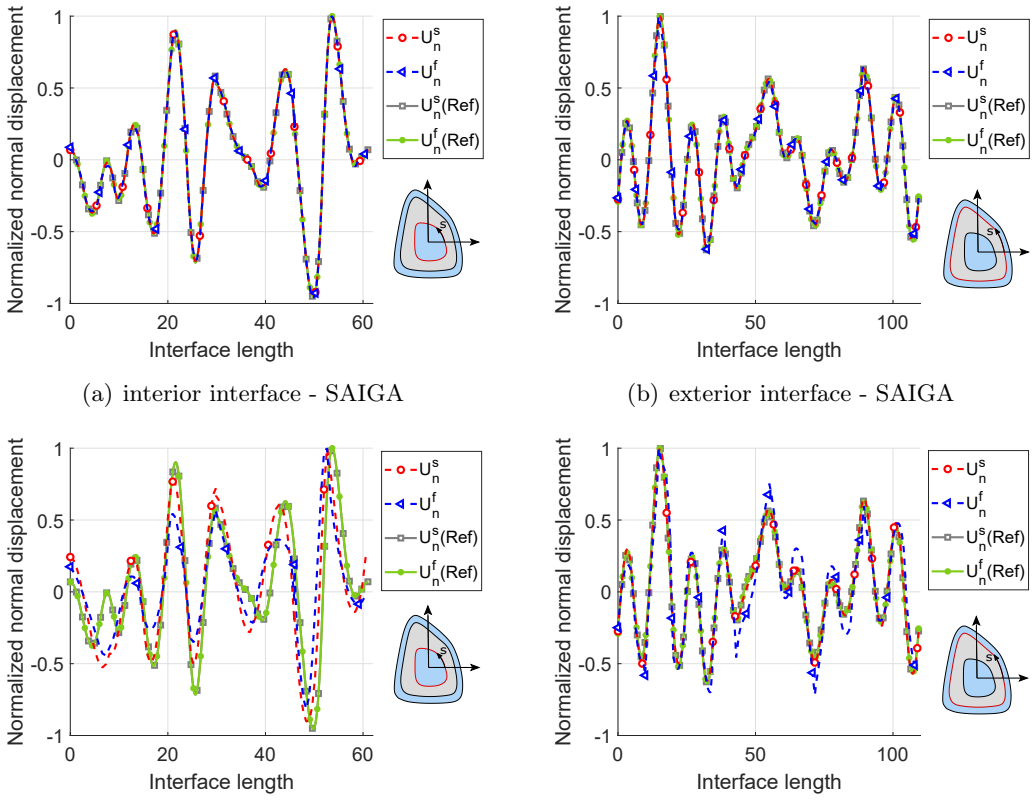

(a) interior interface - SAIGA

(b) exterior interface - SAIGA

(c) interior interface - SAFE

(d) exterior interface - SAFE

Figure 4.18 – Continuity of displacement for the solid-fluid interfaces of a flexural mode at the $f = 100$ kHz and C_{ph}=3980 m/s : U_n^s (solid domain) and U_n^f (fluid domain) of cortical bone (a,b) SAIGA solution ($p = 8$, N_{dof}=2689); (c,d) SAFE solution ($p = 3$, N_{dof}=2675)

4.6 Conclusion

In this chapter, a semi-analytical isogeometric analysis (SAIGA) for the anisotropic elastic waveguides coupled with fluid was proposed to improve the efficiency of guided wave modeling in comparison with the conventional SAFE method. The convergence analysis for isotropic homogeneous hollow cylinder and fluid-filled cylinder showed that increasing the order of NURBS basis function yields a much faster convergence rate in comparison with a similar process using Lagrange polynomials. When considering elastic waveguides coupled with fluids, using NURBS basis functions can significantly improve the evaluation of not only dispersed wavenumbers but also mode shapes. In particular, using SAIGA allows to obtain excellent continuity at the solid-fluid interface, which is much more difficult to achieve when using conventional SAFE. Moreover, it has been shown that waveguides immersed in an infinite fluid may efficiently be modeled by introducing perfectly matched layers (PML) and then employing SAIGA procedure.

In terms of computational time, our numerical experiences showed that using SAIGA allows to reduce significantly the computational time to archive a similar precision. It was also observed that using the same number of DOFs, SAFE and SAIGA required similar computational times. However, a rigorous comparison of computational times requires that both methods should be implemented in

a same environment. Note that in this work, while the SAFE simulation was performed in Comsol Multiphysics, the SAIGA method was implemented in an in-house Matlab code.

For wave propagation simulation using FEM, it is well-known that the discretization needs to ensure a number of elements which is sufficient not only for simulating interested wavelengths, but also for correctly describing the curved boundaries. The advantage of SAIGA in this context, besides its better continuity feature as mentioned before, is that using NURBS allows representing exact curvature, hence it does not require as much number of elements as the one required by the conventional SAFE method for describing the curved interface between fluid and solid domains. The proposed SAIGA procedure was shown to be particularly interesting for studying arbitrary cross-section waveguides in terms of computational cost as well as of accuracy.

Extensions of the proposed SAIGA formulation may be developed for studying guided-wave propagation in poroelastic [48], for which the high-order continuity of NURBS would be interesting to improve the simulation efficiency. In the next chapter we investigate the higher order finite element methods such as spectral finite element and SAIGA methods to evaluate the reflection and transmission of guided waves in poroelastic waveguides.

Chapter 5

Wave reflection and transmission from functionally-graded poroelastic plates

5.1 Introduction

This chapter [1] aims to develop a SAFE formulation for computing the reflection/transmission coefficients of poroelastic plates immersed in fluids. Modeling of wave propagation in porous waveguides has received much of attention in the past. This attention is motivated by characterization and optimization problems of different materials such as sound absorbing materials, industrial foams, biological materials (such as bone or wood), concrete, sandstone etc. In many applications, the macroscopic material properties of the studied waveguide are relatively homogeneous along its longitudinal direction but heterogeneous (with functionally graded or layered profiles) in the cross-section plan. Different methods have been used to study the wave propagation problem in functionally-graded/layered waveguides. The numerical method allows to analyse the dynamic behaviour of these porous waveguides not only in the time domain but also in the frequency domain, *e.g.*the wave dispersion and reflection/transmission coefficients.

For multilayered systems, the Transfer Matrix Method, also known as Thomson-Haskell method, is often used (see *e.g.*[97, 98]). By using this method, the wave fields in each horizontal homogeneous layer are analytically decomposed into downward and upward wave components. The wave propagation problem in the layered medium is then performed through the interface operators which are derived from boundary conditions at the upper and lower interfaces of the layers. Using of the interface operators are also convenient for considering multiphysics systems such as coupled acoustic/elastic/poroelastic media. When the material properties are not piecewise-constant as in layered media but continuously vary, the asymptotic formulation using Peano's series has been developed [99, 100]. Although the method is not only rigourous because analytically derived but also very fast, it has been shown that numerical instabilities may occur due to positive exponential terms for the cases of large layer thickness (in comparing with wavelengths in the medium), requiring some particular techniques [101, 102].

Recently, the SAFE method has also been employed in the context of wave propagation in porous waveguide. Liu *et al.* [103] used this method to obtain the dispersion relations of a multilayer panel

[1] The work presented in this chapter is submitted for a publication.

which consists of an isotropic poroelastic core sandwiched between two elastic layers. Nguyen *et al.* [48] has developed a SAFE formulation for computing the time-domain wave propagation in an anisotropic poroelastic plate immersed in fluids. It has been shown that using SAFE method allows us to gain some significant advantageous on computational costs such as memory requirement or computational time, especially for simulation in high frequency range. Moreover, as the problem was first formulated in frequency domain, the memory effect can be straightforwardly taken into account.

The main objective of this study is to develop a SAFE formulation which is relevant for computing the reflection/transmission coefficients of poroelastic plates immersed in fluids. Note that the minima (or maxima) of reflection (or transmission) coefficients are directly correlated to dispersion curves. This procedure involves constructing an appropriate functional in an optimization process of material properties *via* iteratively minimizing the squares of the differences between the theoretically and experimentally generated dispersion curves. In this framework, the accuracy of the evaluation of these coefficients is a key point. By using SAFE method, both functionally-graded and multilayered anisotropic poroelastic plate may be treated by the same manner. Furthermore, it allows us to easily consider coupling between poroelastic material with fluid or elastic ones. In particular, we aims to investigate the effectiveness of high-order finite element approximation for computing of reflection/transmission coefficients at high frequency ranges of poroelastic plates with arbitrary porosity. To do so, we investigated two different methods for approximating the displacement fields. First, we employed the spectral element technique in which the nodes are located at Gauss-Lobatto-Legendre (GLL) points. Second, the isogeometric approximation basing on Non-uniform rational basis splines (NURBS) was used.

The chapter is organized as follows. After this introduction, Section 5.2 reviews the governing equations for modeling a poroelastic plate immersed in fluids under excitation of an incident plane wave. The Biot theory is used to model the anisotropic poroelastic material. Next, in Section 5.3, we provide formulations for analytically estimating the reflection/transmission coefficients of an homogeneous poroelastic plate. Section 5.4 presents the finite element formulations with two kinds of shape functions to solve the considered problem. The validation of developed formulations and numerical examples are presented in Section 5.5. Finally, Section 5.6 sets out some conclusions.

5.2 Governing equations

5.2.1 Problem description

Let $\mathbf{R}(\mathrm{O}; \mathbf{e}_1, \mathbf{e}_2)$ be the reference Cartesian frame where O is the origin and $(\mathbf{e}_1, \mathbf{e}_2)$ is the orthonormal basis for the bi-dimensional space. The coordinates of a point M in $\mathbf{R}$ are denoted by (x_1, x_2), the associated position vector is denoted by $\boldsymbol{x}$ and the time is denoted by t. Figure 5.1 presents a two-dimensional geometrical description of the considered problem for which both the incident wave and the mechanical system are assumed to be invariant with respect to the Cartesian coordinate x_3. A poroelastic layer with constant thickness h, which occupies the unbounded domain Ω^b in $\mathbf{e}_1$-axis, is surrounded by two fluid half-spaces Ω_1^f and Ω_2^f. The interfaces between the poroelastic layer Ω^b and the fluid domains Ω_1^f and Ω_2^f are assumed to be flat and denoted by Γ_1^{bf} and Γ_2^{bf}, respectively, as shown in Fig. 5.1.

The surrounding fluids in the domains Ω_1^f and Ω_2^f are assumed to be homogeneous and inviscid. The layer Ω^b is assumed to be a fluid-saturated transversely isotropic poroelastic medium. We also assume that the material properties of the porous layer is homogeneous along its longitudinal direction, given by $\mathbf{e}_1$-axis, but may be inhomogeneous in its depth direction, given by $\mathbf{e}_2$-axis. Despite the

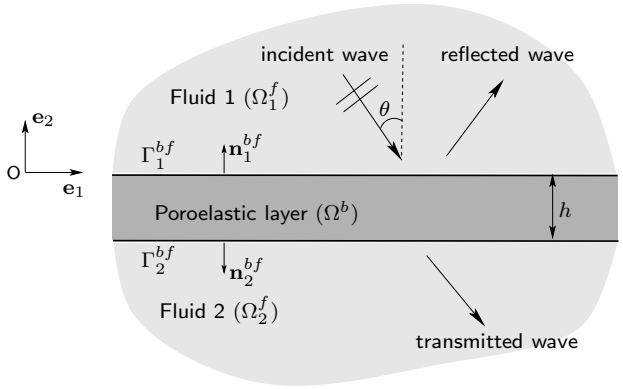

Figure 5.1 – Geometry description

fluid viscosity is neglected in the surrounding fluid domains, it is taken into account in the porous plate pores. A plane and harmonic wave with an angular frequency ω, propagating in the upper fluid domain, is incident under angle θ_I to the interface Γ_1^{bf}. To determine the reflection and transmission coefficients of the poroelastic layer, we assume a time-dependence $\exp(-\mathrm{i}\omega t)$ (where $\mathrm{i} = \sqrt{-1}$) for all movement quantities $Y(\boldsymbol{x}, t)$, *i.e.*$Y(\boldsymbol{x}, t) = y(\boldsymbol{x}, \omega)\exp(-\mathrm{i}\omega t)$.

In what follows, the term ω in $y(\boldsymbol{x}, \omega)$ will be omitted for simplification purposes. Moreover, the summation convention over repeated indices is used and the subscript indices after comma stand for the partial derivatives with respect to the space.

5.2.2 Wave propagation in the fluids of domains Ω_1^f and Ω_2^f

The mass densities of fluids in domains Ω_1^f and Ω_2^f are respectively denoted by ρ_1 and ρ_2. The wave celerity of the fluids are respectively denoted by c_1 and c_2. The Helmholtz and Euler equations describing the fluid motion in these domains read:

$$-\frac{\omega^2}{c_n^2}p^{(n)} - p^{(n)}_{,jj} = 0, \tag{5.1}$$

$$-\omega^2 u_j^{(n)} + \frac{1}{\rho_n}\, p^{(n)}_{,j} = 0, \tag{5.2}$$

where $p^{(n)}$ and $u_j^{(n)}$ denote respectively the pressure and components of displacement vector of the fluid in Ω_n^f $(n = 1, 2)$.

Let us consider an incident plane and harmonic wave p_I propagating with an angular frequency ω in the upper fluid domain Ω_1^f and arriving to the interface Γ_1^{bf} from an angle θ_I (see Fig. 5.1). The wavenumber vector of the field p_I may be expressed by $\boldsymbol{k}_I = k_0 \boldsymbol{n}_I$ where $k_0 = \omega/c_1$ is the wavenumber and $\boldsymbol{n}_I = (\sin\theta_I, -\cos\theta_I)^T$ is the propagation's direction. In the domain Ω_1^f, the pressure field p_I should satisfy the relation (5.1) and thus has the form given by:

$$p_I = P_I \exp(\mathrm{i}(k_1 x_1 - k_2^{(1)} x_2)), \tag{5.3}$$

where P_I denotes the wave amplitude, k_1 and $-k_2^{(1)}$ are the projections of the wavenumber vector $\boldsymbol{k}_I$ on $\mathbf{e}_1$-axis and $\mathbf{e}_2$-axis, respectively, and are given by $k_1 = k_0 \sin\theta_I$ and $k_2^{(1)} = k_0 \cos\theta_I$. Under the

excitation of p_I, the total pressure field in Ω_1^f may be expressed as a superposition of the incident and reflected wave fields:

$$p^{(1)} = p_I + p_R, \tag{5.4}$$

where p_R is the reflected wave field which may be shown to have the form:

$$p_R = P_R \exp(\mathrm{i}(k_1 x_1 + k_2^{(1)} x_2)), \tag{5.5}$$

where P_R denotes the reflected wave amplitude. Similarly, the solution of the transmitted wave field in the domain Ω_2^f reads:

$$p^{(2)} = P_T \exp(\mathrm{i}(k_1 x_1 - k_2^{(2)}(x_2 + h))), \tag{5.6}$$

where P_T denotes the amplitude of the transmitted wave and $-k_2^{(2)}$ is the projection of the wavenumber vector $\boldsymbol{k}^{(2)}$ on $\mathbf{e}_2$-axis:

$$k_2^{(2)} = \sqrt{\frac{\omega^2}{c_2^2} - k_1^2}. \tag{5.7}$$

5.2.3 Wave propagation in the anisotropic poroelastic layer Ω^b

Neglecting the body forces (other than inertia), the equations describing the wave propagation in the anisotropic poroelastic layer in the frequency domain read:

$$\sigma_{jk,k} = -\omega^2 \rho\, u_j - \omega^2 \rho_f\, w_j\,, \tag{5.8}$$

$$-p_{,j} = -\omega^2 \rho_f\, u_j - \omega^2 \tilde{a}_{jk} w_k\,, \tag{5.9}$$

where $\rho = \phi\,\rho_f + (1-\phi)\,\rho_s$ is the mass density of the poroelastic layer where ρ_s and ρ_f are the solid skeleton and fluid mass densities, respectively; $\tilde{a}_{ij}$ are the components of a frequency dependent viscodynamic tensor which depend on the permeability and tortuosity of the medium. For a transversely isotropic poroelastic material, $\tilde{\boldsymbol{a}}$ is a diagonal tensor in which $\tilde{a}_{jj},\ j = 1, 2$, is the dynamic tortuosity in $\mathbf{e}_1$- and $\mathbf{e}_2$-axis and is estimated *via* the relation:

$$\tilde{a}_{jj}(\omega) = \frac{\rho_f}{\phi}\left(a_j^\infty + \frac{\mathrm{i}\phi\eta F_j(\omega)}{\omega \rho_f \kappa_{jj}}\right) \tag{5.10}$$

where a_j^∞ is the static tortuosity, η is the dynamic viscosity of the interstitial fluid, κ_{jj} is the intrinsic permeability in $\mathbf{e}_j$-axis; $F_j(\omega)$ is the correction factor which are introduced to take into account the viscous resistance of the fluid flow at high frequencies. We recall that all mechanical characteristics above are x_2-dependent functions. The constitutive equations for an anisotropic poroelastic material are given by:

$$\sigma_{jk} = C_{jklm}\epsilon_{lm} - \alpha_{jk}\, p\,, \tag{5.11}$$

$$-\frac{1}{M}\, p = w_{j,j} + \alpha_{jk}\epsilon_{jk}\,, \tag{5.12}$$

where σ_{jk} denote the components of the total stress tensor; ϵ_{jk} denote the components of the strain tensor given by the relation $\epsilon_{jk} = \frac{1}{2}(u_{j,k} + u_{k,j})$ where u_j are components of the solid skeleton's displacement vector; w_j are the fluid/solid relative displacement components weighted by the porosity given by $w_j = \phi(u_j - u_j^f)$ where u_j^f denote the fluid displacement components and ϕ denotes the porosity; C_{jklm} are the components of the elasticity fourth-order tensor of the drained skeleton; α_{jk} are the Biot effective coefficients and M is the Biot's modulus.

For the subsequent mathematical development, we rewrite the equations below in a matrix form. Let us then use the Voigt's notation which expresses the symmetric second-order tensors as vectors, so the stress is denoted by $\boldsymbol{s} = (\sigma_{11}, \sigma_{22}, \sigma_{12})^T$, the strain by $\boldsymbol{e} = (\epsilon_{11}, \epsilon_{22}, 2\epsilon_{12})^T$, the Biot effective coefficients by $\check{\boldsymbol{\alpha}} = (\alpha_{11}, \alpha_{22}, \alpha_{12})^T$ where the superscript $(\star)^T$ designates the transpose operator. We also introduce an operator $\mathbf{L}$ which takes the form:

$$\mathbf{L} = \mathbf{L}_1\partial_1 + \mathbf{L}_2\partial_2, \text{ with } \mathbf{L}_1 = \begin{bmatrix} 1 & 0 \\ 0 & 0 \\ 0 & 1 \end{bmatrix}, \ \mathbf{L}_2 = \begin{bmatrix} 0 & 0 \\ 0 & 1 \\ 1 & 0 \end{bmatrix}, \tag{5.13}$$

where ∂_1 and ∂_2 denote the partial derivatives with respect to x_1 and x_2, respectively.

Using these notations, the equations of linear momentum (5.8)-(5.9) may be rewritten as:

$$-\omega^2\rho\ \boldsymbol{u} - \omega^2\rho_f\boldsymbol{w} - \mathbf{L}^T\boldsymbol{s} = \mathbf{0}, \tag{5.14}$$

$$-\omega^2\rho_f\boldsymbol{u} - \omega^2\tilde{\boldsymbol{a}}\ \boldsymbol{w} + \mathbf{L}^T\boldsymbol{m}\,p = \mathbf{0}, \tag{5.15}$$

where $\boldsymbol{m} = (1, 1, 0)^T$. The constitutive equations (5.11)-(5.12) read:

$$\boldsymbol{s} = \mathbf{C}\ \boldsymbol{e} - \check{\boldsymbol{\alpha}}\ p, \tag{5.16}$$

$$p = -M\left(\boldsymbol{m}^T\,\mathbf{L}\,\boldsymbol{w} + \check{\boldsymbol{\alpha}}^T\mathbf{L}\boldsymbol{u}\right), \tag{5.17}$$

where $\mathbf{C}$ is the 3-by-3 matrix of the drained elastic tensor written in the Voigt's notation. By noting that $\boldsymbol{e} = \mathbf{L}\boldsymbol{u}$ and by substituting (5.17) into (5.16), the constitutive equations (5.16)-(5.17) may be written as:

$$\boldsymbol{s} = \mathbf{C}_u\mathbf{L}\boldsymbol{u} + \mathbf{C}_\alpha\mathbf{L}\boldsymbol{w}, \tag{5.18}$$

$$\boldsymbol{m}p = -\left(\mathbf{C}_M\mathbf{L}\boldsymbol{w} + \mathbf{C}_\alpha^T\mathbf{L}\boldsymbol{u}\right), \tag{5.19}$$

where the quantities $\mathbf{C}_u, \mathbf{C}_\alpha$ and $\mathbf{C}_M$ are defined as:

$$\mathbf{C}_u = \mathbf{C} + M\,\check{\boldsymbol{\alpha}}\,\check{\boldsymbol{\alpha}}^T, \mathbf{C}_\alpha = M\,\check{\boldsymbol{\alpha}}\,\boldsymbol{m}^T,\ \mathbf{C}_M = M\,\boldsymbol{m}\,\boldsymbol{m}^T. \tag{5.20}$$

The matrix $\mathbf{C}_u$ is known as the undrained elasticity which represents the rigidity of an equivalent elastic medium in which the relative movement between the interstitial fluid and solid skeleton is vanished (*i.e.* when $\boldsymbol{w} = \mathbf{0}$). Note that while $\mathbf{C}_u$ and $\mathbf{C}_M$ are symmetric, $\mathbf{C}_\alpha$ is not. The unsymmetric form of $\mathbf{C}_\alpha$ is due to the anisotropy of poroelastic medium.

For an isotropic poroelastic medium, the Biot effective tensor $\check{\boldsymbol{\alpha}}$ may be represented by a spherical tensor which is defined by only one scalar $\check{\boldsymbol{\alpha}} = \alpha\,\boldsymbol{m}$ and all of the matrices are symmetric:

$$\mathbf{C}_M = M\,\boldsymbol{m}\,\boldsymbol{m}^T,\ \mathbf{C}_\alpha = \alpha\,\mathbf{C}_M,\ \mathbf{C}_u = \mathbf{C} + \alpha^2\,\mathbf{C}_M. \tag{5.21}$$

By considering the plane wave nature of presented problem, the solutions of (5.14) and (5.15) may be taken under the harmonic form: $y(x_1, x_2) = \hat{y}(k_1, x_2)\,\exp(\mathrm{i}k_1x_1)$. Noting that the operator $\mathbf{L}$ now becomes $\mathbf{L} = \mathrm{i}k_1\mathbf{L}_1 + \partial_2\mathbf{L}_2$, one has:

$$-\omega^2\mathbb{A}_1\mathbb{v} + k_1^2\mathbb{A}_2\mathbb{v} - \mathrm{i}k_1\mathbb{A}_3\partial_2\mathbb{v} - \partial_2\mathbb{t} = \mathbf{0}, \tag{5.22}$$

where

$$\mathbb{v} = \begin{pmatrix} \hat{\boldsymbol{u}} \\ \hat{\boldsymbol{w}} \end{pmatrix},\ \mathbb{t} = \begin{pmatrix} \mathbf{L}_2^T\hat{\boldsymbol{s}} \\ -\mathbf{L}_2^T\boldsymbol{m}\hat{p} \end{pmatrix} = ik_1\mathbb{A}_3^T\mathbb{v} + \mathbb{A}_4\partial_2\mathbb{v}, \tag{5.23}$$

and

$$\mathbb{A}_1 = \begin{bmatrix} \rho\,\mathbf{I} & \rho_f\,\mathbf{I} \\ \rho_f\,\mathbf{I} & \tilde{\boldsymbol{a}} \end{bmatrix}, \quad \mathbb{A}_2 = \begin{bmatrix} \mathbf{C}_u^{11} & \mathbf{C}_\alpha^{11} \\ (\mathbf{C}_\alpha^{11})^T & \mathbf{C}_M^{11} \end{bmatrix}, \tag{5.24a}$$

$$\mathbb{A}_3 = \begin{bmatrix} \mathbf{C}_u^{12} & \mathbf{C}_\alpha^{12} \\ (\mathbf{C}_\alpha^{21})^T & \mathbf{C}_M^{12} \end{bmatrix}, \quad \mathbb{A}_4 = \begin{bmatrix} \mathbf{C}_u^{22} & \mathbf{C}_\alpha^{22} \\ (\mathbf{C}_\alpha^{22})^T & \mathbf{C}_M^{22} \end{bmatrix}. \tag{5.24b}$$

in which $\mathbf{I}$ denotes the 2-by-2 identity matrix; the 2-by-2 matrices $\mathbf{C}_u^{ab}, \mathbf{C}_\alpha^{ab}$ and $\mathbf{C}_M^{ab}$ $(a, b = 1, 2)$ are defined by:

$$\mathbf{C}_u^{ab} = \mathbf{L}_a^T \mathbf{C}_u \mathbf{L}_b, \ \mathbf{C}_\alpha^{ab} = \mathbf{L}_a^T \mathbf{C}_\alpha \mathbf{L}_b, \ \mathbf{C}_M^{ab} = \mathbf{L}_a^T \mathbf{C}_M \mathbf{L}_b. \tag{5.25}$$

One may notice that while matrices $\mathbb{A}_1, \mathbb{A}_2$ and $\mathbb{A}_4$ are symmetric, the matrix $\mathbb{A}_3$ is not because of the unsymmetrical form of $\mathbf{C}_\alpha$ (see Eq. (5.20)).

5.2.4 Interface conditions

At the interfaces Γ_1^{bf} and Γ_2^{bf}, the continuity of pressure and stress fields between the poroelastic medium and the fluid domains requires:

$$p = p^{(n)}, \quad \forall\, \boldsymbol{x} \in \Gamma_n^{bf} \ (n = 1, 2), \tag{5.26a}$$

$$\boldsymbol{\sigma} \boldsymbol{n}_n^{bf} = -p^{(n)} \boldsymbol{n}_n^{bf}, \quad \forall\, \boldsymbol{x} \in \Gamma_n^{bf} \ (n = 1, 2), \tag{5.26b}$$

where $\boldsymbol{n}_n^{bf}$ is the normal unit vector to Γ_n^{bf} pointing from the poroelastic domain Ω^b toward the fluid domain Ω_n^f (see Fig. 5.1). In addition, the open-pore condition at the interfaces Γ_n^{bf} $(n = 1, 2)$ is assumed, requiring the continuity of fluid displacement in normal direction (see Eq. (5.2)):

$$\left(\frac{1}{\rho_n} \nabla p^{(n)} - \omega^2 (\boldsymbol{w} + \boldsymbol{u}) \right) \cdot \boldsymbol{n}_n^{bf} = 0, \quad \forall\, \boldsymbol{x} \in \Gamma_n^{bf}. \tag{5.27}$$

By using the harmonic forms of the solutions defined by $p^{(n)} = \hat{p}^{(n)} \exp(\mathrm{i} k_1 x_1)$ and by noting that the normal unit vectors of Ω^b at two interfaces Γ_1^{bf} and Γ_2^{bf} (see Fig. 5.1) are defined by: $\boldsymbol{n}_1^{bf} = -\boldsymbol{n}_2^{bf} = \{0, 1\}^T$, the interface conditions may be expressed as follows:

$$\hat{u}_2 + \hat{w}_2 = \frac{1}{\rho_n \omega^2} \, \partial_2 \hat{p}^{(n)}, \quad \forall\, \boldsymbol{x} \in \Gamma_n^{bf} \ (n = 1, 2), \tag{5.28a}$$

$$\hat{p} = \hat{p}^{(n)}, \quad \forall\, \boldsymbol{x} \in \Gamma_n^{bf} \ (n = 1, 2), \tag{5.28b}$$

$$\hat{\boldsymbol{t}} = \{\, 0, -\hat{p}^{(n)}\}^T, \quad \forall\, \boldsymbol{x} \in \Gamma_n^{bf} \ (n = 1, 2), \tag{5.28c}$$

where $\hat{\boldsymbol{t}}$ is the traction vector and is defined by $\hat{\boldsymbol{t}} = \mathbf{L}_2^T \hat{\boldsymbol{s}} = \{\hat{\sigma}_{12}, \hat{\sigma}_{22}\}^T$.

5.3 Analytical solution of reflection and transmission coefficients for an homogeneous layer

If the poroelastic layer is homogeneous, the solution of the system given by (5.22) may be analytically derived [104, 105]. Here, we present a simple procedure for calculating the analytical solution of reflection and transmission coefficients by using the displacement-based equation (see (5.22)):

$$-\omega^2\mathbb{A}_1\mathbb{v} + k_1^2\mathbb{A}_2\mathbb{v} - \mathrm{i}k_1\left(\mathbb{A}_3 + \mathbb{A}_3^T\right)\partial_2\mathbb{v} - \mathbb{A}_4\partial_2^2\mathbb{v} = \mathbf{0}. \tag{5.29}$$

Assuming that $\mathbb{v}$ has the form $\mathbb{v} = \mathbf{D}\exp(\gamma x_2)$, where $\mathbf{D}$ and γ are constants to be determined. The condition for a non-trivial solution of Eq. (5.29) leads to a characteristic equation:

$$\mathcal{D}(\gamma) := \det\left(-\omega^2\mathbb{A}_1 + k_1^2\mathbb{A}_2 - \mathrm{i}k_1\gamma\left(\mathbb{A}_3 + \mathbb{A}_3^T\right) + \gamma^2\mathbb{A}_4\right) = 0, \tag{5.30}$$

where det is the determinant operator.

The analytical expression of $\mathcal{D}(\gamma)$ may be found without difficulties with the helps of a symbolic software. In this paper, Matlab Symbolic Toolbox has been used. It has been shown that although the size matrices in (5.29) is 4-by-4, the derived expression for $\mathcal{D}(\gamma)$ is a 6^{th}-order polynomial:

$$\mathcal{D}(\gamma) := b_0\gamma^6 + b_1\gamma^4 + b_2\gamma^2 + b_3, \tag{5.31}$$

where b_j $(j = 0, ..., 3)$ are constants. Equation (5.31) allows to determine 6 roots γ_j, $(j = 1, ..., 6)$ verifying $\gamma_4 = -\gamma_1$, $\gamma_5 = -\gamma_2$, $\gamma_6 = -\gamma_3$ and 6 associated to normalized eigenvectors $\mathbf{B}_j$, $(j = 1, ..., 6)$. As a consequence, the general solution $\mathbb{v}$ may be expressed by the linear combination $\mathbb{v} = \sum_{j=1}^{6}\mathbf{D}_j\exp(\gamma_j x_2)$, where $\mathbf{D}_j = A_j\mathbf{B}_j$ $(j = 1, .., 6)$. The quantities A_j are six unknown constants which will be determined by using the boundary conditions. Without loss of generality, we may assume that $\mathrm{Re}\left(()\,\gamma_j\right) > 0$ for $j = 1, 2, 3$ where $\mathrm{Re}\left(()\,\gamma_j\right)$ stands for the real part of γ_j.

To solve this problem with the boundary conditions given in (5.28a)-(5.28c), we first use the solution of $\mathbb{v}$ to calculate the general solutions of concerning displacement and stress components $\hat{u}_1, \hat{u}_2, \hat{w}_2, \hat{\sigma}_{12}, \hat{\sigma}_{22}, \hat{p}$. Then by making some algebraic manipulations, we can be able to write the general solution of these terms under matrix form as follows:

$$\begin{pmatrix}\bar{\mathbf{v}}\\ \bar{\mathbf{t}}\end{pmatrix} = \begin{bmatrix}\mathbf{B}_{11} & \mathbf{B}_{12}\\ \mathbf{B}_{21} & \mathbf{B}_{22}\end{bmatrix}\begin{bmatrix}\mathbf{e}^- & \mathbf{0}\\ \mathbf{0} & \mathbf{e}^+\end{bmatrix}\begin{pmatrix}\mathbf{A}^-\\ \mathbf{A}^+\end{pmatrix}, \tag{5.32}$$

where $\bar{\mathbf{v}} = (\hat{u}_1, \hat{u}_2, \hat{w}_2)^T$, $\bar{\mathbf{t}} = (\hat{\sigma}_{12}, \hat{\sigma}_{22}, -\hat{p})^T$, $\mathbf{B}_{11}, \mathbf{B}_{12}, \mathbf{B}_{21}$ and $\mathbf{B}_{22}$ are the 3-by-3 matrices which are extracted from $\mathbf{D}_j$ (see Eq. (5.23)). The quantities $\mathbf{e}^+$ and $\mathbf{e}^-$ are defined by:

$$\mathbf{e}^+ = \mathrm{diag}(\exp\gamma_1 x_2, \exp\gamma_2 x_2, \exp\gamma_3 x_2), \quad \mathbf{e}^- = \mathrm{diag}(\exp -\gamma_1 x_2, \exp -\gamma_2 x_2, \exp -\gamma_3 x_2), \tag{5.33}$$

where $\mathbf{A}^+ = (A_1, A_2, A_3)^T$ and $\mathbf{A}^- = (A_4, A_5, A_6)^T$.

Noting that $\hat{u}_2 + \hat{w}_2 = \bar{\mathbf{d}}^T\bar{\mathbf{v}}$ with $\bar{\mathbf{d}} = (0, 1, 1)^T$, the continuity conditions (Eq. (5.28a)) read:

$$\bar{\mathbf{d}}^T\bar{\mathbf{v}}|_{x_2=0} = \frac{ik_2^{(1)}}{\rho_1\omega^2}(P_I - P_R), \quad \bar{\mathbf{t}}|_{x_2=0} = -\bar{\mathbf{d}}(P_I + P_R), \tag{5.34a}$$

$$\bar{\mathbf{d}}^T\bar{\mathbf{v}}|_{x_2=-h} = -\frac{ik_2^{(2)}}{\rho_2\omega^2}P_T, \quad \bar{\mathbf{t}}|_{x_2=-h} = -\bar{\mathbf{d}}P_T \tag{5.34b}$$

what becomes

$$\beta^{(1)}P_R + \bar{\mathbf{d}}^T\mathbf{B}_{11}\mathbf{A}^- + \bar{\mathbf{d}}^T\mathbf{B}_{12}\mathbf{A}^+ = \alpha^{(1)}P_I, \tag{5.35a}$$
$$\bar{\mathbf{d}}P_R + \mathbf{B}_{21}\mathbf{A}^- + \mathbf{B}_{22}\mathbf{A}^+ = -\bar{\mathbf{d}}P_I, \tag{5.35b}$$
$$\beta^{(2)}P_T + \bar{\mathbf{d}}^T\mathbf{B}_{11}\mathbf{e}_h^+\mathbf{A}^- + \bar{\mathbf{d}}^T\mathbf{B}_{12}\mathbf{e}_h^-\mathbf{A}^+ = 0, \tag{5.35c}$$
$$\bar{\mathbf{d}}P_T + \mathbf{B}_{21}\mathbf{e}_h^+\mathbf{A}^- + \mathbf{B}_{22}\mathbf{e}_h^-\mathbf{A}^+ = \mathbf{0}, \tag{5.35d}$$

where

$$\beta^{(1)} = \frac{\rho_1\omega^2}{ik_2^{(1)}}, \quad \beta^{(2)} = \frac{\rho_2\omega^2}{ik_2^{(2)}}, \quad \mathbf{e}_h^+ = \mathrm{diag}(\exp\gamma_1 h, \exp\gamma_2 h, \exp\gamma_3 h), \quad \mathbf{e}_h^- = \left(\mathbf{e}_h^+\right)^{-1}. \tag{5.36}$$

In order to avoid numerical difficulties due to the exponential term with large value of $\mathrm{Re}\,((\,)\,\gamma_j)$, we make some arrangements in (5.35a)-(5.35d) to obtain a system of linear equations as follows:

$$\begin{bmatrix} \beta^{(1)} & \bar{\mathbf{d}}^T\mathbf{B}_{11}\mathbf{e}_h^- & \bar{\mathbf{d}}^T\mathbf{B}_{12}\mathbf{e}_h^- & 0 \\ \bar{\mathbf{d}} & \mathbf{B}_{21}\mathbf{e}_h^- & \mathbf{B}_{22}\mathbf{e}_h^- & \mathbf{0} \\ \mathbf{0} & \mathbf{B}_{21} & \mathbf{B}_{22}\mathbf{e}_{2h}^- & \bar{\mathbf{d}} \\ 0 & \bar{\mathbf{d}}^T\mathbf{B}_{11} & \bar{\mathbf{d}}^T\mathbf{B}_{12}\mathbf{e}_{2h}^- & \beta^{(2)} \end{bmatrix} \begin{pmatrix} P_R \\ \mathbf{e}_h^+\mathbf{A}^- \\ \mathbf{e}_h^+\mathbf{A}^+ \\ P_T \end{pmatrix} = \begin{pmatrix} \beta^{(1)}P_I \\ -P_I\bar{\mathbf{d}} \\ \mathbf{0} \\ 0 \end{pmatrix}. \tag{5.37}$$

The amplitudes of reflected and transmitted waves P_I and P_R may be obtained by solving the linear system of equations (5.37). Consequently, the reflection and transmission coefficients may be computed by:

$$R = \frac{P_R}{P_I} \quad \text{and} \quad T = \frac{P_T}{P_I}. \tag{5.38}$$

5.4 Finite element formulation

5.4.1 Weak formulation

The weak formulation of the boundary value problem given by Eq. (5.22) and the boundary conditions (5.28a)-(5.28c) may be now carried out by using an usual procedure.

Let $\mathscr{C}^{ad}$ be the set of admissible functions constituted by the sufficiently differentiable complex-valued functions such as: $x_2 \in H^b =]-h, 0[\to \delta\mathbb{v}(x_2) \in \mathbb{C}^4$ where $\mathbb{C}$ is the set of complex numbers. Upon integrating (5.22) against a test vector function $\delta\mathbb{v}$ and applying the Gauss theorem, then using the boundary condition (5.28c), the weak formulation of Eq. (5.22) reads:

$$\begin{aligned} &-\omega^2\int_{-h}^{0}\delta\mathbb{v}^*\mathbb{A}_1\mathbb{v}\;dx_2 + k_1^2\int_{-h}^{0}\delta\mathbb{v}^*\mathbb{A}_2\mathbb{v}\;dx_2 + ik_1\int_{-h}^{0}\left(\partial_2(\delta\mathbb{v}^*)\mathbb{A}_3^T\mathbb{v} - \delta\mathbb{v}^*\mathbb{A}_3\partial_2\mathbb{v}\right)\;dx_2 \\ &+\int_{-h}^{0}\partial_2(\delta\mathbb{v}^*)\mathbb{A}_4\partial_2\mathbb{v}\;dx_2 + \;\delta\mathbb{v}^*(0)\mathbf{d}\;\hat{p}(0) - \delta\mathbb{v}^*(-h)\mathbf{d}\;\hat{p}(-h) = 0, \forall\;\delta\mathbb{v} \in \mathscr{C}^{ad}, \end{aligned} \tag{5.39}$$

where $\delta\mathbb{v}^*$ denotes the conjugate transpose of $\delta\mathbb{v}$ and $\mathbf{d} = (0,1,0,1)^T$.

In the weak formulation given by Eq. (5.39), the pore pressure $\hat{p}$ at $x_2 = 0$ and at $x_2 = -h$ are unknowns but may be determined in terms of the displacement by using the conditions (5.28a)-(5.28b)

and by taking into account the forms of the general solution in fluid domains presented in 5.3. At the upper interface between Ω^b and Ω_1^f ($x_2 = 0$), we have:

$$\hat{u}_2 + \hat{w}_2 = \frac{ik_2^{(1)}}{\rho_1\omega^2}(-P_I + P_R), \tag{5.40a}$$

$$\hat{p} = P_I + P_R, \tag{5.40b}$$

which lead to an impedance boundary condition:

$$\hat{p}(0) = \frac{\rho_1\omega^2}{ik_2^{(1)}}(\hat{u}_2(0) + \hat{w}_2(0)) + 2P_I. \tag{5.41}$$

Similarly the impedance boundary condition at the lower interface ($x_2 = -h$) reads:

$$\hat{p}(-h) = -\frac{\rho_2\omega^2}{ik_2^{(2)}}(\hat{u}_2(-h) + \hat{w}_2(-h)). \tag{5.42}$$

By noting that $\hat{u}_2 + \hat{w}_2 = \mathbf{d}^T\mathbb{v}$ and by substituting (5.41)-(5.42) into (5.39), we obtain:

$$\begin{aligned} &-\omega^2\int_{-h}^{0}\delta\mathbb{v}^*\mathbb{A}_1\mathbb{v}\;dx_2 + k_1^2\int_{-h}^{0}\delta\mathbb{v}^*\mathbb{A}_2\mathbb{v}\;dx_2 + ik_1\int_{-h}^{0}\left(\partial_2(\delta\mathbb{v}^*)\mathbb{A}_3^T\mathbb{v} - \delta\mathbb{v}^*\mathbb{A}_3\partial_2\mathbb{v}\right)\;dx_2 \\ &\quad + \int_{-h}^{0}\partial_2(\delta\mathbb{v}^*)\mathbb{A}_4\partial_2\mathbb{v}\;dx_2 + \delta\mathbb{v}^*(0)\mathbf{D}\mathbb{v}(0) + \delta\mathbb{v}^*(-h)\mathbf{D}\mathbb{v}(-h) = -2P_I\delta\mathbb{v}^*(0)\mathbf{d}, \\ &\quad \forall\;\delta\mathbb{v} \in \mathscr{C}^{ad}, \end{aligned} \tag{5.43}$$

where $\mathbf{D} = \mathbf{d}\mathbf{d}^T$.

5.4.2 Finite element discretization

The domain $[-h, 0]$ is discretized into n^{el} elements: $[-h, 0] = \bigcup_e \Omega_e$ with $e = 1, ..., n^{el}$. By mapping each element Ω_e to the reference domain $\bar{\Omega}_e = [-1, 1]$, the ith component of $\mathbf{v}$ is approximated by:

$$v_i^e = \sum_{j=1}^{q} N_j(\xi)v_i^e(\xi_j), \tag{5.44}$$

where q is the number of nodes used for this approximation, $N_j(\xi)$ is the jth shape function, ξ_j is the position of jth node and $v_i^e(\xi_j)$ is the nodal solution at jth node. Using the standard Galerkin method, the test function of δv_i^e is approximated by the same shape function. These approximations may be expressed as follows:

$$\mathbb{v}(\xi) = \mathbf{N}^e(\xi)\mathbf{V}^e, \quad \delta\mathbb{v}(\xi) = \mathbf{N}^e(\xi)\delta\mathbf{V}^e, \tag{5.45}$$

where $\mathbf{N}^e$ is the interpolation matrix constructed from 1D shape functions given by Eq. (5.44), $\mathbf{V}^e$ and $\delta\mathbf{V}^e$ are the vectors of nodal solutions of $\mathbb{v}$ and $\delta\mathbb{v}$ within the element Ω_e, respectively.

Substituting (5.45) into (5.43) and assembling the elementary matrices lead to a system of linear equations:

$$\left(\mathbf{K}^b + \mathbf{K}^\Gamma\right)\mathbf{V} = \mathbf{F}, \tag{5.46}$$

where $\mathbf{V}$ is the global nodal solution vector; $\mathbf{K}^b$ is the global "stiffness matrix" of the poroelastic layer; $\mathbf{K}_\Gamma$ represents the coupling operator between the fluid and poroelastic layers; the vector $\mathbf{F}$ is the external force vector due to the incident waves. Note that the element number of the vectors $\mathbf{V}$ and $\mathbf{F}$ is $n = 4(n^{el} \times q - 1)$ because each node has 4 degrees of freedom. Thus, the sizes of $\mathbf{K}^b$ and $\mathbf{K}^\Gamma$ equal to $n \times n$ and are defined by:

$$\mathbf{K}^b = -\omega^2\ \mathbf{K}_1 + k_1^2\ \mathbf{K}_2 + ik_1\ \mathbf{K}_3 + \mathbf{K}_4 \tag{5.47a}$$

$$\mathbf{K}^\Gamma_{jk} = \begin{cases} \dfrac{\rho_2\omega^2}{ik_2^{(2)}} & \text{if } (j,k) = (2,2),(2,4),(4,2),(4,4) \\ \dfrac{\rho_1\omega^2}{ik_2^{(1)}} & \text{if } (j,k) = (n-2,n-2),\ (n-2,n), \\ & \qquad (n,n-2),\ (n,n) \\ 0 & \text{otherwise} \end{cases} \tag{5.47b}$$

$$\mathbf{F}_j = \begin{cases} -2P_I & \text{if } j = n-2, n \\ 0 & \text{otherwise} \end{cases} \tag{5.47c}$$

where the matrices $\mathbf{K}_1, \mathbf{K}_2, \mathbf{K}_3$ and $\mathbf{K}_4$ are defined by:

$$\mathbf{K}_1 = \bigcup_e \int_{-1}^{1} (\mathbf{N}^e(\xi))^T\, \mathbb{A}_1(\xi)\mathbf{N}^e(\xi)\mathcal{J}(\xi)\, d\xi, \tag{5.48a}$$

$$\mathbf{K}_2 = \bigcup_e \int_{-1}^{1} (\mathbf{N}^e(\xi))^T\, \mathbb{A}_2(\xi)\mathbf{N}^e(\xi)\mathcal{J}(\xi)\, d\xi, \tag{5.48b}$$

$$\mathbf{K}_3 = \bigcup_e \int_{-1}^{1} 2\left[(\partial_2\mathbf{N}^e(\xi))^T\, \mathbb{A}_3(\xi)\mathbf{N}^e(\xi)\right]_a d\xi, \tag{5.48c}$$

$$\mathbf{K}_4 = \bigcup_e \int_{-1}^{1} (\partial_2\mathbf{N}^e(\xi))^T\, \mathbb{A}_4(\xi)\, (\partial_2\mathbf{N}^e(\xi))\, \mathcal{J}^{-1}(\xi)\, d\xi, \tag{5.48d}$$

in which $\mathcal{J}$ is the jacobian operator and $[\star]_a$ designates the anti-symmetric part of $[\star]$.

By using the standard finite element method (FEM) to solve Eq. (5.43), the elements size of the spatial discretization has to be sufficiently refined, *i.e.*a sufficient number of grid points per wavelength has to be adjusted, to be able to capture the oscillation of the solution. Thus, the quality of numerical solutions depends on the wave-number k_1. When solving an Helmholtz-type equation, the rule that must be respected is that the ratio $k_1\ell^e$ must be constant where ℓ^e is the element size. However, as shown in studies on the error bound estimation when the FEM is used for solving Helmholtz equation, as k_1 increases the accuracy of FE solution still significantly decreases while the ratio $k_1\ell^e$ is kept to be constant, due to the so-called "pollution effect". It has also been shown that for large wave-number problems, using high-order interpolation polynomials would be better to reduce the pollution effect than using lower-order ones with refined element sizes. To do so, we proposed to use two different high-order approximation techniques: the first one uses the spectral element method (SEM) and the second one uses isogeometric analysis (IGA) method.

5.4.3 On the use of high-order spectral-elements

The high-order spectral-element method (SEM) has been widely used for wave propagation simulation (see *e.g.* [106]). Likes standard FEM, the SEM uses the Lagrange polynomials as interpolation

functions. In the reference element $[-1,1]$, one may define q Lagrange polynomials of degree $(q-1)$ based on q-nodes ξ_i (for $-1 \leq \xi_i \leq 1$):

$$N_j^{q-1}(\xi) = \prod_{i=1, i\neq j}^{q} \frac{(\xi - \xi_i)}{(\xi_j - \xi_i)}, \tag{5.49}$$

which imposes the condition given by $N_j^{q-1}(\xi_i) = \delta_{ij}$ where δ_{ij} denotes the Kronecker symbol for which $\delta_{ij} = 1$ if $i = j$ else $\delta_{ij} = 0$ if $i \neq j$. One important difference between FEM and SEM is the node distribution within an element. In SEM, the coordinates of nodes are chosen to be located at the q Gauss-Lobatto-Legendre (GLL) points which are the roots of the following equation:

$$(1-\xi^2)P'_{q-1}(\xi) = 0, \tag{5.50}$$

where $P'_{q-1}(\xi)$ denotes the first-order derivative of the Legendre polynomial of degree $(q-1)$ with respect to ξ. It worths noting that in the time-domain simulation, this choice is motivated by the fact that the mass matrix will become a diagonal matrix which is very convenient for employing an explicit time integration scheme.

5.4.4 On the use of NURBS basis functions

In this paper, we adopt an isogeometric-based approach where the non-uniform rational B-spline (NURBS) basis functions [87] were used for discretizing the weak problem presented in Sec. 5.4.1. Basically, B-spline basis functions of order q are determined in a parameter domain $\hat{\Omega} \subset \mathbb{R}$ using a sequence of non-decreasing set of coordinates called *knot vector* defined as $\Xi = \{\xi_1, \xi_2, \xi_3, ..., \xi_{n+q+1}\}$, where $\xi_i \in \mathbb{R}$ $(i = 1, 2, ..., n)$ is the i^{th} knot and n is the number of basis functions used to construct the B-spline curve. For a given knot vector, the corresponding set of B-spline basis functions $B_{i,q}$ are defined by the well-known Cox-de Boor recursion formula as:

$$q = 0 \ : \quad B_{i,0}(\xi) = \begin{cases} 1 & \text{if } \xi_i < \xi < \xi_{i+1}, \\ 0 & \text{otherwise,} \end{cases} \tag{5.51a}$$

$$q > 0 \ : \quad B_{i,q}(\xi) = \frac{(\xi - \xi_i)}{(\xi_{i+q} - \xi_i)} B_{i,q-1}(\xi) + \frac{(\xi_{i+q+1} - \xi)}{(\xi_{i+q+1} - \xi_{i+1})} B_{i+1,q-1}(\xi). \tag{5.51b}$$

Note that the quotient $0/0$ is assumed to be zero. Open knot vectors, where the first and the last knot each have a multiplicity of $(q+1)$, are standard in CAD Non-uniform rational B-spline (NURBS) basis functions $N_{i,q}(\xi)$ are built from the B-spline functions by assigning a weight w_i to every B-spline function $B_{i,q}(\xi)$:

$$N_{i,q}(\xi) = \frac{B_{i,q}(\xi) w_i}{\sum_{j=1}^{n} B_{j,q}(\xi) w_j}. \tag{5.52}$$

The NURBS basis functions have some advantages such as higher continuity across the element boundaries, partition of unity, variation diminishing, linear independence and compact support.

5.4.5 Reflection and transmission coefficients

By solving the linear system of equations (5.46), one obtains the displacements at all the nodes. Then, the reflection and transmission coefficients, denote R and T respectively, can be computed by

using the displacement values at the upper and the lower surfaces, respectively (see Eqs. (5.40a) and (5.42)):

$$R = \frac{P_R}{P_I} = \frac{\rho_1 \omega^2}{i k_2^{(1)}} \times \frac{\hat{u}_2(0) + \hat{w}_2(0)}{P_I} + 1, \tag{5.53a}$$

$$T = \frac{P_T}{P_I} = -\frac{\rho_2 \omega^2}{i k_2^{(2)}} \times \frac{\hat{u}_2(-h) + \hat{w}_2(-h)}{P_I}. \tag{5.53b}$$

5.5 Numerical results

5.5.1 Material parameters

As an example of the capability of the method presented, we studied the effect of porosity on the dynamic response of cortical bone while using ultrasound diagnostic devices. Many of the past studies have focused on the modeling of guided waves in long bones by using fluid-loaded homogeneous/multilayer/functional graded plate models. The understanding of wave phenomena involved in the multilayer structures has been studied by many authors in the frequency-domain [107, 99, 108] or in the time-domain [109, 110, 111]. In these studies, the cortical bone material has been considered as an equivalent (visco-)elastic medium of which the effective macroscopic mass density and effective macroscopic elasticity tensor are estimated from its porosity. The presence of the interstitial fluid, which was considered in many works for the analysis of the behaviour of cortical bone tissue under low frequency loading (*e.g.*[112, 113, 63, 114]) or of ultrasonic wave propagation through cancellous bones (*e.g.*[115, 116, 58, 117, 118]), has usually been neglected when studying ultrasonic wave propagation in cortical bones.

The observations at all ages and for both genders show that the mean porosity in the endosteal region (inner part of the bone) is significantly higher than the porosity in the periosteal region (outer part of the bone) [119, 120]. This observation may be explained by the fact that the cortical bone is affected by age-related bone resorption and osteoporosis, causing reduction of bone shell thickness as well as increase of porosity, namely in the endosteal region. Moreover, the macroscopic mechanical properties of bone have been shown to strongly depend on its porosity [64]. As a consequence, cortical bone may naturally be considered as a functionally graded material.

In this study, both surround fluid domains Ω_1^f and Ω_2^f are also assumed to be the water with the mass densities and wave celerities given by $\rho_1 = \rho_2 = 1000$ kg.m^{-3} and $c_1 = c_2 = 1500$ m.s^{-1}, respectively. The parameters for the poroelastic plate are determined by assuming that the skeleton solid is an isotropic elastic material and the pores has cylindrical sharp. Here, the poroelastic constants (see Eqs. (5.11) and (5.12), $\mathbf{C}$, $\boldsymbol{\alpha}$ and M) were determined following a micro-mechanical approach presented in [121]. Moreover, the permeability is calculated in function of the porosity, the pore surface area and the cross section parameters by using the Kozeny-Carman law (see details in [122]). In all examples in what follows, the solid and fluid phases' parameters were fixed as shown in Tab. 5.1 and only the porosity ϕ was varied. The poroelastic constants were determined for each value of ϕ. For example, Tab. 5.2 shows the numerical values of the poroelastic constants computed for $\phi = 0.05$ and $\phi = 0.5$, respectively.

Table 5.1 – Values of the parameters for cortical bone

Mass density of the fluid ρ_{f}	1000	$\mathrm{kg.m^{-3}}$
Bulk modulus of the fluid K_{f}	2.25	GPa
Mass density of the solid ρ_s	1722	$\mathrm{kg.m^{-3}}$
Young's modulus of the solid E_s	20	GPa
Poisson's coefficient of the solid ν_s	0.3	-
Viscosity of the fluid η	10^{-3}	Pa.s
Characteristic length in $\boldsymbol{e}_1$-direction Λ_1	2	μm
Characteristic length in $\boldsymbol{e}_2$-direction Λ_2	0.2	μm
Tortuosity in a_1^∞-direction $\boldsymbol{e}_1$	1	-
Tortuosity in a_2^∞-direction $\boldsymbol{e}_2$	1	-

Table 5.2 – Parameters of poroelastic materials with different porosities

ϕ [–]	C_{11} [GPa]	C_{22} [GPa]	C_{12} [GPa]	C_{66} [GPa]	α_{11} [–]	α_{22} [–]	M [GPa]	κ_{11} [$\mathrm{m^{-2}}$]	κ_{22} [$\mathrm{m^{-2}}$]
0.05	26.668	20.252	8.452	6.294	0.1083	0.1463	35.574	2.5×10^{-12}	2.5×10^{-14}
0.5	12.672	5.708	2.327	1.865	0.6605	0.765	4.1941	2.5×10^{-11}	2.5×10^{-13}

5.5.2 Cases of homogeneous poroelastic plates

5.5.2.1 Reference solutions

We first consider a homogeneous anisotropic poroelastic bone plate with thickness $h = 5$ mm immersed in water for which the analytical solutions may be determined using the procedure described in 5.3. For illustration purposes, we present in Figs. 5.2(a,b) the variation of the coefficient R as a function of the incidence angle θ at two frequencies ($f = 0.25$ MHz and $f = 1$ MHz). For each frequency, the graphs of $|R(\theta)|$ of plates with different porosities ($\phi = 0.01, 0.05, 0.2, 0.5$) were shown. When ϕ is very small (case of $\phi = 0.01$, shown by solid black curves), the poroelastic plate behaves similarly to an elastic plate one. On the other hand, when ϕ increases, the behaviour of poroelastic plate is very different of an elastic plate one. Notes that the reflection coefficient $|R|$ get the minimum values (close to zero) at some angles of incidence corresponding to the guided-wave modes of which the phase velocities are given by $C_{\mathrm{ph}} = c_1/\sin\theta$ [4]. For example, when $f = 250$ kHz (see Fig. 5.2a), three zero-peaks found at $\theta \sim 12.5°, 25°$ and $51.5°$ correspond to the A_1, S_0 and A_0 modes, respectively. At high frequency ($f = 1$ MHz), as the plate's thickness is important in comparing with the incident wavelength, there exists a critical angle ($\theta \sim 50°$) above which the incident plane wave is nearly totally reflected (see Fig. 5.2b). By increasing the porosity ϕ, both elasticity and absorption of the poroelastic material are accordingly changed, causing significant modifications not only of the amplitudes of reflected waves but also of the phase velocity of the modes. This effect is more pronounced at high frequency. For higher porosity, when the stiffness of the plate is smaller the one of precedent case, we may check that the reflection coefficient has globally smaller values.

In Fig. 5.3, we present the variation of $|R|$ with respect to both incident angle θ and the frequency f in two case of porosity $\phi = 0.05$ and $\phi = 0.5$. As it would be expected, a greater number of modes may be observed for the plate with $\phi = 0.5$ than the one with $\phi = 0.05$ in a same frequency range (0 – 1 MHz).

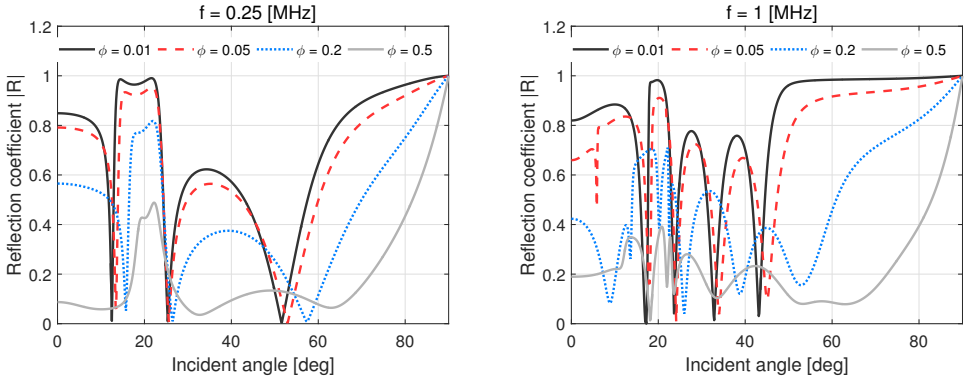

(a) $f = 250$ kHz (b) $f = 1$ MHz

Figure 5.2 – Reflection coefficient R versus *incident angle θ for a homogeneous plate.*

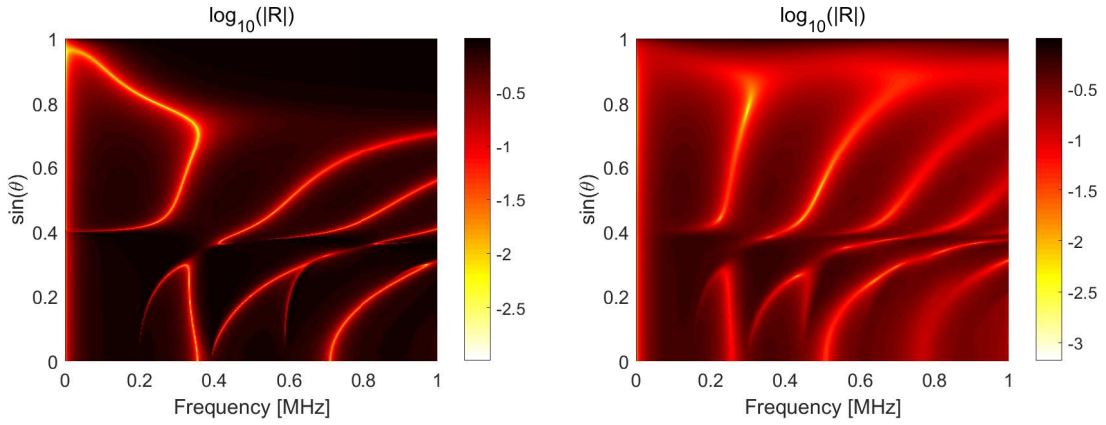

(a) $\phi = 0.05$ (b) $\phi = 0.5$

Figure 5.3 – Case of homogeneous plates: reflection coefficient R versus *incident angle (θ) and frequency ($f = \omega/2\pi$)*

5.5.2.2 Validation

To validate the proposed numerical methods, we investigated the reflection and transmission coefficients (R and T, respectively) obtained for $f = 1$ MHz with various incident angles as shown in Fig. 5.4. As the plate is homogeneous, the reflection and transmission coefficients can be analytically calculated (see 5.3) and are served as reference solutions. Three finite element solutions are shown in this figure. The first one was obtained by using the standard SAFE method with 6 quadratic Lagrange elements ($p = 2$). The second one was computed by using only one high-order spectral GLL element with $p = 12$. The third one was obtained by one NURBS-based element with $p = 12$. As a consequence, all of these three FE meshes contain in total 13 nodes with 52 degrees of freedom. At the studied frequency ($f = 1$ MHz), both real and imaginary parts of R and T solutions obtained by using the high-order elements (GLL or NURBS) perfectly match to the analytical ones for all values of θ. On the contrary, the $R-$ and $T-$curves computed by using low-order elements ($p = 2$) were shown to significantly be less accurate, namely for the small incident angle values between 0° and 20°. In particular, some lacks of precision at some incident angles. For example, the peaks of both

reflection and transmission coefficients at the incident angle $\theta \sim 6°$ displayed in zoomed windows were shown to be not precisely evaluated when using the standard quadratic elements.

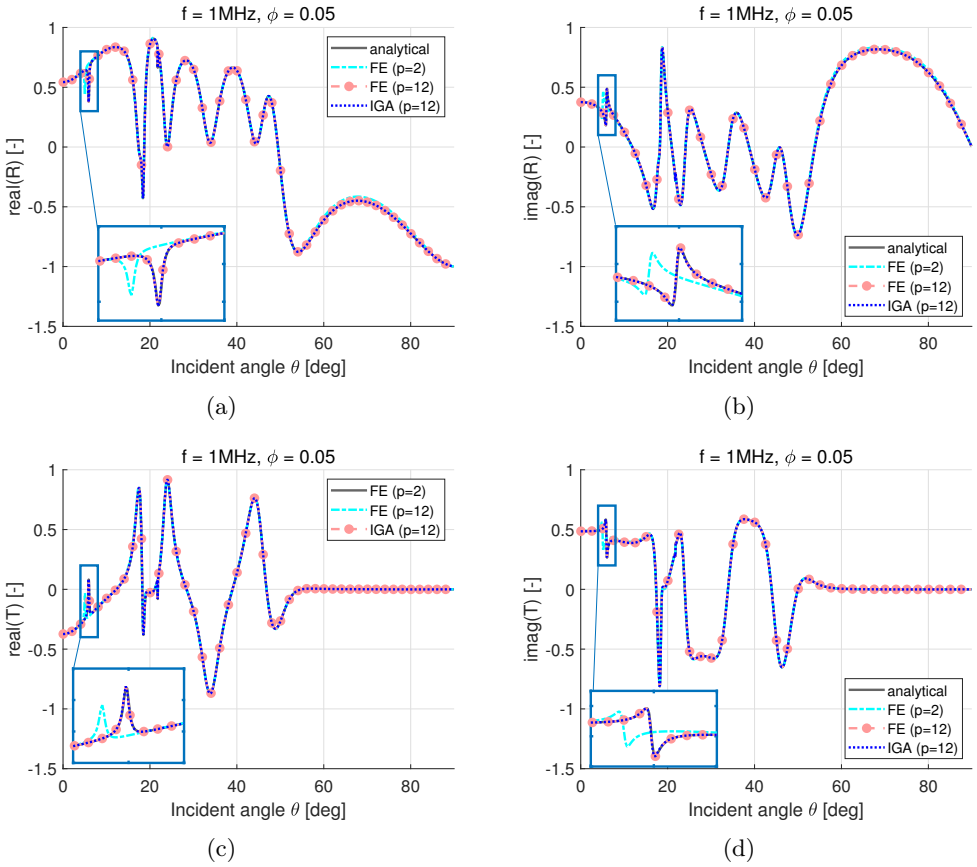

Figure 5.4 – Exact and FE solutions of the reflection and transmission coefficients versus *incident angle θ.*

In Figs 5.5(a,b), we presented the R- and $T-$ solutions of the same problem computed by employing two different orders of interpolation functions ($p = 4$ and $p = 6$) but keeping the same total number of degrees of freedoms to be 52 as the one used in the previous analysis with $p = 12$. For clarifying the comparison between different solutions, we focused on the peak found at $\theta \sim 6°$. It could be observed that the solutions computed using NURBS-based shape functions are correctly approached, even when using $p = 4$ for which both standard SAFE and GLL solutions led to inaccurate results. Using $p = 6$ seems to allow improving remarkably the accuracy of solutions computed by using Lagrange elements.

Next, we examined the case of a bone plate with the same thickness but with a higher porosity ($\phi = 0.5$) of which the poroelastic properties are given in Tab. 5.2. As the porosity is higher, the material's stiffness decreases and the permeability increases. Again, the FE solutions were computed by using six quadratic elements (standard SAFE) or one 12^{th}-order element (GLL or NURBS) when $f = 1$ MHz. The obtained numerical solutions of $|R|$ and of $|T|$ were compared to the analytical ones as shown in Fig. 5.6. The results obtained with quadratic elements were shown to have a significant difference with respect to the analytical solution. The errors of both R and T seem to be more significant than the ones obtained when $\phi = 0.05$ (see Fig. 5.5). On the contrary, the solutions obtained with only one 12^{th}-order GLL element still match very well to the analytical ones (see

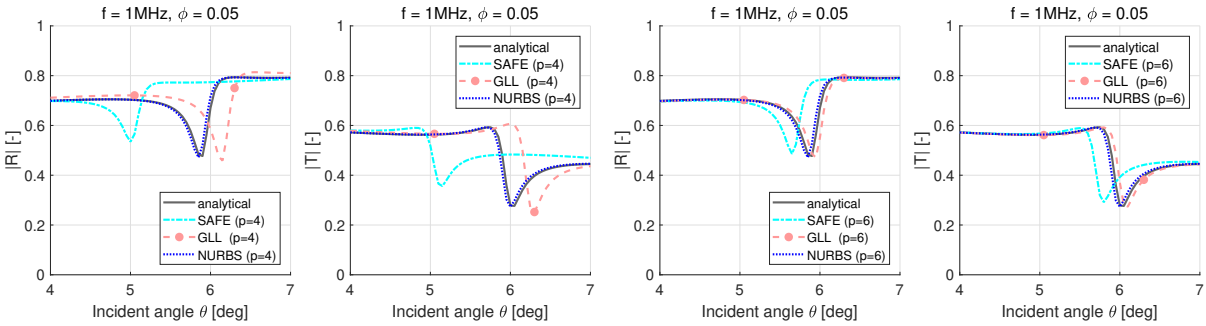

(a) $p = 4$ (b) $p = 6$

Figure 5.5 – Exact and FE solutions of the refection and transmission coefficients computed with $p = 4$ and $p = 6$

Figs. 5.6-a). Interestingly, using NURBS-based shape function with $p = 2$ leads to a much more accurate estimation of R and T (see Figs. 5.6-b).

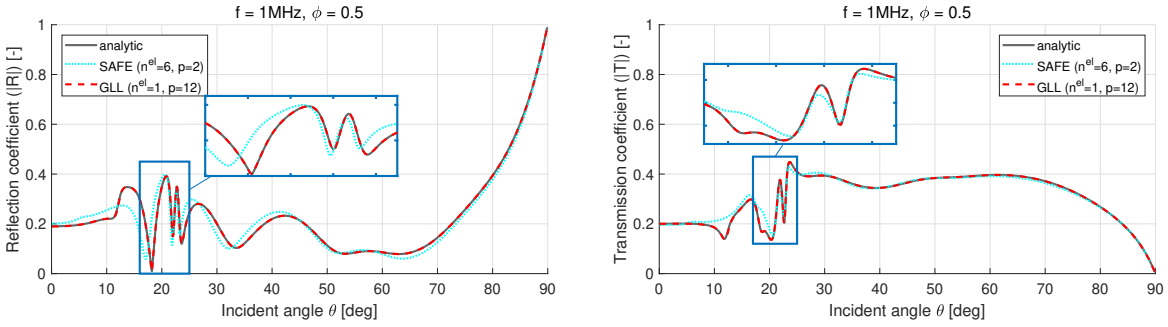

(a) solutions using SAFE and GLL

(b) solutions using NURBS

Figure 5.6 – Homogeneous plate with $\phi = 0.5$: Exact and FE solutions of the refection and transmission coefficients versus *the incident angle θ.*

5.5.2.3 Convergence study

The later examples show that the use of high-order GLL or NURBS elements may significantly reduce the numerical errors when computing the reflection and transmission coefficients. In order to examine in more detail this feature, we performed a convergence study of R and T computed with different interpolation function's orders p. For estimating the error, we introduced a function E^{refl} which is defined as a the mean value of the relative error estimated over the range of incident angles from 0° to 90°:

$$E^{\text{refl}} = \left(\frac{1}{n^{\theta}} \sum_{i=1}^{n^{\theta}} \left| \frac{R^{\text{FE}}(\theta_i) - R^{\text{exact}}(\theta_i)}{R^{\text{exact}}(\theta_i)} \right|^2 \right)^{\frac{1}{2}}, \tag{5.54}$$

where n^{θ} is the number of incident value considered. In Fig. 5.7, the relative error on R with respect to the total number of nodes are presented in a logarithmic scale. In Fig. 5.7(a) and (b), we depicted the error obtained by using GLL elements (spectral element method) or NURBS elements (isogeometric analysis), respectively. For both methods, the computations were performed with $p = 2$, $p = 4$, $p = 8$, $p = 10$ and $p = 12$.

Regarding the use of GLL elements (see Fig. 5.7(a)), one may notice that by using lower-order elements ($p = 2, 4$) the slopes of the error curves were much more smaller than the ones obtained with the high-order elements ($p = 8, 10, 12$). For a same total number of nodes ($n^{\text{node}} = 25$), while the mesh based on two elements with $p = 12$ leads to an error of order 10^{-6}, the one based on 9 elements with $p = 4$ leads to an error of order 10^{-2}. Thus, using high-order elements ($p = 12$) could allows to improve the significantly accuracy of the estimations R and T in comparing with the results obtain with $p = 2$ or $p = 4$. However, the accuracy gains is not so significant if we compare the results obtained with $p = 8$, $p = 10$ and $p = 12$, even the one obtained with $p = 12$ is still the best.

When using NURBS-base shape functions (see Fig. 5.7(b)), further increasing the order p more than 8 does not lead to a significant improvement of the convergence, similarly to the previous remark on the use of GLL elements. However, the convergence could be achieved much more faster by using

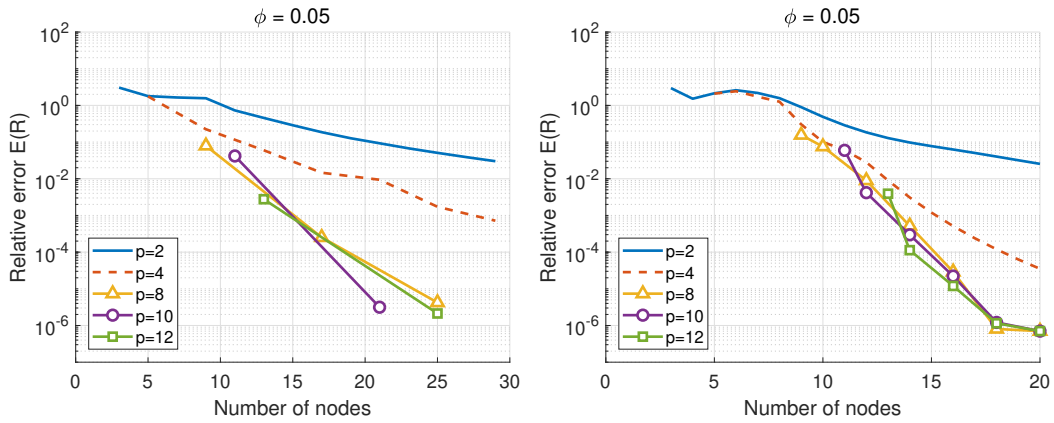

(a) spectral elements (b) isogeometric

Figure 5.7 – Error of reflection and transmission coefficients versus *the total number of nodes*

NURBS. For example, in the case $p = 4$, while using GLL elements required a mesh of 25 nodes to get $E(R) \sim 10^{-3}$, using IGA only requires a mesh with only 15 nodes (control points) to achieve the same precision. This advantage feature may be explained by the fact that by using NURBS, C^1-continuity condition was always fulfilled over the domain $\bar{\Omega} = [-h, 0]$.

5.5.2.4 Determination of poroelastic parameters

To describe the behavior of the poroelastic bone plate, the drained elasticity tensor $\mathbb{C}$ as well as Biot's effective coefficients $\boldsymbol{\alpha}$ and $\boldsymbol{M}$ used in (6.3) and (6.4) should be provided. For this study, these parameters are derived from the characteristics of the interstitial fluid and solid skeleton phases by using a continuum micro-mechanics model proposed by Hellmich et al. [121]. According to this model, the micro-pores at the micro-structural scale are regarded as cylindrical pores with a circular cross section. In drained condition, the constitutive behavior of the material inside the pores does not possess stiffness. Hence, the estimated drained micro-structural stiffness of the bone whose solid bone matrix's elasticity tensor is $\mathbb{C}^m$ reads:

$$\mathbb{C} = (1-\phi)\mathbb{C}^m : \left\{(1-\phi)\mathbb{I} + \phi\left[\mathbb{I} - \mathbb{P}^{cyl} : \mathbb{C}^m\right]^{-1}\right\}^{-1}, \tag{5.55}$$

where $\mathbb{I}$ denotes the fourth-order identity tensor; $\mathbb{P}^{cyl}$ the fourth-order tensor is the Hill's tensor for materials with periodical cylindrical inclusions, which may be derived in closed form [121]. The tensor $\boldsymbol{\alpha}$ the constant M can be then evaluated by [123, 124]:

$$\boldsymbol{\alpha} = \mathbf{I} - \mathbb{C} : (\mathbb{S}^m : \mathbf{I}), \qquad -\frac{1}{M} = C - \boldsymbol{\alpha} : \mathbb{S} : \boldsymbol{\alpha}\,, \tag{5.56}$$

where $\mathbb{S} = (\mathbb{C})^{-1}$ and $\mathbb{S}_m = (\mathbb{C}_m)^{-1}$ are respectively the drained and solid material compliance tensors, I designates the second-order tensor identity and the scalar C denotes the effective compressibility of porous matrix material, which is given by

$$C = \frac{1}{K} - \frac{1}{K_m} + \phi\left(\frac{1}{K_f} - \frac{1}{K_m}\right), \tag{5.57}$$

where $K = (\mathbf{I} : \mathbb{S} : \mathbf{I})^{-1}$, K_f and $K_m = (\mathbf{I} : \mathbb{S}_m : \mathbf{I})^{-1}$ are the bulk moduli of the drained porous matrix and of the interstitial fluid and of the poroelastic material, respectively.

5.5.3 Cases of poroelastic plates with linear gradient of porosity

In this section, the bone plate has a functionally-graded porosity variation. To do so, the porosity at the upper surface is fixed at the value $\phi_1 = 0.05$. A linear-gradient of porosity is defined by giving a value ϕ_2 at the lower surface as follows:

$$\phi(x_2) = \frac{1}{h}(\phi_1 - \phi_2)x_2 + \phi_1. \tag{5.58}$$

Then, one can estimate the physical parameters of the poroelastic material in function of the depth-coordinate x_2 following the procedure presented in 5.5.2.4. For example, Fig. 5.8 depicts the profiles of the components of the elasticity tensor (given in Voigt notation C_{ij}), the Biot coefficients (α_{ij}, M) and the permeability κ_{ij}.

As it can be observed in Fig. 5.9 in which the cases $\phi_2 = 0.2$, $\phi_2 = 0.5$ and $\phi_2 = 0.8$ were considered, the reflection coefficient is shown to strongly depend not only to the porosity at the upper surface but

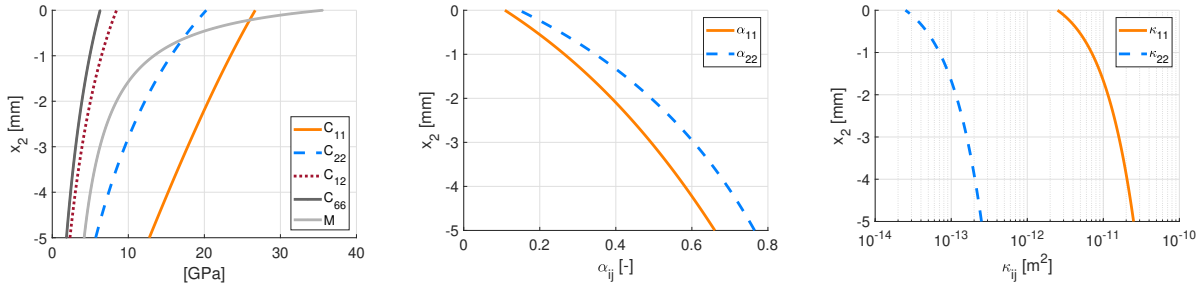

(a) C_{ij} and M (b) α_{ij} (c) κ_{ij}

Figure 5.8 – Profile of poroelastic properties with respect to the depth-coordinate x_2

also on the gradient of the porosity in the in-depth direction. Moreover, this effect is more significant in the high frequency range. In Fig. 5.10, the graphs of R versus θ computed at two frequencies given at $f = 0.25$ MHz and $f = 1$ MHz were plotted. At each frequency, the comparison between the homogeneous case $\phi_2 = 0.05$ and the linear gradient cases ($\phi_2 = 0.2$, $\phi_2 = 0.5$) confirms that at low frequency ($f = 0.25$ MHz), the porosity gradient affects slightly the behavior of the reflection coefficient R. The minima's locations of the case $\phi = 0.5$ are nearly unchanged in comparing with the homogeneous plate case. However, the graphs of $R(\theta)$ are completely changed when regarding a higher frequency ($f = 1$ MHz) for which the wavelengths are shorter and are more sensible to the porosity variation.

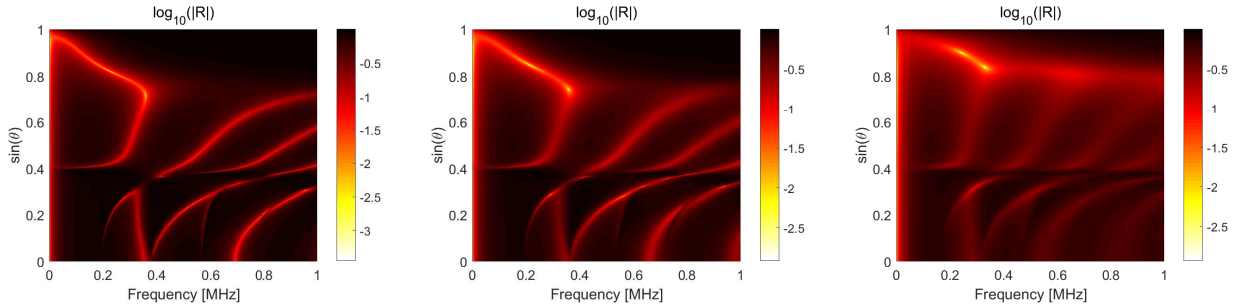

(a) $\phi_2 = 0.2$ (b) $\phi_2 = 0.5$ (c) $\phi_2 = 0.8$

Figure 5.9 – Reflection coefficient R versus θ and f for functionally-graded plates ($\phi_1 = 0.05$)

The convergence study was also carried out for these functionally-graded poroelastic plates in order to check the performance of the proposed numerical methods. Similarly to the convergence study previously performed for the homogeneous plate (see Sec. 5.5.2.3), in Figs. 5.11(a) and (b), numerical errors obtained by using GLL and NURBS-based discretizations, respectively, were presented. As exact solutions are not available for the functionally-graded cases, standard SAFE solutions using overkill meshes were served as the reference solutions. Once again, using high-order shape functions ($p \geq 8$) for both methods was shown to be efficient to reduce the numerical errors. Moreover, the IGA solutions were shown to be converged faster the ones computed by using GLL discretization.

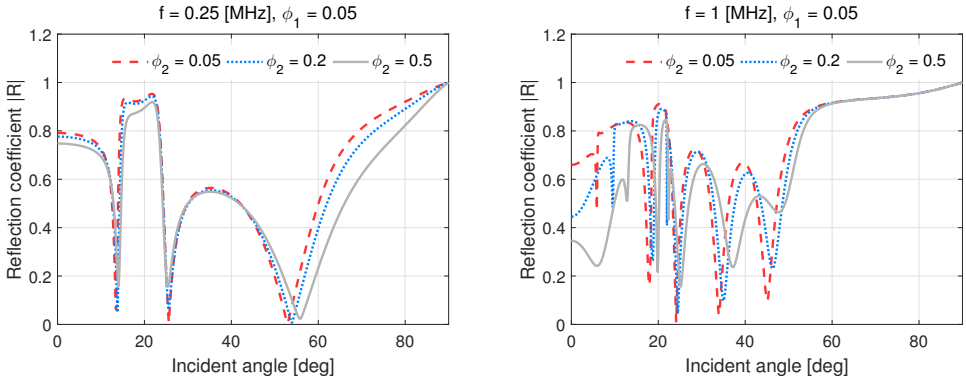

Figure 5.10 – Reflection coefficient R versus *incident angle θ: influence of a porosity gradient.*

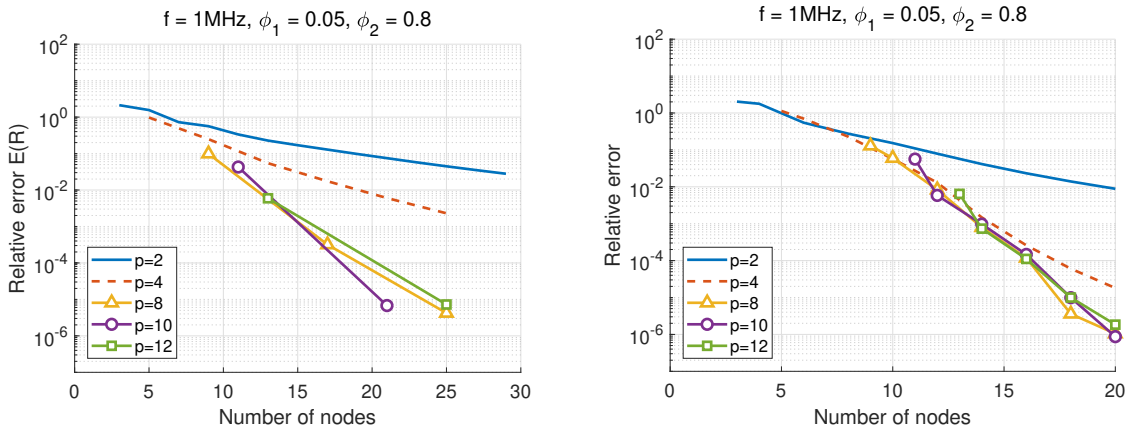

(a) spectral elements

(b) isogeometric

Figure 5.11 – Case of a functionally-graded-porosity plate: Error on reflection and transmission coefficients versus *the total number of nodes.*

5.6 Conclusion

In this paper, an approach based on the semi-analytical high-order finite element method is proposed for the determination of the reflection and transmission coefficients of a two-dimensional poroelastic waveguide wherein the material properties could be heterogeneous and anisotropic. Two strategies have been proposed for the discretization and approximation of solutions : the first one employed the spectral elements based on Gauss-Lobatto-Legendre (GLL) nodes and second one employed the NURBS-based shape functions. The convergence analysis shows that the standard SAFE method with quadratic Lagrange elements has relatively slow rate of convergence, especially at the high frequency range. Using high-order elements was shown to be interesting as it allow to significantly improve the accuracy of numerical solutions of R and T. Both proposed methods were shown to be efficient in this context. Even though, the NURBS-based approximation was likely leads to faster convergence in comparing with the one obtained by using spectral element approximations. For the computation using spectral element method, the use of elements with an order more than 8 would be recommended to get a significant effectiveness. When using IGA, the use of a NURBS-based shape function with

$p = 4$ would be already sufficient to achieve the same accuracy.

It is worth noting that, the numerical procedure proposed in this paper is not only limited for long bone ultrasound characterization but also for other applications in acoustical engineering, in which the functionally-graded material properties should be taken into account. For examples, the proposed methods could be useful for studies on the acoustic absorption optimization of poroelastic composites [125, 126].

Chapter 6

Wave dispersion in fluid-coupled poroelastic plates

6.1 Introduction

A poroelastic material consists of two phases, being the elastic solid phase and the fluid phase filling the pore spaces. Many materials encountered in civil, mechanical, geophysical and biomedical engineering can be considered as poroelastic media such as composites, rock, bone, etc. This work is concerned by studying the guided-wave propagation behavior in poroelastic media, which has a broad range of applications, for (non-exhaustive) example, the design of sound absorbing materials [127] or the development of non-destructive testing (NDT) methods [128, 129, 118]. The wave propagation problem in poroelastic materials has been studied many investigations. When the dominant wavelengths of interests are sufficiently large with respect to the characteristic length of microscopic scale, Biot's and mixture theories were mostly employed [44, 130, 89], for which the governed dynamic equations are based on the displacement field of both solid and fluid phases.

Morganti et al. [131] presented an isogeometric collocation method for studying an 1D poroleastic wave propagation problem. The IGA collocation method [132] has been developed to combine the accuracy and the smoothness advantages of the IGA method with the computational efficiency of the collocation method. Since there are no volume integrals in the IGA collocation, the collocation methods is considerably cheaper from a computational point of view. Moreover, its implementation is simple, since one only need to evaluate the shape functions and the right-hand side data at chosen collocation points. The boundary conditions are imposed as additional constraints in the linear system, which is typically non-symmetric even for self-adjoint problem but more sparse as in the Galerkin method.

This chapter[1] aims to investigate the potential of IGA-based computational methods for studying the dispersion guided-waves in poroelastic media. To do so, we develop two semi-analytical procedures for solving the dispersion relation equations of guided waves in an anisotropic poroelastic plate immersed in acoustic fluids. The first one employs the isogeometric Galerkin method, which is based on the NURBS discretization of the weak formulation derived in the frequency-wavenumber domain to derive the eigenvalue (dispersion) system of equations. The second one uses the collocation isogeometric method, which based on an NURBS approximation of the strong form of the considered

[1] The work presented in this chapter is published in the International Journal of Mechanical Sciences [133].

problem to derive the eigenvalue (dispersion) system of equations. To the best of authors' knowledge, the numerical performance of IGA-based methods for computing the dispersion curves of guided waves in poroelastic plates has not been studied in the literature.

The chapter is organized as follows. Section 6.2 describes the governing equations of the problem, where we present a detailed derivation of the weak form for the isotropic and anisotropic poroelastic material. After introducing the main concepts of IGA, including the definition of B-splines and NURBS, section 6.4 formulates the SAIGA-C and SAIGA-G methods. Section 6.5 subsequently carries out the numerical dispersion analysis through several numerical examples. The displacement mode shapes will be discussed for each cases. The chapter ends with a conclusion.

In the following, the symbol $\partial_i(\star)$ $(i = 1, 2)$ stands for the partial derivative of $(\star)$ with respect to x_i; the symbol '$\cdot$' for the scalar product and the symbol ':' between tensors of any order for their double contraction; $\mathbf{a}^*$ stands for the conjugate transpose (or Hermitian transpose) of a matrix $\mathbf{a}$. Einstein summation convention is not used in this manuscript.

6.2 Problem statement

6.2.1 Geometry description

Consider an anisotropic poroelastic layer (Ω^b) with infinite extents having a constant thickness h along $\mathbf{e}_1$-axis. The surfaces of this layer may be stress or loaded by two surrounding fluid halfspaces, respectively denoted by Ω_1^f and Ω_2^f, as shown in Fig. 6.1. The domains occupied by the poroelastic layer and the fluids are denoted by $\Omega^b = \{(x_1, x_2) \in [-\infty, \infty] \times [0, h]\}$, $\Omega_1^f = \{(x_1, x_2) \in (-\infty, \infty) \times (-\infty, 0]\}$, $\Omega_2^f = \{(x_1, x_2) \in (-\infty, \infty) \times [h, +\infty)\}$, respectively. The interfaces between Ω and the fluid domains Ω_j^f are denoted by Γ_j^{bf} $(j = \{1, 2\})$, respectively. As the thickness is constant, the outward directed, normal vectors of Ω^b at Γ_1^{bf} and Γ_2^{bf} are given by $\boldsymbol{n}_1^b = \{0, -1\}^T$ and $\boldsymbol{n}_2^b = \{0, 1\}^T$, respectively.

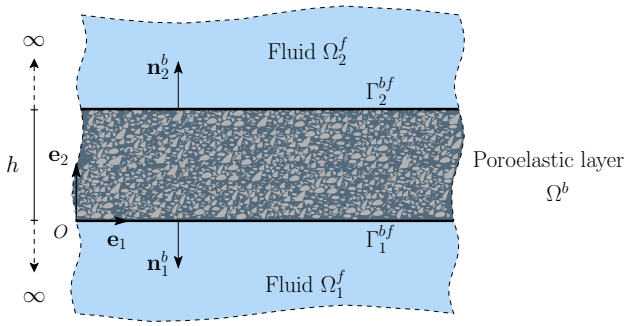

Figure 6.1 – Schematic of a two-dimensional poroelastic waveguide coupled with infinite fluids

6.2.2 Wave equations in the fluids

The fluids occupying the domains Ω_j^f $(j = \{1, 2\})$ are modeled by an acoustic fluid whose mass density and bulk modulus at rest are denoted by K_j and ρ_j, respectively. The linearized wave and

Euler equations in fluids are expressed as follows:

$$\rho_j \ddot{p}_j - K_j \nabla^2 p_j = 0 \,, \tag{6.1}$$

$$\rho_j \dot{\boldsymbol{v}}_j + \nabla p_j = \mathbf{0} \,, \tag{6.2}$$

where p_j and $\boldsymbol{v}_j(\boldsymbol{x}, t)$ denote the acoustic pressure and velocity of fluids in Ω_j^f; $\nabla^2(\star)$ is the Laplace operator. The wave celerity in Ω_j^f can be defined by $c_j = \sqrt{K_j/\rho_j}$.

6.2.3 Dynamic equations in the poroelastic domain

The anisotropic poroelasticity theory is used to describe the behavior of porous domain (Ω^b). The poroelastic equations employed here are based upon Biot's original works [44, 46, 130] as well as the recent developments in anisotropic constitutive equations [123, 134, 124]. In Biot's theory the porous media is assumed to consist of a solid skeleton and a connected pore network saturated by fluid (with mass density ρ_f). The sealed pores are considered as part of the solid. It also assumes that the size of the pores are small compared to the characteristic wavelength, and applicability of continuum mechanics to macroscopic two-phase medium. At a point $\boldsymbol{x}$ and at time t, the vectors of displacement of the solid skeleton and of the interstitial fluid are denoted by $\boldsymbol{u}^s(\boldsymbol{x}, t)$ and $\boldsymbol{u}^f(\boldsymbol{x}, t)$, respectively; the relative displacement between the fluid and the solid frame weighted by the porosity ϕ is denoted by $\boldsymbol{w} = \phi(\boldsymbol{u}^f - \boldsymbol{u}^s)$. For the purpose of convenience, the Voigt's notation was used for representing the stress, strain and Biot's effective tensors under the vectorial forms as : $\boldsymbol{s}(\mathbf{x}, t) = \{\sigma_{11}, \sigma_{22}, \sigma_{12}\}^T$, $\boldsymbol{e}(\mathbf{x}, t) = \{\varepsilon_{11}, \varepsilon_{22}, 2\varepsilon_{12}\}^T$, $\boldsymbol{\alpha}(\mathbf{x}, t) = \{\alpha_{11}, \alpha_{22}, \alpha_{12}\}^T$,

where σ_{ij}, ε_{ij} and α_{ij} are the components of the corresponding tensors. By using Voigt's notation, the Biot's constitutive equations for the anisotropic linear poroelastic material [89] read:

$$\boldsymbol{s} = \mathbf{C}\boldsymbol{e} - \boldsymbol{\alpha} p \,, \tag{6.3}$$

$$p = -M(\boldsymbol{m}^T \mathbf{L}\boldsymbol{w} + \boldsymbol{\alpha}^T \mathbf{L}\boldsymbol{u}^s) \,, \tag{6.4}$$

where p is the interstitial pore pressure; $\mathbf{C}_{3\times3}$ is the drained elastic tensor; the scalar M is the Biot's modulus; $\boldsymbol{m} = (1, 1, 0)^T$; and the operator $\mathbf{L}$ is defined by: $\mathbf{L} = \mathbf{L}_1\partial_1 + \mathbf{L}_2\partial_2$, in which $\mathbf{L}_1$ and $\mathbf{L}_2$ are 3×2 matrices whose the elements are zeros except the following ones: $L_1(1,1) = L_1(3,2) = L_2(2,2) = L_2(3,1) = 1$.

The wave propagation in the poroelastic medium is described by a system of two coupled equations representing the momentum equation and the dynamic Darcy law [89]. Neglecting the body forces (other than inertia), this system reads:

$$\rho \ddot{\boldsymbol{u}}^s + \rho^f \ddot{\boldsymbol{w}} - \mathbf{L}^T \boldsymbol{s} = 0 \,, \tag{6.5}$$

$$\rho_f \ddot{\boldsymbol{u}}^s + \tilde{\boldsymbol{a}} * \ddot{\boldsymbol{w}} + \mathbf{L}^T \boldsymbol{m} p = 0 \,, \tag{6.6}$$

where $\rho = \phi\rho_f + (1-\phi)\rho_s$ is the mixture density (or apparent density); ρ_s and ρ_f are mass densities of the solid (matrix) material and the saturating fluid, respectively and ϕ is the porosity. The viscodynamic operator $\tilde{\boldsymbol{a}}$ is a frequency-dependent symmetric second-order tensor which depend on the permeability and tortuosity of the medium. For materials with orthorhombic symmetry, it has only non-zero diagonal components. In this work, we used the Johnson-Koplik-Dashen (JKD) model [135] in which the diagonal components of $\tilde{\boldsymbol{a}}$ are given by :

$$a_{jj}(\omega) = \frac{\rho^f}{\phi}\left(a_j^\infty + \frac{\mathrm{i}\phi\eta F_j(\omega)}{\omega\rho\kappa_j}\right) \,, \tag{6.7}$$

where, η denotes the dynamic viscosity of the pore fluid, a_j^∞ and κ_j are the tortuosity and the low-frequency limit permeability of the skeleton in the direction $\mathbf{e}_j$, respectively.

By noting that $\boldsymbol{e} = \mathbf{L}\boldsymbol{u}^s$ and by substituting Eq. (6.4) into Eq. (6.3), the vectors $\boldsymbol{s}$ and $\boldsymbol{m}p$ in Eqs. (6.5-6.6) may be expressed in terms of $\boldsymbol{u}^s$ and $\boldsymbol{w}$ as follows:

$$\boldsymbol{s} = \mathbf{C}_u\mathbf{L}\boldsymbol{u}^s + \mathbf{C}_\alpha\mathbf{L}\boldsymbol{w} \,, \tag{6.8}$$

$$\boldsymbol{m}p = -(\mathbf{C}_M\mathbf{L}\boldsymbol{w} + \mathbf{C}_\alpha^T\mathbf{L}\boldsymbol{u}^s) \,, \tag{6.9}$$

where $\mathbf{C}_u = \mathbf{C} + M\boldsymbol{\alpha}\boldsymbol{\alpha}^T$, $\mathbf{C}_\alpha = M\boldsymbol{\alpha}\boldsymbol{m}^T$, $\mathbf{C}_M = M\boldsymbol{m}\boldsymbol{m}^T$. The tensor $\mathbf{C}_u$ is known as the undrained elasticity tensor, which may be considered as the rigidity of an equivalent elastic medium in which the relative movement between the interstitial fluid and solid skeleton is null (*i.e.* when $\boldsymbol{w} = \mathbf{0}$). One may also notice that while $\mathbf{C}_u$ and $\mathbf{C}_M$ are symmetric, $\mathbf{C}_\alpha$ of an anisotropic medium is not; it could be symmetric only if the considered poroelastic medium is isotropic (*i.e.* when $\alpha_{11} = \alpha_{22}$ and $\alpha_{12} = 0$).

6.2.4 Boundary conditions

At interfaces between the porous media and the fluid domains At both interfaces Γ_1^{bf} and Γ_2^{bf}, open pore condition was assumed, leading to a continuity condition of the normal velocity between the poroelastic medium and the surrounding fluids [89] :

$$\dot{\boldsymbol{w}} \cdot \mathbf{n}_j^b = (\boldsymbol{v}_j - \dot{\boldsymbol{u}}^s) \cdot \mathbf{n}_j^b \,, \quad \forall \boldsymbol{x} \in \Gamma_j^{bf} \ (j = \{1, 2\}). \tag{6.10}$$

In view of the Euler equation (Eq. (6.2)), this interface condition may be rewritten as:

$$\Big(\frac{1}{\rho_j}\nabla p_j + \ddot{\boldsymbol{w}} + \ddot{\boldsymbol{u}}^s\Big) \cdot \mathbf{n}_j^b = 0 \,, \quad \forall \boldsymbol{x} \in \Gamma_j^{bf} \ (j = \{1, 2\}). \tag{6.11}$$

In addition, the conditions of stress continuity at the porous-fluid interfaces [89] impose that :

$$\left.\begin{array}{l} \boldsymbol{t} = -p_j\mathbf{n}_j^b \\ p = p_j \end{array}\right\} \quad \forall \boldsymbol{x} \in \Gamma_j^{bf} \ (j = \{1, 2\}), \tag{6.12}$$

where $\boldsymbol{n}_j^b$ is the outward normal unit vector at the interfaces from Ω^b toward Ω_j^f and $\boldsymbol{t}$ is the traction vector. It is worth to note that the outward unit vector of the solid domain is related to unit vector of the fluid domain by $\mathbf{n}_j^b{=}{-}\mathbf{n}_j^f$ and $\boldsymbol{t} = \mathbf{L}_2^T\boldsymbol{s} = \{\sigma_{12}, \sigma_{22}\}^T$.

Exterior boundaries The radiation condition of fluid pressure in Ω_j^f $(j = \{1, 2\})$ may be formally written by :

$$p_j \to 0 \quad \text{when } |\boldsymbol{x}| \to \pm\infty, \tag{6.13}$$

6.2.5 Weak formulations

Weak formulation in the fluid domains The pressure field in the fluid occupying the domain Ω_j^f is described by Eq. (6.1). The weak form of this equation by taking into account the boundary conditions Eqs. (6.13)-(6.11) reads

$$\int_{\Omega_j^f} \delta p_j^* \rho_j \ddot{p}_j d\Omega_j^f + \int_{\Omega_j^f} \nabla\delta p_j^* K_j \nabla p_j d\Omega_j^f - \int_{\Gamma_j^{bf}} \delta p_j^* \rho_j K_j (\ddot{\boldsymbol{u}}^s + \ddot{\boldsymbol{w}}) \cdot \mathbf{n}_j^f d\Gamma_j^{bf} \,, \quad \forall \delta p_j \in \mathcal{C}^{ad}, \tag{6.14}$$

Weak formulation in the poroelastic domain Upon integrating Eqs. (6.5) and Eqs. (6.6) against the test function $\delta\boldsymbol{u}$ and $\delta\boldsymbol{w}$, respectively and considering the interface conditions Eqs. (6.13)-(6.11), the weak formulation of the boundary valued problem in the poroelastic layer Ω^b may be derived as:

$$\begin{aligned}
&\int_{\Omega^b} \delta\boldsymbol{u}^*\rho\ddot{\boldsymbol{u}}^s \mathrm{d}v + \int_{\Omega^b} \delta\boldsymbol{u}^*\rho^f\ddot{\boldsymbol{w}}\mathrm{d}v + \int_{\Omega^b} \mathbf{L}^T\delta\boldsymbol{u}^*(\mathbf{C}_u\mathbf{L}\boldsymbol{u}^s + \mathbf{C}_\alpha\mathbf{L}\boldsymbol{w})\mathrm{d}v + \int_{\Gamma_j^{bf}} \delta\boldsymbol{u}^*\big(p_j\boldsymbol{n}^b\big)\mathrm{d}s = \mathbf{0}\,,\\
&\int_{\Omega^b} \delta\boldsymbol{w}^*(\tilde{\boldsymbol{a}}\ddot{\boldsymbol{w}})\mathrm{d}v + \int_{\Omega^b} \delta\boldsymbol{w}^*\rho^f\ddot{\boldsymbol{u}}^s\mathrm{d}v + \int_{\Omega^b} \mathbf{L}^T\delta\boldsymbol{w}^*(\mathbf{C}_M\mathbf{L}\boldsymbol{w} + \mathbf{C}_\alpha^T\mathbf{L}\boldsymbol{u}^s)\mathrm{d}v + \int_{\Gamma_j^{bf}} \delta\boldsymbol{w}^*\big(p_j\boldsymbol{n}^b\big)\mathrm{d}s = \mathbf{0}\,,\\
&\quad \forall(\delta\boldsymbol{u},\delta\boldsymbol{w}) \in \mathcal{C}^{ad}.
\end{aligned} \tag{6.15}$$

6.3 Equations in the frequency-wavenumber domain

By looking for harmonic solutions of waves propagating along the axial direction ($\mathbf{e}_1$) for which a field φ ($\varphi \in \{u_1, u_2, w_1, w_2, p_1, p_2\}$) in Ω is expressed under following form:

$$\varphi(x_1, x_2, t) = \tilde{\varphi}(x_2)e^{\mathrm{i}(k_1x_1 - \omega t)}\,, \tag{6.16}$$

where $\mathrm{i}^2 = -1$; k_1 is the wavenumber in the $\mathbf{e}_1$-direction. Note that in the frequency-wavenumber ($\omega - k_1$) domain, the derivatives with respect to t and to x_1 can be replaced by: $(\dot{\star}) \to -\mathrm{i}\omega(\star)$ and $\partial_1(\star) \to \mathrm{i}k_1(\star)$, respectively. Hence, the considered two-dimensional problem may be simplified into a system of one-dimensional (1D) PDEs with respect only to x_2. Moreover, in this study, as the semi-infinite fluid domains were modeled by using the well-known Perfect Matched Layer (PML) technique (see 4.3.1), following finite 1D domains could be introduced $\bar{\Omega}^b = [0, h]$, $\bar{\Omega}^{f_1} = [-h_1^f, 0]$ and $\bar{\Omega}^{f_2} = [h, h + h_2^f]$ for modeling the poroelastic and fluid regions.

6.3.1 Strong form

By replacing Eq. (6.16) into Eqs. (6.1,6.5 & 6.6), the performing some algebraic manipulations, the later equations may be transformed into the ($\omega - k_1$) domain as follows:

$$-\omega^2\rho_j\tilde{p}_j + k_1^2K_j\tilde{p}_j - K_j\partial_2^2\tilde{p}_j = 0\,, \quad \forall x_2 \in \bar{\Omega}_j^f, \quad j = \{1, 2\}\,, \tag{6.17}$$

$$-\omega^2\mathbf{B}_\rho\mathbf{v} + k_1^2\mathbf{B}_0\mathbf{v} - \mathrm{i}k_1(\mathbf{B}_1 + \mathbf{B}_1^T)\partial_2\mathbf{v} - \mathbf{B}_2\partial_2^2\mathbf{v} = \mathbf{0}, \quad \forall x_2 \in \bar{\Omega}^b. \tag{6.18}$$

where $\mathbf{v} = (\tilde{\boldsymbol{u}}^s, \tilde{\boldsymbol{w}})^T$ and:

$$\mathbf{B}_\rho = \begin{bmatrix} \rho\mathbf{I}_2 & \rho^f\mathbf{I}_2 \\ \rho^f\mathbf{I}_2 & \tilde{\boldsymbol{a}} \end{bmatrix}, \quad \mathbf{B}_0 = \begin{bmatrix} \mathbf{A}_u^{11} & \mathbf{A}_\alpha^{11} \\ \mathbf{A}_\alpha^{11} & \mathbf{A}_M^{11} \end{bmatrix}, \quad \mathbf{B}_1 = \begin{bmatrix} \mathbf{A}_u^{12} & \mathbf{A}_\alpha^{12} \\ \mathbf{A}_\alpha^{12} & \mathbf{A}_M^{12} \end{bmatrix}, \quad \mathbf{B}_2 = \begin{bmatrix} \mathbf{A}_u^{22} & \mathbf{A}_\alpha^{22} \\ \mathbf{A}_\alpha^{22} & \mathbf{A}_M^{22} \end{bmatrix} \tag{6.19}$$

in which $\mathbf{I}_2$ denotes the 2-by-2 identity matrix; the matrices $\mathbf{A}_u^{ab}$, $\mathbf{A}_\alpha^{ab}$ and $\mathbf{A}_M^{ab}$ with $a, b = \{1, 2\}$ are defined by: $\mathbf{A}_u^{ab} = \mathbf{L}_a^T\mathbf{C}_u\mathbf{L}_b$, $\mathbf{A}_\alpha^{ab} = \mathbf{L}_a^T\mathbf{C}_\alpha\mathbf{L}_b$, $\mathbf{A}_M^{ab} = \mathbf{L}_a^T\mathbf{C}_M\mathbf{L}_b$.

The boundary conditions (Eqs. 6.11,6.13) for the fluid domains $\bar{\Omega}^{f_j}$ ($j = \{1, 2\}$) may be now expressed as:

$$\partial_2\tilde{p}_j = \omega^2\rho_j(\tilde{u}_2^s + \tilde{w}_2), \qquad \text{at } x_2 = x_2^{\Gamma_j^b}, \tag{6.20}$$

$$\tilde{p}_1 = \tilde{p}_2 = 0 \qquad \text{at } x_2 = x_2^{\Gamma_j^\infty} \tag{6.21}$$

where $x_2^{\Gamma_1^b}=0$, $x_2^{\Gamma_2^b}=h$, $x_2^{\Gamma_j^\infty}=-h_1^f$, $x_2^{\Gamma_2^\infty}=h+h_2^f$ are the vertical coordinates of fluid domains' boundaries, respectively. Similarly, the stress continuity conditions (Eq. 6.12) transformed into ($\omega-k_1$) domain read:

$$\left.\begin{aligned}&\mathrm{i}k_1\left(\mathbf{A}_u^{21}\tilde{\boldsymbol{u}}+\mathbf{A}_u^{22}\tilde{\boldsymbol{w}}\right)+\left(\mathbf{A}_\alpha^{21}\partial_2\tilde{\boldsymbol{u}}+\mathbf{A}_\alpha^{22}\partial_2\tilde{\boldsymbol{w}}\right)=(0,-\tilde{p}_j)^T\\&-\mathrm{i}k_1M\left(\alpha_{11}\tilde{u}_1+\alpha_{12}\tilde{u}_2+\tilde{w}_1\right)-M\left(\alpha_{12}\partial_2\tilde{u}_1+\alpha_{22}\partial_2\tilde{u}_2+\partial_2\tilde{w}_2\right)=\tilde{p}\end{aligned}\right\}\quad\text{at } x_2=x_2^{\Gamma_j^b}\tag{6.22}$$

6.3.2 Weak form

In the frequency-wavenumber domain, the weak formulations of the fluids ($\bar{\Omega}^{f_j},\ j=\{1,2\}$), and of the poroelastic layer ($\bar{\Omega}^b$) may be derived by replacing Eq. (6.16) into Eqs. (6.14,6.15):

$$\begin{aligned}&-\omega^2\int_{\bar{\Omega}_j^f}\delta\tilde{p}_j^*\rho_j\tilde{p}_j\gamma_2dx_2+k_1^2\int_{\bar{\Omega}_j^f}\delta\tilde{p}_j^*K_j\tilde{p}_j\gamma_2dx_2+\int_{\bar{\Omega}_j^f}\partial_2\delta\tilde{p}_j^*K_j\partial_2\tilde{p}_j(1/\gamma_2)dx_2\\&\qquad-\omega^2\delta p_j^*\rho_jK_j\left(\tilde{u}_2^s(x_2^{\Gamma_j})+\tilde{w}_2(x_2^{\Gamma_j})\right)=0,\end{aligned}\tag{6.23}$$

$$\begin{aligned}&-\omega^2\int_{\bar{\Omega}^b}\delta\mathbf{v}\cdot\mathbf{B}_\rho\mathbf{v}dx_2+k_1^2\int_{\bar{\Omega}^b}\delta\mathbf{v}\cdot\mathbf{B}_0\mathbf{v}dx_2+\mathrm{i}k_1\int_{\bar{\Omega}^b}\left(\partial_2\delta\mathbf{v}\cdot\mathbf{B}_1\mathbf{v}-\delta\mathbf{v}\cdot\mathbf{B}_2\partial_2\mathbf{v}\right)dx_2\\&\quad+\int_{\bar{\Omega}^b}\partial_2\delta\mathbf{v}\cdot\mathbf{B}_2\partial_2\mathbf{v}dx_2+(\delta\tilde{u}_2(0)+\delta\tilde{w}_2(0))\tilde{p}_1(0)+(\delta\tilde{u}_2(h)+\delta\tilde{w}_2(h))\tilde{p}_2(h)=0,\end{aligned}\tag{6.24}$$

in which $\gamma_2(x_2)$ is a continuous function which was introduced in the PMLs of the fluid domains (see 4.3.1).

6.4 Numerical resolutions using NURBS-based approximations

6.4.1 B-spline and NURBS basis functions

In the framework of standard SAFE method [4], Lagrange polynomials usually served as interpolation functions for the discretization of weak formulations presented in Sec. 6.3.2. In this work, we adopt isogeometric-based approaches where the non-uniform rational B-spline (NURBS) basis functions are used for discretizing the problems (in strong or weak forms) presented in Sec. 6.3. Basically, B-spline basis functions of order q are determined in a parameter domain $\hat{\Omega}\subset\mathbb{R}$ using a sequence of non-decreasing set of coordinates called *knot vector* defined as $\Xi=\{\xi_1,\xi_2,\xi_3,...,\xi_{n+q+1}\}$, where $\xi_i\in\mathbb{R}$ ($i=1,2,...,n$) is the i^{th} knot and n is the number of basis functions used to construct the B-spline curve. For a given knot vector, the corresponding set of B-spline basis functions $B_{i,q}$ are defined by the well-known Cox-de Boor recursion formula as:

$$q=0\ :\quad B_{i,0}(\xi)=\begin{cases}1 & \text{if } \xi_i<\xi<\xi_{i+1},\\0 & \text{otherwise,}\end{cases}\tag{6.25a}$$

$$q>0\ :\quad B_{i,q}(\xi)=\frac{\xi-\xi_i}{\xi_{i+q}-\xi_i}B_{i,q-1}(\xi)+\frac{\xi_{i+q+1}-\xi}{\xi_{i+q+1}-\xi_{i+1}}B_{i+1,q-1}(\xi).\tag{6.25b}$$

Note that the quotient $0/0$ is assumed to be zero. Open knot vectors, where the first and the last knot each have a multiplicity of $q+1$, are standard in CAD Non-uniform rational B-spline (NURBS) basis

functions are built from the B-spline functions by assigning a weigh w_i to every B-spline function $B_{i,q}(\xi)$:

$$R_{i,q}(\xi) = \frac{B_{i,q}(\xi) w_i}{\sum_{j=1}^{n} B_{j,q}(\xi) w_j}. \tag{6.26}$$

The NURBS basis functions have some advantage such as higher continuity across the element boundaries, partition of unity, variation diminishing, linear independence and compact support. Such a complete set of basis functions can be employed in any finite finite element or collocation framework. According to the isogeometric concept in which the same basis functions are used for the approximation of solution fields and for geometry representation, the approximation of a complex-valued function $\varphi(x)$, denoted by $\hat{\varphi}^h$, is given by :

$$\varphi(x) \approx \hat{\varphi}^h = \sum_{i=1}^{n} R_{i,q}(\xi) \Phi_i \ , \tag{6.27}$$

where the complex-valued coefficients Φ_i are the corresponding control variables (values at the control points). Using the inversion of geometrical mapping $x_2(\xi)$ the function $\hat{v}^h$ over the physical domain Ω can be define such that $v^h = \hat{v}^h \circ x^{-1}$.

6.4.2 Semi-analytical isogeometric Galerkin method (SAIGA-G)

For simplify the presentation, we assume that each domain $\bar{\Omega}_1^f$, $\bar{\Omega}_2^f$ and $\bar{\Omega}^b$ is discretized using only one patch with n_1, n_b, n_2 being the number of basis functions in the patches of $\bar{\Omega}^{f_1}$, $\bar{\Omega}^b$, $\bar{\Omega}^{f_2}$, respectively. By using the Galerkin finite element method, same approximations are applied for both functions $\tilde{\boldsymbol{u}}^h$ and $\delta\tilde{\boldsymbol{u}}^h$ (as well as for $\tilde{\boldsymbol{w}}^h$ and $\delta\tilde{\boldsymbol{w}}^h$; $\tilde{p}_\alpha^h$ and $\delta\tilde{p}_\alpha^h$) on each patch:

$$\tilde{\boldsymbol{u}}^h = \mathbf{R}^u \mathbf{U}, \quad \delta\tilde{\boldsymbol{u}}^h = \mathbf{R}^u \delta\mathbf{U}, \tag{6.28a}$$

$$\tilde{\boldsymbol{w}}^h = \mathbf{R}^w \mathbf{W}, \quad \delta\tilde{\boldsymbol{w}}^h = \mathbf{R}^w \delta\mathbf{W}, \tag{6.28b}$$

$$\tilde{p}_j^h = \mathbf{R}_j^p \mathbf{P}_j, \quad \delta\tilde{p}_j^h = \mathbf{R}_j^p \delta\mathbf{P}_j, \tag{6.28c}$$

where $\mathbf{R}^u_{2\times 2n_b}$, $\mathbf{R}^w_{2\times 2n_b}$ and $(\mathbf{R}_j^p)_{1\times n_j}$ are the interpolation matrix containing the NURBS basis functions (Eq. (6.26)); $\mathbf{U}_{2n_b\times 1}$, $\delta\mathbf{U}_{2n_b\times 1}$, $\mathbf{W}_{2n_b\times 1}$ and $\delta\mathbf{W}_{2n_b\times 1}$ are the vectors of control displacements; $(\mathbf{P}_j)_{n_j\times 1}$ and $(\delta\mathbf{P}_j)_{n_j\times 1}$ are the pressure vectors of control pressures. In this work, we used the same NURBS basis functions for approximation of the solution fields in Eqs. (6.28a-6.28c). By substituting the approximations (Eqs. 6.28a-6.28c) into the weak formulations (Eqs. 6.23-6.24), one obtains a eigenvalue problem:

$$(-\omega^2 \mathbf{M} + \mathbf{K}_0 + \mathrm{i}k_1 \mathbf{K}_1 + k_1^2 \mathbf{K}_2)\mathbf{V} = \mathbf{0} \ , \tag{6.29}$$

where $\mathbf{V} = (\mathbf{P}_1, \mathbf{U}, \mathbf{W}, \mathbf{P}_2)^T$ contains the global eigenvectors the fluid pressures ($\mathbf{P}_1$, $\mathbf{P}_2$) in fluids and of displacements ($\mathbf{U}$, $\mathbf{W}$) in the poroelastic domain, respectively; the global matrices $\mathbf{M}$ and $\mathbf{K}_0$, $\mathbf{K}_1$, $\mathbf{K}_2$ are are square matrices of order $(n_1 + 4n_b + n_2)$ and may be determined from the assembling of corresponding elementary matrices in poroelastic and fluid domains:

$$\mathbf{M} = \begin{bmatrix} \mathbf{M}^{p_1} & \mathbf{M}^{p_1 u} & \mathbf{M}^{p_1 w} & \mathbf{0} \\ \mathbf{0} & \mathbf{M}^{u} & \mathbf{M}^{uw} & \mathbf{0} \\ \mathbf{0} & \mathbf{M}^{wu} & \mathbf{M}^{w} & \mathbf{0} \\ \mathbf{0} & \mathbf{M}^{p_2 u} & \mathbf{M}^{p_2 w} & \mathbf{M}^{p_2} \end{bmatrix}, \mathbf{K}_0 = \begin{bmatrix} \mathbf{K}_0^{p_1} & \mathbf{0} & \mathbf{0} & \mathbf{0} \\ \mathbf{K}_0^{up_1} & \mathbf{K}_0^{u} & \mathbf{K}_0^{uw} & \mathbf{K}_0^{up_2} \\ \mathbf{K}_0^{wp_1} & \mathbf{K}_0^{wu} & \mathbf{K}_0^{w} & \mathbf{K}_0^{wp_2} \\ \mathbf{0} & \mathbf{0} & \mathbf{0} & \mathbf{K}_0^{p_2} \end{bmatrix}, \tag{6.30a}$$

$$\mathbf{K}_1 = \begin{bmatrix} \mathbf{0} & \mathbf{0} & \mathbf{0} & \mathbf{0} \\ \mathbf{0} & \mathbf{K}_1^{u} & \mathbf{K}_1^{uw} & \mathbf{0} \\ \mathbf{0} & \mathbf{K}_1^{wu} & \mathbf{K}_1^{w} & \mathbf{0} \\ \mathbf{0} & \mathbf{0} & \mathbf{0} & \mathbf{0} \end{bmatrix}, \mathbf{K}_2 = \begin{bmatrix} \mathbf{K}_2^{p_1} & \mathbf{0} & \mathbf{0} & \mathbf{0} \\ \mathbf{0} & \mathbf{K}_2^{u} & \mathbf{K}_2^{uw} & \mathbf{0} \\ \mathbf{0} & \mathbf{K}_2^{wu} & \mathbf{K}_2^{w} & \mathbf{0} \\ \mathbf{0} & \mathbf{0} & \mathbf{0} & \mathbf{K}_2^{p_2} \end{bmatrix}, \tag{6.30b}$$

In these matrices, the sub-matrices related to the poroelastic solution fields $(\mathbf{U}, \mathbf{W})$ and fluid pressure fields $(\mathbf{P}_1, \mathbf{P}_2)$ may be distinguished. For the poroelastic layer, the matrices related to the $\mathbf{U}$ are defined as:

$$\mathbf{M}^u = \int_{\bar{\Omega}^b} (\mathbf{R}^u)^T \rho \mathbf{R}^u dx_2, \quad \mathbf{M}^{uw} = \int_{\bar{\Omega}^b} (\mathbf{R}^u)^T \rho_f \mathbf{R}^w dx_2 \,, \tag{6.31a}$$

$$\mathbf{K}_2^u = \int_{\bar{\Omega}^b} (\mathbf{R}^u)^T \mathbf{A}_u^{11} \mathbf{R}^u dx_2, \quad \mathbf{K}_2^{uw} = \int_{\bar{\Omega}^b} (\mathbf{R}^u)^T \mathbf{A}_\alpha^{11} \mathbf{R}^w dx_2 \,, \tag{6.31b}$$

$$\mathbf{K}_1^u = \int_{\bar{\Omega}^b} 2\left\{(\partial_2 \mathbf{R}^u)^T \mathbf{A}_u^{21} \mathbf{R}^u\right\}_a dx_2 \,, \quad \mathbf{K}_1^{uw} = \int_{\bar{\Omega}^b} 2\left\{\partial_2 (\mathbf{R}^u)^T \mathbf{A}_\alpha^{21} \mathbf{R}^w\right\}_a dx_2 \,, \tag{6.31c}$$

$$\mathbf{K}_0^u = \int_{\bar{\Omega}^b} \partial_2 (\mathbf{R}^u)^T \mathbf{A}_u^{22} \partial_2 \mathbf{R}^u dx_2, \quad \mathbf{K}_0^{uw} = \int_{\bar{\Omega}^b} \partial_2 (\mathbf{R}^u)^T \mathbf{A}_\alpha^{22} \partial_2 \mathbf{R}^w dx_2 \,, \tag{6.31d}$$

$$\left(\mathbf{K}_0^{up_1}\right)_{\ell k} = \delta_{\ell 2} \delta_{k n_1}, \quad \left(\mathbf{K}_0^{up_2}\right)_{\ell k} = \delta_{\ell (2n_b)} \delta_{k1}, \tag{6.31e}$$

where $\{\cdot\}_a$ denotes the anti-symmetric part of a matrix; δ_{jk} denotes the Kronecker's delta; the upper indexes ^{uw} or ^{up} represent the couplings between $\mathbf{U}$ & $\mathbf{W}$ or $\mathbf{U}$ & $\mathbf{P}_j$, respectively. Similarly, the matrices related to the $\mathbf{W}$ are given by :

$$\mathbf{M}^w = \int_{\bar{\Omega}^b} (\mathbf{R}^w)^T \tilde{\boldsymbol{a}} \mathbf{R}^w dx_2 \,, \quad \mathbf{M}^{wu} = \int_{\bar{\Omega}^b} (\mathbf{R}^w)^T \rho_f \mathbf{R}^u dx_2 \,, \tag{6.32a}$$

$$\mathbf{K}_2^w = \int_{\bar{\Omega}^b} (\mathbf{R}^w)^T \mathbf{A}_M^{11} \mathbf{R}^w dx_2 \,, \quad \mathbf{K}_2^{wu} = \int_{\bar{\Omega}^b} (\mathbf{R}^w)^T \mathbf{A}_\alpha^{11} \mathbf{R}^u dx_2 \,, \tag{6.32b}$$

$$\mathbf{K}_1^w = \int_{\bar{\Omega}^b} 2\left\{(\partial_2 \mathbf{R}^w)^T \mathbf{A}_M^{21} \mathbf{R}^w\right\}_a dx_2 \,, \quad \mathbf{K}_1^{wu} = \int_{\bar{\Omega}^b} 2\left\{(\partial_2 \mathbf{R}^w)^T \mathbf{A}_\alpha^{21} \mathbf{R}^u\right\}_a dx_2 \,, \tag{6.32c}$$

$$\mathbf{K}_0^w = \int_{\bar{\Omega}^b} (\partial_2 \mathbf{R}^w)^T \mathbf{A}_M^{22} \partial_2 \mathbf{R}^w dx_2 \,, \quad \mathbf{K}_0^{wu} = \int_{\bar{\Omega}^b} (\partial_2 \mathbf{R}^w)^T \mathbf{A}_\alpha^{22} \partial_2 \mathbf{R}^u dx_2 \,, \tag{6.32d}$$

$$\left(\mathbf{K}_0^{wp_1}\right)_{\ell k} = \delta_{\ell (2n_b+2)} \delta_{k n_1}, \quad \left(\mathbf{K}_0^{wp_2}\right)_{\ell k} = \delta_{\ell (4n_b)} \delta_{k1}, \,, \tag{6.32e}$$

where the upper indexes ^{wu} or ^{wp} represent the couplings between $\mathbf{W}$ & $\mathbf{U}$ or $\mathbf{W}$ & $\mathbf{P}_j$, respectively. The matrices related to the $\mathbf{P}_1$ and $\mathbf{P}_2$ are defined as:

$$\mathbf{M}^{p_j} = \int_{\bar{\Omega}} \rho_j \gamma_{2j} (\mathbf{R}_j^p)^T \mathbf{R}_j^p dx_2, \tag{6.33a}$$

$$\mathbf{K}_0^{p_j} = \int_{\bar{\Omega}} (K_j/\gamma_{2j}) (\partial_2 \mathbf{R}_j^p)^T \partial_2 \mathbf{R}_j^p dx_2, \quad \mathbf{K}_2^{p_j} = \int_{\bar{\Omega}} K_j \gamma_{2j} (\mathbf{R}^p)^T \mathbf{R}^p dx_2, \tag{6.33b}$$

$$\left(\mathbf{M}^{p_1 u}\right)_{\ell k} = \rho_1 K_1 \delta_{\ell (n_1)} \delta_{k2}, \quad \left(\mathbf{M}^{p_1 w}\right)_{\ell k} = \rho_1 K_1 \delta_{\ell (n_1)} \delta_{k (2n_b+2)}, \tag{6.33c}$$

$$\left(\mathbf{M}^{p_2 u}\right)_{\ell k} = \rho_2 K_2 \delta_{\ell 1} \delta_{k (2n_b)}, \quad \left(\mathbf{M}^{p_2 w}\right)_{\ell k} = \rho_2 K_2 \delta_{\ell 1} \delta_{k (4n_b)} \tag{6.33d}$$

Further more due to the fact that $\mathbf{A}_{\alpha\beta} = \mathbf{A}_{\beta\alpha}^T$, it can be shown that that the sub-matrices of the $\mathbf{M}$, $\mathbf{K}_0$, $\mathbf{K}_2$ are symmetric while the sub-matrices of $\mathbf{K}_1$ is anti-symmetric. Note that the in the case where there is no fluid half-spaces the fluid contribution and the corresponding coupling matrices are zeros matrices. All these sub-matrices are computed by using Gauss–Legendre quadrature formula with $r = q + 1$ quadrature nodes per element along each parametric direction which has been shown to be efficient [82].

6.4.3 Semi-analytical isogeometric collocation (SAIGA-C)

To construct the 1D isogeometric collocation method, we follow [132] by firstly choosing three sets of collocation points $\tau_i^{f_1}$ $(i = 1, .., n_1^{\text{col}})$, τ_j^b $(j = 1, .., n_b^{\text{col}})$ and $\tau_k^{f_2}$ $(k = 1, .., n_2^{\text{col}})$ for $\bar{\Omega}^{f_1}$, $\bar{\Omega}^{f_2}$ and $\bar{\Omega}^b$,

respectively. Then we seek the approximations of the fields $\tilde{p}_1$, $\tilde{p}_2$, $\tilde{\boldsymbol{u}}$, $\tilde{\boldsymbol{w}}$ at the collocation points by using the associated NURBS basis functions. In this study, the employed collocation points (τ_i^{φ}) of a field φ ($\varphi = \{u_1, u_2, w_1, w_2, p_1, p_2\}$) are located at the images of the so-called "Greville abscissa". In general, using a given open knot vector $\Xi = \{\xi_1 = 0, \xi_2, \xi_3, ..., \xi_{n+q+1} = 1\}$, in which the first and the last knots have multicity $q+1$, the Greville abscissae points $\bar{\xi}_i$ $(i = 1, 2, ..., n)$ in a parametric space are calculated by

$$\bar{\xi}_i = \frac{\xi_{i+1} + \xi_{i+2} + ... + \xi_{i+q}}{q}. \tag{6.34}$$

By building matrices which contain the k-th derivatives $(k = 0, 1, 2)$ of the NURBS shape functions of the field φ at all collocation points (τ_i^{φ}), the k-th derivatives of φ may be approximated by (Eq. 6.26)

$$\begin{pmatrix} \partial_2^{(k)}\varphi(\tau_1^{\varphi}) \\ \partial_2^{(k)}\varphi(\tau_2^{\varphi}) \\ \vdots \\ \partial_2^{(k)}\varphi(\tau_{n_\varphi^{\text{col}}}^{\varphi}) \end{pmatrix} \approx \begin{bmatrix} \partial_2^{(k)}R_1^{\varphi}(\tau_1^{\varphi}) & \partial_2^{(k)}R_2^{\varphi}(\tau_1^{\varphi}) & \cdots & \partial_2^{(k)}R_{n_\varphi^{\text{col}}}^{\varphi}(\tau_1^{\varphi}) \\ \partial_2^{(k)}R_1^{\varphi}(\tau_2^{\varphi}) & \partial_2^{(k)}R_2^{\varphi}(\tau_2^{\varphi}) & \cdots & \partial_2^{(k)}R_{n_\varphi^{\text{col}}}^{\varphi}(\tau_2^{\varphi}) \\ \cdots & \cdots & \cdots & \cdots \\ \partial_2^{(k)}R_1^{\varphi}(\tau_{n_\varphi^{\text{col}}}^{\varphi}) & \partial_2^{(k)}R_1^{\varphi}(\tau_{n_\varphi^{\text{col}}}^{\varphi}) & \cdots & \cdots \partial_2^{(k)}R_{n_\varphi^{\text{col}}}^{\varphi}(\tau_{n_\varphi^{\text{col}}}^{\varphi}) \end{bmatrix} \begin{pmatrix} \Phi_1 \\ \Phi_2 \\ \vdots \\ \Phi_{n_\varphi^{\text{col}}} \end{pmatrix}, \tag{6.35}$$

where Φ_i denotes the solution of $\varphi(\tau_i^{\varphi})$ at the control points.

In the fluid domain $\bar{\Omega}_j^f$ $(j = 1, 2)$, giving a set of collocation points $\tau_i^{f_j}$ $(i = 1, ..., n_j^{\text{col}})$, one may *a priori* derive from (Eq. (6.17)) a system of (n_j^{col}) equations at every collocations points:

$$-\omega^2\rho_j\tilde{p}_j(\tau_i^{f_j}) + k_1^2K_j\tilde{p}_j(\tau_i^{f_j}) - K_j\partial_2^2\tilde{p}_j(\tau_i^{f_j}) = 0\,. \tag{6.36}$$

However, as this system should satisfy the boundary conditions (6.20), two equations at the first and last collocation points should be replaced, for instance in the lower fluid domain $\bar{\Omega}_1^f$, by:

$$\tilde{p}_1(\tau_1^{f_1}) = 0, \tag{6.37}$$

$$\partial_2\tilde{p}_1(\tau_{n_1^{\text{col}}}^{f_1}) + \rho_1\omega^2\left(\tilde{u}_2(\tau_1^b) + \tilde{w}_2(\tau_1^b)\right) = 0. \tag{6.38}$$

Similar conditions may be set for the upper fluid domain $\bar{\Omega}_2^f$.

Considering the poroelastic domain $\bar{\Omega}^b$, the approximate solutions $\tilde{\boldsymbol{u}}$ and $\tilde{\boldsymbol{w}}$ are evaluated at the collocation points τ_i^b $(i = 1, ..., n_b^{\text{col}})$ should satisfy (6.18):

$$-\omega^2\mathbf{B}_\rho\mathbf{v}(\tau_i^b) + k_1^2\mathbf{B}_0\mathbf{v}(\tau_i^b) - \mathrm{i}k_1(\mathbf{B}_1 + \mathbf{B}_1^T)\partial_2\mathbf{v}(\tau_i^b) - \mathbf{B}_2\partial_2^2\mathbf{v}(\tau_i^b) = \mathbf{0}, \tag{6.39}$$

At the Γ_1^{bf} (interface between Ω_1^f and Ω^b), the stress continuity conditions (6.22) may be expressed in matrix form as follows:

$$\mathrm{i}k_1\begin{bmatrix} \mathbf{A}_u^{21} & \mathbf{A}_u^{22} \\ [M\alpha_{11}, M\alpha_{12}] & [1, 0] \end{bmatrix}\mathbf{v}(\tau_1^b) + \begin{bmatrix} \mathbf{A}_\alpha^{21} & \mathbf{A}_\alpha^{22} \\ [M\alpha_{12}, M\alpha_{22}] & [0, 1] \end{bmatrix}\partial_2\mathbf{v}(\tau_1^b) = -\begin{pmatrix} 0 \\ 1 \\ 1 \end{pmatrix}\tilde{p}_1(\tau_{n_1^{\text{col}}}^{f_1}) \tag{6.40}$$

Again, a similar condition may be set at the interface Γ_2^{bf}.

By applying the approximations (6.35) to the Eqs. (6.36-6.40), then performing some algebraic manipulations for assembling the matrices, we can establish a eigenvalue system containingn $n_1^{\text{col}} + 4\times n_b^{\text{col}} + n_2^{\text{col}}$ equations which has the same form as the one derived by SAIGA-G procedure (Eq. (6.29)):

$$(\mathbf{K}_0 + \mathrm{i}k_1\mathbf{K}_1 + k_1^2\mathbf{K}_2 - \omega^2\mathbf{M})\mathbf{V} = \mathbf{0}\,, \tag{6.41}$$

6.4.4 Resolution of dispersion equations

The system of characteristic equations (6.29) and (6.41) is an eigenvalue problem which is used to determine the relationship between the pulsation ω and the wavenumber k_1. By noting that all global matrices $\mathbf{K}_0$, $\mathbf{K}_1$, and $\mathbf{K}_2$ do not depend on k_1, Eqs. (6.29) and (6.41) are a quadratics eigenvalue problem with respect to k_1 and could be solved by reformulating them under following linearized eigenvalue problem:

$$\left(\begin{bmatrix} \mathbf{0} & -\omega^2\mathbf{M} + \mathbf{K}_0 \\ -\omega^2\mathbf{M} + \mathbf{K}_0 & \mathrm{i}\mathbf{K}_1 \end{bmatrix} - k_1 \begin{bmatrix} -\omega^2\mathbf{M} + \mathbf{K}_0 & \mathbf{0} \\ \mathbf{0} & -\mathbf{K}_2 \end{bmatrix} \right) \begin{pmatrix} \mathbf{V} \\ k_1\mathbf{V} \end{pmatrix} = \mathbf{0} \, . \tag{6.42}$$

For each value of the angular frequency ω, solving Eq. (6.42) allows us to determine the eigenvalues k_1 and their associated eigenvectors (also called by wave structures), $\mathbf{V}(\omega, k_1)$ of guided modes. The frequency-dependent phase velocity ($C_{\mathrm{ph}}(\omega)$) and the attenuation ($\gamma(\omega)$) of a guided mode are given by:

$$C_{\mathrm{ph}} = \frac{\omega}{\mathrm{Re}\left(() \, k_1\right)} \ [\mathrm{m.s}^{-1}], \quad \gamma = \mathrm{Im}\left(() \, k_1\right) \ [\mathrm{Np.m}^{-1}] \, , \tag{6.43}$$

where $\mathrm{Re}\left(()\right)$ and $\mathrm{Im}\left(()\right)$ denote the real and imaginary parts of a complex function.

6.5 Numerical examples

In this section, we will investigate the performance of the proposed NURBS-based methods (*i.e* SAIGA-C and SAIGA-G methods) for computing the dispersion of poroelastic guided-waves in free and fluid coupled anisotropic poroelastic layers. For all examples, the evaluation of the phase velocities, the attenuations as well the mode shapes have been performed by using three approaches SAIGA-C, SAIGA-G and conventional SAFE. As the closed form of analytical solutions are not available, the SAFE's solutions obtained by very fine meshes, which are assumed to be the converged solutions, are served as the reference ones for estimating the numerical errors.

6.5.1 Case of free-boundaries homogeneous poroelastic layers

6.5.1.1 Reference solutions

We consider a 4-mm-thick saturated anisotropic poroelastic plate, which represents a typical cortical bone sample [48]. The porous bone material is assumed to be saturated by water of which the bulk modulus is $K_f = 2.5$ GPa and the density is $\rho_f = 1000$ kg.m^{-3}. The bone's matrix has a density $\rho_s = 1772$ kg.m^{-3} and its components of the elastic tensor (using the Voigt's notations) are given by : $c_{11}^m = 28.7$ GPa, $c_{22}^m = 23.6$ GPa, $c_{12}^m = 9.9$ GPa, $c_{66}^m = 7.25$ GPa and $c_{16}^m = c_{26}^m = 0$ GPa. By using the procedure presented in 5.5.2.4, one can estimate the components of the drained elastic tensor $\mathbf{C}$. For example, the components of $\mathbf{C}$ are given in Tab. 6.1 for the porosity of $\phi = 0.1$ and $\phi = 0.5$. In this numerical study, we assume that the permeability an the tortuosity in the considered medium are isotropic. The diagonal terms of the tortuosity tensor is given by: $a_{11} = a_{22} = 1$.

We first present in Figs. 6.2(a,b) the results of the phase velocity and attenuation computed by using the conventional SAFE formulation with a very fine mesh ($N_{\mathrm{dof}} = 404$ and $q = 2$), which would be sufficient to be considered as a reference solutions. Due to the presence of fluid-filled pores,

Table 6.1 – Parameters of the poroelastic medium for different values of the porosity.

ϕ	c_{11}	c_{12}	c_{22}	c_{66}	$c_{16} = c_{26}$	M	$\kappa_{11} = \kappa_{22}$
-	(GPa)	(GPa)	(GPa)	(GPa)	(GPa)	(GPa)	(m^2)
0.1	24.84	7.27	17.5	5.49	0	18.32	3.33×10^{-13}
0.5	12.76	2.33	5.71	1.87	0	4.19	1.67×10^{-12}

there exist some guided-wave modes with high attenuation. In Fig. 6.2(a,b), the dispersion curves are displayed in two different colors for separated the "low attenuation" (group 1) and "high attenuation" (group 2) modes, which have attenuation ($\gamma = \mathrm{Im}\,(()\,k_1)$) greater or smaller than a value $\bar{\gamma} = 100\ \mathrm{m}^{-1}$, respectively. The phase velocity curves of low-attenuation modes (Fig. 6.2a) are similar to the well-known Lamb-type modes in elastic plates, which are usually designated by the modes A or the modes S in depending to their antisymmetric/symmetric natures. For these modes, the relative fluid-solid displacement ($\boldsymbol{w}$), which is the main cause of viscous effect in poroelastic materials, are much weaker than the displacements of the solid ($\boldsymbol{u}$). As an illustration, Fig. 6.3(a) depicts the shape modes of u_2 and w_2 of the mode A_1 at the frequency $f = 1$ MHz, in which w_2 is found much smaller than u_2. Moreover, for this anti-symmetric mode, one may check that $u_2(0) = u_2(h)$ and $w_2(0) = w_2(h)$ with one wavelength over the plate thickness. Figs. 6.3(b,c) present the in-depth variation of u_2 and w_2 of two high attenuated modes, which correspond to two points B and C at the same frequency ($f = 1\ MHz$) as marked in Fig. 6.2. One may observe that the orders of these modes are higher with more wavelengths over the thickness. Moreover, the fluid-solid relative displacement becomes more significant in comparing to the solid displacement u_2, which induce more important attenuation as expected.

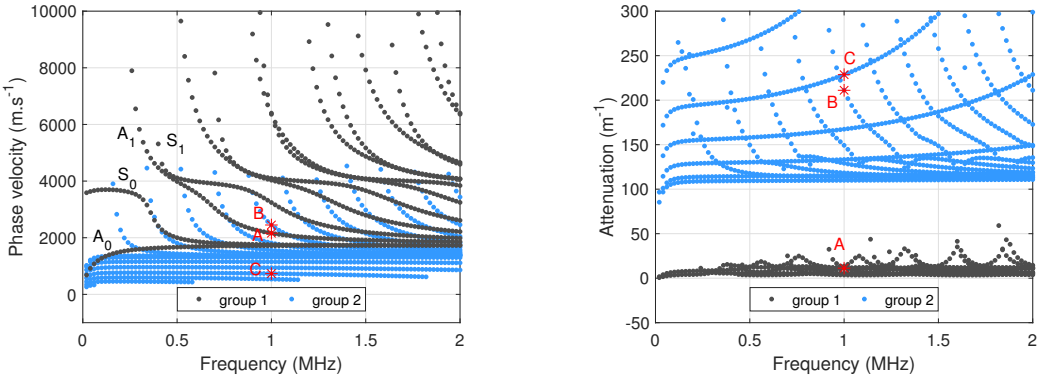

(a) phase velocity ($\omega/\mathrm{Re}\,(()\,k_1)$)

(b) attenuation ($\mathrm{Im}\,(()\,k_1)$)

Figure 6.2 – Dispersion curves of a free poroelastic bone layer; groups 1 and 2 represent low and high attenuated waves, respectively; a filtering criteria $\bar{\gamma} = 100\ m^{-1}$

The wave dispersion in poroelastic plates depends on its porosity [136]. In Fig. 6.4, the phase velocity (C_{ph}) and attenuation (γ) of the first symmetric mode S_0 are shown to be strongly modified while the porosity changes. To visualize the effect of porosity on the wave dispersion, we present in Fig. 6.4(a) the variation of real and imaginary parts of the wavenumber (k_1) *versus* frequency in a 3D graph. Different to the case of elastic plates in which the real wavenumber solutions exist, the wavenumbers of guided-waves poroelatic plates are complex. When $\phi = 0.1$, $\mathrm{Im}\,(()\,k_1)$ is small even

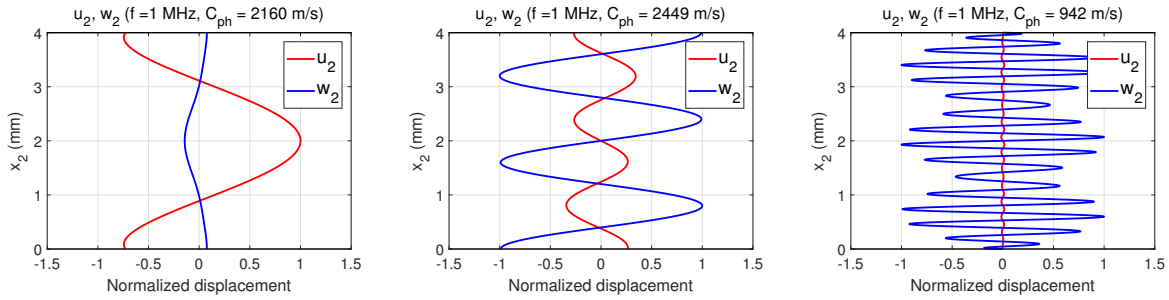

(a) low att. mode (point A) (b) high att. mode (point B) (c) high att. mode (point C)

Figure 6.3 – (Color online) (u_2, w_2) shape modes corresponding to the points (A),(B),(C) marked in Fig. 6.2

at high frequency and the k_1-curve is found closely to the plane $\omega - \mathrm{Re}\,(()\,k_1)$. When $\phi = 0.5$, the imaginary part $\mathrm{Im}\,(()\,k_1)$ may be found to be much more important, especially at high frequency, as the viscous effect due to fluid-solid relative movement becomes significant. As the increase of porosity leads to reducing the material's elasticity and increasing its permeability, we may observe that C_{ph} decreases (Fig. 6.4(b)) and γ significantly increases (Fig. 6.4(c)) when the porosity is varied from 10% to 60%.

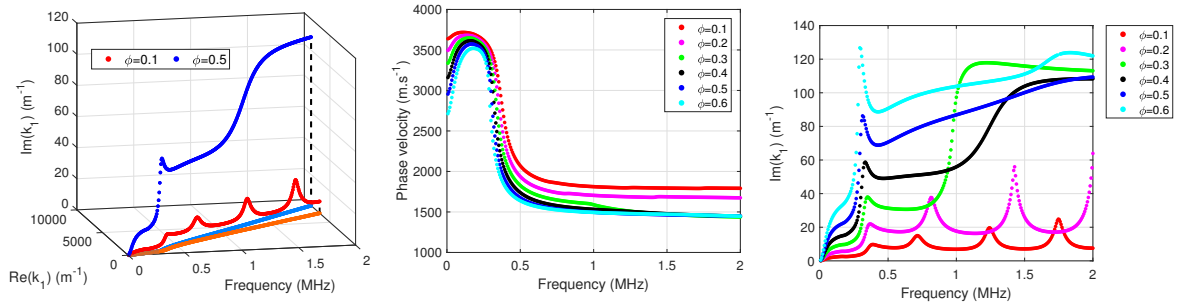

(a) (b) (c)

Figure 6.4 – (Color online) Dependence of S_0-mode dispersion on porosity: (a) wavenumber ($Re\,(()\,k_1)$ and $Im\,(()\,k_1)$); (b) phase velocity; (c) attenuation

6.5.1.2 Validation of SAIGA-G and SAIGA-C methods

The results obtained by the proposed SAIGA-G and SAIGA-C methods were validated by comparing with the reference solution computed by conventional SAFE method. In this example, both SAIGA-G and SAIGA-C modeling are based on a single patch in which the NURBS basis functions with order q over an uniform knot vector were used. The number of elements (spans) in the patch is then given by $N_{\mathrm{el}} = n_{\mathrm{P}} - q = N_{\mathrm{dof}}/n_{\mathrm{dof}} - q$. Consequently, the total number of degrees of freedom (N_{dof}) is: $N_{\mathrm{dof}}^{\text{SAIGA-G}} = N_{\mathrm{dof}}^{\text{SAIGA-C}} = n_{\mathrm{P}} \times n_{\mathrm{dof}}$, where n_{P} is the number of control points (or nodes) and $n_{\mathrm{dof}} = 4$ which is the number of unknowns (u_1, u_2, w_1, w_2) at each control point. On the other hand, by using the conventional SAFE method with $N_{\mathrm{el}}^{\mathrm{SAFE}}$ elements with q^{th}-order Lagrange interpolation function, the total number of degree of freedom is given by: $N_{\mathrm{dof}}^{\mathrm{SAFE}} = (q \times N_{\mathrm{el}}^{\mathrm{SAFE}} + 1) \times n_{\mathrm{dof}}$.

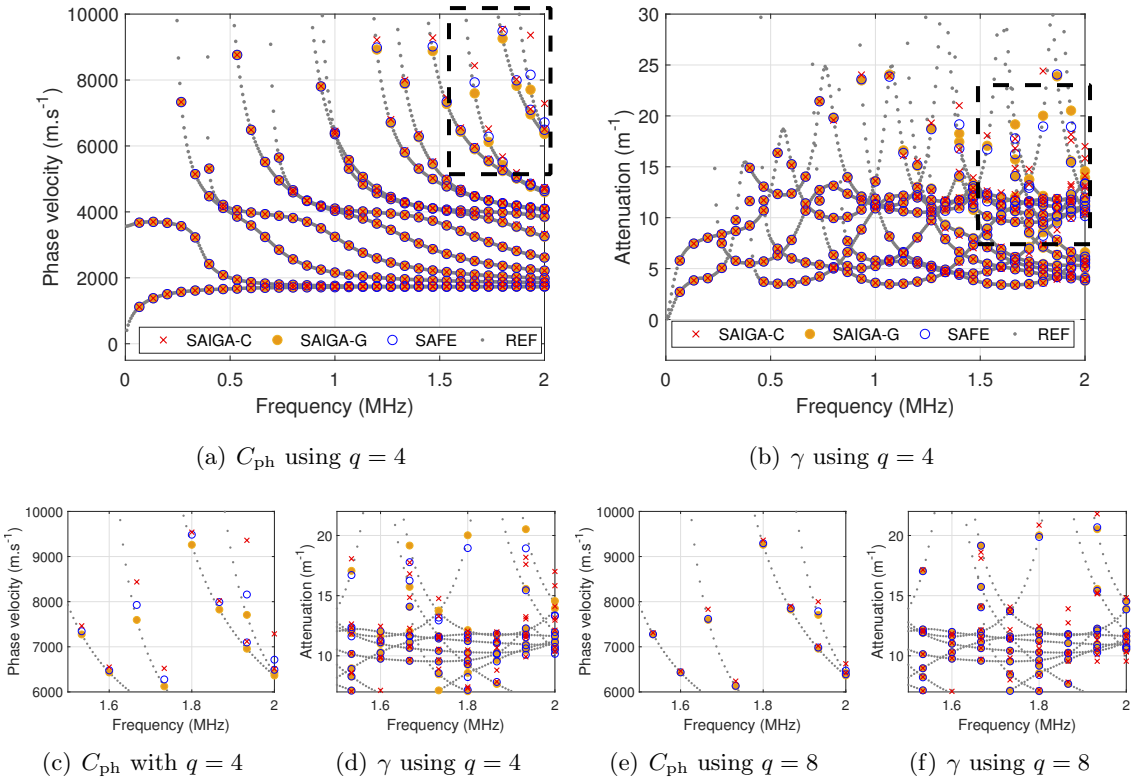

(a) C_{ph} using $q = 4$ (b) γ using $q = 4$

(c) C_{ph} with $q = 4$ (d) γ using $q = 4$ (e) C_{ph} using $q = 8$ (f) γ using $q = 8$

Figure 6.5 – (Color online) Case of a free poroelastic layer ($\phi = 0.1$): validation of SAIGA-C, SAIGA-G and SAFE solutions computed with $q = 4$, $N_{dof} = 68$; sub-figures (c) and (d) are zoomed from the dashed-line windows in sub-figures (a) and (b), respectively.

Dispersion curves of the phase velocity and attenuation *versus* the frequency of the first 14 modes in the frequency range of f =0–2 MHz were computed by using SAIGA-G, SAIGA-C and SAFE methods. Then theses solutions were compared with the reference solution ($q = 2$, $N_{\text{dof}} = 404$) as shown in Figs. 6.5(a,b). In this example, all methods employed quartic-order ($q = 4$) basis functions and have the same $N_{\text{dof}} = 68$: the SAIGA-G method used 13 elements, the SAIGA-C method used 17 collocation points , and the SAFE method used 4 elements. At low frequencies, all of three methods provide accurate estimations of C_{ph} as well as of γ. However, at high frequencies (1.5-2 MHz), the SAIGA-G solution has better precision than the ones obtained by SAIGA-C and SAFE methods, especially the modes presented in the dashed-line windows plotted in Fig. 6.5(a,b), which respectively are zoomed in Figs. 6.5(c,d) for a clearer comparison. Moreover, it may be observed in Figs. 6.5(c,d) that SAFE solutions didn't capture exactly the reference ones as the SAIGA-G solutions did, but they are better than SAIGA-C ones. In Figs. 6.5(e,f), we present the solutions computed by using $q = 8$ and by arranging the number of elements/spans ($N_{\text{el}}^{\text{SAIGA-C}} = N_{\text{el}}^{\text{SAIGA-G}} = 9$ and $N_{\text{el}}^{\text{SAFE}} = 2$) so that we still have $N_{\text{dof}} = 68$. It may be seen that using $q = 8$ improves the precision of SAFE solution. The precision the SAIG-C solution was even more significantly improved, although the attenuation of some modes were still not exactly predicted. This comparison affirms the fact that the collocation based approach generally requires a higher order of NURBS basis functions than the Galerkin based approach.

Figs. 6.6(a,b) affirm the validation of C_{ph} solutions computed using SAIGA-G, SAIGA-C and SAFE methods for higher porosity cases ($\phi = 0.5$ and $\phi = 0.6$). Similar to the case ($\phi = 0.1$),

the results of higher modes at higher frequency range (1.5-2 MHz) were shown to be less accurate. Moreover, the numerical errors seem to be more important when considering plates with higher porosity, in which the pore fluid movement becomes more significant. We may observe that the branch of mode S_0, which was continuous in the cases ($\phi = 0.1, 0.5$), turned out to be discontinuous at frequencies around 0.3 MHz, due to excessive values of attenuation.

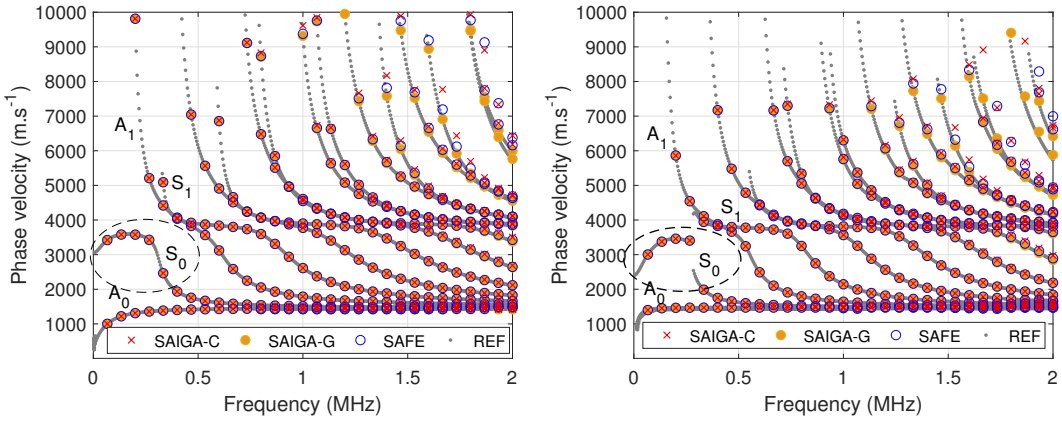

(a) $\phi = 0.5$ (b) $\phi = 0.6$

Figure 6.6 – (Color online) Phase velocity curves of poroelastic bone layer: comparison between the SAIGA-C ($q = 4$ and $N_{dof} = 68$), SAIGA-G ($q = 4$ and $N_{dof} = 68$) and SAFE ($q = 4$ and $N_{dof} = 68$) and REF solution ($q = 2$ and $N_{dof} = 404$)

6.5.1.3 Convergence study

We aim to study the convergence rate of the proposed methods for evaluating the phase velocity in poroelastic plates. In particular, we are interested in investigating the accuracy of the numerical results when considering a specific mode over a frequency range. To do so, we introduce a function $\texttt{err}(m)$ which estimates the relative errors of the numerical solution for a mode m as

$$\texttt{err}(m) = \sqrt{\frac{1}{N_f}\sum_{i=1}^{N_f}\left(\frac{C_{\text{ph}}^{num}(f_i,m) - C_{\text{ph}}^{REF}(f_i,m)}{C_{\text{ph}}^{REF}(f_i,m)}\right)^2}, \tag{6.44}$$

where N^f is the number of the frequency values used for the computation in the considered frequency range, $C_{\text{ph}}^{num}(f_i,m)$ and $C_{\text{ph}}^{REF}(f_i,m)$ denote the phase velocities of the mode m evaluated at the frequency (f_i) by using three numerical approaches, and its reference values, respectively.

The convergence analysis were performed for the mode S_0 in two cases of porosity $\phi = 0.1$ and $\phi = 0.5$. Figs. 6.7(a,b) depict the variation of the errors of the phase velocity of S_0-mode over the frequency range $f = 0-2$ MHz *versus* the number of DOF. Different orders q of NURBS and Lagrange basis functions were investigated. Overall, the error analysis presented in Figs. 6.7(a,b) shows that all methods (SAFE, SAIGA-C, SAIGA-G) implied the h- and p-convergences as expected.

While using the SAFE method with $q = 4$, we found that the numerical errors (in the both cases $\phi = 0.1$ and $\phi = 0.5$) are not efficiently reduced by applying mesh refinement. Using higher-orders ($q = 6, 8, 10$) allows to improve significantly the accuracy solutions. Moreover, the convergence rate

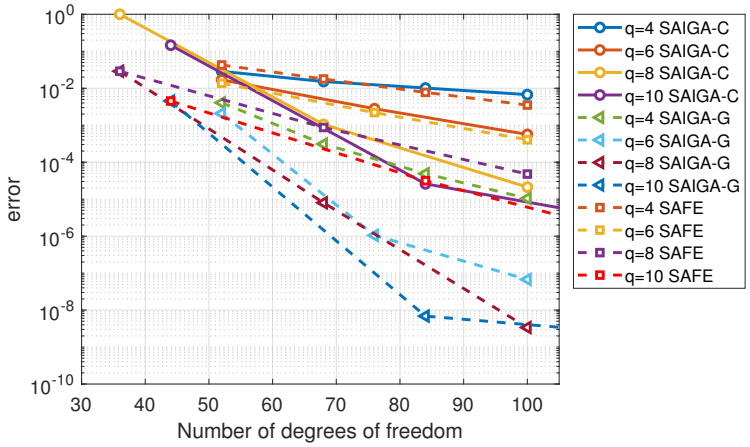

(a) ϕ=0.1

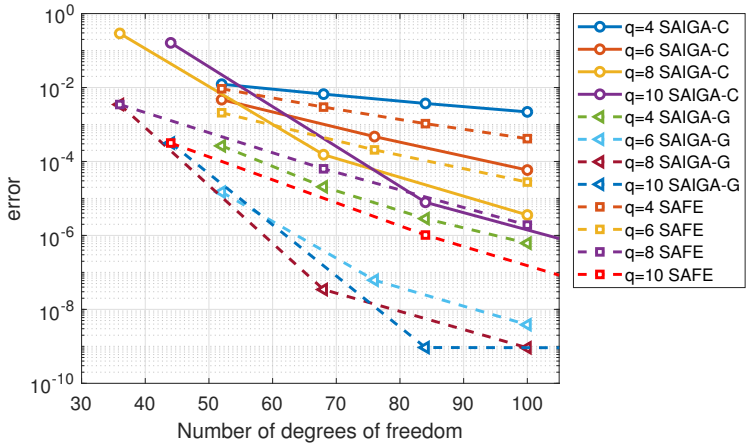

(b) ϕ=0.5

Figure 6.7 – (Color online) Error convergence of S_0-mode computed by using SAFE, SAIGA-C and SAIGA-G methods

(*i.e* the slope of the error curves) are shown to be increases when using higher-order Lagrangian shape function. A similar comment would be made regarding the errors of SAIGA-C solutions. It would also notice that the numerical errors of SAFE are slightly different than the one of SAIGA-C and this difference seems to be more significant when the porosity is higher ($\phi = 0.5$). However, the convergence rate of SAIGA-C, which is slower than of SAFE when using *low-order* basis functions ($q = 4, 6$), may be faster than when using *high-order* basis functions ($q = 8, 10$).

For both cases $\phi = 0.1$ and $\phi = 0.5$, it may be found that the SAIGA-G errors using a q-order NURBS basis function is much smaller comparing with the errors obtained from SAIGA-C or SAFE methods which used the same order basis function. For example, to achieve a solution having numerical error about 10^{-3}, while using $q = 6$ SAIGA-C and SAFE require solving a system of about N_{dof}=100, using $q = 6$ SAIGA-G only requires a system with only N_{dof}=56. Overall, the convergence rates *versus* N_{dof} using SAIGA-G method were shown to be much faster than using SAIGA-C or SAFE methods. Moreover, the numerical errors weren't significantly reduced by increasing q from 8 to 10. Hence, using $p = 8$ would be a reasonable choice for this problem in practice.

6.5.2 Case of a poroelastic plate immersed in fluids

Let us consider the case of a poroelastic bone plate, which has been studied in the previous section, but now is coupled with two half-spaces of water loaded on both sides as shown in Fig. 6.1. The acoustic properties of water are given by $\rho_1 = \rho_2 = 1000$ kg.m^{-3} and $c_1 = c_2 = 1500$ m.s^{-1}. The infinite fluid domains Ω_1^f and Ω_2^f are modeled as finite-thickness layers with $h_1^f = h_2^f = 4$ mm. To avoid the non-physical reflection from the upper and lower boundaries, we introduce 2.5 mm-thickness PMLs at the top $\bar{\Omega}_1^f$ and at the down of $\bar{\Omega}_2^f$, respectively. It worth notice the PMLs have been shown to be efficient for the SAFE-based simulation of leaky guided waves in several previous works [91, 41]. In this study, the range of frequencies of interest is from 0 to 2 MHz, then PML parameters h^{pml} (PML thickness) and $\gamma_2(x_2)$ (PML function) were chosen by: $\hat{\gamma}_2 = 3 + 12\text{i}$ and $h^{\text{pml}} = 2.5$ mm. In addition, free pressure boundary conditions ($p_j = 0$) were imposed at the exterior boundaries of two fluid domains.

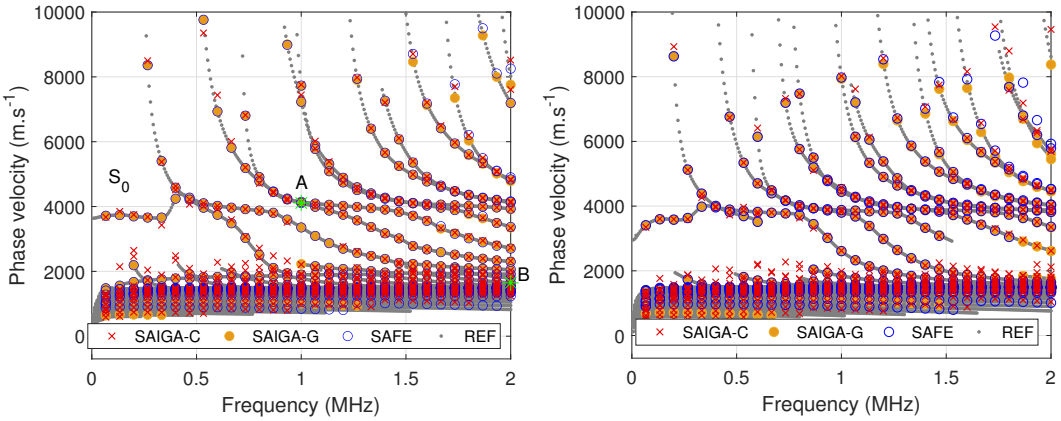

(a) $\phi = 0.1$ (b) $\phi = 0.5$

Figure 6.8 – (Color online) Dispersion curves of immersed poroelastic bone layer: comparison between the SAIGA-C ($q = 4$ and $N_{dof} = 118$), SAIGA-G ($q = 4$ and $N_{dof} = 118$) and SAFE ($q = 4$ and $N_{dof} = 118$) and REF solution ($q = 2$ and $N_{dof} = 566$).

Fig. 6.8 aims to compare the dispersion curves of leaky guided waves obtained using SAIGA-G, SAIGA-C and the conventional SAFE method with respect to the reference solution (REF) obtained by using SAFE with a very fine mesh. All of three solutions were computed by using $q = 4$ (NURBS or Lagrange functions), and all associated systems have $N_{\text{dof}} = 118$, in which the numbers of DOF in the poroelastic layer and each fluid layer are $N_{\text{dof}}^s = 68$ and $N_{\text{dof}}^{hs} = 25$, respectively. Two cases of porosity ($\phi = 0.1$ and $\phi = 0.5$) were considered as shown in Fig. 6.8(a) and Fig. 6.8(b), respectively. For both porosities, the SAIGA-G solutions were shown to have better agreement with the REF solutions. In the case $\phi = 0.1$, the numerical evaluation of C_{ph} using SAIGA-C or SAFE were failed for some modes (*e.g* on the S_0 branches). Note that similar issues has also been reported Hayashi *et al* [91] when studying an elastic plate immersed in fluids. Interestingly, it was found that using SAIGA-G method (with the same shape function order $q = 4$), allows to capture perfectly all the points along the dispersion curve. These results show the advantageous of NUBRS-based shape function in this context. In the case $\phi = 0.1$, SAIGA-C and SAFE have a significant errors at the higher modes and frequencies whereas SAIGA-G is in very good agreement with the REF solution. The good approximation of SAIGA-G bring to a better presentation of discontinuous modes.

The attenuation of the S_0 mode is presented in Fig 6.9 for the porosity of $\phi = 0.1$ and $\phi = 0.5$. In the case $\phi = 0.1$, it may be seen that the presence of exterior fluids completely changes the attenuation of the considered mode. In this case, as the porosity is small, the attenuation caused by Darcy's infiltration effect in the considered porelastic material is weak. Hence the main contribution to the attenuation to the S_0 mode is due to the leaky phenomena, in which some energies of guided-waves are leaked into the surrounded fluid domains. When the porosity is more important ($\phi = 0.5$), the Darcy's infiltration effect in the porous material becomes much more important. Consequently, the contribution of leaky effect to the attenuation of guided waves is not dominant, even it is shown to be very significant, especially at high frequency range.

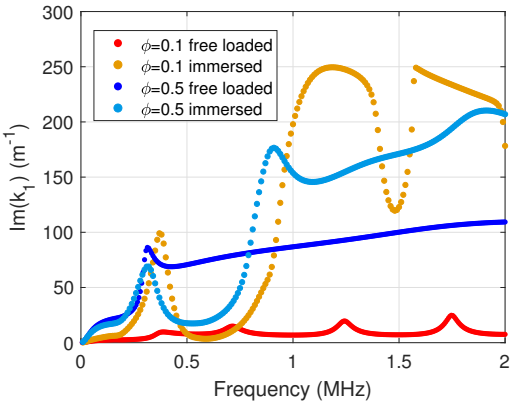

Figure 6.9 – (Color online) Attenuation curves of S_0 mode for $\phi = 0.1$ and $\phi = 0.5$ for (a) free loaded and (b) immersed poroelastic plate

In order to examine the continuity in the shape modes, we first consider a mode in the dispersion curve (marked as point A in Fig. 6.8) which has C_{ph}=4047 m.s^{-1} at f=1 MHz. Figures 6.10(a,b) present the shape modes of the displacement and pressure fields of this mode computed by three proposed methods. Note that the displacements in the fluid domains were derived from the gradient of pressure field (see Eq. 6.2). In the poroelastic layer, the stresses and pressure were derived the solutions of $\mathbf{U}$ and $\mathbf{W}$ by using Eqs. (6.3) and (6.9), respectively. At the fluid-solid interface, the expected conditions of continuity of u_2 and p was perfectly verified for the SAIGA-G's solutions. However, some small discontinuities were found when using SAFE or SAIGA-C methods. As it could be expected, the SAIGA and SAFE solutions of displacement (u_2) and pressure (p_j) fields are progressively attenuated in the PML domains. It has also been checked that the obtained numerical solutions are not influenced by the distance between the PML and the poroelastic-fluid interface (data not shown). Thus, the use of PMLs as shown in previous chapters is an efficient way to consider the halfspace fluid domains in the considered study.

We next consider a mode at high frequency (f = 2 MHz) which corresponds to the point B in Fig. 6.8(a)). Figs 6.11(a,b) depicts images of the displacement and pressure fields of this mode in the $(\mathbf{e}_1, \mathbf{e}_2)$ plane. The comparison of mode shapes computed by using SAFE, SAIGA-C and SAIGA-G methods are presented in Figs. 6.12(a,b,c,d). For this mode , using SAGA-G method ($q = 4$ and $N_{\text{dof}} = 118$) may produce perfectly the reference solutions of u_2, w_2, p and σ_{22}, which are expected to be continuous over all domains, even at the interfaces. However, at this high frequency, the considered mode shapes computed by SAFE and SAIGA-C methods, which were based on the same q and N_{dof}, may be found to be very erroneous, not only at the solid-fluid interfaces, but also over all domains. Hence, using the SAIGA-G method would be more appropriate for computing the mode shapes when higher frequency needs to considered.

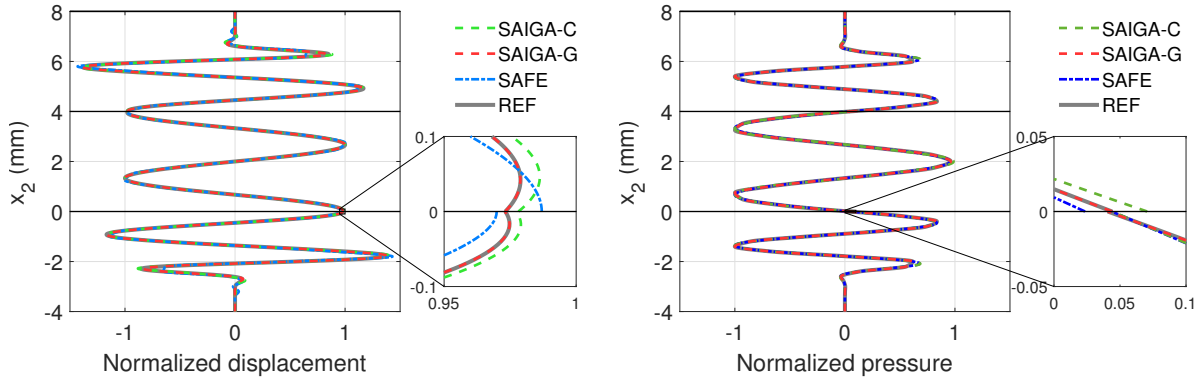

(a) displacement u_2^f, u_2, u_2^f (b) pressure p_1, p, p_2

Figure 6.10 – (Color online) Continuity of the mode shapes at f =1 MHz , C_{ph}=4047 m.s^{-1} (point A in Fig. 6.8(a)) of immersed poroelastic cortical bone plate $\phi = 0.1$: comparison between the SAIGA-C ($q = 4$ and $N_{dof} = 118$), SAIGA-G ($q = 4$ and $N_{dof} = 118$),SAFE ($q = 4$ and $N_{dof} = 118$) and REF solution ($q = 2$ and $N_{dof} = 566$).

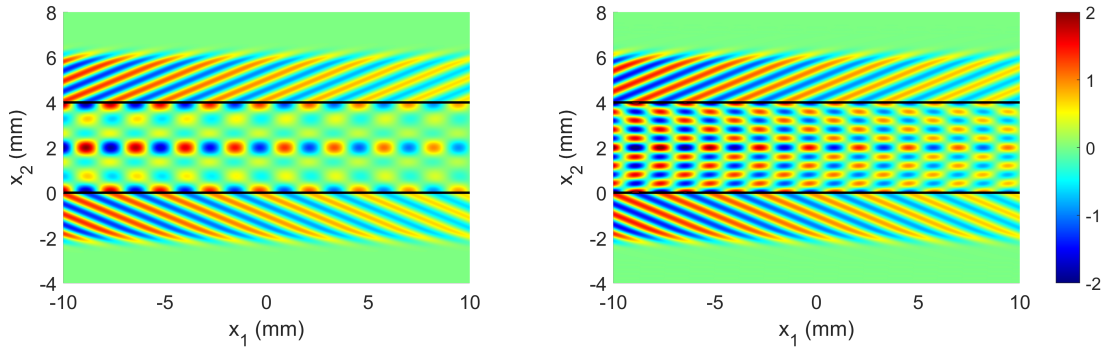

(a) displacement $u_2^{f_1}$, u_2, $u_2^{f_2}$ (b) pressure p_1, p^f, p_2

Figure 6.11 – (Color online) Leaky wave propagation in an immersed poroelastic plate $\phi = 0.1$: symmetric mode shapes at f =2 MHz , C_{ph}=2218 m.s^{-1} (point B in Fig. 6.8(a)) (a) displacement and (b) pressure fields

6.6 Conclusion

This presented works attempted to enlighten the potential of two SAIGA-based methods for studying the guided-waves in two-dimensional poroelastic plates coupled with fluids. To do so, two semi-analytical approaches, based on isogeometric Galerkin or collocation analysis (denoted by SAIGA-G and SAIGA-C, respectively) were proposed. Their efficiency in terms of the precision and the computational cost in compared with the conventional SAFE method were investigated. The numerical studies were carried out on two examples: (i) a free anisotropic poroelastic plate and (ii) a fluid-loaded anisotropic poroelastic plate. As the presence of the interstitial fluid in porous material may strongly attenuate guided waves in the poroelastic plate, especially when considering the cases of higher porosity and/or at high frequency, all solutions of the wavenumber are complex-valued and some criteria, which based on the the attenuation of modes, need to be introduced to select the propagating modes

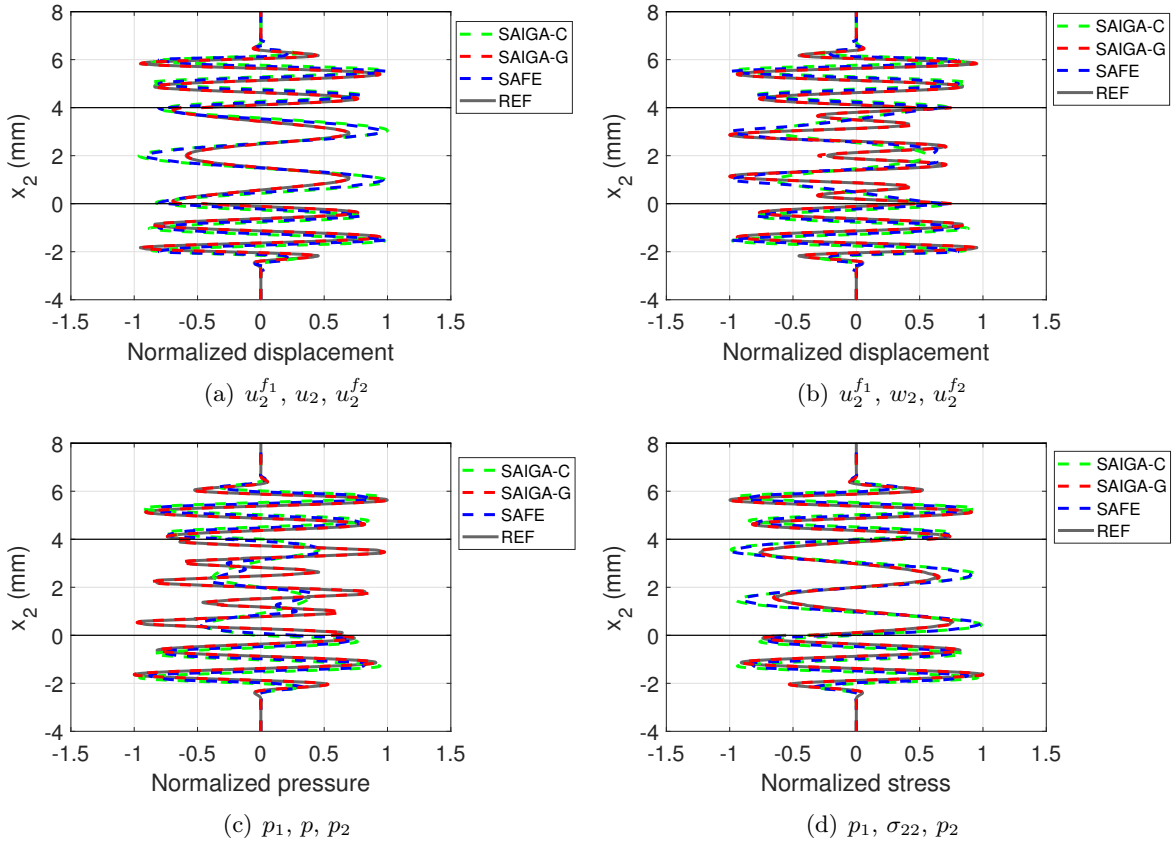

(a) $u_2^{f_1}$, u_2, $u_2^{f_2}$

(b) $u_2^{f_1}$, w_2, $u_2^{f_2}$

(c) p_1, p, p_2

(d) p_1, σ_{22}, p_2

Figure 6.12 – (Color online) Mode shapes at f=2 MHz , C_{ph}=2218 $m.s^{-1}$ (point B in Fig. 6.8(a)) for an immersed poroelastic cortical bone plate $\phi = 0.1$: comparison between the SAFE ($q = 4$ and $N_{dof} = 118$), SAIGA ($q = 4$ and $N_{dof} = 118$) and REF solution ($q = 2$ and $N_{dof} = 566$).

in the plate. Some remarks may be concluded from this numerical study as follows :

- The convergence analysis showed that increasing the order of NURBS basis function of the SAIGA-G method yields a much faster convergence rate in comparison with a similar procedure using the SAIGA-C and SAFE methods. For example, to obtain solutions with the same error (10^{-5}), while using SAFE and SAIGA-C method of order $q = 6$ requires solving a system of 120 DOFs, using SAIGA-G of order $q = 6$ functions only requires a system with 50 DOFs.

- When considering the waveguides immersed in a fluid, the SAIGA-G method also provided a much better prediction of the phase velocity as well of the mode shapes in compared with SAIGA-C and SAFE. The PMLs were also shown to be efficient for simulating the infinite surrounding fluid domains in the context.

- It was shown that using SAIGA-C method doesn't give significant advantages in terms of accuracy in comparison with the conventional SAFE method. However, the computational cost may be slightly reduced by using the SAIGA-C method. Note that this reduction of computational cost would be more significant when considering 3D structures in which the systems of equations with much larger number of DOF should be deal with. Furthermore, the implementation of SAIGA-C method, which is based on the discretization of strong forms, is straightforward and easier than the ones of SAFE or SAIGA-G methods, which are based on the discretization of weak forms [137].

The results results would be useful for choosing appropriate methods in practice. Furthermore, the proposed formulations can straightforwardly be extended for studying the dispersion of three-dimensional poroelastic guided-waves.

Chapter 7

Conclusion

In this work, numerical methods have been developed and applied in order to model the propagation of elastic guided waves in the heterogeneous and multiphysics media. These simulations are of high relevance in non-destructive testing and structural health monitoring applications as well as material characterization. The present work develops a highly efficient computational approach so-called semi-analytical isogeometric Galerkin (SAIGA-G) and semi analytical isogeometric collocation (SAIGA-C) to compute the wave dispersion in different types of waveguide possessing a complex geometry and/or heterogeneity. For the case where the waveguide is immersed in a fluid or coupled to a semi-infinite media, perfectly matched layers (PML) were employed and for which it has been shown that the method is very efficient for describing leaky guided-waves. These approaches are based on the use of Non-Uniform Rational B-splines (NURBS) in the framework of isogeometric analysis as the basis functions for the geometry representation as well as for the approximation of pressure/displacement solution fields. The difference between these two approaches is based on the use of numerical integration. The SAIGA-G uses a numerical integration of type Gauss quadrature to evaluate the integrals. However, the SAIGA-C deals directly with the strong form of the PDE. The IGA collocation method has been developed to combine the accuracy and the smoothness advantages of the IGA method with the computational efficiency of the collocation method. The dispersion curves (phase velocity, wavenumber and energy velocity) are obtained from the resolution of the eigenvalue problem. The main findings and contributions brought by this thesis can be summarised briefly as follows:

- The advantage of using higher order NURBS basis functions is more significant for computing the dispersion curves of functionally graded plates. We proposed a strategy to use only one patch to model multilayered plates which allows to obtain a very good continuity of the stresses at the interfaces of layers.
- When considering elastic waveguides coupled with fluids, using NURBS basis functions can significantly improve the evaluation of not only dispersed wavenumbers but also mode shapes. In particular, using SAIGA allows to obtain excellent continuity at the solid-fluid interface, which is much more difficult to achieve when using conventional SAFE. Moreover, it has been shown that waveguides immersed in an infinite fluid may efficiently be modeled by introducing perfectly matched layers (PML) and then employing SAIGA procedure.
- The convergence analysis showed that increasing the order of NURBS basis function of the SAIGA-G method yields a much faster convergence rate in comparison with a similar procedure using the SAIGA-C and SAFE methods.

- It was shown that using SAIGA-C method doesn't give significant advantages in terms of accuracy in comparison with the conventional SAFE method. However, the computational cost may be slightly reduced by using the SAIGA-C method. Note that this reduction of computational cost would be more significant when considering 3D structures in which the systems of equations with much larger number of DOF should be deal with. Furthermore, the implementation of SAIGA-C method, which is based the discretization of strong forms, is straightforward and easier than the ones of SAFE or SAIGA-G methods, which are based on the discretization of weak forms

Bibliography

[1] L. Gavrić, Computation of propagative waves in free rail using a finite element technique, Journal of Sound and Vibration 185 (3) (1995) 531–543.

[2] D. Thompson, C. Jones, Sound radiation from a vibrating railway wheel, Journal of Sound and Vibration 253 (2) (2002) 401–419.

[3] S. K. Dwivedi, M. Vishwakarma, A. Soni, Advances and researches on non destructive testing: A review, Materials Today: Proceedings 5 (2) (2018) 3690–3698.

[4] J. L. Rose, Ultrasonic guided waves in solid media, Cambridge University Press, 2014.

[5] M. Mitra, S. Gopalakrishnan, Guided wave based structural health monitoring: A review, Smart Materials and Structures 25 (5) (2016) 053001.

[6] Z. Su, L. Ye, Y. Lu, Guided Lamb waves for identification of damage in composite structures: A review, Journal of Sound and Vibration 295 (3-5) (2006) 753–780.

[7] X. Wei, Y. Yang, N. Yu, Research on broken rail real-time detection system for ultrasonic guided wave, in: 2017 International Conference on Electromagnetics in Advanced Applications (ICEAA), IEEE, 2017, pp. 906–909.

[8] H. Lamb, On waves in an elastic plate, Proceedings of the Royal Society of London. Series A, Containing papers of a mathematical and physical character 93 (648) (1917) 114–128.

[9] G. Hevin, O. Abraham, H. Pedersen, M. Campillo, Characterization of surface cracks with rayleigh waves: a numerical model, NDT & E International 31 (4) (1998) 289–297.

[10] R. Edwards, S. Dixon, X. Jian, Enhancement of the rayleigh wave signal at surface defects, Journal of Physics D: Applied Physics 37 (16) (2004) 2291.

[11] C.-W. In, J.-Y. Kim, K. E. Kurtis, L. J. Jacobs, Characterization of ultrasonic rayleigh surface waves in asphaltic concrete, NDT & E International 42 (7) (2009) 610–617.

[12] S. Foti, S. Parolai, D. Albarello, M. Picozzi, Application of surface-wave methods for seismic site characterization, Surveys in Geophysics 32 (6) (2011) 777–825.

[13] A. El Baroudi, J.-Y. Le Pommellec, Surface wave in a maxwell liquid-saturated poroelastic layer, Applied Acoustics 159 (2020) 107076.

[14] W. T. Thomson, Transmission of elastic waves through a stratified solid medium, Journal of Applied Physics 21 (2) (1950) 89–93.

[15] L. Knopoff, A matrix method for elastic wave problems, Bulletin of the Seismological Society of America 54 (1) (1964) 431–438.

[16] M. J. Lowe, Matrix techniques for modeling ultrasonic waves in multilayered media, IEEE transactions on ultrasonics, ferroelectrics, and frequency control 42 (4) (1995) 525–542.

[17] B. N. Pavlakovic, Leaky guided ultrasonic waves in ndt. (1998).

[18] C. Baron, Propagation of elastic waves in an anisotropic functionally graded hollow cylinder in vacuum, Ultrasonics 51 (2) (2011) 123–130.

[19] P. Shorter, Wave propagation and damping in linear viscoelastic laminates, The Journal of the Acoustical Society of America 115 (5) (2004) 1917–1925.

[20] N. A. Kampanis, V. Dougalis, J. A. Ekaterinaris, Effective computational methods for wave propagation, CRC Press, 2008.

[21] K. J. Bathe, Finite element procedures, Prentice Hall, 1996.

[22] R. Balasubramanyam, D. Quinney, R. Challis, C. Todd, A finite-difference simulation of ultrasonic Lamb waves in metal sheets with experimental verification, Journal of Physics D: Applied Physics 29 (1) (1996) 147.

[23] J. Virieux, P-sv wave propagation in heterogeneous media: Velocity-stress finite-difference method, Geophysics 51 (4) (1986) 889–901.

[24] C. Willberg, S. Duczek, J. V. Perez, D. Schmicker, U. Gabbert, Comparison of different higher order finite element schemes for the simulation of Lamb waves, Computer Methods in Applied Mechanics and Engineering 241 (2012) 246–261.

[25] C. Willberg, S. Duczek, J. Vivar-Perez, Z. Ahmad, Simulation methods for guided wave-based structural health monitoring: a review, Applied Mechanics Reviews 67 (1) (2015) 010803.

[26] S. K. Datta, A. H. Shah, R. Bratton, T. Chakraborty, Wave propagation in laminated composite plates, The Journal of the Acoustical Society of America 83 (6) (1988) 2020–2026.

[27] J. M. Galán, R. Abascal, Numerical simulation of Lamb wave scattering in semi-infinite plates, International Journal for Numerical Methods in Engineering 53 (5) (2002) 1145–1173.

[28] H. Gravenkamp, C. Song, J. Prager, A numerical approach for the computation of dispersion relations for plate structures using the scaled boundary finite element method, Journal of Sound and Vibration 331 (11) (2012) 2543–2557.

[29] F. Benmeddour, E. Moulin, J. Assaad, L. Dupont, Numerical investigation of the functionally graded materials by the interaction of the plate guided waves with discontinuities and cracks, in: Proceedings of Meetings on Acoustics ICA2013, Vol. 19, Acoustical Society of America, 2013, p. 030074.

[30] V. Maupin, The radiation modes of a vertically varying half-space: a new representation of the complete green's function in terms of modes, Geophysical Journal International 126 (3) (1996) 762–780.

[31] M. Mazzotti, A. Marzani, I. Bartoli, Dispersion analysis of leaky guided waves in fluid-loaded waveguides of generic shape, Ultrasonics 54 (1) (2014) 408 – 418.

[32] M. Mazzotti, I. Bartoli, A. Marzani, Ultrasonic leaky guided waves in fluid-coupled generic waveguides: hybrid finite-boundary element dispersion analysis and experimental validation, Journal of Applied Physics 115 (14) (2014) 143512.

[33] M. Mazzotti, I. Bartoli, A. Marzani, E. Viola, A coupled SAFE-2.5D BEM approach for the dispersion analysis of damped leaky guided waves in embedded waveguides of arbitrary cross-section, Ultrasonics 53 (7) (2013) 1227–1241.

[34] H. Gravenkamp, C. Birk, C. Song, Numerical modeling of elastic waveguides coupled to infinite fluid media using exact boundary conditions, Computers & Structures 141 (2014) 36–45.

[35] H. Gravenkamp, C. Birk, C. Song, Computation of dispersion curves for embedded waveguides using a dashpot boundary condition, The Journal of the Acoustical Society of America 135 (3) (2014) 1127–1138.

[36] A.-C. Hladky-Hennion, P. Langlet, R. Bossut, M. De Billy, Finite element modelling of radiating

waves in immersed wedges, Journal of Sound and Vibration 212 (2) (1998) 265–274.

[37] Z. Fan, M. Lowe, M. Castaings, C. Bacon, Torsional waves propagation along a waveguide of arbitrary cross section immersed in a perfect fluid, The Journal of the Acoustical Society of America 124 (4) (2008) 2002–2010.

[38] M. Castaings, M. Lowe, Finite element model for waves guided along solid systems of arbitrary section coupled to infinite solid media, The Journal of the Acoustical Society of America 123 (2) (2008) 696–708.

[39] F. Treyssede, K.-L. Nguyen, A.-S. Bonnet-BenDhia, C. Hazard, Finite element computation of trapped and leaky elastic waves in open stratified waveguides, Wave Motion 51 (7) (2014) 1093–1107.

[40] F. Treyssede, Spectral element computation of high-frequency leaky modes in three-dimensional solid waveguides, Journal of Computational Physics 314 (2016) 341–354.

[41] P. Zuo, Z. Fan, SAFE-PML approach for modal study of waveguides with arbitrary cross sections immersed in inviscid fluid, Journal of Sound and Vibration 406 (2017) 181–196.

[42] J. M. de Oliveira Barbosa, J. Park, E. Kausel, Perfectly matched layers in the thin layer method, Computer Methods in Applied Mechanics and Engineering 217 (2012) 262–274.

[43] M. Gallezot, F. Treyssede, L. Laguerre, A modal approach based on perfectly matched layers for the forced response of elastic open waveguides, Journal of Computational Physics 356 (2018) 391–409.

[44] M. A. Biot, Theory of elasticity and consolidation for a porous anisotropic solid, Journal of Applied physics 26 (2) (1955) 182–185.

[45] M. A. Biot, Theory of propagation of elastic waves in a fluid-saturated porous solid. ii. higher frequency range, The Journal of the Acoustical Society of America 28 (2) (1956) 179–191.

[46] M. A. Biot, D. Willis, The elastic coefficients of the theory of consolidation, J. Appl. Mech 24 (1957) 594–601.

[47] K. Terzaghi, et al., Erdbaumechanik auf bodenphysikalischer grundlage (1925).

[48] V.-H. Nguyen, S. Naili, Simulation of ultrasonic wave propagation in anisotropic poroelastic bone plate using hybrid spectral/finite element method, International Journal for Numerical Methods in Biomedical Engineering 28 (8) (2012) 861–876.

[49] T. J. Hughes, The finite element method: linear static and dynamic finite element analysis, Courier Corporation, 2012.

[50] K.-L. Nguyen, F. Treyssede, C. Hazard, Numerical modeling of three-dimensional open elastic waveguides combining semi-analytical finite element and perfectly matched layer methods, Journal of Sound and Vibration 344 (2015) 158–178.

[51] F. Teixeira, W. C. Chew, Complex space approach to perfectly matched layers: a review and some new developments, International Journal of Numerical Modelling: Electronic Networks, Devices and Fields 13 (5) (2000) 441–455.

[52] C. Soize, Non-gaussian positive-definite matrix-valued random fields for elliptic stochastic partial differential operators, Computer Methods in Applied Mechanics and Engineering 195 (1-3) (2006) 26–64.

[53] V.-H. Nguyen, A. Abdoulatuf, C. Desceliers, S. Naili, A probabilistic study of reflection and transmission coefficients of random anisotropic elastic plates, Wave Motion 64 (2016) 103–118.

[54] E. T. Jaynes, Information theory and statistical mechanics, Physical Review 106 (4) (1957) 620.

[55] E. T. Jaynes, Information theory and statistical mechanics. ii, Physical Review 108 (2) (1957) 171.

[56] M. L. Mehta, Random matrices, Elsevier, 2004.

[57] C. Soize, Maximum entropy approach for modeling random uncertainties in transient elastodynamics, The Journal of the Acoustical Society of America 109 (5) (2001) 1979–1996.

[58] V.-H. Nguyen, S. Naili, V. Sansalone, Simulation of ultrasonic wave propagation in anisotropic cancellous bone immersed in fluid, Wave Motion 47 (2) (2010) 117–129.

[59] V.-H. Nguyen, S. Naili, Ultrasonic wave propagation in viscoelastic cortical bone plate coupled with fluids: a spectral finite element study, Computer Methods in Biomechanics and Biomedical Engineering 16 (9) (2013) 963–974.

[60] D. Pereira, G. Haiat, J. Fernandes, P. Belanger, Simulation of acoustic guided wave propagation in cortical bone using a semi-analytical finite element method, The Journal of the Acoustical Society of America 141 (4) (2017) 2538–2547.

[61] T. N. Tran, L. H. Le, M. D. Sacchi, V.-H. Nguyen, Sensitivity analysis of ultrasonic guided waves propagating in trilayered bone models: a numerical study, Biomechanics and Modeling in Mechanobiology 17 (5) (2018) 1269–1279.

[62] L. Wang, S. P. Fritton, S. C. Cowin, S. Weinbaum, Fluid pressure relaxation depends upon osteonal microstructure: modeling an oscillatory bending experiment, Journal of Biomechanics 32 (7) (1999) 663–672.

[63] V.-H. Nguyen, T. Lemaire, S. Naili, Poroelastic behaviour of cortical bone under harmonic axial loading: A finite element study at the osteonal scale, Medical engineering & physics 32 (4) (2010) 384–390.

[64] X. N. Dong, X. E. Guo, The dependence of transversely isotropic elasticity of human femoral cortical bone on porosity, Journal of Biomechanics 37 (8) (2004) 1281–1287.

[65] C. Aristegui, M. Lowe, P. Cawley, Guided waves in fluid-filled pipes surrounded by different fluids, Ultrasonics 39 (5) (2001) 367–375.

[66] A. V. Astaneh, M. N. Guddati, Dispersion analysis of composite acousto-elastic waveguides, Composites Part B: Engineering 130 (2017) 200–216.

[67] M. Lowe, B. Pavlakovic., DISPERSE. Users Manual (2013).

[68] M. K. Kalkowski, J. M. Muggleton, E. Rustighi, Axisymmetric semi-analytical finite elements for modelling waves in buried/submerged fluid-filled waveguides, Computers & Structures 196 (2018) 327–340.

[69] S. C. Cowin, et al., Bone mechanics handbook, CRC press, 2001.

[70] F. Seyfaddini, H. Nguyen-Xuan, V.-H. Nguyen, A semi-analytical isogeometric analysis for wave dispersion in functionally graded plates immersed in fluids, Acta Mechanica 232 (2021) 15–32.

[71] R. Echter, B. Oesterle, M. Bischoff, A hierarchic family of isogeometric shell finite elements, Computer Methods in Applied Mechanics and Engineering 254 (2013) 170 – 180.

[72] C. H. Thai, H. Nguyen-Xuan, N. Nguyen-Thanh, T.-H. Le, T. Nguyen-Thoi, T. Rabczuk, Static, free vibration, and buckling analysis of laminated composite Reissner–Mindlin plates using NURBS-based isogeometric approach, International Journal for Numerical Methods in Engineering 91 (6) (2012) 571–603.

[73] C. H. Thai, S. Kulasegaram, L. V. Tran, H. Nguyen-Xuan, Generalized shear deformation theory for functionally graded isotropic and sandwich plates based on isogeometric approach, Computers & Structures 141 (2014) 94–112.

[74] H. X. Nguyen, E. Atroshchenko, H. Nguyen-Xuan, T. P. Vo, Geometrically nonlinear isogeometric analysis of functionally graded microplates with the modified couple stress theory, Computers & Structures 193 (2017) 110–127.

[75] Y. Bazilevs, I. Akkerman, Large eddy simulation of turbulent taylor-couette flow using isogeometric analysis and the residual-based variational multiscale method, Journal of Computational Physics 229 (9) (2010) 3402 – 3414.

[76] J. Cottrell, A. Reali, Y. Bazilevs, T. Hughes, Isogeometric analysis of structural vibrations, Computer Methods in Applied Mechanics and Engineering 195 (41) (2006) 5257 – 5296.

[77] D. Wang, W. Liu, H. Zhang, Novel higher order mass matrices for isogeometric structural vibration analysis, Computer Methods in Applied Mechanics and Engineering 260 (2013) 92 – 108.

[78] Y. Bazilevs, L. Beirao da Veiga, J. A. Cottrell, T. J. Hughes, G. Sangalli, Isogeometric analysis: approximation, stability and error estimates for h-refined meshes, Mathematical Models and Methods in Applied Sciences 16 (07) (2006) 1031–1090.

[79] J. Cottrell, T. Hughes, A. Reali, Studies of refinement and continuity in isogeometric structural analysis, Computer Methods in Applied Mechanics and Engineering 196 (41) (2007) 4160 – 4183.

[80] T. J. Hughes, J. A. Evans, A. Reali, Finite element and NURBS approximations of eigenvalue, boundary-value, and initial-value problems, Computer Methods in Applied Mechanics and Engineering 272 (2014) 290 – 320.

[81] T. Hughes, A. Reali, G. Sangalli, Duality and unified analysis of discrete approximations in structural dynamics and wave propagation: Comparison of p-method finite elements with k-method NURBS, Computer Methods in Applied Mechanics and Engineering 197 (49) (2008) 4104 – 4124.

[82] L. DedÃ¨, C. JÃ¤ggli, A. Quarteroni, Isogeometric numerical dispersion analysis for two-dimensional elastic wave propagation, Computer Methods in Applied Mechanics and Engineering 284 (2015) 320 – 348.

[83] Y. Liu, Q. Han, Y. Liang, G. Xu, Numerical investigation of dispersive behaviors for helical thread waveguides using the semi-analytical isogeometric analysis method, Ultrasonics 83 (2018) 126–136.

[84] H. Gravenkamp, S. Natarajan, W. Dornisch, On the use of NURBS-based discretizations in the scaled boundary finite element method for wave propagation problems, Computer Methods in Applied Mechanics and Engineering 315 (2017) 867–880.

[85] P. Zuo, X. Yu, Z. Fan, Numerical modeling of embedded solid waveguides using SAFE-PML approach using a commercially available finite element package, NDT & E International 90 (2017) 11–23.

[86] L. Piegl, W. Tiller, The NURBS book, Springer Science & Business Media, 2012.

[87] J. A. Cottrell, T. J. Hughes, Y. Bazilevs, Isogeometric analysis: toward integration of CAD and FEA, John Wiley & Sons, 2009.

[88] A. Bernard, M. Lowe, M. Deschamps, Guided waves energy velocity in absorbing and non-absorbing plates, The Journal of the Acoustical Society of America 110 (1) (2001) 186–196.

[89] J. M. Carcione, Wave fields in real media: Wave propagation in anisotropic, anelastic, porous and electromagnetic media, Vol. 38, Elsevier, 2007.

[90] T. Tjahjowidodo, et al., A direct method to solve optimal knots of B-spline curves: An application for non-uniform B-spline curves fitting, PloS One 12 (3) (2017) e0173857.

[91] T. Hayashi, D. Inoue, Calculation of leaky Lamb waves with a semi-analytical finite element method, Ultrasonics 54 (6) (2014) 1460 – 1469.

[92] F. Seyfaddini, H. Nguyen-Xuan, V.-H. Nguyen, Wave dispersion analysis of three-dimensional vibroacoustic waveguides with semi-analytical isogeometric method, Computer Methods in Ap-

plied Mechanics and Engineering 385 (2021) 114043.

[93] C. Li, Q. Han, Y. Liu, Z. Wang, Wave isogeometric analysis method for calculating dispersive properties of guided waves in rotating damped cylinders, Meccanica 54 (1) (2019) 169–182.

[94] Y. Liu, S. Lin, Y. Li, C. Li, Y. Liang, Numerical investigation of rayleigh waves in layered composite piezoelectric structures using the siga-pml approach, Composites Part B: Engineering 158 (2019) 230–238.

[95] V.-H. Nguyen, T. N. Tran, M. D. Sacchi, S. Naili, L. H. Le, Computing dispersion curves of elastic/viscoelastic transversely-isotropic bone plates coupled with soft tissue and marrow using semi-analytical finite element (SAFE) method, Computers in Biology and Medicine 87 (2017) 371–381.

[96] J. H. Gosman, Z. R. Hubbell, C. N. Shaw, T. M. Ryan, Development of cortical bone geometry in the human femoral and tibial diaphysis, The Anatomical Record 296 (5) (2013) 774–787.

[97] B. Hosten, M. Castaings, Transfer matrix of multilayered absorbing and anisotropic media. measurements and simulations of ultrasonic wave propagation through composite materials, The Journal of the Acoustical Society of America 94 (3) (1993) 1488–1495.

[98] E. Kausel, Fundamental solutions in elastodynamics: a compendium, Cambridge University Press, 2006.

[99] C. Baron, S. Naili, Propagation of elastic waves in a fluid-loaded anisotropic functionally graded waveguide: Application to ultrasound characterization, The Journal of the Acoustical Society of America 127 (3) (2010) 1307–1317.

[100] A. Geslain, J.-P. Groby, O. Dazel, S. Mahasaranon, K. Horoshenkov, A. Khan, An application of the peano series expansion to predict sound propagation in materials with continuous pore stratification, The Journal of the Acoustical Society of America 132 (1) (2012) 208–215.

[101] O. Dazel, J.-P. Groby, B. Brouard, C. Potel, A stable method to model the acoustic response of multilayered structures, Journal of Applied Physics 113 (8) (2013) 083506.

[102] J. Jocker, D. Smeulders, G. Drijkoningen, C. van der Lee, A. Kalfsbeek, Matrix propagator method for layered porous media: Analytical expressions and stability criteria, Geophysics 69 (4) (2004) 1071–1081.

[103] H. Liu, S. Finnveden, M. Barbagallo, I. Lopez Arteaga, Wave propagation in sandwich panels with a poroelastic core, The Journal of the Acoustical Society of America 135 (5) (2014) 2683–2693.

[104] Z. E. A. Fellah, J. Y. Chapelon, S. Berger, W. Lauriks, C. Depollier, Ultrasonic wave propagation in human cancellous bone: Application of biot theory, The Journal of the Acoustical Society of America 116 (1) (2004) 61–73.

[105] A. K. Vashishth, P. Khurana, Waves in stratified anisotropic poroelastic media: a transfer matrix approach, Journal of Sound and Vibration 277 (1-2) (2004) 239–275.

[106] D. Komatitsch, J.-P. Vilotte, The spectral element method: an efficient tool to simulate the seismic response of 2d and 3d geological structures, Bulletin of the seismological society of America 88 (2) (1998) 368–392.

[107] C. Baron, S. Naili, Elastic wave propagation in a fluid-loaded anisotropic waveguide with laterally varying properties, Comptes Rendus Mecanique 336 (9) (2008) 722–730.

[108] A. Shuvalov, O. Poncelet, M. Deschamps, Analysis of the dispersion spectrum of fluid-loaded anisotropic plates: leaky-wave branches, Journal of Sound and Vibration 296 (3) (2006) 494–517.

[109] E. Bossy, M. Talmant, P. Laugier, Effect of bone cortical thickness on velocity measurements using ultrasonic axial transmission: A 2D simulation study, The Journal of the Acoustical

Society of America 112 (1) (2002) 297–307.

[110] Q. Grimal, S. Naïli, A theoretical analysis in the time-domain of wave reflection on a bone plate, Journal of Sound and Vibration 298 (1-2) (2006) 12–29.

[111] G. Haïat, S. Naili, Q. Grimal, M. Talmant, C. Desceliers, C. Soize, Influence of a gradient of material properties on ultrasonic wave propagation in cortical bone: Application to axial transmission, The Journal of the Acoustical Society of America 125 (6) (2009) 4043–4052.

[112] S. C. Cowin, Bone poroelasticity, Journal of Biomechanics 32 (3) (1999) 217–238.

[113] D. Zhang, S. C. Cowin, Oscillatory bending of a poroelastic beam, Journal of the Mechanics and Physics of Solids 42 (10) (1994) 1575–1599.

[114] V.-H. Nguyen, T. Lemaire, S. Naili, Influence of interstitial bone microcracks on strain-induced fluid flow, Biomechanics and Modeling in Mechanobiology 10 (6) (2011) 963–972.

[115] J. L. Williams, Ultrasonic wave propagation in cancellous and cortical bone: Prediction of some experimental results by biot's theory, The Journal of the Acoustical Society of America 91 (2) (1992) 1106–1112.

[116] Y. Nagatani, K. Mizuno, T. Saeki, M. Matsukawa, T. Sakaguchi, H. Hosoi, Numerical and experimental study on the wave attenuation in bone–fdtd simulation of ultrasound propagation in cancellous bone, Ultrasonics 48 (6-7) (2008) 607–612.

[117] V.-H. Nguyen, S. Naili, V. Sansalone, A closed-form solution for in vitro transient ultrasonic wave propagation in cancellous bone, Mechanics Research Communications 37 (4) (2010) 377–383.

[118] V.-H. Nguyen, S. Naili, Semi-analytical solution of transient plane waves transmitted through a transversely isotropic poroelastic plate immersed in fluid, Journal of Engineering Mathematics 86 (1) (2014) 125–138.

[119] V. Bousson, A. Meunier, C. Bergot, É. Vicaut, M. A. Rocha, M. H. Morais, A.-M. Laval-Jeantet, J.-D. Laredo, Distribution of intracortical porosity in human midfemoral cortex by age and gender, Journal of Bone and Mineral Research 16 (7) (2001) 1308–1317.

[120] C. D. L. Thomas, S. A. Feik, J. G. Clement, Regional variation of intracortical porosity in the midshaft of the human femur: age and sex differences, Journal of Anatomy 206 (2) (2005) 115–125.

[121] C. Hellmich, F.-J. Ulm, Microporodynamics of bones: prediction of the Frenkel–Biot slow compressional wave, Journal of Engineering Mechanics 131 (9) (2005) 918–927.

[122] G. Rosi, V.-H. Nguyen, S. Naili, Numerical investigations of ultrasound wave propagating in long bones using a poroelastic model, Mathematics and Mechanics of Solids 21 (1) (2016) 119–133.

[123] A.-D. Cheng, Material coefficients of anisotropic poroelasticity, International Journal of Rock Mechanics and Mining Sciences 34 (2) (1997) 199–205.

[124] M. Thompson, J. Willis, A reformation of the equations of anisotropic poroelasticity, Journal of Applied Mechanics 58 (3) (1991) 612–616.

[125] N. Gorbushin, S. Naili, V.-H. Nguyen, Optimizing microstructure of a poroelastic layer with cylindrical pores for absorption properties, Mechanics Research Communications 102 (2019) 103422.

[126] N. Gorbushin, V.-H. Nguyen, S. Naili, Design optimisation of acoustic absorbers with cross-like pores via a homogenisation method, Acta Acustica United with Acustica 105 (4) (2019) 638–649.

[127] J. Allard, N. Atalla, Propagation of sound in porous media: modelling sound absorbing mate-

rials, John Wiley & Sons, 2009.

[128] D. Chimenti, Review of air-coupled ultrasonic materials characterization, Ultrasonics 54 (7) (2014) 1804–1816.

[129] M. Thelen, N. Bochud, M. Brinker, C. Prada, P. Huber, Laser-excited elastic guided waves reveal the complex mechanics of nanoporous silicon, arXiv preprint arXiv:2010.14947 (2020).

[130] O. Coussy, Poromechanics, John Wiley & Sons, 2004.

[131] S. Morganti, C. Callari, F. Auricchio, A. Reali, Mixed isogeometric collocation methods for the simulation of poromechanics problems in 1D, Meccanica 53 (6) (2018) 1441–1454.

[132] F. Auricchio, L. B. Da Veiga, T. J. Hughes, A. Reali, G. Sangalli, Isogeometric collocation for elastostatics and explicit dynamics, Computer Methods in Applied Mechanics and Engineering 249 (2012) 2–14.

[133] F. Seyfaddini, H. Nguyen-Xuan, V.-H. Nguyen, Semi-analytical iga-based computation of wave dispersion in fluid-coupled anisotropic poroelastic plates, International Journal of Mechanical Sciences (2021) 106830.

[134] S. C. Cowin, A recasting of anisotropic poroelasticity in matrices of tensor components, Transport in Porous Media 50 (1-2) (2003) 35–56.

[135] D. L. Johnson, J. Koplik, R. Dashen, Theory of dynamic permeability and tortuosity in fluid-saturated porous media, Journal of Fluid Mechanics 176 (1987) 379–402.

[136] J. O. Parra, P.-c. Xu, Dispersion and attenuation of acoustic guided waves in layered fluid-filled porous media, The Journal of the Acoustical Society of America 95 (1) (1994) 91–98.

[137] A. Reali, T. J. Hughes, An introduction to isogeometric collocation methods, in: Isogeometric methods for numerical simulation, Springer, 2015, pp. 173–204.